



applied sciences

Applications of Molecularly Imprinted Films

Edited by

Andrei Sarbu

Printed Edition of the Special Issue Published in *Applied Sciences*

Applications of Molecularly Imprinted Films

Applications of Molecularly Imprinted Films

Editor

Andrei Sarbu

MDPI • Basel • Beijing • Wuhan • Barcelona • Belgrade • Manchester • Tokyo • Cluj • Tianjin



Editor

Andrei Sarbu

The National Institute for Research & Development in
Chemistry and Petrochemistry—ICECHIM
Romania

Editorial Office

MDPI

St. Alban-Anlage 66
4052 Basel, Switzerland

This is a reprint of articles from the Special Issue published online in the open access journal *Applied Sciences* (ISSN 2076-3417) (available at: https://www.mdpi.com/journal/applsci/special_issues/molecularly_imprinted_films).

For citation purposes, cite each article independently as indicated on the article page online and as indicated below:

LastName, A.A.; LastName, B.B.; LastName, C.C. Article Title. <i>Journal Name</i> Year , Volume Number, Page Range.
--

ISBN 978-3-0365-5403-7 (Hbk)

ISBN 978-3-0365-5404-4 (PDF)

© 2022 by the authors. Articles in this book are Open Access and distributed under the Creative Commons Attribution (CC BY) license, which allows users to download, copy and build upon published articles, as long as the author and publisher are properly credited, which ensures maximum dissemination and a wider impact of our publications.

The book as a whole is distributed by MDPI under the terms and conditions of the Creative Commons license CC BY-NC-ND.

Contents

About the Editor	vii
----------------------------	-----

Andrei Sarbu

Special Issue on the Applications of Molecularly Imprinted Films Reprinted from: <i>Appl. Sci.</i> 2022 , <i>12</i> , 8533, doi:10.3390/app12178533	1
---	---

Sónia Cláudia Ribeiro, Rúben Fernandes, Felismina T. C. Moreira and Maria Goreti Ferreira Sales

Potentiometric Biosensor Based on Artificial Antibodies for an Alzheimer Biomarker Detection Reprinted from: <i>Appl. Sci.</i> 2022 , <i>12</i> , 3625, doi:10.3390/app12073625	5
---	---

Thandiwe Crystal Totito, Katri Laatikainen, Omoniyi Perea, Chris Bode-Aluko and Leslie Petrik

Adsorptive Recovery of Cu ²⁺ from Aqueous Solution by Polyethylene Terephthalate Nanofibres Modified with 2-(Aminomethyl)Pyridine Reprinted from: <i>Appl. Sci.</i> 2021 , <i>11</i> , 11912, doi:10.3390/app112411912	19
--	----

Maria Pesavento, Nunzio Cennamo, Luigi Zeni and Letizia De Maria

A Molecularly Imprinted Polymer Based SPR Sensor for 2-Furaldehyde Determination in Oil Matrices Reprinted from: <i>Appl. Sci.</i> 2021 , <i>11</i> , 10390, doi:10.3390/app112110390	45
--	----

Ana-Mihaela Gavrila, Ionut-Cristian Radu, Hermine Stroescu, Anamaria Zaharia, Elena-Bianca Stoica, Ana-Lorena Ciurlica, Tanța-Verona Iordache and Andrei Sârbu

Role of Functional Monomers upon the Properties of Bisphenol A Molecularly Imprinted Silica Films Reprinted from: <i>Appl. Sci.</i> 2021 , <i>11</i> , 2956, doi:10.3390/app11072956	59
---	----

Ana-Mihaela Gavrila, Elena-Bianca Stoica, Tanța-Verona Iordache and Andrei Sârbu

Modern and Dedicated Methods for Producing Molecularly Imprinted Polymer Layers in Sensing Applications Reprinted from: <i>Appl. Sci.</i> 2022 , <i>12</i> , 3080, doi:10.3390/app12063080	75
---	----

About the Editor

Andrei Sarbu

Andrei Sarbu. Graduated in 1972 from the University “Politehnica” Bucharest, Faculty of Industrial Chemistry. In 1984, he received a doctoral degree in engineering from the University for Oil and Natural Gas Ploiesti. In the period of 1972 to 2022, he has been researcher at the National Research—Development Institute for Chemistry and Petrochemistry—ICECHIM in Bucharest, where he worked in the Polymer Department. Since 1990, he has been the main scientific researcher. From 2004 until 2013, he was the Vice Director of the Polymer Department. Between 2013 and 2020, he was the leader of Team 1: Polymer Advanced Materials and Polymer Recycling. He has written 230 technological research works and has 155 published and accepted papers (124 ISI); He has also written 4 book chapters, 444 scientific communications, and 43 patents, including 1 European patent and 19 patent application. Between 1990 and 2008, he was an associated teacher at the University “Politehnica” Bucharest, Faculty of Industrial Chemistry. From 2003 to 2021, he was an associated researcher at the University of Bucharest, PROTMED Center. From May 2000 to May 2002, he was an invited researcher at the Technical Superior Institute of Lisbon. From 2011 to 2022, he has been invited to spend between 2 weeks to 1 month as a professor at the University of Toulon.

Editorial

Special Issue on the Applications of Molecularly Imprinted Films

Andrei Sarbu

Team 1, Polymer Department, National Institute for Research & Development for Chemistry and Petrochemistry—ICECHIM, Spl. Independentei 202, Sector 6, 060021 Bucharest, Romania; andr.sarbu@gmail.com

1. Introduction

Modern separation science and technology require the development of new materials with enhanced properties that are able to separate a substance from complex matrices. To this end, a great deal of research has attempted to develop and characterize highly selective new materials. One innovative way of improving the selectivity and retention capacity is to develop molecularly imprinted polymers (MIPs).

The most common definition of this new class is that they are polymers possessing voids with a shape, size, and group functionality complementary to the molecule used for the imprinting, known as the template. In order to understand the principle underlying MIP preparation, we can imagine a coin being pushed into plasticine. When the coin is taken off the plasticine, a trace remains, having the shape and size of the face of the coin that was pushed into it. If one does the same thing with a template molecule in a polymer matrix, firstly, a composite is obtained at a molecular scale. After the template extraction, a MIP is prepared with voids corresponding to the shape, size, and group functionality of the template. It is very important to keep these voids unchanged after the template extraction. To achieve this, structure stabilization is required, with properties such as a high degree of crosslinking. The MIP preparation methods presented in the state-of-the-art studies can be divided into two categories: chemical methods, based on polymerization (bulk [1], suspension [2], emulsion [3], precipitation [4], etc.) or on sol-gel reactions, [5] and physical methods, referring especially to phase inversion [6], which are implemented far more rarely. MIPs can be produced in various shapes, such as beads [7,8], pearls [9], irregular particles [10], hydrogels [11], membranes [12], and films [13]. Due to the requirement that MIPs have a high specific surface, a very fast-growing area of development concerns the use of membranes and films. The application of these new materials refers mostly to the purification of a liquid, the separation of a substance from a complex mixture, analysis, and sensing, but other applications have been studied as well, such as catalysis or the slow release of bioactive substances, explaining the need for this Special Issue of *Applied Sciences*. However, the sensing surfaces and the solid phase extraction are at present the main application methods of MIPs membranes and films.

2. Molecularly Imprinted Films

This Special Issue contains five articles, four research articles, and one review.

The first paper, “Role of Functional Monomers upon the Properties of Bisphenol A Molecularly Imprinted Silica Films” [14], is dedicated to the production of molecularly imprinted films using a chemical method, namely the sol-gel process for preparing sensitive layers of biomimetic sensors. Two types of MIPs were prepared based on two different organosilane functional monomers, N-(2-aminoethyl)-3-aminopropyl trimethoxysilane (DAMO-T) or (3-mercaptopropyl) trimethoxysilane (MPTES).

The second paper, “A Molecularly Imprinted Polymer Based SPR Sensor for 2-Furaldehyde Determination in Oil Matrices” [15], is also dedicated to optical biomimetic sensors and based on surface plasmonic resonance (SPR). For this purpose, a polymer optical fibre (POF) was used.

Citation: Sarbu, A. Special Issue on the Applications of Molecularly Imprinted Films. *Appl. Sci.* **2022**, *12*, 8533. <https://doi.org/10.3390/app12178533>

Received: 29 June 2022

Accepted: 24 August 2022

Published: 26 August 2022

Publisher’s Note: MDPI stays neutral with regard to jurisdictional claims in published maps and institutional affiliations.



Copyright: © 2022 by the author. Licensee MDPI, Basel, Switzerland. This article is an open access article distributed under the terms and conditions of the Creative Commons Attribution (CC BY) license (<https://creativecommons.org/licenses/by/4.0/>).

Another article published in this Special Issue and dedicated to sensors is “Potentiometric Biosensor Based on Artificial Antibodies for an Alzheimer Biomarker Detection” [16]. In this case, an electrochemical biomimetic sensor was targeted. This paper presented a potentiometric biosensor for the detection of amyloid-42 (A-42) in a point-of-care analysis.

The fourth article, namely, “Modern and Dedicated Methods for Producing Molecularly Imprinted Polymer Layers in Sensing Applications” [17], is a review, presenting the main approaches to sensing surface preparation.

The last article in this Special Issue, “Adsorptive Recovery of Cu^{2+} from Aqueous Solution by Polyethylene Terephthalate Nanofibers Modified with 2-(aminomethyl) Pyridine” [18], deals with the second main field of the application of MIP surfaces, namely, the solid phase extraction. In this study, a solution of modified PET or waste PET from plastic bottles was prepared, to which a silica-supported 2-(aminomethyl)pyridine powder was added, and the mixed solution was electrospun into composite nano-fibres.

3. Future of Molecularly Imprinted Films

Although this Special Issue has been concluded, more in-depth research on MIP films and membranes is expected. It can be predicted that more films and membranes with improved characteristics, such as selectivity and permeability, will be produced, and that the application fields will be expanded to include, for instance, enantiomer detection and separation.

Funding: This work was funded by the Romanian Funding Agency UEFISCDI, through the supporting Project no. 157ERA-NET/2020 COFUND-BLUEBIO-BIOSHELL and by the Ministry of Research, Innovation and Digitalization through project NUCLEU PN.19.23.02.01 (Sub-theme MAT-INNOVA).

Acknowledgments: Thanks are due to all the authors and peer reviewers for their valuable contributions to this Special Issue. I am also indebted to the editorial team of *Applied Sciences* for their constant support, particularly Delia Pan.

Conflicts of Interest: The authors declare no conflict of interest.

References

- Long, J.P.; Chen, Z.B. Preparation and Adsorption Property of Solanesol Molecular Imprinted Polymers. *Des. Monomers Polym.* **2015**, *18*, 641–649. [CrossRef]
- Liu, X.; Wu, F.; Au, C.; Tao, Q.; Pi, M.; Zhang, W. Synthesis of Molecularly Imprinted Polymer by Suspension Polymerization for Selective Extraction of p-hydroxybenzoic Acid from Water. *J. Appl. Polym. Sci.* **2019**, *136*, 46984. [CrossRef]
- Zhao, G.; Liu, J.; Liu, M.; Han, X.; Peng, Y.; Tian, X.; Liu, J.; Zhang, S. Synthesis of Molecularly Imprinted Polymer via Emulsion Polymerization for Application in Solanesol Separation. *Appl. Sci.* **2020**, *10*, 2868. [CrossRef]
- Bakhtiar, S.; Bhawani, S.A.; Shafqat, S.R. Synthesis and Characterization of Molecular Imprinting Polymer for the Removal of 2-phenylphenol from Spiked Blood Serum and River Water. *Chem. Biol. Technol. Agric.* **2019**, *6*, 15. [CrossRef]
- Moein, M.M.; Abdel-Rehim, A.; Abdel-Rehim, M. Recent Applications of Molecularly Imprinted Sol-Gel Methodology in Sample Preparation. *Molecules* **2019**, *24*, 2889. [CrossRef] [PubMed]
- Gavrila, A.-M.; Nicolescu (Iordache), T.-V.; Sandu, T.; Zaharia (Lungu), A.; Radu, A.L.; Branger, C.; Brisset, H.; Stoica, E.B.; Apostol, S.; Sarbu, A. Molecularly Imprinted Polymer Pearls Obtained by Phase Inversion for the Selective Recognition of Hypericin. *Mater. Plast.* **2019**, *56*, 315–320. [CrossRef]
- Ye, L.; Zhou, T.; Shen, X. Molecular imprinting in particle-stabilized emulsions: Enlarging template size from small molecules to proteins and cells. *Mol. Impr.* **2015**, *3*, 8–16. [CrossRef]
- Shen, X.; Xu, C.; Ye, L. Imprinted polymer beads enabling direct and selective molecular separation in water. *Soft Matter* **2012**, *27*, 7169–7176. [CrossRef]
- Florea, A.-M.; Iordache, T.-V.; Branger, C.; Ghiurea, M.; Avramescu, S.; Hubca, G.; Sarbu, A. An innovative approach to prepare hypericin molecularly imprinted pearls using a “phyto-template”. *Talanta* **2016**, *148*, 37–45. [CrossRef] [PubMed]
- Roshan, S.; Mujahid, A.; Afzal, A.; Nisar, I.; Ahmad, M.N.; Hussain, T.; Bajwa, S.Z. Molecularly Imprinted Polymer-Silica Hybrid Particles for Biomimetic Recognition of Target Drugs. *Adv. Polym. Technol.* **2019**, *2019*, 9432412. [CrossRef]
- Scrivano, L.; Parisi, O.I.; Iacopetta, D.; Ruffo, M.; Ceramella, J.; Sinicropi, M.S.; Puoci, F. Molecularly Imprinted Hydrogels for Sustained Release of Sunitinib in Breast Cancer Therapy. *Polym. Adv. Technol.* **2019**, *30*, 743–748. [CrossRef]
- Pereira, I.; Rodrigues, M.F.; Chaves, A.R.; Vaz, B.G. Molecularly Imprinted Polymer (MIP) Membrane Assisted Direct Spray Ionization Mass Spectrometry for Agrochemicals Screening in Foodstuffs. *Talanta* **2018**, *178*, 507–514. [CrossRef] [PubMed]

13. Shakhoseini, F.; Langille, E.A.; Azizi, A.; Bottaro, C.S. Thin Film Molecularly Imprinted Polymer (TF-MIP), a Selective and Single-use Extraction Device for High-throughput Analysis of Biological Samples. *Analyst* **2021**, *146*, 3157–3168. [[CrossRef](#)] [[PubMed](#)]
14. Gavrilă, A.-M.; Radu, I.-C.; Stroescu, H.; Zaharia, A.; Stoica, E.-B.; Ciurlica, A.-L.; Iordache, T.-V.; Sârbu, A. Role of Functional Monomers upon the Properties of Bisphenol A Molecularly Imprinted Silica Films. *Appl. Sci.* **2021**, *11*, 2956. [[CrossRef](#)]
15. Pesavento, M.; Cennamo, N.; Zeni, L.; De Maria, L. A Molecularly Imprinted Polymer Based SPR Sensor for 2-Furaldehyde Determination in Oil Matrices. *Appl. Sci.* **2021**, *11*, 10390. [[CrossRef](#)]
16. Ribeiro, S.C.; Fernandes, R.; Moreira, F.T.C.; Sales, M.G.F. Potentiometric Biosensor Based on Artificial Antibodies for an Alzheimer Biomarker Detection. *Appl. Sci.* **2022**, *12*, 3625. [[CrossRef](#)]
17. Gavrilă, A.-M.; Stoica, E.-B.; Iordache, T.-V.; Sârbu, A. Modern and Dedicated Methods for Producing Molecularly Imprinted Polymer Layers in Sensing Applications. *Appl. Sci.* **2022**, *12*, 3080. [[CrossRef](#)]
18. Totito, T.C.; Laatikainen, K.; Pereao, O.; Bode-Aluko, C.; Petrik, L. Adsorptive Recovery of Cu²⁺ from Aqueous Solution by Polyethylene Terephthalate Nanofibres Modified with 2-(Aminomethyl)Pyridine. *Appl. Sci.* **2021**, *11*, 11912. [[CrossRef](#)]

Article

Potentiometric Biosensor Based on Artificial Antibodies for an Alzheimer Biomarker Detection

Sónia Cláudia Ribeiro ¹, Rúben Fernandes ^{2,3}, Felismina T. C. Moreira ^{1,4,*} and Maria Goreti Ferreira Sales ^{1,4,5}

¹ BioMark Sensor Research—ISEP, School of Engineering, Polytechnic Institute of Porto, 4249-015 Porto, Portugal; s.claudia.ribeiro@gmail.com (S.C.R.); goretisales@eq.uc.pt (M.G.F.S.)

² LaBMI, Laboratory of Medical and Industrial Biotechnology, Polytechnic Institute of Porto, 4249-015 Porto, Portugal; ruben.fernandes@ufp.edu.pt

³ HEFP, FCS-UFP—Fernando Pessoa Hospital, Faculty of Health Sciences, Fernando Pessoa University, 4249-015 Porto, Portugal

⁴ CEB, Centre of Biological Engineering, University of Minho, 4715-000 Braga, Portugal

⁵ BioMark, Sensor Research@UC, Department of Chemical Engineering, Faculty of Science and Technology, Coimbra University, 3030-790 Coimbra, Portugal

* Correspondence: ftm@isep.ipp.pt

Abstract: This paper presents a potentiometric biosensor for the detection of amyloid β -42 ($A\beta$ -42) in point-of-care analysis. This approach is based on the molecular imprint polymer (MIP) technique, which uses covalently immobilised $A\beta$ -42 to create specific detection cavities on the surface of single-walled carbon nanotubes (SWCNTs). The biosensor was prepared by binding $A\beta$ -42 to the SWCNT surface and then imprinting it by adding acrylamide (monomer), N,N'-methylene-bis-acrylamide (crosslinker) and ammonium persulphate (initiator). The target peptide was removed from the polymer matrix by the proteolytic action of an enzyme (proteinase K). The presence of imprinting sites was confirmed by comparing a MIP-modified surface with a negative control (NIP) consisting of a similar material where the target molecule had been removed from the process. The ability of the sensing material to rebind $A\beta$ -42 was demonstrated by incorporating the MIP material as an electroactive compound in a PVC/plasticiser mixture applied to a solid conductive support of graphite. All steps of the synthesis of the imprinted materials were followed by Raman spectroscopy and Fourier transform infrared spectroscopy (FTIR). The analytical performance was evaluated by potentiometric transduction, and the MIP material showed cationic slopes of $75 \text{ mV-decade}^{-1}$ in buffer pH 8.0 and a detection limit of $0.72 \text{ }\mu\text{g/mL}$. Overall, potentiometric transduction confirmed that the sensor can discriminate $A\beta$ -42 in the presence of other biomolecules in the same solution.

Keywords: amyloid β -42; molecularly imprinted polymers; potentiometric sensor; Alzheimer biomarker

Citation: Ribeiro, S.C.; Fernandes, R.; Moreira, F.T.C.; Sales, M.G.F.

Potentiometric Biosensor Based on Artificial Antibodies for an Alzheimer Biomarker Detection.

Appl. Sci. **2022**, *12*, 3625.

<https://doi.org/10.3390/app12073625>

app12073625

Academic Editor: Andrei Sarbu

Received: 10 February 2022

Accepted: 29 March 2022

Published: 2 April 2022

Publisher's Note: MDPI stays neutral with regard to jurisdictional claims in published maps and institutional affiliations.



Copyright: © 2022 by the authors. Licensee MDPI, Basel, Switzerland. This article is an open access article distributed under the terms and conditions of the Creative Commons Attribution (CC BY) license (<https://creativecommons.org/licenses/by/4.0/>).

1. Introduction

Several peptides/proteins are being considered as potential biomarkers for predicting the early stages of Alzheimer's disease (AD). Numerous clinical studies show that the concentrations of these biomarkers in biological fluids correlate with the progression of early-stage disease [1]. The mechanism driving the progression of AD is related to the formation of senile plaques and neurofibrillary tangles, which are responsible for the death of neurons and lead to memory loss and symptomatic behavioural changes [2–5]. Current hypotheses also include circulating $A\beta$ -42 oligomers as potentially neurotoxic (not just the plaques) [6–12]. The detection of $A\beta$ -42 is based on immunochemical reactions, e.g., conventional ELISAs [13], which are highly sensitive and selective, but time-consuming, unstable, and expensive.

Several biosensors have been described in the literature for the detection of $A\beta$ -42 by electrochemical [14,15], surface plasmon resonance (SPR) [16–21] and field-effect transistor (FET) [22–25] detection. Electrochemical biosensors have been extensively studied due to

their promising properties in terms of scalability and price. This transduction technique has a higher sensitivity and reproducibility compared to other transduction instruments and allows for point-of-care (PoC) analysis [15,26–31], but requires a sensitive and selective antigen recognition material. Antibodies are commonly used as capture and recognition elements [27,32–35]. However, this biological element of recognition has some limitations in terms of its stability, price, and reusability. For this reason, we have developed in this work a plastic antibody for the selective recognition of A β -42. Some plastic antibodies for the selective recognition of A β -42 have been described in the literature with electrochemical transduction using impedance or square wave voltammetry techniques [14,15,36–39]. To the best of our knowledge, this is the first plastic antibody-based sensor with potentiometric transduction for the detection of AD biomarkers in PoC described in the literature.

Potentiometric sensors have several advantages in terms of simple procedures and highly specific/sensitive properties. Ion-selective electrodes (ISEs) with polymeric-selective membranes and solid-state contact have been used extensively and offer several advantages in terms of their precision, response time, cost of analysis, selectivity and sensitivity over a wide concentration range [40–43]. The development of sensing materials based on molecular imprinting polymer technology (MIP) with the size and charge of a specific ion can lead to precise selective interactions [44,45]. Various immobilization strategies for the integration of MIPs and biosensors have been described in the literature. These include: (i) in situ polymerization (bulk) [46], (ii) epitope method [47] or (iii) surface imprinting with chemical or UV initiation [48,49]. In surface imprinting, the molecules are attached to the surfaces in a layer-by-layer approach. In this strategy, the number of binding sites or cavities tends to increase, which is crucial for reaching the desired detection limit [50,51].

Some nanomaterials, such as carbon allotropes and metallic or magnetic nanoparticles, are used to improve binding sites due to their high surface-to-area ratio [52–54]. Carbon nanotubes (CNTs) are widely used in biosensing as conducting transducers or as carriers for the immobilization of target molecules. CNTs exhibit good properties in terms of their conductivity and high surface-to-area ratio and are an ideal nanomaterial for protein/peptide immobilization [55–61].

Overall, this work describes the synthesis of a plastic antibody for an AD biomarker detection with potentiometric transduction in PoC. The peptide is bound to the surface of SWCNTs that were previously carboxylated. Acrylamide (AAM, functional monomer) and N,N'-methylenebisacrylamide (NNMBA, crosslinker) were then reacted, and polymerization began with the addition of ammonium persulfate (APS, initiator) and TEMED at 38 °C. Finally, the peptide was removed from the polymer matrix by the proteolytic action of proteinase K. In parallel, a similar process was performed without peptide to assemble the NIP material. These sensors were used as electroactive materials in a PVC membrane for potentiometric transduction. Thus, this research presents a new concept for the development of low-cost and sensitive sensor platforms for AD diagnostics in PoC.

2. Materials and Methods

2.1. Apparatus

Potentials were measured using a Crison pH meter GLP 21 (± 0.1 mV sensitivity) at room temperature with constant stirring. The output signal was passed to a commutation unit and connected to one of the six outputs, which allowed for synchronized measurements. The setup of the potentiometric cell was as follows: epoxy-graphite | A β -42 selective membrane | buffered sample solution of 3-(N-morpholino)propanesulfonic acid (MOPS), 1×10^{-3} mol/L, pH 8.0 | AgCl (s) | Ag. An Ag/AgCl electrode served as the reference electrode.

Infrared spectra were recorded using a Nicolet 6700 FTIR spectrometer coupled to an attenuated total reflectance (ATR) and equipped with a Nicolet diamond contact crystal. Raman spectroscopy data were obtained with a Thermo Scientific DXR Raman microscope equipped with a 532 nm laser. A laser power of 8 mW was left on the sample at a slit aperture of 50 μ m.

The SEM analysis was performed using a high-resolution (Schottky) scanning electron microscope with X-ray microanalysis and electron backscattered diffraction analysis: Quanta 400 FEG ESEM/EDAX Genesis X4M.

2.2. Reagents and Solutions

All chemicals were of analytical grade and de-ionized water (conductivity 0.1 $\mu\text{S}/\text{cm}$). 3-Morpholinopropane-1-sulfonic acid (MOPS) from Applichem; A β -amyloid 42 (A β -42) from GeneScript; SWCNTs, *o*-nitrophenyloctyl (oNPOE), high molecular weight poly (vinyl chloride) (PVC), acrylamide (AAM), *N,N'*-methylenebisacrylamide (NNMBA), ammonium persulfate (APS), oxalic acid (Oac), *N*-hydroxysuccinimide (NHS), *N*-ethyl-*N'*-(3-dimethylaminopropyl)carbodiimide hydrochloride (EDAC) and sodium chloride (NaCl), creatinine (Crea), albumin (Alb), 2-aminoethyl methacrylate hydrochloride (AEMA), proteinase K and sulfuric acid (H_2SO_4) were purchased from Fluka; tetrahydrofuran (THF) was purchased from Riedel-deHaen; hydrogen peroxide (H_2O_2) and potassium chloride from MERCK; potassium dihydrogen phosphate (KH_2PO_4) and sodium phosphate dibasic dihydrate (Na_2HPO_4) from Panreac; tetramethylethylenediamine (TEMED) and urea from TLC; and CORMAY serum from Cormay diagnostics.

Phosphate buffer solution (PBS) buffer was prepared with the following composition: NaCl, 8 g/L; KCl, 0.2 g/L; Na_2HPO_4 , 1.42 g/L; KH_2PO_4 , 0.24 g/L. The pH was adjusted to a value of 8.0. The standard solutions of A β -42 were prepared from a successive dilution of the stock solution (0.05 mg/mL) previously prepared in ultrapure water. The MOPS 1.0×10^{-3} mol/L were prepared in deionized water.

The interfering species were prepared in MOPS buffer 1.0×10^{-3} mol/L, pH 8 with the following concentrations: Crea 1.2×10^{-5} g/mL, Alb 5.2×10^{-3} g/mL and urea 4.0×10^{-4} g/mL.

2.3. Synthesis of Biomimetic Materials

2.3.1. SWCNT Oxidation

Briefly, 0.5 g of SWCNT was added to a ten-fold diluted solution of concentrated $\text{H}_2\text{SO}_4\text{:H}_2\text{O}_2$ (4:1). Then, the solution was stirred overnight, centrifuged and washed three times with water. The material was then stirred in PBS buffer, pH 7.2, for 2 h to increase the pH. This procedure was repeated three times. Finally, the nanotubes were oven-dried overnight at 40 °C.

2.3.2. Imprinting Stage

Approximately 10 mg of oxidized SWCNT was suspended in 1.0 mL of deionized water by ultrasonically stirring the mixture for approximately 1 min. Then, 1.0 mL of an aqueous solution containing 5 mmol/L NHS and 2 mmol/L EDAC was added, and the mixture was stirred at room temperature for 45 min. The suspension was then filtered, and the solid was thoroughly rinsed with deionized water to remove unreacted reagents. After activation of the carboxylic acids by EDAC/NHS treatment, 1 mL of 0.01 $\mu\text{g}/\text{mL}$ A β -42 prepared in MOPS buffer pH 8.0 was added to the modified material for 2.0 h at 4 °C to bind the template. The imprinting phase began with overnight incubation of the modified SWCNTs with 1 mL 5.0×10^{-4} mol/L AEMA. The materials were then washed several times with deionized water. The polymerization phase starts with the addition of 0.5 mL of a monomer (AAM, 5.0×10^{-4} mol/L) and a crosslinker (NNMBA, 1.0×10^{-4} mol/L) to the SWCNTs previously modified with the peptide. After incubation at room temperature for 60 min, 0.5 mL of APS, 1×10^{-4} mol/L and 0.5 mL of TEMED, 10%, solution in MOPS buffer pH 8.0 were added to start polymerization. The polymerization was carried out at room temperature for 2 h. After that, the sensor was washed thoroughly with deionized water. Finally, the template was removed by exposed to proteinase K (500 $\mu\text{g}/\text{mL}$) for 3 h at 37 °C. The imprinted sensor material was washed with phosphate buffer, pH 7.2, to remove the peptide fractions formed by the enzyme treatment, and dried in an oven at 40 °C.

2.4. Preparation of Sensory Membranes

Different compositions of PVC membranes were prepared to evaluate the potentiometric response of the MIP-based sensors. Approximately 0.05 g PVC, 0.06 g plasticizer (oNPOE) and 2.0 mg MIP and NIP were mixed (see Table 1). The mixture was stirred until complete dispersion of the PVC in 3.5 mL THF. These membranes were dropped onto the graphite electrode surface and dried for 48 h. Then, the membranes were conditioned in an Aβ-42, 0.01 µg/mL solution. The electrodes were stored in this solution when not in use.

Table 1. Membrane composition of Aβ-42 sensors casted in 50 mg of PVC and their potentiometric features in 1.0 × 10^{−2} M MOPS buffer, pH 6 and 8.

pH	Membrane Composition			Weight (mg)	Slope (mV/Decade)	R ² (n = 3)	LOD (µg/mL)	LLLR (µg/mL)	Response Time (s)
	Active Ingredient	Plasticizer	Additive						
6	MIP/AAM	oNFOE	—	2:60	62.2 ± 1.3	0.970	1.23	1.20	>60
	NIP/AAM	oNFOE	—	2:60	—	0.920	—	—	>60
8	MIP/AAM	oNFOE	—	2:60	75.1 ± 1.0	0.992	0.97	1.20	>60
	NIP/AAM	oNFOE	—	2:60	44.0 ± 1.0	0.970	0.99	0.75	>60

LOD: limit of detection; LLR: lower limit of linear range.

2.5. Potentiometric Procedures

The analytical performance of the electrodes was evaluated using calibration curves according to IUPAC recommendations. Potentiometric measurements were performed at two pH values (6 and 8), at room temperature, with constant agitation and recording of potentials after stabilization of ±0.2 mV. The e.m.f. value was measured at constant values of ionic strength, and pH. MOPS solution was used for this purpose; aliquots of 0.4 to 15 mL of 1.0 × 10^{−4} mol/L MOPS were transferred to 0.25 mL of Aβ-42 solution 0.01 µg/mL and 1.75 mL of buffer in a 100 mL beaker. Calibration data for each calibration included limit of detection (LOD), slope, linear ranges and squared correlation coefficient (R²). Serum samples were analyzed by adding 100-fold diluted commercial human Cormay[®] serum and an appropriate amount of Aβ-42 standard. The Aβ-42 concentration was calculated from the analytical data of a control calibration curve in serum.

2.6. Selectivity Study

The potentiometric selectivity coefficients were determined by mixed solutions method (MSM). The selectivity of the biosensor was assessed by quantifying LOD of each calibration curve through the presence of an interfering compound [62]. The selectivity coefficients were calculated according to this equation:

$$K_{A\beta-42,J}^{POT} = a_{A\beta-42} / (a_j)^{Z_{A\beta-42} / Z_j} \tag{1}$$

In Equation (1), a_j is the concentration of interfering species, Z the ionic charges of the interfering ions and a_{Aβ-42} the intersection of the extrapolated linear section of the plot Emf vs. the logarithm of Aβ-42 concentration. Alb, Crea and urea were evaluated as interfering species. For this propose, a fixed concentration of interfering species within the physiological level in serum was added as background, while the concentration of primary ion (Aβ-42) was varied. (Crea, 1.2 × 10^{−5} g/mL), (Alb, 5.2 × 10^{−3} g/mL) and (urea, 4.0 × 10^{−4} g/mL) were evaluated as interfering species.

3. Results and Discussion

3.1. Design of the Plastic Antibodies

Herein, a plastic antibody synthesized on the oxidized SWCNT surface was successfully used for Aβ-42 detection with potentiometric transduction. The SWCNTs were selected for this propose due to their large surface area, which promotes an increase in the number of binding sites of the MIP material. The overall process for preparing the MIP

involved the attachment of A β -42 to the surface of the SWCNTs (Figure 1), filling the vacant places around the A β -42 with an appropriate rigid structure and removing the peptide from the polymer. The polymerization steps were carried out under mild conditions in order to guarantee that 3D-structure and electrostatic environment of A β -42 remained stable.

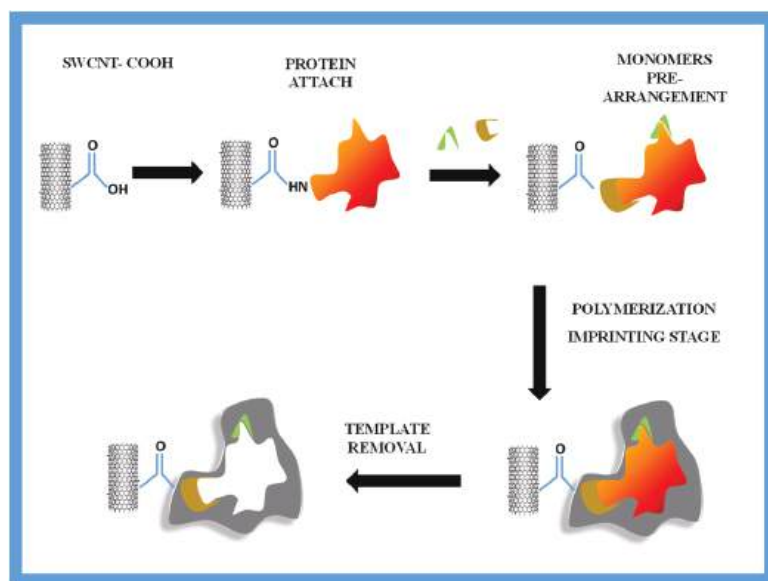


Figure 1. Synthesis of the plastic antibody.

First, the peptide was covalently bound to the previously oxidized SWCNT. The carboxyl groups were activated by an EDAC and NHS reaction. In the first step, a highly reactive *O*-acylurea intermediate is formed [59], which reacts rapidly with NHS to form a more stable ester (succinimidyl intermediate). This ester performs a nucleophilic substitution with any accessible amine group on A β -42, leading to the formation of an amide bond between the SWCNTs and A β -42.

The formation of stable complexes between the monomers and the target molecule and their preservation in solution are crucial for achieving a suitable selectivity of the imprinting polymer. In this work, electrostatic interactions were established between the target and the monomers. For this purpose, 2-AEMA was used as the functional monomer, forming hydrogen bonds with A β -42 [63]. Polymerization then starts with the addition of the monomer AAM, the crosslinker NNMB and the initiators APS and TEMED after peroxide (OO) bond cleavage by the initiator. Crosslinking between the NNMB chains was ensured by two terminal vinyl groups. The modified SWCNTs were washed three times with the MOPS buffer [64]. The A β -42 was then removed from the polymer by proteinase K treatment. Several washing steps were then performed to remove the free peptide fractions from the surface of the biomimetic material.

3.2. Raman Spectroscopy Studies

The chemical profile of the different materials was evaluated by analysing the Raman spectra. The analysis was performed for the following materials: (i) SWCNT, (ii) SWCNT-COOH and (iii) MIP and NIP. RAMAN spectra give information about the efficiency of the nanotube carboxylation, polymerization and template removal [65].

In general, the structure of the spectrum highlights four distinctive peaks (Figure 2): the first peak in the region around 1300 cm^{-1} (D), the second in the region around 1600 cm^{-1} (G), the third in the high frequencies around 2600 cm^{-1} (G') and the fourth in the region

around 1930 cm^{-1} . Figure 2 shows the Raman spectra for each sample separately, and the ratio of the intensity between G and D band, which is useful for determining the purity of and the degree of the chemical modification of the material. As a result, we observe a significant difference in terms of the peak intensity and shift between different materials. The shifts are essentially perceptible for the G and D bands.

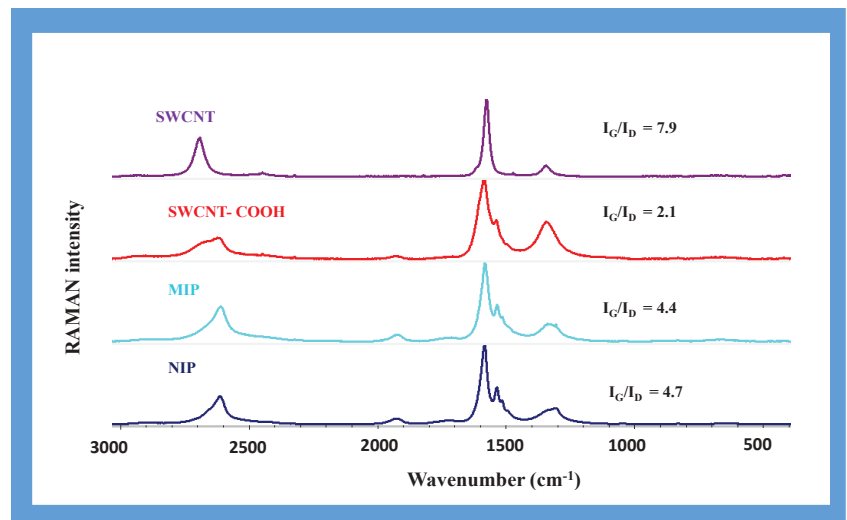


Figure 2. Raman spectra of SWCNT, CNT-COOH and MIP and NIP.

Carbon nanotubes are rolled-up graphene sheets that have been wound into tubes. These nanomaterials are cylindrical tubes with a single outer wall and a diameter typically around 1–2 nm. Due to their exceptional mechanical, electrical and thermal assets, carbon nanotubes are widely used in the field of carbon nanotechnology nowadays.

The Raman spectrum of an SWCNT is similar to graphene, which is to be expected as it is a rolled-up sheet of graphene. In Figure 2, in the Raman spectrum of SWCNT, prominent G and G' peaks are visible. The band relative to the frequency of tangential displacement (G) is close to 1590 cm^{-1} , and the band associated with the second order peak (G') is related to the charge transfer between the nanotubes and the reaction mixture [66]. It is also possible to see a well-defined band near 1350 cm^{-1} . This band is denominated as the D band. The D band is ascribed to hybridized vibrational mode, which is related to the graphene edges, and it designates the presence of some disorder to the carbon structure [67].

Comparing the RAMAN spectra of SWCNT and SWCNT-COOH, the latter shows two additional bands near 1540.7 and 267.7 cm^{-1} , and a peak shift of the G' and G bands approximately 60 and 9 cm^{-1} to the right. These changes are associated with defects in the walls of the nanotubes caused by chemical oxidation by introducing groups (OH, CHO and COOH) on their surface. Additionally, a decrease in the I_G/I_D of the SWCNT after chemical modification from 7.9 to 2.1 was observed, confirming the presence of additional defects in the nanomaterial.

Regarding the RAMAN spectra of MIP and NIP materials, the most relevant information involves changes at the level of the G and D bands and the respective peak ratio (Figure 2). The I_G/I_D for MIP and NIP were 4.4 and 4.7, respectively. These values are very similar, which would be expected, since the polymeric matrix is identical. Besides, this ratio increased in comparison to SWCNT-COOH, indicating the presence of a crystalline structure, since the G band is the Raman signature for sp^2 carbons. Additionally, we can observe a shift of the peaks G', G and D to the right compared to the previous step of the chemical modification of SWCNT-COOH, and an enhancement of an additional band at approximately 1900 cm^{-1} .

The shift of these bands was approximately 13.9 and 12 cm^{-1} , respectively. Overall, this result confirms the SWCNT oxidation and MIP and NIP polymerization.

3.3. FTIR Analysis

FTIR analysis is useful to evaluate the chemical structure of the nanomaterial and to identify existing compounds by surface analysis. The FTIR / ATR spectra were plotted for SWCNT, SWCNT-COOH, MIP and NIP (Figure 3).

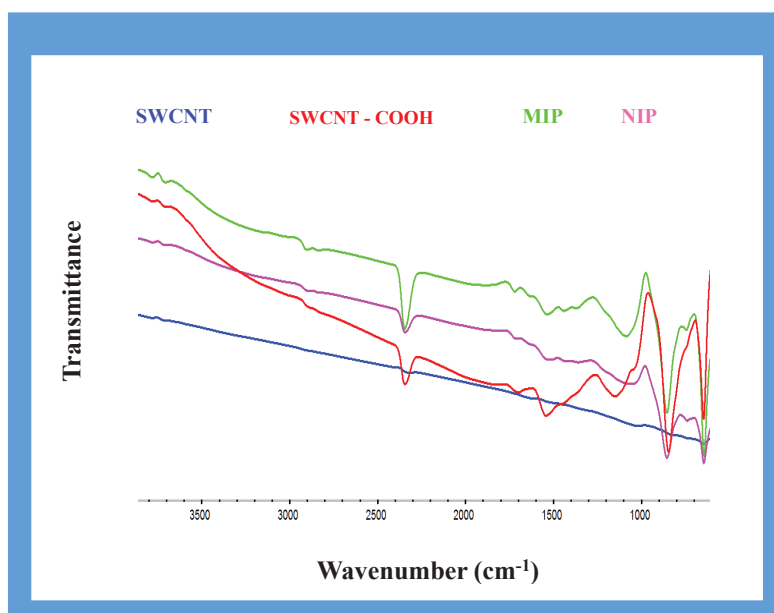


Figure 3. FTIR spectra of SWCNT, CNT-COOH and MIP and NIP.

As observed in Figure 3, the SWCNT does not present relevant visible peaks; however, after acidic treatment, many new peaks appear. The peak observed for SWCNT-COOH at 1701 cm^{-1} can be attributed to the C=O stretch of the carboxylic group, whereas the peak at 1545 cm^{-1} can be related to the C=C stretch of SWCNTs and the peak at 1150 cm^{-1} to the C-O stretch [68,69]. These bands may be related to the chemical oxidation of SWCNT.

Both MIP and NIP materials showed intense peaks at 1723, 1539, 1444, 1087.67 and 856 cm^{-1} , respectively. These peaks have been attributed to the carboxylic/acetone groups, C=C stretch and C-O/C=O stretch bonds. Although these peaks are also present in the SWCNT; however, they showed a peak shift to the left or right. This characteristic allows us to confirm the modification of the surface after polymerization.

3.4. SEM Analysis

The SEM images of the carboxylated SWCNTs and MIP materials are shown in Figure 4. The SWCNTs have a thickness of a few nanometers; however, the SEM images show that the oxidized SWCNTs have some impurities or are in an agglomerated state. The chemical modification of the surface was clearly visible. This was confirmed by magnifying the original material 100,000 times. However, the occurrence of the imprinting could not be verified by SEM, since we cannot observe cavities. In addition, the surface modification with the imprinting polymer significantly increased the thickness of the SWCNT, and some agglomerates were observed, which can be attributed to the presence of the polymer. (see Figure 4).

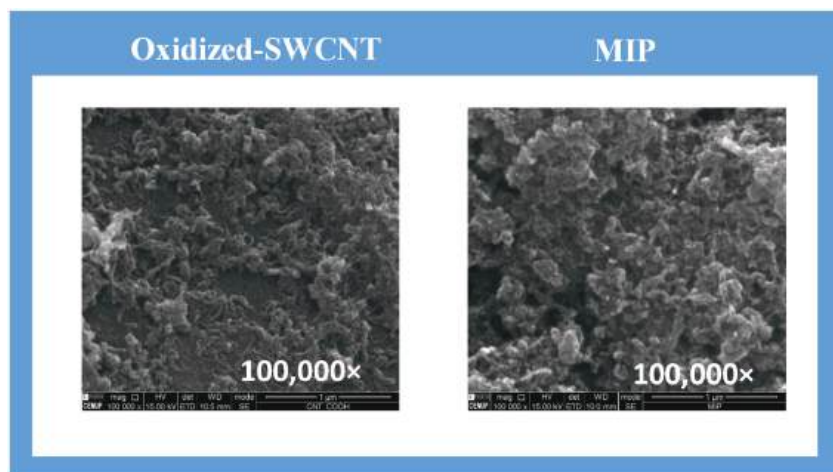


Figure 4. SEM images of oxidized SWCNT and MIP materials.

3.5. Sensory Surfaces

The materials MIP and NIP were incorporated into the PVC membrane and tested as sensing materials with potentiometric transduction. The effect of membrane composition on the potential response was investigated and the results are shown in Table 1.

Overall, the membranes were prepared by dispersing the active compounds (MIP or NIP) in a high dielectric constant plasticizer, oNPOE and PVC. The type of plasticizer employed is important to the analytical performance of PVC-based sensors. Some plasticizers cause leakage or migration from the membrane, which limits the lifetime of sensor materials based on plasticized membranes. Almeida and co-authors have previously described the effects of the plasticizer dielectric constant on the analytical performance of sensors. When oNFOE was used as plasticizing solvent, the detection limit of the sensor was lower due to the higher dielectric constant compared to other conventional solvents [70].

PH Effect

ISEs were calibrated in the MOPS buffer, 1.0×10^{-1} mol/L, pH 6.0 and 8.0. Under these conditions, the peptide is slightly negatively charged because its isoelectric point is 5.5 [64]. However, all electrodes exhibited cationic slopes, and an opposite behavior was expected. A possible explanation for this behaviour is related to the presence of several ionizable functional groups on the amyloid surface that can interact with the PVC membrane, causing the protein to approach the MIP binding sites within the PVC membrane by its positively charged groups. At pH 6, the MIP showed linear behavior after $1.23 \mu\text{g/mL}$, a cationic slope of 62.1 mV/dec and a detection limit of $1.20 \mu\text{g/mL}$. The NIP showed a nonlinear behavior with an R^2 of 0.92, indicating that the (re)binding mechanism of the peptide in the imprinted material dominates the potentiometric response (Table 1). Overall, the ISEs with the MIP material showed the best operating characteristics in terms of the slope and R^2 .

For the calibration curve at pH 8.0, the MIP sensor showed overernstian slopes of 75.0 mV/decade and an NIP material of 44.0 mV/decade , respectively. The MIP showed a linear response after $1.20 \mu\text{g/mL}$ and LOD after $0.97 \mu\text{g/mL}$ (Figure 5). The particles of NIP showed acceptable properties in terms of LOD, but a lower Nernstian slope compared to the MIP material, indicating that the binding sites of MIP led to the analytical response.

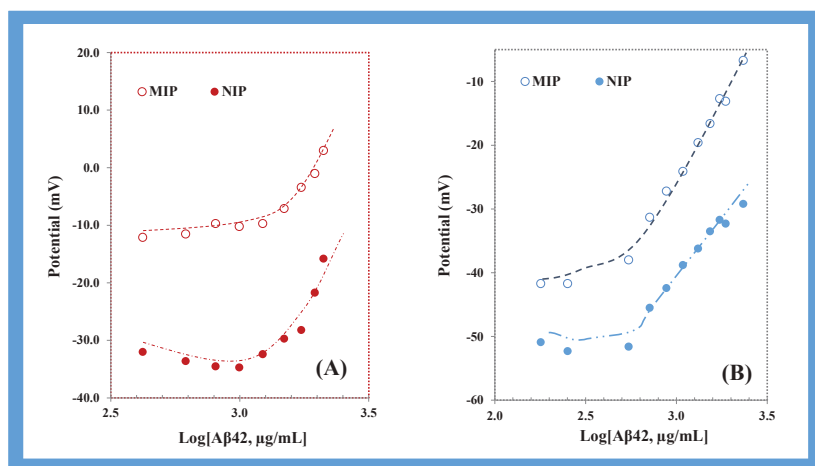


Figure 5. Calibration curve of the ISE-based sensors in MPOS buffer: (A) pH 6.0 and (B) pH 8.0.

Overall, the best results in terms of the analytical performance were obtained for the membranes with MIP as an ionophore at pH 8.0. These conditions were used for further studies.

The analytical performance of the biosensor was compared (Table S2) with previously reported electrochemical biosensors with different recognition elements for A β -42 detection. Overall, these methods show a better analytical performance compared to this approach. However, to our knowledge, this research demonstrates for the first time a simple approach based on potentiometric transduction. We are aware that improvements should be made in terms of the analytical performance. However, we present a low-cost and simple system based on two electrodes made of graphite carbon electrode (reference and working electrode).

3.6. Response Time

The time required to reach a stable potential (± 3 mV) in the A β -42, 5 μ g/mL solution with a rapid 10-fold increase in concentration was 300 s. A low potential drift and long-term stability were observed with successive calibrations. Wash periods with the buffer were inserted between calibrations to remove bound proteins and adjust the potential to a “blank” value. In general, LODs, response times, the linear range and calibration slopes were reproducible within $\pm 5\%$ of their original values over ≈ 2 weeks.

3.7. Selectivity Study

The selectivity study of ISEs is a critical key factor for the success of the overall performance of the biosensing device in applications in real or close-to-real conditions. There are several methodologies adopted for estimating the potentiometric selectivity coefficients, including the mixed solutions, the separated solutions or the matched potential. Herein, we selected the mixed solution method and tested against the MIP-based ISE sensor. The selectivity behaviour of A β -42 ISEs was estimated by calculating the logarithmic potentiometric selectivity coefficients, $\log K^{\text{POT}}$. As the $\log K^{\text{POT}}$ decreased, the sensor increased its preference for A β -42, as these coefficients established the ability of an ISE to differentiate a particular (primary) ion from others (interfering species). The interfering compounds designated for this study were, Crea, Alb and urea prepared in spiked serum. (see Table S1). Overall, a decreased $\log K^{\text{POT}}$ was expected to be observed for Crea and urea when compared with Alb. As Alb is a protein with many amino acids with functional groups, such as amino and carboxyl groups, and a high molecular weight, an increased $\log K^{\text{POT}}$ was expected to be observed, and, in contrast, all interfering species were expected to

demonstrate quite similar behaviour. This could be ascribed to their net charge at pH 8.0. Thus, the addition of a cationic additive to the membrane is expected to improve the selectivity. However, this study could be conducted in future studies.

3.8. Spiked Serum Samples Analysis

An analytical application of the sensor was performed on the membrane with MIP in a spiked serum sample. Each analysis was performed immediately after the calibration of the ISEs in 100-fold diluted serum.

The concentration of A β -42 in serum was 1.31, 1.08 and 0.71 $\mu\text{g/mL}$, respectively (Table 2). The results obtained for the MIP sensor showed an average recovery of 104.2%, ranging from 102.3% to 107.05%. The relative error ranged from 2.34% to 7.49%. Thus, the results show that the MIP-ISE membranes are suitable for practical use in serum samples. However, the sensor still needs to be improved in terms of the detection limit required to sample analysis.

Table 2. Analytical application of the sensor in spiked serum samples in serum pH 8.0.

[A β -42], ($\mu\text{g/mL}$)	Recovery (%)	Error (%)
1.31	103.5 \pm 0.083	3.54 \pm 0.08
1.08	107.5 \pm 0.22	7.49 \pm 0.11
0.71	102.3 \pm 0.08	2.34 \pm 0.08

4. Conclusions

This research describes the development and characterization of potentiometric sensors based on MIP for the determination of the target molecule A β -42.

In essence, MIP technology allows for the production of synthetic receptors with binding constants comparable to those of natural receptors but capable of withstanding extreme conditions, such as temperature, pressure, pH and organic solvents. In theory, synthetic antibodies are very stable and robust, much cheaper than natural receptors and can be stored for long periods of time. The proper selection of the imprinting method is critical, as is the type of polymer material. Conventional bulk imprinting has proven to be a complicated process. Major difficulties include a reduced mass transfer and entrapment of the analyte in the polymer matrix, compromised integrity of the polymer structure, limited solvent choices and formation of heterogeneous binding sites. These limitations can be overcome by surface polymerizations. In surface imprinting, nanometer-sized molecules are immobilized on the surface of nanostructured materials.

In this work, the synthesis of a nanostructured molecular imprint polymer immobilized on a SWCNT surface is described. Due to its small size, a high surface-to-volume ratio is achieved, which favors miniaturization. This material showed good affinity and sensitivity for the A β -42 peptide.

The imprinted material was immobilized on a PVC membrane and evaluated by potentiometry. The potentiometric response was controlled by the properties of the medium in which the membranes were located so that the pH had a major influence. In alkaline, more precisely at pH 8.0, the membranes showed good analytical properties. Overall, these membranes have several advantages: a simple design, low response time, and good selectivity. Moreover, this method proved to be simple, cheap, accurate and cost effective in terms of the reagent and equipment consumption. Further developments are needed to reduce the LOD of the imprinted materials.

Supplementary Materials: The following supporting information can be downloaded at: <https://www.mdpi.com/article/10.3390/app12073625/s1>, Table S1: Log KPOT for different interfering species in MOPS pH 8.0; Table S2: Electrochemical biosensors for the detection of AD peptide biomarkers using nanomaterials as electrode modifiers or as labels published over the last ten years. References [31,32,39,71–81] are cited in the Supplementary Materials.

Author Contributions: Conceptualization, F.T.C.M. and M.G.F.S.; methodology, S.C.R. validation, S.C.R. formal analysis, F.T.C.M. and S.C.R.; investigation, S.C.R.; resources, F.T.C.M. and M.G.F.S.; writing—original draft preparation, F.T.C.M.; writing—review and editing, F.T.C.M., M.G.F.S. and R.F.; supervision, F.T.C.M., R.F. and M.G.F.S.; project administration, F.T.C.M. and M.G.F.S.; funding acquisition, F.T.C.M. All authors have read and agreed to the published version of the manuscript.

Funding: 0624_2IQBIONEURO_6_E, 2QBioneuro, Impulso de una red de I + i en química biológica para diagnóstico y tratamiento de enfermedades neurológicas EP-INTERREG V A España Portugal (POCTEP).

Institutional Review Board Statement: Not applicable.

Informed Consent Statement: Not applicable.

Data Availability Statement: Not applicable.

Conflicts of Interest: The authors declare no conflict of interest.

References

1. Blennow, K.; Zetterberg, H. Biomarkers for Alzheimer's disease: Current status and prospects for the future. *J. Intern. Med.* **2018**, *284*, 643–663. [\[CrossRef\]](#) [\[PubMed\]](#)
2. Popp, J.; Oikonomidi, A.; Tautvydaitė, D.; Dayon, L.; Bacher, M.; Migliavacca, E.; Henry, H.; Kirkland, R.; Severin, I.; Wojcik, J.; et al. Markers of neuroinflammation associated with Alzheimer's disease pathology in older adults. *Brain Behav. Immun.* **2017**, *62*, 203–211. [\[CrossRef\]](#) [\[PubMed\]](#)
3. Henriksen, K.; O'Bryant, S.E.; Hampel, H.; Trojanowski, J.Q.; Montine, T.J.; Jeromin, A.; Blennow, K.; Lönneborg, A.; Wyss-Coray, T.; Soares, H.; et al. The future of blood-based biomarkers for Alzheimer's disease. *Alzheimer's Dement.* **2014**, *10*, 115–131. [\[CrossRef\]](#) [\[PubMed\]](#)
4. Mapstone, M.; Cheema, A.K.; Fiandaca, M.S.; Zhong, X.; Mhyre, T.R.; MacArthur, L.H.; Hall, W.J.; Fisher, S.G.; Peterson, D.R.; Haley, J.M.; et al. Plasma phospholipids identify antecedent memory impairment in older adults. *Nat. Med.* **2014**, *20*, 415–418. [\[CrossRef\]](#)
5. Doecke, J.D.; Laws, S.M.; Faux, N.G.; Wilson, W.; Burnham, S.C.; Lam, C.-P.; Mondal, A.; Bedo, J.; Bush, A.I.; Brown, B.; et al. Blood-Based Protein Biomarkers for Diagnosis of Alzheimer Disease. *Arch. Neurol.* **2012**, *69*, 1318–1325. [\[CrossRef\]](#)
6. Wang, X.; Wang, L. Screening and Identification of Potential Peripheral Blood Biomarkers for Alzheimer's Disease Based on Bioinformatics Analysis. *Med. Sci. Monit.* **2020**, *26*, e924263. [\[CrossRef\]](#)
7. Chaudhry, A.; Houlden, H.; Rizig, M. Novel fluid biomarkers to differentiate frontotemporal dementia and dementia with Lewy bodies from Alzheimer's disease: A systematic review. *J. Neurol. Sci.* **2020**, *415*, 116886. [\[CrossRef\]](#)
8. Song, Y.; Xu, T.; Zhu, Q.; Zhang, X. Integrated individually electrochemical array for simultaneously detecting multiple Alzheimer's biomarkers. *Biosens. Bioelectron.* **2020**, *162*, 112253. [\[CrossRef\]](#)
9. Kim, K.; Lee, C.H.; Park, C.B. Chemical sensing platforms for detecting trace-level Alzheimer's core biomarkers. *Chem. Soc. Rev.* **2020**, *49*, 5446–5472. [\[CrossRef\]](#)
10. Zetterberg, H.; Burnham, S.C. Blood-based molecular biomarkers for Alzheimer's disease. *Mol. Brain* **2019**, *12*, 26. [\[CrossRef\]](#)
11. Janelidze, S.; Mattsson, N.; Stomrud, E.; Lindberg, O.; Palmqvist, S.; Zetterberg, H.; Blennow, K.; Hansson, O. CSF biomarkers of neuroinflammation and cerebrovascular dysfunction in early Alzheimer disease. *Neurology* **2018**, *91*, e867–e877. [\[CrossRef\]](#) [\[PubMed\]](#)
12. Mayeux, R.; Schupf, N. Blood-based biomarkers for Alzheimer's disease: Plasma A β 40 and A β 42, and genetic variants. *Neurobiol. Aging* **2011**, *32*, S10–S19. [\[CrossRef\]](#) [\[PubMed\]](#)
13. Cullen, V.C.; Fredenburg, R.A.; Evans, C.; Conliffe, P.R.; Solomon, M.E. Development and Advanced Validation of an Optimized Method for the Quantitation of A β 42 in Human Cerebrospinal Fluid. *AAPS J.* **2012**, *14*, 510–518. [\[CrossRef\]](#) [\[PubMed\]](#)
14. Moreira, F.; Rodriguez, B.A.; Dutra, R.A.; Sales, M.G.F. Redox probe-free readings of a β -amyloid-42 plastic antibody sensory material assembled on copper@carbon nanotubes. *Sens. Actuators B Chem.* **2018**, *264*, 1–9. [\[CrossRef\]](#)
15. Moreira, F.T.; Sales, M.G.F. Smart naturally plastic antibody based on poly(α -cyclodextrin) polymer for β -amyloid-42 soluble oligomer detection. *Sens. Actuators B Chem.* **2017**, *240*, 229–238. [\[CrossRef\]](#)
16. Špringer, T.; Hemmerová, E.; Finocchiaro, G.; Křištofiková, Z.; Vyhňálek, M.; Homola, J. Surface plasmon resonance biosensor for the detection of tau-amyloid β complex. *Sens. Actuators B Chem.* **2020**, *316*, 128146. [\[CrossRef\]](#)
17. Nair, R.V.; Yi, P.J.; Padmanabhan, P.; Gulyás, B.Z.; Murukeshan, V.M. Au nano-urchins enabled localized surface plasmon resonance sensing of beta amyloid fibrillation. *Nanoscale Adv.* **2020**, *2*, 2693–2698. [\[CrossRef\]](#)
18. Kim, H.J.; Kim, C.D.; Sohn, Y.S. Thiolated Protein A-functionalized Bimetallic Surface Plasmon Resonance Chip for Enhanced Determination of Amyloid Beta 42. *Appl. Chem. Eng.* **2019**, *30*, 379–383. [\[CrossRef\]](#)
19. Wang, X.Y.; Li, H.; Ma, H.; Seeram, N.; Zhou, F.M. Surface plasmon resonance and related biophysical techniques for the studies of amyloid peptide and protein aggregation and the Inhibition of aggregation by natural products. In *Abstracts of Papers of the American Chemical Society*; American Chemical Society: Washington, DC, USA, 2018; p. 256.

20. Palladino, P.; Aura, A.M.; Spoto, G. Surface plasmon resonance for the label-free detection of Alzheimer's β -amyloid peptide aggregation. *Anal. Bioanal. Chem.* **2015**, *408*, 849–854. [\[CrossRef\]](#)
21. Yi, X.; Feng, C.; Hu, S.; Li, H.; Wang, J. Surface plasmon resonance biosensors for simultaneous monitoring of amyloid-beta oligomers and fibrils and screening of select modulators. *Analyst* **2015**, *141*, 331–336. [\[CrossRef\]](#)
22. Park, H.; Lee, H.; Jeong, S.H.; Lee, E.; Lee, W.; Liu, N.; Yoon, D.S.; Kim, S.; Lee, S.W. MoS₂ Field-Effect Transistor-Amyloid- β 1–42 Hybrid Device for Signal Amplified Detection of MMP-9. *Anal. Chem.* **2019**, *91*, 8252–8258. [\[CrossRef\]](#) [\[PubMed\]](#)
23. Hideshima, S.; Wustoni, S.; Kuroiwa, S.; Nakanishi, T.; Koike-Takeshita, A.; Osaka, T. Monitoring Amyloid Sup35NM Growth with Label-Free Electrical Detection Using a Field-Effect Transistor Biosensor. *ChemElectroChem* **2013**, *1*, 51–54. [\[CrossRef\]](#)
24. Oh, J.; Yoo, G.; Chang, Y.W.; Kim, H.J.; Jose, J.; Kim, E.; Pyun, J.-C.; Yoo, K.-H. A carbon nanotube metal semiconductor field effect transistor-based biosensor for detection of amyloid-beta in human serum. *Biosens. Bioelectron.* **2013**, *50*, 345–350. [\[CrossRef\]](#) [\[PubMed\]](#)
25. Kim, C.-B.; Chae, C.-J.; Song, K.-B. In Vitro Detection of Beta-Amyloid Peptides using a Photo-Sensitive Field Effect Transistor Integrated with a Single Layer On-Chip Optical Filter. *Biophys. J.* **2012**, *102*, 186a. [\[CrossRef\]](#)
26. Carneiro, M.C.; Moreira, F.T.; Dutra, R.A.; Fernandes, R.; Sales, M.G.F. Homemade 3-carbon electrode system for electrochemical sensing: Application to microRNA detection. *Microchem. J.* **2018**, *138*, 35–44. [\[CrossRef\]](#)
27. Kaushik, A.; Shah, P.; Vabbina, P.K.; Jayant, R.D.; Tiwari, S.; Vashist, A.; Yndart, A.; Nair, M. A label-free electrochemical immunosensor for beta-amyloid detection. *Anal. Methods* **2016**, *8*, 6115–6120. [\[CrossRef\]](#)
28. Liu, L.; Xia, N.; Jiang, M.; Huang, N.; Guo, S.; Li, S.; Zhang, S. Electrochemical detection of amyloid- β oligomer with the signal amplification of alkaline phosphatase plus electrochemical–chemical–chemical redox cycling. *J. Electroanal. Chem.* **2015**, *754*, 40–45. [\[CrossRef\]](#)
29. Negahdary, M.; Heli, H. An ultrasensitive electrochemical aptasensor for early diagnosis of Alzheimer's disease, using a fern leaves-like gold nanostructure. *Talanta* **2019**, *198*, 510–517. [\[CrossRef\]](#)
30. Moreira, F.T.; Sale, M.G.F.; Di Lorenzo, M. Towards timely Alzheimer diagnosis: A self-powered amperometric biosensor for the neurotransmitter acetylcholine. *Biosens. Bioelectron.* **2017**, *87*, 607–614. [\[CrossRef\]](#)
31. Xia, N.; Wang, X.; Zhou, B.; Wu, Y.; Mao, W.; Liu, L. Electrochemical Detection of Amyloid- β Oligomers Based on the Signal Amplification of a Network of Silver Nanoparticles. *ACS Appl. Mater. Interfaces* **2016**, *8*, 19303–19311. [\[CrossRef\]](#)
32. Rama, E.C.; González-García, M.B.; Costa-García, A. Competitive electrochemical immunosensor for amyloid-beta 1–42 detection based on gold nanostructured Screen-Printed Carbon Electrodes. *Sens. Actuators B Chem.* **2014**, *201*, 567–571. [\[CrossRef\]](#)
33. Miao, J.; Li, X.; Li, Y.; Dong, X.; Zhao, G.; Fang, J.; Wei, Q.; Cao, W. Dual-signal sandwich electrochemical immunosensor for amyloid β -protein detection based on Cu–Al₂O₃–g–C₃N₄–Pd and UiO-66@PANI-MB. *Anal. Chim. Acta* **2019**, *1089*, 48–55. [\[CrossRef\]](#) [\[PubMed\]](#)
34. Lien, T.T.; Takamura, Y.; Tamiya, E.; Vestergaard, M.C. Modified screen printed electrode for development of a highly sensitive label-free impedimetric immunosensor to detect amyloid beta peptides. *Anal. Chim. Acta* **2015**, *892*, 69–76. [\[CrossRef\]](#) [\[PubMed\]](#)
35. Veloso, A.J.; Chow, A.M.; Ganesh, H.V.S.; Li, N.; Dhar, D.; Wu, D.C.H.; Mikhaylichenko, S.; Brown, I.R.; Kerman, K. Electrochemical Immunosensors for Effective Evaluation of Amyloid-Beta Modulators on Oligomeric and Fibrillar Aggregation Processes. *Anal. Chem.* **2014**, *86*, 4901–4909. [\[CrossRef\]](#)
36. Truta, L.A.; Moreira, F.T.; Sales, M.G.F. A dye-sensitized solar cell acting as the electrical reading box of an immunosensor: Application to CEA determination. *Biosens. Bioelectron.* **2018**, *107*, 94–102. [\[CrossRef\]](#)
37. Pereira, M.V.; Marques, A.C.; Oliveira, D.; Martins, R.; Moreira, F.T.C.; Sales, M.G.F.; Fortunato, E. Paper-Based Platform with an In Situ Molecularly Imprinted Polymer for β -Amyloid. *ACS Omega* **2020**, *5*, 12057–12066. [\[CrossRef\]](#)
38. You, M.; Yang, S.; An, Y.; Zhang, F.; He, P. A novel electrochemical biosensor with molecularly imprinted polymers and aptamer-based sandwich assay for determining amyloid- β oligomer. *J. Electroanal. Chem.* **2020**, *862*, 114017. [\[CrossRef\]](#)
39. Özcan, N.; Medetalibeyoglu, H.; Akyildirim, O.; Atar, N.; Yola, M.L. Electrochemical detection of amyloid- β protein by delaminated titanium carbide MXene/multi-walled carbon nanotubes composite with molecularly imprinted polymer. *Mater. Today Commun.* **2020**, *23*, 101097. [\[CrossRef\]](#)
40. Moreira, F.T.C.; Freitas, V.A.P.; Sales, M.G.F. Biomimetic norfloxacin sensors made of molecularly-imprinted materials for potentiometric transduction. *Mikrochim. Acta* **2010**, *172*, 15–23. [\[CrossRef\]](#)
41. Guerreiro, J.R.; Sales, M.G.F.; Moreira, F.T.C.; Rebelo, T.S.R. Selective recognition in potentiometric transduction of amoxicillin by molecularly imprinted materials. *Eur. Food Res. Technol.* **2010**, *232*, 39–50. [\[CrossRef\]](#)
42. Moreira, F.; Queirós, R.; Truta, L.; Silva, T.I.; Castro, R.M.; Amorim, L.R.; Sales, M.G.F. Host-Tailored Sensors for Leucomalachite Green Potentiometric Measurements. *J. Chem.* **2012**, *2013*, 605403. [\[CrossRef\]](#)
43. Moreira, F.T.; Kamel, A.H.; Guerreiro, R.L.; Azevedo, V.; Sales, M.G.F. New potentiometric sensors based on two competitive recognition sites for determining tetracycline residues using flow-through system. *Procedia Eng.* **2010**, *5*, 1200–1203. [\[CrossRef\]](#)
44. Moreira, F.T.; Kamel, A.H.; Guerreiro, J.R.; Sales, M.G.F. Man-tailored biomimetic sensor of molecularly imprinted materials for the potentiometric measurement of oxytetracycline. *Biosens. Bioelectron.* **2010**, *26*, 566–574. [\[CrossRef\]](#) [\[PubMed\]](#)
45. Blanco-López, M.; Lobo-Castañón, M.; Miranda-Ordieres, A.; Tuñón-Blanco, P. Electrochemical sensors based on molecularly imprinted polymers. *TrAC Trends Anal. Chem.* **2004**, *23*, 36–48. [\[CrossRef\]](#)
46. Henry, O.Y.; Piletsky, S.; Cullen, D. Fabrication of molecularly imprinted polymer microarray on a chip by mid-infrared laser pulse initiated polymerisation. *Biosens. Bioelectron.* **2008**, *23*, 1769–1775. [\[CrossRef\]](#) [\[PubMed\]](#)

47. Steinfeld, U.; Palm, B.D.; Lee, H.H. Polymer Matrix, Process for Their Preparation and Their Use. Patent DE102006040772A1, 20 March 2008.
48. Piletsky, S.A.; Piletska, E.V.; Chen, B.; Karim, K.; Weston, D.; Barrett, G.; Lowe, P.; Turner, A.P.F. Chemical Grafting of Molecularly Imprinted Homopolymers to the Surface of Microplates. Application of Artificial Adrenergic Receptor in Enzyme-Linked Assay for β -Agonists Determination. *Anal. Chem.* **2000**, *72*, 4381–4385. [\[CrossRef\]](#)
49. And, M.-M.T.; Sellergren, B. Thin Molecularly Imprinted Polymer Films via Reversible Addition–Fragmentation Chain Transfer Polymerization. *Chem. Mater.* **2006**, *18*, 1773–1779. [\[CrossRef\]](#)
50. Liang, R.; Ding, J.; Gao, S.; Qin, W. Mussel-Inspired Surface-Imprinted Sensors for Potentiometric Label-Free Detection of Biological Species. *Angew. Chem. Int. Ed.* **2017**, *56*, 6833–6837. [\[CrossRef\]](#)
51. Wang, Y.; Zhou, Y.; Sokolov, J.; Rigas, B.; Levon, K.; Rafailovich, M. A potentiometric protein sensor built with surface molecular imprinting method. *Biosens. Bioelectron.* **2008**, *24*, 162–166. [\[CrossRef\]](#)
52. Golmohammadi, H.; Morales-Narváez, E.; Naghdi, T.; Merkoçi, A. Nanocellulose in Sensing and Biosensing. *Chem. Mater.* **2017**, *29*, 5426–5446. [\[CrossRef\]](#)
53. Su, S.; Wu, W.; Gao, J.; Lu, J.; Fan, C. Nanomaterials-based sensors for applications in environmental monitoring. *J. Mater. Chem.* **2012**, *22*, 18101–18110. [\[CrossRef\]](#)
54. Holzinger, M.; Le Goff, A.; Cosnier, S. Nanomaterials for biosensing applications: A review. *Front. Chem.* **2014**, *2*, 63. [\[CrossRef\]](#) [\[PubMed\]](#)
55. Ji, S.; Lee, M.; Kim, D. Detection of early stage prostate cancer by using a simple carbon nanotube@paper biosensor. *Biosens. Bioelectron.* **2018**, *102*, 345–350. [\[CrossRef\]](#)
56. Khosravi, F.; Loeian, S.M.; Panchapakesan, B. Ultrasensitive Label-Free Sensing of IL-6 Based on PASE Functionalized Carbon Nanotube Micro-Arrays with RNA-Aptamers as Molecular Recognition Elements. *Biosensors* **2017**, *7*, 17. [\[CrossRef\]](#) [\[PubMed\]](#)
57. Li, N.; Wang, Y.; Cao, W.; Zhang, Y.; Yan, T.; Du, B.; Wei, Q. An ultrasensitive electrochemical immunosensor for CEA using MWCNT-NH₂ supported PdPt nanocages as labels for signal amplification. *J. Mater. Chem. B* **2015**, *3*, 2006–2011. [\[CrossRef\]](#) [\[PubMed\]](#)
58. Peng, Y.; Wu, Z.; Liu, Z. An electrochemical sensor for paracetamol based on an electropolymerized molecularly imprinted o-phenylenediamine film on a multi-walled carbon nanotube modified glassy carbon electrode. *Anal. Methods* **2014**, *6*, 5673–5681. [\[CrossRef\]](#)
59. Gomes-Filho, S.; Dias, A.; Silva, M.; Silva, B.; Dutra, R.F. A carbon nanotube-based electrochemical immunosensor for cardiac troponin T. *Microchem. J.* **2013**, *109*, 10–15. [\[CrossRef\]](#)
60. Choong, C.-L.; Bendall, J.S.; Milne, W.I. Carbon nanotube array: A new MIP platform. *Biosens. Bioelectron.* **2009**, *25*, 652–656. [\[CrossRef\]](#)
61. Wang, J.; Musameh, M. Carbon-nanotubes doped polypyrrole glucose biosensor. *Anal. Chim. Acta* **2005**, *539*, 209–213. [\[CrossRef\]](#)
62. Bakker, E.; Bühlmann, P.; Pretsch, E. Carrier-Based Ion-Selective Electrodes and Bulk Optodes. General Characteristics. *Chem. Rev.* **1997**, *97*, 3083–3132. [\[CrossRef\]](#)
63. Moreira, F.; Sharma, S.; Dutra, R.A.; Noronha, J.P.; Cass, A.E.; Sales, M.G.F. Smart plastic antibody material (SPAM) tailored on disposable screen printed electrodes for protein recognition: Application to myoglobin detection. *Biosens. Bioelectron.* **2013**, *45*, 237–244. [\[CrossRef\]](#) [\[PubMed\]](#)
64. Moreira, F.; Dutra, R.A.; Noronha, J.P.; Cunha, A.L.; Sales, M.G.F. Artificial antibodies for troponin T by its imprinting on the surface of multiwalled carbon nanotubes: Its use as sensory surfaces. *Biosens. Bioelectron.* **2011**, *28*, 243–250. [\[CrossRef\]](#) [\[PubMed\]](#)
65. Bokobza, L.; Bruneel, J.-L.; Couzi, M. Raman spectroscopy as a tool for the analysis of carbon-based materials (highly oriented pyrolytic graphite, multilayer graphene and multiwall carbon nanotubes) and of some of their elastomeric composites. *Vib. Spectrosc.* **2014**, *74*, 57–63. [\[CrossRef\]](#)
66. Graupner, R. Raman spectroscopy of covalently functionalized single-wall carbon nanotubes. *J. Raman Spectrosc.* **2007**, *38*, 673–683. [\[CrossRef\]](#)
67. Burghard, M. Electronic and vibrational properties of chemically modified single-wall carbon nanotubes. *Surf. Sci. Rep.* **2005**, *58*, 1–109. [\[CrossRef\]](#)
68. Dyke, C.A.; Tour, J.M. Covalent Functionalization of Single-Walled Carbon Nanotubes for Materials Applications. *J. Phys. Chem. A* **2004**, *108*, 11151–11159. [\[CrossRef\]](#)
69. Titus, E.; Ali, N.; Cabral, G.; Grácio, J.; Babu, P.R.; Jackson, M.J. Chemically Functionalized Carbon Nanotubes and Their Characterization Using Thermogravimetric Analysis, Fourier Transform Infrared, and Raman Spectroscopy. *J. Mater. Eng. Perform.* **2006**, *15*, 182–186. [\[CrossRef\]](#)
70. Almeida, S.; Moreira, F.; Heitor, A.; Montenegro, M.; Aguilar, G.; Sales, M. Sulphonamide-imprinted sol-gel materials as ionophores in potentiometric transduction. *Mater. Sci. Eng. C* **2011**, *31*, 1784–1790. [\[CrossRef\]](#)
71. Wu, C.C.; Ku, B.C.; Ko, C.H.; Chiu, C.C.; Wang, G.J.; Yang, Y.H.; Wu, S.J. Electrochemical impedance spectroscopy analysis of A-beta (1–42) peptide using a nanostructured biochip. *Electrochim. Acta* **2014**, *134*, 249–257. [\[CrossRef\]](#)
72. Carneiro, P.; Loureiro, J.; Delerue-Matos, C.; Morais, S.; do Carmo Pereira, M. Alzheimer’s disease: Development of a sensitive label-free electrochemical immunosensor for detection of amyloid beta peptide. *Sens. Actuators B-Chem.* **2017**, *239*, 157–165. [\[CrossRef\]](#)

73. Amor-Gutiérrez, O.; Costa-Rama, E.; Arce-Varas, N.; Martínez-Rodríguez, C.; Novelli, A.; Fernández-Sánchez, M.T.; Costa-García, A. Competitive electrochemical immunosensor for the detection of unfolded p53 protein in blood as biomarker for Alzheimer's disease. *Anal. Chim. Acta* **2020**, *1093*, 28–34. [[CrossRef](#)] [[PubMed](#)]
74. Diba, F.S.; Kim, S.; Lee, H.J. Electrochemical immunoassay for amyloid-beta 1-42 peptide in biological fluids interfacing with a gold nanoparticle modified carbon surface. *Catal. Today* **2017**, *295*, 41–47. [[CrossRef](#)]
75. Liu, L.; Zhao, F.; Ma, F.; Zhang, L.; Yang, S.; Xia, N. Electrochemical detection of beta-amyloid peptides on electrode covered with N-terminus-specific antibody based on electrocatalytic O₂ reduction by A beta(1-16)-heme-modified gold nanoparticles. *Biosens. Bioelectron.* **2013**, *49*, 231–235. [[CrossRef](#)]
76. Cabral-Miranda, G.; Cardoso, A.R.; Ferreira, L.C.; Sales, M.G.F.; Bachmann, M.F. Biosensor-based selective detection of Zika virus specific antibodies in infected individuals. *Biosens. Bioelectron.* **2018**, *113*, 101–107. [[CrossRef](#)] [[PubMed](#)]
77. Zhou, Y.; Zhang, H.; Liu, L.; Li, C.; Chang, Z.; Zhu, X.; Ye, B.; Xu, M. Fabrication of an antibody-aptamer sandwich assay for electrochemical evaluation of levels of beta-amyloid oligomers. *Sci. Rep.* **2016**, *6*, 35186. [[CrossRef](#)] [[PubMed](#)]
78. Qin, J.; Cho, M.; Lee, Y. Ultrasensitive Detection of Amyloid-beta Using Cellular Prion Protein on the Highly Conductive Au Nanoparticles-Poly(3,4-ethylene dioxithiophene)-Poly(thiophene-3-acetic acid) Composite Electrode. *Anal. Chem.* **2019**, *91*, 11259–11265. [[CrossRef](#)] [[PubMed](#)]
79. Wustoni, S.; Wang, S.; Alvarez, J.R.; Hidalgo, T.C.; Nunes, S.P.; Inal, S. An organic electrochemical transistor integrated with a molecularly selective isoporous membrane for amyloid-beta detection. *Biosens. Bioelectron.* **2019**, *143*, 111561. [[CrossRef](#)] [[PubMed](#)]
80. Yu, Y.; Sun, X.; Tang, D.; Li, C.; Zhang, L.; Nie, D.; Yin, X.; Shi, G. Gelsolin bound beta-amyloid peptides((1-40/1-42)): Electrochemical evaluation of levels of soluble peptide associated with Alzheimer's disease. *Biosens. Bioelectron.* **2015**, *68*, 115–121. [[CrossRef](#)]
81. Qin, J.; Cho, M.; Lee, Y. Ferrocene-Encapsulated Zn Zeolitic Imidazole Framework (ZIF-8) for Optical and Electrochemical Sensing of Amyloid-beta Oligomers and for the Early Diagnosis of Alzheimer's Disease. *ACS Appl. Mater. Interfaces* **2019**, *11*, 11743–11748. [[CrossRef](#)]

Article

Adsorptive Recovery of Cu^{2+} from Aqueous Solution by Polyethylene Terephthalate Nanofibres Modified with 2-(Aminomethyl)Pyridine

Thandiwe Crystal Totito ¹, Katri Laatikainen ², Omoniye Pereao ^{1,*}, Chris Bode-Aluko ¹ and Leslie Petrik ¹

- ¹ Environmental and Nanoscience Research Group, Department of Chemistry, University of the Western Cape, Private Bag X17, Bellville 7535, South Africa; tctotito@gmail.com (T.C.T.); 3471837@myuwc.ac.za (C.B.-A.); lpatrik@uwc.ac.za (L.P.)
² Department of Separation Science, School of Engineering Science, Lappeenranta-Lahti University of Technology LUT, Yliopistonkatu 34, FI-53850 Lappeenranta, Finland; katri.laatikainen@lut.fi
* Correspondence: pereao kola@gmail.com

Featured Application: Adsorption of Cu^{2+} ions from aqueous solution and desorption of Cu^{2+} from WPET-SiAMPy composite nanofibres.

Abstract: The accumulation of plastic waste products in the environment has adversely affected wildlife and human beings. Common plastics that accumulate in the environment are plastics that are made of polyethylene terephthalate (PET) polymer. PET plastic waste products can be recycled for beneficial use, which would reduce their negative impacts. In this study, modified PET or waste PET (WPET) from plastic bottles was blended with powder commercial 2-(aminomethyl)pyridine (SiAMPy) resin and electrospun into composite nanofibres and applied for Cu^{2+} adsorption. PET-SiAMPy or WPET-SiAMPy composite nanofibres fibre diameters from the HRSEM images were 90–140 nm and 110–155 nm, respectively. In batch adsorption experiments, PET-SiAMPy or WPET-SiAMPy composite nanofibres achieved Cu^{2+} adsorption equilibrium within 60 secs of contact time with 0.98 mmol/g (89.87%) or 1.24 mmol/g (96.04%) Cu^{2+} adsorption capacity. The Cu^{2+} complex formation rate (k) with WPET-SiAMPy was 0.0888 with the mole ratio of Cu^{2+} and WPET-SiAMPy nanofibres 1:2. The complex molecular formula formed was $\text{Cu}(\text{WPET-SiAMPy})_2$ with a square planar geometry structure. The WPET-SiAMPy nanofibres' adsorption was best fitted to the Freundlich isotherm. WPET-SiAMPy composite nanofibres were considered highly efficient for Cu^{2+} adsorption from aqueous solution and could be regenerated at least five times using 5 M H_2SO_4 .

Keywords: waste plastic; polyethylene terephthalate; electrospinning; 2-(aminomethyl)pyridine; adsorption; copper ion; nanofibre

Citation: Totito, T.C.; Laatikainen, K.; Pereao, O.; Bode-Aluko, C.; Petrik, L. Adsorptive Recovery of Cu^{2+} from Aqueous Solution by Polyethylene Terephthalate Nanofibres Modified with 2-(Aminomethyl)Pyridine. *Appl. Sci.* **2021**, *11*, 11912. <https://doi.org/10.3390/app112411912>

Academic Editor: Sergio Torres-Giner

Received: 12 October 2021

Accepted: 12 November 2021

Published: 15 December 2021

Publisher's Note: MDPI stays neutral with regard to jurisdictional claims in published maps and institutional affiliations.



Copyright: © 2021 by the authors. Licensee MDPI, Basel, Switzerland. This article is an open access article distributed under the terms and conditions of the Creative Commons Attribution (CC BY) license (<https://creativecommons.org/licenses/by/4.0/>).

1. Introduction

Globally, the growth of our economy and modern life depends on industries that use plastic in near-unlimited applications such as packaging, textiles, agriculture, automotive, electronics, building, and construction, or machinery. These applications increase the quantity of plastic waste being discarded into our environment [1]. Common plastics that accumulate in the environment are plastics made of polyethylene terephthalate (PET) polymer, adding to chemical persistence, and their mechanical fragmentation into microplastics promotes their ingestion by even small organisms such as zooplankton, and their entry into the human food chain [2]. These plastic waste products can be recycled for beneficial use which would reduce their negative impacts and help minimize a vast number of organic pollutants reported in water [3]. The organic and inorganic contaminants present in drinking water sources and in industrial waste streams need to be controlled to an acceptable level according to environmental regulations worldwide [4] and this requires the

protection of natural resources such as ground water, rivers, oceans, and lakes. Moreover, the inorganic contaminants present in various waste effluents are not only toxic metals, but these effluents also contain some valuable metals that can be extracted and reused. Some of these metal ions are not biodegradable or bio transformable, therefore they exist in the environment for longer periods of time [5]. Thus, this research will report the repurposing of waste PET materials for the recovery of Cu metal ions from aqueous solutions.

Electrospinning is an easy and inexpensive process of forming ultrafine fibres in the range from the nano- to micrometre. The electrospinning process can produce sub-micron-sized polymer fibres with a small interfibrous pore size using the electrostatically driven jets of polymer solutions [6]. When an adequate, high voltage is applied to the solution droplet, the body of the solution becomes charged and electrostatic repulsion counteracts the surface tension. Thus, the droplet is stretched and the jet spurt solidifies into a fibre, which is collected by an aluminium collector [7]. Modified nanofibres' applications in adsorption are considerably growing and are projected to double by 2040 due to unique properties such as high surface area per unit mass, high porosity, low basis weight, layer thinness, high permeability, superior directional strength, and cost-effectiveness [8,9].

Adsorption depends on a selection of process conditions, for example the pH, metal concentration, adsorbent concentration, and type of metal ions. The adsorption process involves several technical aspects that can be analysed from a process intensification perspective. Van Gerven and Stankiewicz [10] have described the process intensification based on several fundamental principles and approaches. These fundamental principles have been identified to be the adsorbent synthesis, process design, optimization of the operating conditions, modelling of the adsorption process, regeneration, and the life cycle analysis of the adsorbent [11]. Thus, process intensification aims to modify the material while also improving the adsorption binding kinetics, with improved specific adsorbent surface area [12]. The supplied SiAMPy contains 2-(aminomethyl)pyridine groups that are supported on silica [13] and the 2-(aminomethyl)pyridine groups are Lewis base chelating ligands and are also called the complexing agent [14]. The 2-(Aminomethyl)pyridine ligand is an N,N'-bidentate ligand containing aromatic pyridine aliphatic amine donor function. It was postulated that the blended WPET-SiAMPy composite nanofibres can form Lewis's acid/base bonds with Cu^{2+} metal ions during the adsorption process. The Cu^{2+} ions should be desorbed from the WPET-SiAMPy composite nanofibres by a simple regeneration process.

Adsorption is performed with activated carbon as the adsorbent is frequently used for the removal of diverse metals present at trace levels, but this adsorbent is nonselective. Compared to conventional resources, carbon-based materials possess useful properties such as hydrophobic surfaces, a high surface area, large pore volume, chemical inertness, good thermal and mechanical stability, easy handling, and low cost of manufacture. In the context of green chemistry, polyethylene terephthalate (PET), which is versatile, lightweight, flexible, moisture resistant, robust, and relatively inexpensive, is especially attractive for its unique physicochemical properties such as excellent chemical stability [9]. The employment of readily available low-cost materials such as waste PET that are reusable as a substitute for carbon adsorbents is prospective for sustainable contaminated water treatment and offers the potential for environment clean-up [15]. Focusing on developing highly effective nanofibres from waste PET thus could decrease plastic waste pollution. This can be achieved by electrospinning PET nanofibres, and by blending these nanofibres with suitable inorganic metal adsorbents, could enhance their kinetics of adsorption because of the highly enhanced surface area the nanofibres possess.

Repurposing WPET into bead-free nanofibres was studied and compared with commercial PET. This study aimed to report the synthesis, characterization, and incorporation of a commercial SiAMPy resin into PET or WPET nanofibres to increase the adsorption capacity of the nanofibres for the selective recovery of valuable metals such as Cu^{2+} from metal laden effluents. Several experiments on the adsorption parameters such as contact time, initial concentration, and solution pH, as well as the kinetics of adsorption on the

removal of Cu^{2+} were studied. The adsorption and desorption conditions were investigated to determine the regeneration of the adsorbent for commercial production.

2. Materials and Methods

The reagents such as polyethylene terephthalate (PET), trifluoroacetic acid (TFA), copper (II) nitrate hemi(pentahydrate) and sodium hydroxide (NaOH) were all purchased from Sigma-Aldrich, South Africa, and used without further purification. The functionalized commercial silica supported 2-aminomethylpyridine (SiAMPy) used to improve the nanofibre adsorption capacity was supplied by the collaborating institute Lappeenranta University of Technology, Laboratory of Industrial Chemistry, in sealed glass vials. The electrospinning process of commercial PET was adopted from previously conducted studies by Pereao, 2018 [16] with inconsequential adjustments.

2.1. Preparation of PET and WPET Nanofibres

The PET was electrospun as the reference material for waste PET nanofibres. Waste polyethylene terephthalate (WPET) was obtained from wastewater bottles (500 mL) collected from the same production batch. All bottles were cleaned and rinsed with ethanol and dried at room temperature. The bottles were thinly shredded into $2 \times 2 \text{ mm}^2$ pieces. The PET or WPET solution was prepared by means of dissolving 1.66 g of PET or WPET with 14.9 g (10 mL) of TFA making a solution with a concentration of 10 wt.%. The 10 wt.% PET was dissolved at room temperature overnight for preparing a homogeneous solution while the dissolution of the WPET bottle pieces was carried out at room temperature for 30 min to ensure a homogeneous solution. The 10 wt.% PET or WPET solutions were electrospun by introducing the PET or WPET polymer solution into two 20 mL syringes, each fitted with a stainless-steel hypodermic needle of gauge 19, respectively. The two syringes were then placed in a pump for controlling the flow rate of the solution which was set at 0.8 mL/h or 0.05 mL/h during electrospinning. An electric field voltage of 17 kV was applied across the needles and the Al foil collector was positioned at a distance of 17 cm or 14 cm. The electrospinning process took place at room temperature to ensure the thorough evaporation of the solvent. The nature of each polymer solution was taken into consideration when electrospinning. The electrospinning lasted for 5 h or 2 h for PET or WPET polymer solution.

2.2. Modification of PET and WPET Nanofibres with SiAMPy

The PET and WPET nanofibres were modified with SiAMPy through a blending process. This process was carried out by grinding using mortar and pestle, then further sieving ($63 \mu\text{m}$) the SiAMPy to select particles with an average size of 92.95 nm as measured in HRSEM image Figure 1a. The ground up SiAMPy (0.01 wt.%) was blended into the PET or WPET (10 wt.%) polymer solutions with TFA as solvent, and used as the sol–gel precursor, respectively. The solutions were stirred for 30 min at room temperature to ensure the homogeneity of the solution upon electrospinning. The PET–SiAMPy or WPET–SiAMPy solutions were electrospun by introducing 5 mL of the blended polymer solution into a 20 mL syringe fitted with 19 G needle. The syringe was fixed in a pump during electrospinning for monitoring the flow rate of the solution and was set at 0.8 mL/h or 0.05 mL/h, respectively. An electric field voltage of 20 kV was applied across the needle and the Al foil collector, which was positioned at a distance 14 cm.

2.3. Characterization Protocol

Characterization techniques provide the chemical, physical and mechanical properties giving information on every material used in this study. The basic principles of the instrumentation and their application used in this research study are discussed below.

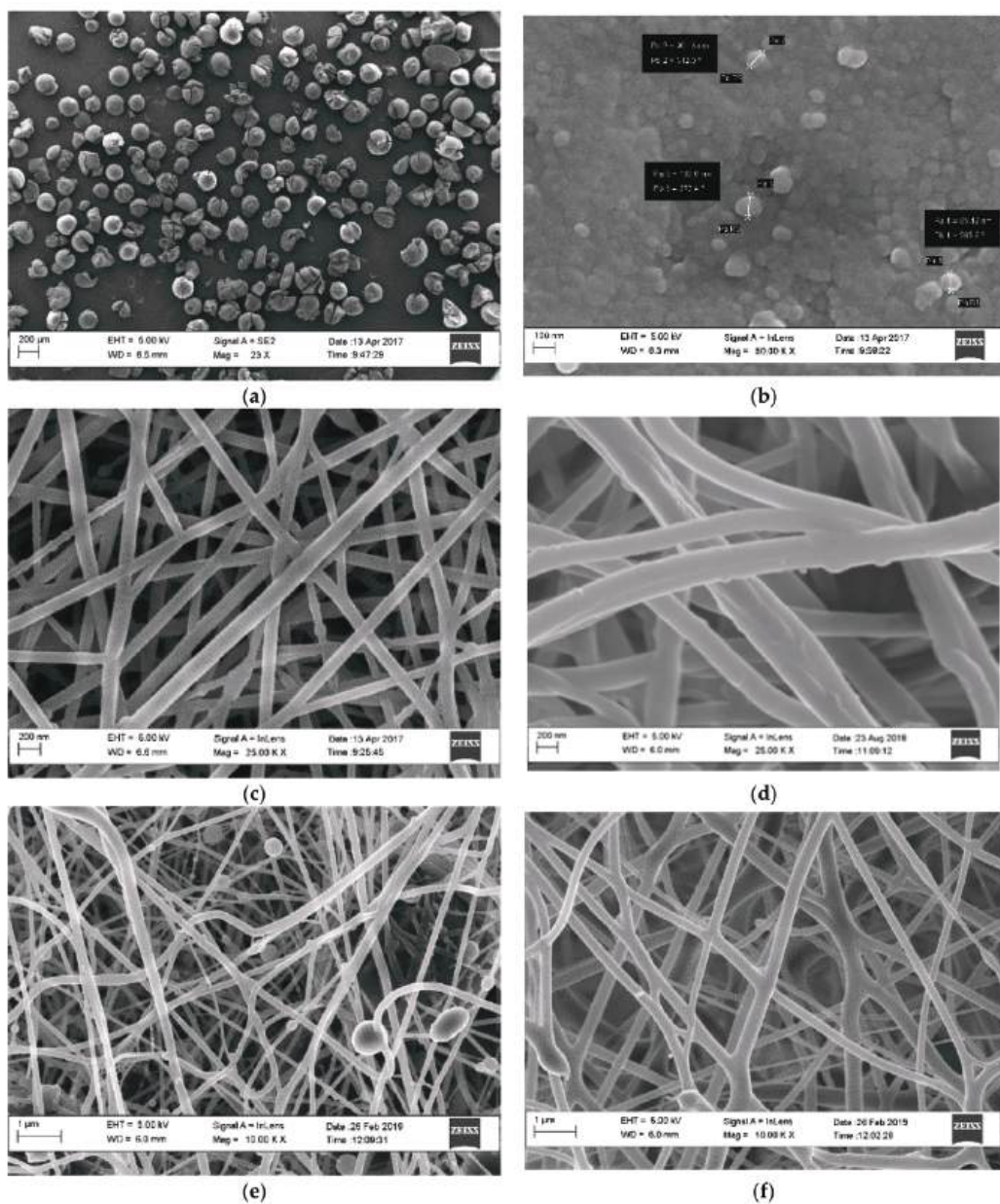


Figure 1. HRSEM images of (a): supplied SiAMPy; (b): ground and sieved SiAMPy; (c): PET (0.8 mL/h, 17 kV, 17 cm); (d): WPET (0.05 mL/h, 17 kV, 14 cm); (e): PET-SiAMPy (0.8 mL/h, 20 kV, 14 cm) and (f): WPET-SiAMPy (0.05 mL/h, 20 kV, 14 cm) nanofibre morphology.

2.3.1. HRSEM Measurement

The surface morphology of the PET, WPET, PET-SiAMPy, and WPET-SiAMPy electrospun nanofibres were determined using a high-resolution field emission gun scanning electron microscope (HRFEGSEM) and an Auriga Gemini FEG SEM (HRSEM). The electrospun nanofibres were coated with conductive carbon using a sputter-coating technique with an electric field and argon gas to prevent the nanofibres charging during analysis. The HRSEM images were taken on various spots of the nanofibre with varying magnification.

2.3.2. ATR-FTIR Measurement

The instrument Perkin Elmer 100 FT-IR spectrometer (ATR-FTIR) was used to determine the functional groups of the surface of electrospun nanofibres (PET and WPET) before and after modification (PET-SiAMPy and WPET-SiAMPy). The samples were individually placed on the diamond crystal of the ATR holder then fixed for the perfect contact of the sample with the crystal. The FTIR instrument wavelength range was set to 4000 cm^{-1} to 650 cm^{-1} against transmittance with 2.0 resolution at 64 scanning times. For every analysis, the baseline of the FTIR was corrected using the background spectrum of the blank scan. The FTIR diamond crystal and ATR holder were cleaned with ethanol before every analysis to prevent the cross-contamination of the samples.

2.3.3. TGA Measurement

The TGA 4000 PerkinElmer thermal analyser instrument was used to determine the changes in physical and chemical composition of the PET, WPET, and CS nanofibres by measuring the weight loss due to an increasing temperature profile applied to the nanofibres. The nanofibres' decomposition was conducted to determine the thermal behaviour of the nanofibres before and after their surface modification. The TGA instrument was calibrated before each analysis to stabilize the instrument baseline. The TGA technique for the PET, WPET, and CS nanofibres was carried out using the TGA 4000 PerkinElmer thermal analyser. The PET, WPET, and SiAMPy (0.05 g) were weighed out in the sample holder and placed in the instrument. The analysis was performed in nitrogen with a flow rate of 20 mL/min and the heating rate was set at 20 $^{\circ}\text{C}/\text{min}$ up to 800 $^{\circ}\text{C}$.

2.3.4. ICP-OES Measurement

The Varian Radial ICP-OES (High Matrix Introduction (HMI) accessory, Collision gas; Ar) instrument was used to determine the concentration of Cu^{2+} after adsorption and regeneration experiments, respectively. The ICP-OES analysis was carried out to determine the concentration of the adsorbate obtained from the adsorption equilibrium of the metal ion solution.

2.4. Adsorption Process Using the PET-SiAMPy or WPET-SiAMPy Nanofibres

Batch adsorption experiments were carried out to determine the optimum contact time, adsorbent dosage, Cu^{2+} aqueous solution pH, and the initial concentration of the adsorbate (Cu^{2+}). The batch experiments were performed by immersing 0.01 g of the adsorbent into the Cu^{2+} aqueous solution of 100 mgL^{-1} initial concentration. The Cu^{2+} aqueous solution with the adsorbent was agitated at 190 rpm for 120 min. Thereafter, the Cu^{2+} aqueous solution concentration was sampled at fixed intervals and determined using ICP-OES. The evolution of the Cu^{2+} aqueous solution concentration was monitored to equilibrium. The adsorption capacity of the adsorbents was calculated using the following Equation:

$$q_e = \frac{(C_o - C_e)V}{W} \quad (1)$$

where q_e is the equilibrium adsorption capacity per gram of dry weight of the adsorbent (mg/g), C_o is the initial concentration of Cu^{2+} , C_e is the final concentration of Cu^{2+} (mgL^{-1}), V is the volume of the solution (L) and W is the weight of the dry adsorbent (g).

The adsorption (R) is defined in Equation (2)

$$R = 1 - \frac{C_e}{C_o} \quad (2)$$

The percentage recovery is defined in Equation (3):

$$R = \left(\frac{C_o - C_e}{C_o} \right) \times 100 \quad (3)$$

Adsorption experiments were studied using the isotherm and kinetics modelling to know the details about the performance, mechanisms, practical design, and the operation of the adsorption systems.

3. Results and Discussion

3.1. Characterization of Electrospun PET, WPET, PET-SiAMPy, and WPET-SiAMPy Nanofibres

The SiAMPy-modified PET and WPET nanofibres were characterized with HRSEM to visualize the morphology of the composite nanofibres as shown in Figure 1.

The HRSEM image of SiAMPy as supplied is shown in Figure 1a while the ground SiAMPy in Figure 1b demonstrated the agglomerated structure of the powder with a size range from 85 to 103 nm. The supplied SiAMPy initially possessed large, agglomerated units that needed to be ground to powder. This was performed to increase the surface area of the SiAMPy, thus increasing the adsorption capacity by limiting diffusional constraints of large units and making the powder SiAMPy easier to incorporate into the polymer solutions, respectively. The powder SiAMPy was completely dissolved in the electrospinning solvent. Figure 1c,d show the HRSEM images with the nanofibre morphology of PET and WPET, both of which consisted of smooth, uniform, homogeneous, and well-structured nanofibres with varying diameters in the range of 90–130 nm, respectively. The polymer solution flow rate and collecting distance of WPET was varied for possible spinnability conditions, with the PET electrospinning conditions as the reference. The WPET polymer solution was spinnable at 0.05 mL/h flow rate and at a collecting distance of 14 cm. The homogeneous structured PET and WPET nanofibres in Figure 1c,d prove the success of the electrospinning procedure and the optimum conditions under which PET and WPET nanofibre formation occurred (see Table 1). In the HRSEM images of PET-SiAMPy (e) and WPET-SiAMPy (f) composite nanofibres showed bead formation on the PET-SiAMPy nanofibres that were spun using a flow rate of 0.8 mL/h. The formation of beading visible in Figure 1e could be due to the repulsive forces between PET polymer and S-AMPy nanoparticles' ionic groups that arise due to the application of the high electric field during electrospinning. Figure 1f showed consistent, smooth, and homogeneous nanofibres for WPET-SiAMPy nanofibres that were spun at a flow rate of 0.05 mL/h. The electrospinning flow rate was set according to the polymer solution viscosity. The WPET-SiAMPy polymer solution was more viscous compared to the PET-SiAMPy polymer solution, thus the WPET-SiAMPy polymer solution electrospinning flow rate was observed to be lower than PET-SiAMPy polymer solution. The HRSEM image (f) shows good blending between the SiAMPy and the WPET polymer under the applied electrospinning conditions which were 0.05 mL/h flow rate, 20 kV applied electric field voltage and 14 cm collecting distance. The interconnected nanofibres in the HRSEM image (e) were due to the polymer concentration and the concentration of the solvent TFA. Biazar et al. [17] previously reported that TFA formed interconnected nanofibres with branches and twigs, due to the high TFA concentration that lowered the evaporation rate and caused bonding between nanofibres. The WPET-SiAMPy nanofibres thus had better nanofibre morphology compared to the PET-SiAMPy nanofibres, showing the benefit of reusing WPET for preparing functional nanofibres.

The FTIR spectra for PET and WPET nanofibres shown in Figure 2a demonstrate similar FTIR patterns which means that the PET commercial nanofibres and the recycled WPET nanofibres possess the same functional groups.

Table 1. Sample codes and optimum electrospinning conditions for each sample.

Sample Code	Polymer Concentration (wt%)	Solvent Type	Flow Rate (mL/h)	Applied Voltage (kV)	Distance (cm)	Modification
PET	10	TFA	0.8	17	17	-
WPET	10	TFA	0.05	17	14	-
PET-SiAMPy	10	TFA	0.8	20	14	Composite/blend
WPET-SiAMPy	10	TFA	0.05	20	14	Composite/blend

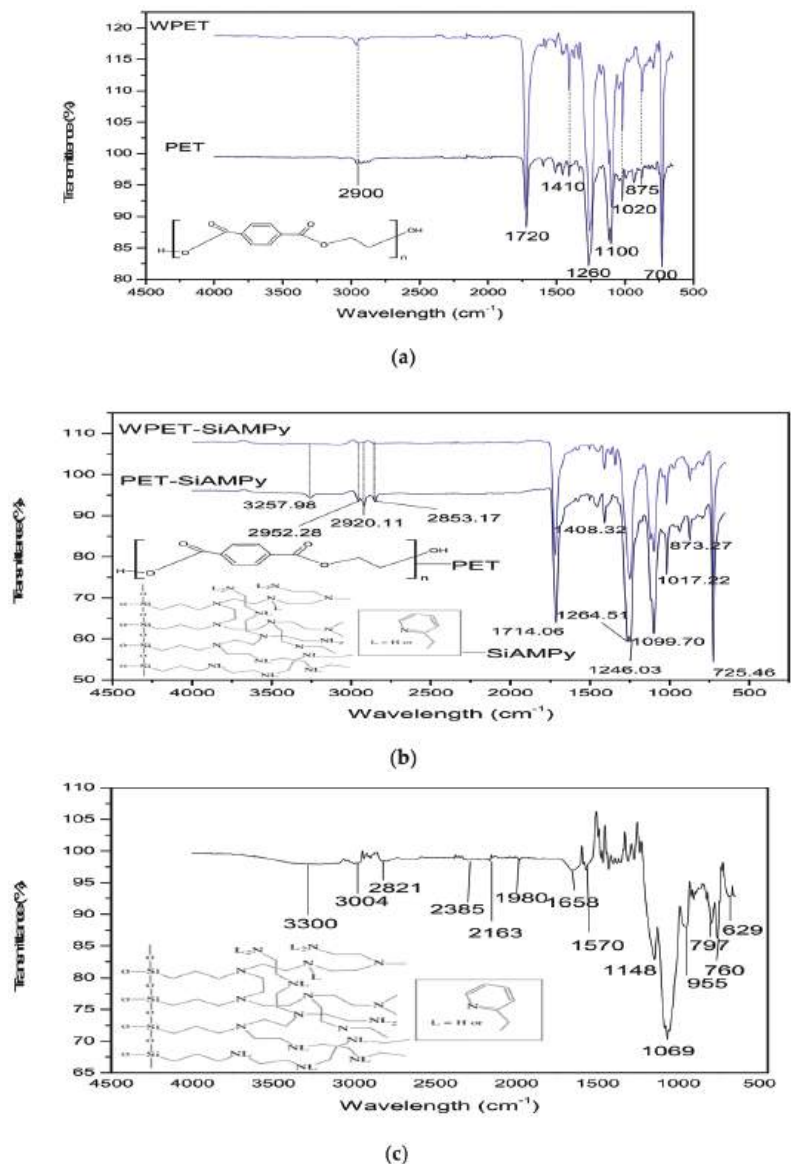


Figure 2. ATR-FTIR patterns of (a): PET (0.8 mL/h, 17 kV, 17 cm) and WPET (0.05 mL/h, 17 kV, 14 cm) nanofibres; (b): PET-SiAMPy (0.8 mL/h, 20 kV, 14 cm) and WPET-SiAMPy (0.05 mL/h, 20 kV, 14 cm) and (c): SiAMPy.

The spectrum of both PET and WPET in Figure 2a shows a weak band at 2900 cm^{-1} that corresponds to the C–H functional group [18]. The carbonyl stretch C=O ester functional group was shown by a strong band at 1720 cm^{-1} . The asymmetric C–C–O is present at 1260 cm^{-1} and the O–C–C stretching at 1100 cm^{-1} band. The strong peak at 700 cm^{-1} represents the shifted aromatic functional group C–H wag, which was affected by the presence of the carbonyl functional group [19]. Figure 2c of SiAMPy itself shows relatively weak absorption bands from 3004 to 3300 cm^{-1} which are indicative of the amine functional group in the functionalized commercial silica supported 2-aminomethylpyridine. The CH functional group vibrations are weakly visible in the wavelength that is between 2821 and 3004 cm^{-1} absorption band [20]. The fingerprint region ranging from 600 to 1148 cm^{-1} presents very strong absorption bands that identify amino-methyl(pyridine). This is affirmed by the absorption band at 955 cm^{-1} which indicates the Si–O functional group stretching modes [21]. The absorption band at 629 cm^{-1} was assigned to NH_2 rocking mode. The region from 600 to 650 cm^{-1} exhibited the CCN functional group which was also present in the functionalized commercial silica supported 2-aminomethylpyridine ring [22].

The FTIR patterns for the PET-SiAMPy and WPET-SiAMPy composite nanofibres formed through the blending process via electrospinning is shown in Figure 2b. The spectra demonstrated the weak band intensity that corresponds to the N–H functional group attributed to the SiAMPy at 3258 cm^{-1} . The carbonyl stretch C=O ester functional group was shown at 1714 cm^{-1} with a strong intensity band. The asymmetric C–C–O was present at 1265 cm^{-1} and 1246 cm^{-1} with a strong intensity band, while the O–C–C stretching was visible with a strong band at 1100 cm^{-1} . The strong peak at 725 cm^{-1} represents the shifted aromatic functional group C–H wag, which was affected by the presence of the carbonyl functional group present in polyethylene terephthalate [19]. The relatively weak absorption band at 3258 cm^{-1} is indicative of the amine functional group which relates to NH vibrations in the functionalized commercial silica supported 2-aminomethylpyridine (SiAMPy). The CH functional group vibrations are weakly visible in the wavelengths between 2952 cm^{-1} and 2853 cm^{-1} absorption bands. The fingerprint region, ranging from 725 cm^{-1} to 1100 cm^{-1} , presents very strong absorption bands that possess the characteristics of aminomethylpyridine, which was also present in the functionalized commercial silica supported 2-aminomethylpyridine ring [22].

The TGA and first derivative weight loss plots obtained under N_2 inert atmosphere are shown in Figure 3. The thermal decomposition of the PET nanofibres under pyrolytic inert conditions with a N_2 flow rate of 20 mL/min started with the gradual 8.12% increase in weight from 15°C to $\sim 380^\circ\text{C}$. The initial 8.12% weight increase in the PET nanofibres was related to the expansion of the PET nanofibres, which was due to an endothermic reaction occurring. The successive thermal degradation of the PET nanofibres begins at $\sim 380^\circ\text{C}$ and ends at $\sim 450^\circ\text{C}$, where 70.40% weight of the PET nanofibres was lost. The depolymerization of the PET nanofibres was occurring at this second stage, forming a carbon black residue. The last stage of the thermal decomposition in the range of $\sim 450^\circ\text{C}$ to 900°C , (8.63% weight) is ascribed to the loss of the carbon by-products that formed [23].

The first stage of the thermal decomposition for the WPET nanofibres started at approximately 290°C to $\sim 350^\circ\text{C}$, which may be the result of the evaporation of volatile gases in the WPET nanofibres. The WPET nanofibres lost approximately 4.55% of their weight in the first stage. Then, the weight of the WPET nanofibres was constant until a successive degradation occurred from 400°C to $\sim 460^\circ\text{C}$. At this stage, the WPET weight loss was approximately 72.96% . The gradual weight loss of 9.10% from $\sim 460^\circ\text{C}$ to 900°C in the last stage of thermal decomposition was the loss of carbon by-products that formed during the degradation of the WPET nanofibres [23].

The shape of the TGA profiles of PET and WPET nanofibres were found to be consistent with the increase in temperature. The first derivative plots corresponds with the TGA plots as the PET and WPET nanofibres pyrolysis at $\sim 380^\circ\text{C}$ to $\sim 460^\circ\text{C}$ are shown with the endothermic peak degradation in the first derivative plot. Finally, the PET and WPET

nanofibres thermal decomposition ended with a residue accumulation of ~9%. This corresponds with the thermal degradation investigation of waste polyethylene terephthalate (PET) under inert and oxidative environments [24].

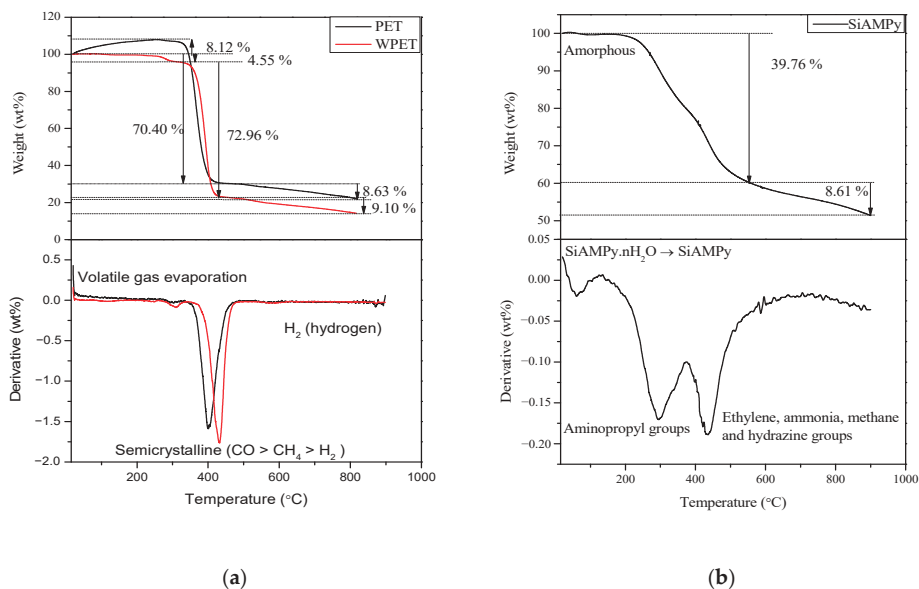
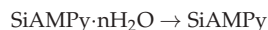


Figure 3. TGA and first derivative pattern of (a) PET, WPET nanofibres (0.8 mL/h, 17 kV, 17 cm) and (b) SiAMPy.

Figure 3b the thermal decomposition of the SiAMPy starts with the dehydration process from 15 °C to ~200 °C, the weight loss is quite insignificant. The SiAMPy weight loss was due to loss of moisture. Thereafter, the successive thermal decomposition of the SiAMPy occurred in sequential stages over a temperature range from 200 °C to 580 °C, where a sharp weight loss of approximately 39.76% was evident. Subsequently, the thermal decomposition rate slowed down with the weight loss of 8.61% between 500 °C and 900 °C as the SiAMPy reached its thermal decomposition end point [24]. The first derivative peaks present the three decomposition stages exhibited by SiAMPy. The first stage represents the elimination of adsorbed moisture as



followed by the decomposition of aminopropyl groups which slowly occurred at approximately 300 °C that led to the rapid degradation that occurred at ~440 °C yielding H₂O, HNO₃ and ethylene groups. The final stage was the formation of residue containing ethylene, ammonia, methane, and hydrazine. Shafqat et al. reported similar data for the amino-functionalized silica nanoparticles used in an investigation of efficient and rapid removal of COD from pre-treated palm oil effluent [25].

3.2. Adsorption Studies of Cu²⁺ Metal Ion

The aim of this section was the optimization of the recovery of the valuable metal Cu²⁺ by the modified chelating adsorbents nanofibres, as described in Section 2.3. The experiment determined the adsorption efficiency of the modified chelating adsorbent nanofibres for Cu²⁺ recovery from aqueous solution by varying parameters in the Cu²⁺ aqueous solution such as pH, initial concentration, contact time, and mass loading.

3.2.1. Effect of Cu^{2+} Aqueous Solution pH Using Modified WPET-SiAMPy Composite Nanofibres

The effect of aqueous solution pH on Cu^{2+} recovery was studied using PET, WPET, and modified nanofibres (WPET-SiAMPy composite nanofibres). The Cu^{2+} aqueous solution pH experiments were made up to pH 6 in order to prevent the precipitation of the Cu^{2+} (see Figure 4). The experiments were carried out in 100 mL of 100 mgL^{-1} of Cu^{2+} aqueous solution using 0.01 g of the nanofibres dosage by manually adjusting the Cu^{2+} aqueous solution with 0.1 M of HNO_3 or NaOH solution to the desired pH value (1, 2, 3, 4, 5 and 6). The equilibrium data shown in Figure 4 were correlated using adsorption capacity (q_e) Equation (1).

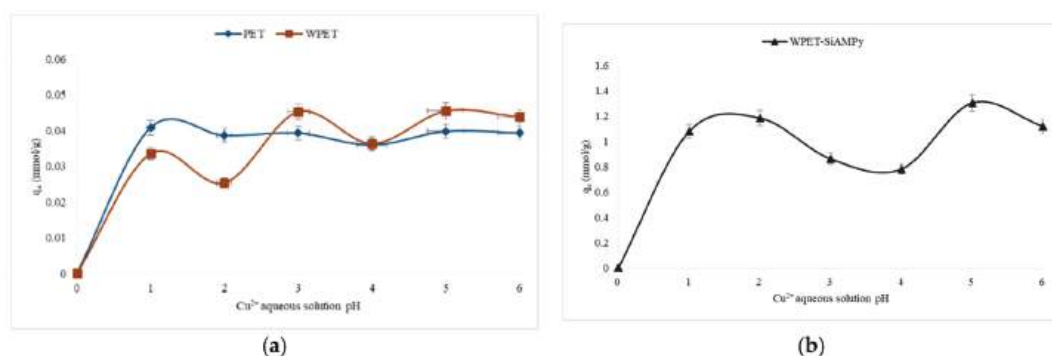


Figure 4. Adsorption capacity of Cu^{2+} from aqueous solution pH using (a) PET, WPET, and (b) WPET-SiAMPy nanofibres (Cu^{2+} concentration 100 mgL^{-1} , 120 min, dosage average, 0.01 g).

Figure 4 shows the pH for optimum adsorption when the modified nanofibres (WPET-SiAMPy) were exposed to 100 mgL^{-1} of Cu^{2+} metal ions in the solution at pH 1 to 6. The results show that the adsorption capacity increased as the pH was increased from 1 to 2. The adsorption capacity started to decline after pH 2 until pH 4 and increased at pH 5 achieving 1.30 mmol/g using WPET-SiAMPy nanofibres. The decline in the Cu^{2+} binding capacity may be due to the hydrogen (H^+) ions being more dominant than Cu^{2+} ions in an aqueous solution [26]. The adsorption capacity gradually increased as the pH of the Cu^{2+} aqueous solution increased from 5 to 6 with the adsorption capacity for Cu^{2+} of 0.04 mmol/g (PET) or 0.046 mmol/g (WPET) at pH 5. Above pH 7, the Cu^{2+} aqueous solution is more alkaline, thus, Cu^{2+} ions start to precipitate and form hydroxides ($\text{Cu}(\text{OH})_2$) [27]. Thus, pH 5 was confirmed as the optimum pH for further adsorption studies in this research.

3.2.2. Effect of Cu^{2+} Contact Time Using the Modified PET-SiAMPy or WPET-SiAMPy Composite Nanofibres

The effect of contact time on Cu^{2+} recovery by the modified chelating adsorbent nanofibres (PET-SiAMPy or WPET-SiAMPy) was studied over different contact times of 1, 5, 10, 20, 30, 60, 90, and 120 min. The main objective in the recovery of Cu^{2+} using the modified chelating adsorbents is the improved adsorption rate at shorter period of adsorption time to reach equilibrium. The adsorption capacity (q_e) calculated according to Equation (1) of the modified chelating adsorbent nanofibres was analysed as shown in Figure 5. The adsorbate results of this experiment were used for comparison in further adsorption experiments.

The effect of contact time on the recovery of Cu^{2+} metal ions by the PET, WPET, PET-SiAMPy, and WPET-SiAMPy nanofibres is shown in Figure 5—showing that low adsorption occurred over time for PET or WPET but high adsorption was attained within the first minute using the modified WPET-SiAMPy composite nanofibre adsorbent. It was found that the adsorption of Cu^{2+} ions achieved equilibrium at 1 min. In the first 1 min, the

Cu^{2+} quantity adsorbed was 1.24 mmol/g (96.04%) of the metal ion concentration present in the Cu^{2+} aqueous solution using the chelating adsorbent WPET-SiAMPy composite nanofibres. WPET-SiAMPy composite nanofibres had the fastest adsorption attributed to the amount of the SiAMPy (0.01 wt%) incorporated in WPET-SiAMPy when compared with the unmodified WPET that achieved 0.05 mmol/g adsorption capacity, which is 35.45% Cu^{2+} recovery efficiency. The PET-SiAMPy nanofibres achieved 0.98 mmol/g in the first minute of adsorption. The adsorption capacity of the unmodified PET nanofibres reached equilibrium from the first minute of adsorption contact time until the adsorption experiment reached 30 min, where slight fluctuations started. The adsorption capacity fluctuated for the unmodified nanofibres adsorbent (WPET), the Cu^{2+} recovery declined from 5 to 10 min of adsorption and increased from 10 to 20 min, only to further decline from 20 to 90 min and slightly increased from 90 to 120 min. The adsorption capacity using all the material, respectively, reached the adsorption equilibrium at 1 min, with the fluctuation of the copper binding capacity of the unmodified nanofibres. The PET and WPET nanofibres achieved only 0.06 mmol/g and 0.05 mmol/g in the first minute with a low adsorption capacity of 0.07 mmol/g noticed at 60 min for PET and 0.08 mmol/g noticed at 20 min for WPET. The 1 min was set as the necessary time needed to attain equilibrium for the modified nanofibre adsorbents. The fast adsorption during the first minute was related to the large amount of active vacant adsorption sites of the SiAMPy incorporated into the nanofibres (see kinetic study in Section 3.4).

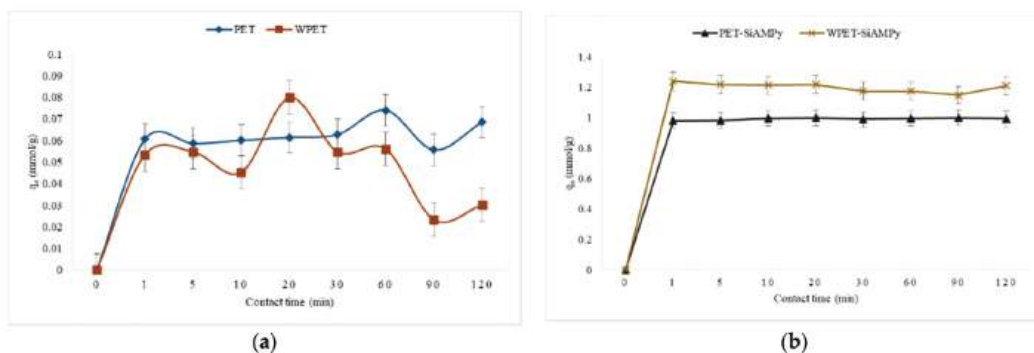


Figure 5. Effect of contact time on the recovery of Cu^{2+} from aqueous solution using (a) PET, WPET; and (b) PET-SiAMPy and WPET-SiAMPy nanofibres (Cu^{2+} concentration 100 mgL^{-1} , pH 5, dosage 0.01 g).

The obtained average adsorption efficiency results in Figure 6 showed that the modified WPET using the chelating ligand SiAMPy had the highest Cu^{2+} metal ion binding capacity compared to that of the PET-SiAMPy because the WPET nanofibres had more SiAMPy compared to PET nanofibre as seen in Figure 1e,f, indicating that the WPET-SiAMPy had an enlarged surface area compared to PET-SiAMPy and therefore more Cu^{2+} adsorption sites. The adsorption performance occurred rapidly when the number of available sites was greater than the number of Cu^{2+} ions to be adsorbed. In the initial stage of adsorption, there is excess active adsorption sites vacant on the adsorbent surface for Cu^{2+} recovery. Thereafter, the adsorption rate dropped slightly due to the aggregation of Cu^{2+} metal ions on adsorbent nanofibres or more likely on excess adsorption sites. Thus, the active sites of WPET-SiAMPy nanofibres were fully exposed to Cu^{2+} ions in aqueous solution, causing the rapid saturation of the surface and yielding high adsorption capacity as seen in Figure 6. The Cu^{2+} recovery rate demonstrated the high rate of binding kinetics, thus suggests that the WPET-SiAMPy composite nanofibres has very high adsorption efficiency and thus has high potential in Cu^{2+} recovery. The modification of WPET polymers using the SiAMPy was beneficial in Cu^{2+} adsorption efficiency, as the SiAMPy was previously proven to be selective for Cu^{2+} [28]. The WPET-SiAMPy composite nanofibres showed

high Cu^{2+} uptake of 1.24 mmol/g (96.04%). This research agrees with the efficient activity of the 2-aminomethylpyridine resin (AMPy) which could only achieve 0.22 mmol/g Cu uptake on its own [29]. Incorporating it into nanofibres significantly improved the Cu^{2+} adsorption capacity, which is in agreement with the adsorption capacity achieved using the fixed-bed column adsorption process for the deep removal of Cu^{2+} from simulated cobalt electrolyte with polystyrene-supported 2-aminomethylpyridine chelating resin [30].

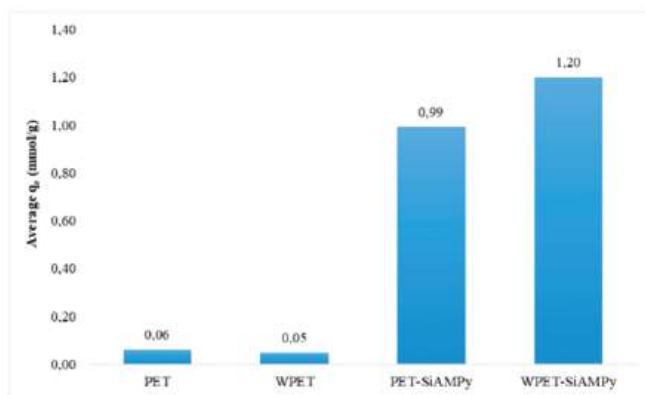


Figure 6. Average adsorption capacity of Cu^{2+} from aqueous solution using PET, WPET, PET-SiAMPy, and WPET-SiAMPy nanofibres (Cu^{2+} concentration 100 mgL^{-1} , pH 5, dosage 0.01 g, 120 min).

3.2.3. Effect of the WPET-SiAMPy Composite Nanofibres Dosage on Cu^{2+} Binding Capacity

The effect of mass loading on the adsorption of Cu^{2+} was carried out using different doses of chelating adsorbents WPET-SiAMPy nanofibres (0.001, 0.005, 0.01 and 0.025 g). The effect of chelating adsorbent dosages were investigated in order to determine the optimum dosage of the modified nanofibres. The effect of PET-SiAMPy as the adsorbent was not investigated because studies in Sections 3.2.1 and 3.2.2 already proved that WPET-SiAMPy was more effective than PET-SiAMPy. The adsorption capacity (q_e) of the resultant solution are shown in Figure 7.

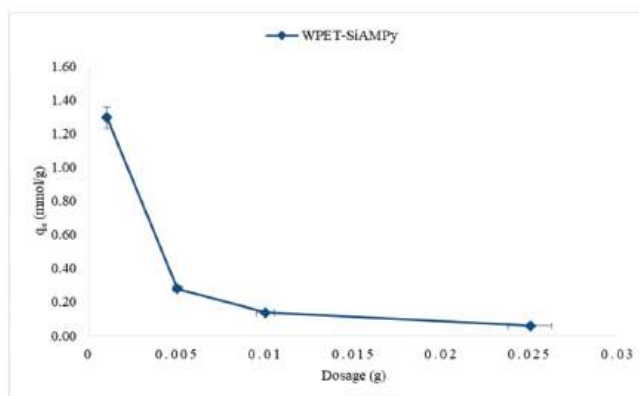


Figure 7. Adsorption capacity of Cu^{2+} from aqueous solution using different WPET-SiAMPy nanofibres dosages (Cu^{2+} concentration 100 mgL^{-1} , 1 min, pH 5).

The adsorption pattern of the Cu^{2+} adsorption against the dosage conducted over a range of masses for WPET-SiAMPy nanofibres of 0.001–0.025 g is illustrated in Figure 7. The

adsorption capacity and the percentage of Cu^{2+} adsorbed on the WPET-SiAMPy composite nanofibres at different doses shows that the adsorption capacity decreased with an increase in dosages. The adsorption capacity decreased from 1.29 to 0.06 mmol/g by increasing the WPET-SiAMPy nanofibres dosage from 0.001 to 0.025 g per adsorption process of 10 mL ($100 \text{ mgL}^{-1} \text{ Cu}^{2+}$). The decrease in Cu^{2+} adsorption capacity may be due to the aggregation of WPET-SiAMPy nanofibres or more likely due to the increase in excess adsorption sites as the dosage increased [31]. Thus, the active sites of WPET-SiAMPy nanofibres were fully exposed to Cu^{2+} ions in aqueous solution even at the lowest dosage, causing the rapid saturation of the surface and yielding high adsorption capacity, as seen in Figure 7. The increase in WPET-SiAMPy composite nanofibres dosage increased the availability of adsorption sites resulting in a high WPET-SiAMPy nanofibres active sites-to- Cu^{2+} ions ratio; thus, the availability of Cu^{2+} ions was insufficient to occupy all adsorbent active sites, hence the decrease in adsorption capacity. Increasing the WPET-SiAMPy nanofibre dosage enhanced the active adsorption sites' availability. As seen in Figure 7, the high Cu^{2+} binding capacity was achieved using 0.001 g dosage of the chelating adsorbents (WPET-SiAMPy nanofibres) if all fixed parameters ($100 \text{ mgL}^{-1} \text{ Cu}^{2+}$ (10 mL) at pH 5 for 1 min) are maintained.

3.2.4. Effect of Cu^{2+} Aqueous Solution Initial Concentration Using WPET-SiAMPy Nanofibres

The effect of the Cu^{2+} metal ion concentration was investigated to determine the optimum Cu^{2+} concentration using the modified nanofibres (WPET-SiAMPy nanofibres) as the adsorbent. The Cu^{2+} adsorption from the 100 mL of different concentrations (10, 50, 100 and $200 \text{ mgL}^{-1} \text{ Cu}^{2+}$) were carried out using the WPET-SiAMPy nanofibres (0.001 g) (see Figure 7) with the pH of the Cu^{2+} aqueous concentrations held at 5 (see Figure 4). The obtained experimental results of the effect of initial concentration of Cu^{2+} on WPET-SiAMPy nanofibres are shown in Figure 8.

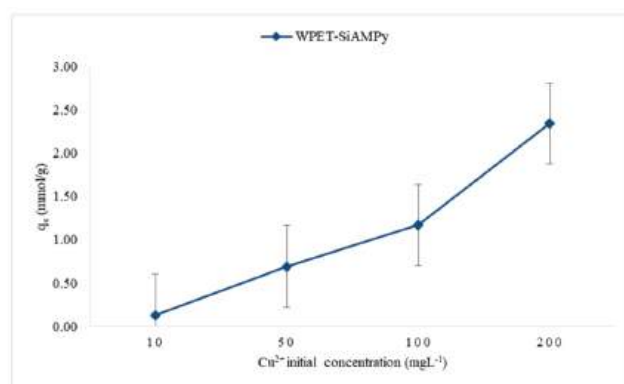


Figure 8. Effect of initial Cu^{2+} concentration on WPET-SiAMPy nanofibres (contact time 1 min, pH 5, dosage 0.001 g, 10 mL).

Figure 8 presents the binding capacity of Cu^{2+} based on Cu^{2+} adsorbed on WPET-SiAMPy nanofibres at different Cu^{2+} initial concentrations. The results obtained show that the binding capacity directly increased with an increase in initial concentration of Cu^{2+} . The effect of the initial concentration of Cu^{2+} provides the necessary experimental data to understand the resistance, if any, to the adsorption of Cu^{2+} ions transferred between the aqueous solution and WPET-SiAMPy nanofibres. The increase in the initial concentration of Cu^{2+} improved the uptake of Cu^{2+} adsorption as the Cu^{2+} concentration increased from 10 mgL^{-1} with a binding capacity of 0.13 mmol/g, to 200 mgL^{-1} , in which case the binding capacity was 2.34 mmol/g. The saturation point was not observed for even the highest

Cu^{2+} initial concentration, showing a very high number of Cu^{2+} binding sites available on the dosed adsorbent. The availability of sufficient Cu^{2+} ions and adsorption sites increased the Cu^{2+} ions binding capacity onto the chelating adsorbent nanofibres [20].

3.3. Adsorption Isotherm Models

The modelling of the adsorption equilibrium data is useful in describing and comparing the interaction between the adsorbate and adsorbent during the adsorption experiments, and is also essential for the design of the adsorption process systems. The adsorption models that are most frequently studied are the Langmuir or Freundlich adsorption isotherms, which have been adopted in this study to describe the adsorption characteristics of chelating adsorbents (WPET-SiAMPy nanofibres). In addition, the Jovanovic–Freundlich adsorption isotherm was also reviewed in this study for the close proximation of adsorption data. All the equilibrium adsorption isotherms were used to draw relationships between the Cu^{2+} concentration in the aqueous solution and the quantity adsorbed onto the WPET-SiAMPy nanofibres. In the adsorption process, the adsorbate is adsorbed on the adsorbent until the adsorbent reaches equilibrium. The WPET-SiAMPy nanofibres' adsorption isotherms were determined using the initial concentration experimental data outcomes to predict the best fitting isotherm.

The effect of the Cu^{2+} aqueous solution initial concentration plot followed the Type II of the five types of adsorption isotherms [32]. Type II adsorption isotherms occur when there is more than one type of adsorption active site on the adsorbent surface [33]. Then, the adsorption of the adsorbate molecules to the macroporous adsorbents takes place when multilayer adsorbed molecules are formed after the coverage of the adsorbent surface with a monolayer of adsorbed molecules [34]. The active adsorption sites initiate rapid initial adsorption and these sites saturate when the first site is filled [35]. Then, adsorption rises for the second time when the second active adsorption site is filled. The second site could be a second monolayer, or in porous materials it can also be a second type of pore [36]. Type II adsorption isotherms do not display any saturation point [37], as seen in Figure 7. The plots of Langmuir ($1/q_e$ vs. $1/C_e$), Freundlich ($\log q_e$ vs. $\log C_e$) and Jovanovic–Freundlich ($\ln q_e$ vs. C_e) are illustrated in Figures 9–11, which were used for the calculation of isotherm parameters in the adsorption of Cu^{2+} ions using WPET-SiAMPy nanofibres as adsorbents. The obtained values of these parameters are summarized in Table 2.

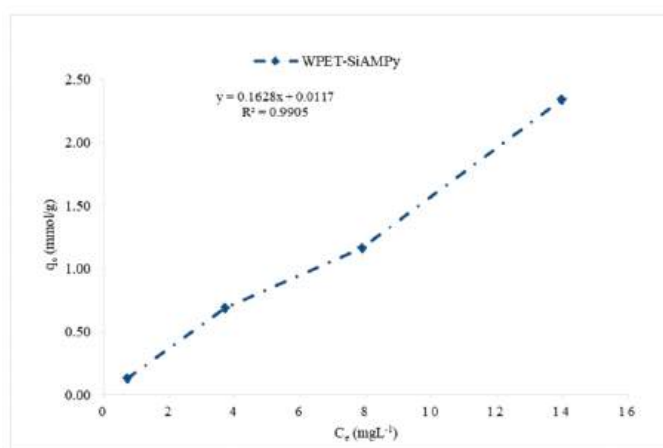


Figure 9. Langmuir model isotherm of Cu^{2+} ions on WPET-SiAMPy nanofibres.

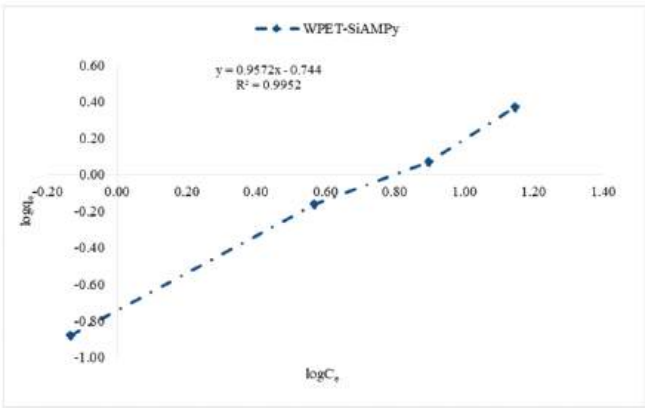


Figure 10. Freundlich model isotherm of Cu²⁺ ion on WPET-SiAMPy nanofibres.

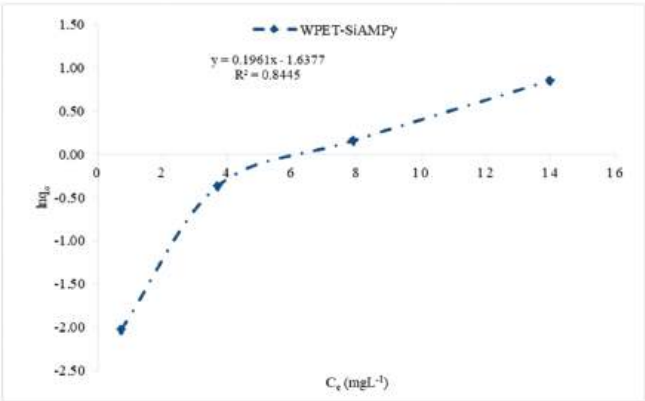


Figure 11. Jovanovic–Freundlich model isotherm of Cu²⁺ ion on WPET-SiAMPy nanofibres.

Table 2. Parameters obtained from the plot of Langmuir, Freundlich isotherms, and Jovanovic–Freundlich for Cu²⁺ adsorption using modified chelating adsorbents WPET-SiAMPy nanofibres.

Isotherm Models	Constants	WPET-SiAMPy
Langmuir	$q_m \text{ (mg/g)}$	0.0117
	$K_L \text{ (L/g)}$	13.9145
	R^2	0.9905
	χ^2	1.0602
Freundlich	$q_F \text{ (mg/g)}$	1.2912
	$K_F \text{ (L/mg)}$	0.1803
	n	0.9572
	R^2	0.9952
	χ^2	0.0398
Jovanovic–Freundlich	$q_{JF} \text{ (mg/g)}$	1.7702
	$K_{JF} \text{ (L/g)}$	0.5289
	n_{JF}	0.4747
	R^2	0.8445
	χ^2	0.4353

In order to choose the best fit between the isotherm model parameters and the experimental outcomes, the statistical function was examined and in each case a set of isotherm parameters were determined by minimizing the respective error function across the concentration range studied [38]. The quality of the isotherm model fit was achieved by the reduced chi-square statistics [39]. The reduced chi-square statistics can be determined by dividing the variance of the isotherm fit by the average variance of the experimental outcome, which should result in the chi-square statistics being less than unity if the isotherm model is in close proximation of the experimental outcome [40]. However, if the reduced chi-square statistics have a larger value, this indicates that the isotherm model fitting is poor or the experimental data are out of approximation [41]. The non-linear chi-square test (χ^2) employed in this study was presented as follows:

$$\chi^2 = \sum_{i=1}^n \frac{(q_{e,calc} - q_{e,mean})^2}{q_{e,mean}} \quad (4)$$

3.3.1. Langmuir Model Isotherm for WPET-SiAMPy Composite Nanofibres

Langmuir adsorption, specifically designed to describe gas–solid adsorption, is additionally used to quantify and distinguish between the adsorptive ability of more than a few adsorbents [42]. The Langmuir isotherm balances the relative costs of adsorption and desorption (dynamic equilibrium). Adsorption is proportional to the fraction of the sites of the adsorbent that are open whilst desorption is proportional to the fraction of the adsorbent sites that are blanketed [43]. The Langmuir adsorption isotherm describes the adsorption of the adsorbate on the surface of the adsorbent in three ways. First, the Langmuir adsorption isotherm states that the surface of the adsorbent is in contact with a solution containing the adsorbate which is strongly attracted to the surface. Secondly, this isotherm states that the surface has a specific number of sites where the adsorbate molecules can be adsorbed. Lastly, the Langmuir adsorption isotherm states that the adsorption involves the attachment of only one layer of molecules to the surface [32]. The Langmuir adsorption isotherm proves that a dynamic equilibrium exists between the adsorbed molecules and free molecules. This isotherm describes the isothermal variation of the free adsorbate and the vacancies on the surface of the adsorbent [44].

The adsorbent and the adsorbate are in dynamic equilibrium, and the fractional coverage of the surface depends on the concentration of the adsorbate. The extent of surface coverage is normally expressed as the fractional coverage, θ . The Langmuir isotherm was used to calculate the monolayer adsorption, which was represented by the following linearized form presented as Equation (5):

$$q_e = \frac{q_m K_L C_e}{1 + K_L C_e} \quad (5)$$

The Langmuir Equation presents q_e as the amount of metal ion adsorbed on adsorbents (mg/g), q_m and K_L are the monolayer adsorption capacity (mg/g) and Langmuir equilibrium constant (L/mg) which indicates the nature of adsorption, respectively. The values of q_m and K_L were graphically determined with a plot of, q_e against C_e that gives a straight line of slope $q_m K_L$ and the intercept is q_m , which corresponds to the complete monolayer coverage [45].

The essential calculation of the Langmuir isotherm is expressed in terms of a dimensionless constant separation factor, R_L [46], which is expressed as Equation (6):

$$R_L = \frac{1}{1 + K_L C_o} \quad (6)$$

where q_e is the equilibrium adsorption uptake of Cu^{2+} ions, q_m is the maximum adsorption capacity corresponding to the complete monolayer coverage, K_L is the Langmuir adsorp-

tion, $R_L = 1$ indicating linear adsorption; $R_L = 0$ indicating irreversible adsorption and $0 < R_L < 1$ indicating optimum/favourable adsorption.

The Langmuir isotherm for the adsorption of Cu^{2+} using WPET-SiAMPy nanofibres is indicated in Figure 9. The correlation coefficient of $R^2 = 0.9905$ indicated that the adsorption of Cu^{2+} from aqueous solution using WPET-SiAMPy nanofibres as adsorbent was optimum and favourable, supported by the separation factor $0 < R_L < 1$. WPET-SiAMPy nanofibres have shown an equilibrium trend of the Type II isotherm which represents unrestricted monolayer-multilayer adsorption, as demonstrated by IUPAC classification of isotherms [47]. The accumulation of Cu^{2+} ion on the surface of the WPET-SiAMPy nanofibres suggests that the Cu^{2+} ions partially saturated the sites and followed the L3 type classification proposed by Dąbrowski, 2001 [48]. The L3 curve presented in Figure 9 indicates that the Cu^{2+} ions, as the adsorbate, have a high affinity such that in diluted solutions, Cu^{2+} is completely adsorbed, or at least no measurable amount of Cu^{2+} remained in the solution that could be further adsorbed. The initial part of the adsorption isotherm is conclusively vertical. The adsorbed single Cu^{2+} ions could be exchanging with the H^+ ions which have a lower affinity for the WPET-SiAMPy nanofibres surface. This model indicates that both the active adsorption sites and nanofibres' surface area contributed equally. The Langmuir isotherm model was also investigated for the study of adsorption from theory to practice and the reported adsorption of Cu^{2+} metal ions on Si-AMP-M-H as a selective adsorbent, with the adsorption equilibrium fitting the Langmuir isotherm model [48].

3.3.2. Freundlich Model Isotherm for WPET-SiAMPy Composite Nanofibres

The Freundlich isotherm is generally applicable to the adsorption that occurs on heterogeneous surfaces [49]. This isotherm gives an expression which defines the surface heterogeneity and the exponential distribution of active sites and their energies [50]. The Freundlich adsorption isotherm represents the relationship between the amount of metal adsorbed per unit mass of the adsorbent q_e and the concentration of the metal in solution at equilibrium. The Freundlich Equation can be described by the linearized form:

$$\log q_e = \log k_F + \frac{1}{n} \log C_e \quad (7)$$

where k_F and n are Freundlich constants. The values of k_F and n were graphically determined. A plot of $\log q_e$ against $\log C_e$ gives a straight line of slope n and the intercept is $\log k_F$ [51].

The results of the Freundlich isotherm of Cu^{2+} ion adsorbed by WPET-SiAMPy nanofibres is presented in Figure 10. The Freundlich constants related to adsorption capacity $K_F = 0.18$ (L/mg), and adsorption intensity $\frac{1}{n} = 0.9572$ indicated the optimum adsorption characteristics of the WPET-SiAMPy composite nanofibres in Cu^{2+} aqueous solution. This is due to the correlation of K_F that indicated that the high K_F coefficient increased with an increase in the initial concentration as a result of an increase in the activated surface characteristics after monolayer adsorption and $\frac{1}{n}$ with high WPET-SiAMPy composite nanofibres' adsorption intensity. Thus, the correlation coefficient R^2 values for the WPET-SiAMPy nanofibres, which was 0.9952 for Cu^{2+} , indicated a favourable adsorption process.

3.3.3. Jovanovic–Freundlich Model Isotherm for WPET-SiAMPy Composite Nanofibres

The Jovanovic model isotherm adopts the same theories as the Langmuir model isotherms and further considers the mechanism between the adsorbate and adsorbent contact [52]. For heterogeneous surfaces, the Jovanovic model extends a semiempirical model named Jovanovic–Freundlich model. The Jovanovic–Freundlich model isotherm was derived from a differential relationship relating the surface coverage and the bulk concentration of the adsorbate for a single component adsorption. The Jovanovic–Freundlich model is reduced to the Jovanovic model when the surface is homogenous, and at high

concentrations, it is reduced to a monolayer; however, it does not obey Henry's law [53]. The Jovanovic–Freundlich model isotherm is expressed as follows:

$$q_e = q_{JF} \left(1 - e^{(-K_{JF} C_e^{n_{JF}})} \right) \quad (8)$$

where q_{JF} is the maximum monolayer coverage capacity, K_{JF} is the equilibrium constant, and n_{JF} is the Jovanovic–Freundlich model isotherm exponent.

Figure 11 shows the Jovanovic–Freundlich isotherm calculated for WPET-SiAMPy nanofibres. The three parameters of the semi-empirical model isotherm were applied to evaluate the Jovanovic–Freundlich model isotherm fit for Cu^{2+} adsorption. The Jovanovic–Freundlich model isotherm exponent $n_{JF} = 0.47$ indicated that the Cu^{2+} ion binding adsorption occurred at a heterogeneous surface as the value of parameter n_{JF} is far greater than unity 1, which means the Jovanovic–Freundlich equation was reduced to the Freundlich isotherm. The correlation coefficient was $R^2 = 0.8445$, which indicated a favourable adsorption process. Khakpay et al. [54] reported the derivation and application of a Jovanovic–Freundlich isotherm model for single component adsorption on heterogeneous surfaces.

The calculated results of all the isotherms modelled for WPET-SiAMPy nanofibres are presented in Table 2.

The Langmuir, Freundlich, and Jovanovic–Freundlich isotherm models were applied to describe the Cu^{2+} ions' adsorption mechanism on the WPET-SiAMPy nanofibres surface using a range of Cu^{2+} aqueous concentrations. The experimental data obtained for adsorption of Cu^{2+} using WPET-SiAMPy nanofibres were compared to the theoretical data obtained from the Langmuir, Freundlich, and Jovanovic–Freundlich isotherm models, and determined that the three isotherms showed the correlation coefficient (R^2) following this sequence: Freundlich > Langmuir > Jovanovic–Freundlich [55]. Thus, the Freundlich isotherm model with the highest correlation coefficient $R^2 = 0.9952$ was the best fit for Cu^{2+} adsorption experimental outcomes. The Freundlich isotherm model had a good agreement with the experimental data obtained, based on the reduced chi-square X^2 that was far less than unity, good correlation coefficient R^2 , and the close approximation of the theoretical maximum uptake of adsorbate q_{JF} to the experimental adsorption uptake of adsorbate q_e . Thus, among the three important compatible applicable isotherm models about adsorption, the Freundlich isotherm model had the best fit to experimental outcomes of Cu^{2+} ions adsorption from aqueous solution using the WPET-SiAMPy nanofibres. This indicated that the WPET-SiAMPy nanofibres' adsorption sites for Cu^{2+} ions were uneven and not restricted to a particular adsorption site. These results proposed that more than one type of WPET-SiAMPy active site took part in Cu^{2+} ion adsorption [56].

3.4. Kinetic Study of WPET-SiAMPy Chelating Adsorbent Nanofibres

The adsorption kinetics focused on the adsorption rate of the adsorbate upon the adsorbent. The experiments of Cu^{2+} binding kinetics using the WPET-SiAMPy chelating adsorbent was conducted to investigate the adsorption mechanism of Cu^{2+} in aqueous solution. The formation of complexes between Cu^{2+} and WPET-SiAMPy chelating adsorbent nanofibres was studied to understand the Cu^{2+} adsorption dynamics, assuming a homogenous system for WPET-SiAMPy chelating adsorbent nanofibres. The kinetic of the Cu^{2+} uptake was illustrated by the effect of contact time on Cu^{2+} ions' adsorption onto WPET-SiAMPy nanofibres, which was previously performed, and the results are shown in Figure 4.

3.4.1. Relative Rates and Stoichiometry of Cu^{2+} Adsorption Based on the WPET-SiAMPy Nanofibres

The general aim of this kinetic study was to determine the form of the reaction rate equations. The reaction rate equations in this study were determined using the differential method. In adsorption kinetics, it is important to relate the reaction rates for the adsorption of the reactant, Cu^{2+} , and the formation of the complex compounds Cu-WPET-SiAMPy

nanofibres. This was performed by varying the Cu^{2+} concentration or the average rate of reaction against the contact time as seen in Figure 11. The average rate of the reaction is the change in the concentration per unit time expressed as

$$\text{Rate of reaction} = \frac{\Delta [\text{Cu}^{2+} \text{ concentration}]}{\Delta \text{time}}$$

with the consideration that the Cu^{2+} ions in the aqueous solution are adsorbed by WPET-SiAMPy nanofibres. These reactions occur according to the following Equations:

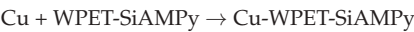


Figure 12 demonstrated the Cu^{2+} uptake by the WPET-SiAMPy nanofibres. During adsorption, a chemical reaction occurred. The quantities of the Cu^{2+} ions taken up from aqueous solution decreased with an increase in time, forming compound complexes. The Cu^{2+} ion concentration after the adsorption experiment with WPET-SiAMPy nanofibres showed three reactions. The average rate of reactions for the equilibria-specified time intervals are tabulated below:

$$\text{Rate of reaction} = \frac{\Delta [\text{Cu} - \text{WPET} - \text{SiAMPy}]}{\Delta t}$$

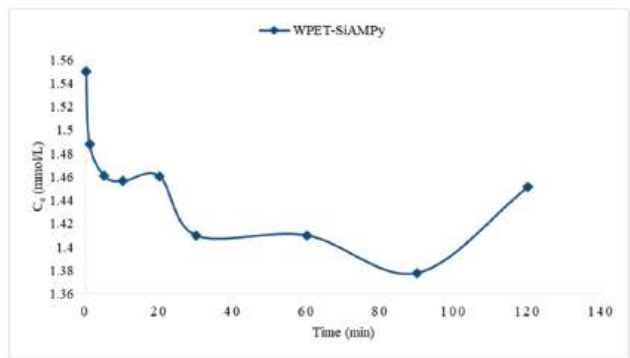


Figure 12. Cu^{2+} metal uptake against contact time using WPET-SiAMPy nanofibres.

The rate expression relating all these rates can be determined by dividing each rate expression by the stoichiometric coefficient of the Cu^{2+} ions in the balanced chemical equation, which is assumed to be 1 in these balanced equations. As seen in Table 3, the rate of reaction decreases as the concentration of Cu^{2+} ions in solution decreases. This illustrated that the rate of reaction is related to the concentration of Cu^{2+} ions. This can also be qualitatively deduced from the fact that the graphing of the average reaction rate against time gave a curved line, as can be seen in Figure 13.

Table 3. Average rate of reactions between Cu^{2+} and WPET-SiAMPy nanofibres.

$\Delta \text{Time (min)}$	Rate of Reaction (mmol/L.min)
0–1	1.4887
1–10	0.0035
20–60	0.0013
90–120	0.0024

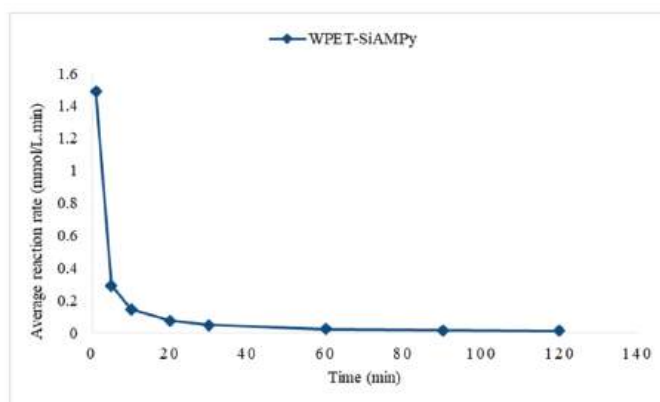


Figure 13. Average reaction rate against contact time using WPET-SiAMPy nanofibres.

Figure 13 illustrates the average reaction rate against time, where a measure of the rate of the reaction at any point in time is found by measuring the slope of the graph through tangent. As seen in Figure 5, the initial adsorption was steep for WPET-SiAMPy nanofibres, as supported by the steep initial metal uptake in Figure 12, which means that the rate of reaction was fast. Hence, the determination of the initial rate of reaction is important in this study, as the slope at the beginning of the reaction is used.

3.4.2. Kinetic Study of Reaction Formation Compound Cu-WPET-SiAMPy Complex

The relationship between Cu^{2+} ion concentration and reaction rate is expressed by an equation called a rate equation. The rate equation of Cu-WPET-SiAMPy complex can be written mathematically as

$$\text{Rate} = k[A]^m[B]^n \quad (9)$$

where k is the reaction rate constant, $[A]$ is the concentration of Cu^{2+} , $[B]$ is the concentration of the WPET-SiAMPy nanofibres, m and n are the order of the reaction. The determination of the reaction order is determined by finding the initial formation rate of the Cu^{2+} ions binding to the WPET-SiAMPy chelating ligand nanofibres. The graph of the concentration versus time is obtained from the experimental data to determine the initial rate of reaction (see Table 2). The graph of the concentration versus time is obtained from the experimental data to determine the initial rate, which can be expressed as

$$\frac{dc}{dt} \approx kc_{py}C_{Cu} \quad (10)$$

where the Cu^{2+} aqueous solution concentration is represented by c calculated from:

$$c_{py} = \frac{q_{py}m}{V} \quad (11)$$

Figure 14 presents the Cu^{2+} complexation formation rate with WPET-SiAMPy nanofibres in aqueous solution. The equilibrium uptake of the Cu^{2+} on WPET-SiAMPy nanofibres was attained within the first minute of contact time, as seen in Figure 5. The fast Cu^{2+} adsorption on the WPET-SiAMPy nanofibres was attributed to the high Cu^{2+} concentration in aqueous solution around the high surface area of the WPET-SiAMPy nanofibres with a high number of active vacant adsorbent sites. The Cu^{2+} complex formation rate (k) with WPET-SiAMPy was $k = 0.0888$, which was the adsorption rate constant.

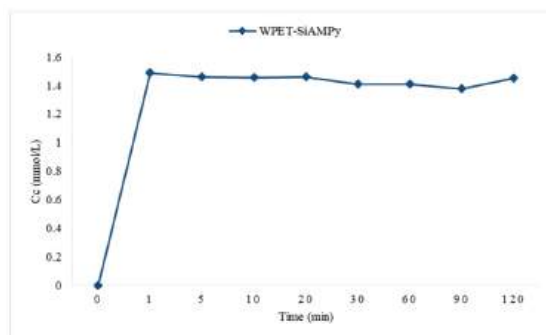
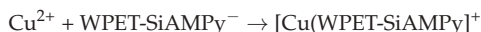


Figure 14. Cu^{2+} complexation with the WPET-SiAMPy nanofibres in aqueous solution.

3.4.3. The Mechanism of Cu-WPET-SiAMPy Complex Formation Reaction

The theoretical study on the mechanism of reaction of the Cu-WPET-SiAMPy complex formation was based on three things: the data of the reaction kinetics, of the obtained value of coordination number n and from the value of the rate constant k . The mole ratio of Cu^{2+} and WPET-SiAMPy nanofibres was 1:2 based on the overall equation. Based on this comparison, then the complex molecular formula formed was $\text{Cu}(\text{WPET-SiAMPy})_2$ with a square planar geometry structure. The mechanism of formation for complex compounds $\text{Cu}(\text{WPET-SiAMPy})_2$ is:



Then, the overall reaction is:



Based on the results, it can be determined that the complex molecular formula is $\text{Cu}(\text{WPET-SiAMPy})_2$ and this is in accordance with the kinetic data. Another fact that supports the above reaction mechanism is the value of k , which is 0.0888:

$$\text{Rate} = k[\text{Cu}^{2+}][\text{WPET-SiAMPy}^-]$$

The $\text{Cu}(\text{WPET-SiAMPy})_2$ complex compound is theoretically expected to have four coordination numbers based on the valence bond theory. This was previously proven by Bai et al. when analysing the Cu^{2+} loaded Si-AMP-M-H with X-ray photoelectron spectroscopy (XPS), compared with the unloaded Si-AMP-M-H [30]. The XPS survey scan spectra showed major peaks in Si-AMP-M-H which were Si_{2p} , O_{1s} , C_{1s} , and N_{1s} . The XPS analysis simultaneously demonstrated the Cu_{2p} and S_{2p} peaks in Cu^{2+} loaded Si-AMP-M-H. This proves the legitimacy of the Cu^{2+} ions adsorbed onto the Si-AMP-M-H surface which was accompanied by SO_4^{2-} ions, indicating that the neutral ligands form charged chelates with metal ions while anions are co-adsorbed as counter-ions to maintain electro-neutrality in both the Cu^{2+} aqueous phase and the WPET-SiAMPy solid phase [57]. This study was supported by research showing that the Cu^{2+} ion has an electron configuration of $1s^2 2s^2 2p^6 3s^2 3p^6 3d^9$; thus, it is possible to form the coordination bond between the bidentate ligand and the central atom and obtain sp^3 tetrahedron orbitals [58]. The Cu^{2+} ion consists of a d^9 configuration and is known to form 1:1 and 1:2 complexes with the AMP chelating ligands [59]. This was supported by Li et al. who reported the silica-based 2-aminomethylpyridine functionalized adsorbent for the hydrometallurgical extraction of low-grade copper ore and formed a 2:1 AMPy-Cu(II) complex ratio [60]. In this research, the Cu^{2+} ions formed 1:2 complexes as seen in the overall reactions; however,

Sirola et al. reported that the Cu^{2+} complex CuWRAM was closer to a 1:1 ratio than a 1:2 complex because of the steric hindrances and mobility limitations of AMP incorporated in the silica matrix [59]. Theoretically, it can be expected that the Cu complex species will have a Cu molecular formula $(\text{WPET-SiAMPy})_2$ with square planar dsp^2 hybridization.

3.5. Regeneration of the WPET-SiAMPy Nanofibres

The regeneration of the WPET-SiAMPy nanofibres was carried out by treating the previously used WPET-SiAMPy nanofibres with 5 M H_2SO_4 for 60 min, respectively. This procedure was carried out to determine the reusability and lifecycle of the adsorbents. The regeneration experiments were carried out to regenerate the sample used as the 0.01 g dose of WPET-SiAMPy nanofibres. After the application of 0.01 g WPET-SiAMPy to adsorb 1.24 mmol/g of Cu^{2+} under constant conditions of pH 5, with an initial Cu^{2+} concentration of 100 mgL^{-1} , with a contact time varying from 1 to 120 min, the acid regenerated WPET-SiAMPy nanofibres were reused for 100 mgL^{-1} Cu^{2+} adsorption at pH 5 with the contact time held constant at 1 min due to the fast kinetics. This regeneration and reuse cycle was repeated five times to determine the regenerability of the nanofibres. After each of the adsorption–desorption regeneration cycles, the solution was analysed and the recovery efficiency for Cu^{2+} was calculated according to Equation (1).

Figure 15 shows five adsorption–desorption regeneration cycles of previously used WPET-SiAMPy nanofibres. After acid regeneration, the desorbed WPET-SiAMPy nanofibres were reused for the first cycle adsorption and achieved 1.04 mmol/g adsorption capacity of Cu^{2+} ions, with a 15.98% decrease in adsorption capacity. Thereafter, the Cu^{2+} adsorption of the desorbed WPET-SiAMPy nanofibres gradually decreased to 1.01 mmol/g binding capacity at the fifth cycle, with a 18.48% decrease in adsorption capacity. The decrease in Cu^{2+} adsorption on WPET-SiAMPy nanofibres could be due to the gradual accumulation of Cu^{2+} traces that were not desorbed from the adsorbent, or to the limited contact time used in the readsorption cycles, or to loss of fibre [61]. Nevertheless, the modified WPET-SiAMPy nanofibres could be regenerated using 5 M H_2SO_4 after previous use for Cu^{2+} adsorption and could be successively reused for at least five adsorption–desorption cycles. This adsorption–desorption regeneration method was successful because after five cycles, the adsorption capacity only decreased by 18.48% compared to the initial adsorption seen in Figure 4. Therefore, the highly replicable Cu^{2+} reabsorptions upon regenerated WPET-SiAMPy blended nanofibres proved the reusability of the WPET-SiAMPy blended nanofibres compared to the parent silica supported 2-aminomethylpyridine resin (AMPy) that had slow desorption and kinetics [30], which limited the operational recycling of the resin [14]. The desorption mechanism occurred with the consideration that the Cu^{2+} ions fully desorbed from the $\text{Cu}(\text{WPET-SiAMPy})_2$ complex. This reaction was assumed to occur according to the following Equation:

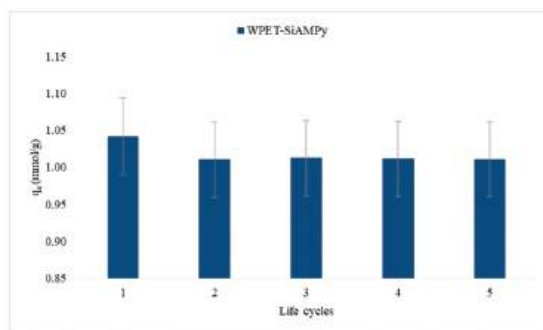


Figure 15. Five adsorption–desorption/regeneration cycles of Cu^{2+} using WPET-SiAMPy nanofibres.

4. Conclusions

This study reported the use of the electrospinning technique to combine and incorporate silica-supported 2-aminomethylpyridine (SiAMPy) into polyethylene terephthalate (PET) and waste plastic bottles (WPET) polymer solutions to produce composite nanofibres (PET-SiAMPy and WPET-SiAMPy) for the first time to our knowledge. The PET and WPET nanofibres were robust with very fine dimensions and a high surface area-to-volume ratio, which makes them ideal for active adsorbent support. In batch adsorption experiments, PET-SiAMPy or WPET-SiAMPy composite nanofibres achieved Cu^{2+} adsorption equilibrium within 60 s of contact time with 0.98 mmol/g (89.87%) or 1.24 mmol/g (96.04%) Cu^{2+} adsorption capacity. WPET-SiAMPy composite nanofibres were found to be effective adsorbents for the recovery of Cu^{2+} ion from aqueous solution, as the WPET-SiAMPy composite nanofibres carried sufficient Cu^{2+} adsorption active sites. The rapid kinetics and high Cu^{2+} recovery was credited to the high surface area and the porosity of the PET-SiAMPy or WPET-SiAMPy composite nanofibres, which resulted in more adsorption sites being available for the Cu metal ion adsorption from the solution. The application of the WPET-SiAMPy composite electrospun nanofibres for Cu^{2+} adsorption with very fast kinetic provides high-performance Cu^{2+} adsorbent that is distinctive to this research. The regeneration of WPET-SiAMPy composite nanofibres allowed replicable high Cu^{2+} readsorption proving the reusability of the WPET-SiAMPy composite nanofibres, compared to the silica-supported 2-aminomethylpyridine resin (AMPy). The deteriorating limit of the WPET-SiAMPy composite nanofibres should be studied to establish the extent of the regeneration of WPET-SiAMPy composite nanofibres in future studies.

Author Contributions: L.P., K.L. and T.C.T. conceptualized, validated, and formally analysed the manuscript. T.C.T. drafted the methodology, investigated, performed the data curation, and prepared the original draft. O.P. and C.B.-A. reviewed and edited the manuscript. L.P. administered the project, organized resources, reviewed, edited, visualized, supervised, and acquired funding for the research project. All authors have read and agreed to the published version of the manuscript.

Funding: The study was supported by Environmental and Nano Sciences Research Group, University of the Western Cape, South Africa; Research Foundation of the Lappeenranta-Lahti University of Technology LUT; and Academy of Finland.

Institutional Review Board Statement: Not applicable.

Informed Consent Statement: Not applicable.

Data Availability Statement: The data presented in this study are available within the article.

Acknowledgments: A. Josephs in the Physics department for HRSEM and K. Yunus in the Pharmacy department of UWC for TGA and FTIR.

Conflicts of Interest: The authors declare no conflict of interest. The funders had no role in the design of the study; in the collection, analyses, or interpretation of data; in the writing of the manuscript, or in the decision to publish the results.

References

1. Annadurai, G.; Juang, R.-S.; Lee, D. Adsorption of heavy metals from water using banana and orange peels. *Water Sci. Technol.* **2003**, *47*, 185–190. [[CrossRef](#)]
2. Ayawei, N.; Angaye, S.S.; Wankasi, D.; Dikio, E.D. Synthesis, characterization and application of Mg/Al layered double hydroxide for the degradation of congo red in aqueous solution. *Open J. Phys. Chem.* **2015**, *5*, 56–70. [[CrossRef](#)]
3. Ayawei, N.; Ebelegi, A.N.; Wankasi, D. Modelling and interpretation of adsorption isotherms. *J. Chem.* **2017**, *2017*, 1–11. [[CrossRef](#)]
4. Ayawei, N.; Ekubo, A.T.; Wankasi, D.; Dikio, E.D. Adsorption of congo red by Ni/Al-CO₃: Equilibrium, thermodynamic and kinetic studies. *Orient. J. Chem.* **2015**, *31*, 1307–1318. [[CrossRef](#)]
5. Bai, L.; Hu, H.; Zhang, W.; Fu, J.; Lu, Z.; Liu, M.; Jiang, H.; Zhang, L.; Chen, Q.; Tan, P. Amine/acid catalyzed synthesis of a new silica-aminomethyl pyridine material as a selective adsorbent of copper. *J. Mater. Chem.* **2012**, *22*, 17293–17301. [[CrossRef](#)]
6. Biazar, E.; Ahmadian, M.; Heidari, S.; Gazmeh, A.; Mohammadi, S.F.; Lashay, A.; Heideri, M.; Eslami, H.; Sahebalzamani, M.; Hashemi, H. Electro-spun polyethylene terephthalate (PET) mat as a keratoprosthesis skirt and its cellular study. *Fibers Polym.* **2017**, *18*, 1545–1553. [[CrossRef](#)]

7. Bode-Aluko, C.A.; Laatikainen, K.; Pereao, O.; Nechaev, A.; Kochnev, I.; Rossouw, A.; Dobretsov, S.; Branger, C.; Sarbu, A.; Petrik, L. Fabrication and characterisation of novel nanofiltration polymeric membrane. *Mater. Today Commun.* **2019**, *20*, 100580. [\[CrossRef\]](#)
8. Bode-Aluko, C.A.; Pereao, O.; Ndayambaje, G.; Petrik, L. Adsorption of toxic metals on modified polyacrylonitrile nanofibres: A review. *Water Air Soil Pollut.* **2017**, *228*, 35. [\[CrossRef\]](#)
9. Bonilla-Petriciolet, A.; Mendoza-Castillo, D.I.; Reynel-Ávila, H.E. Adsorption processes for water treatment and purification. *Adsorpt. Process. Water Treat. Purif.* **2017**, 1–256. [\[CrossRef\]](#)
10. Cai, Y.; Ke, H.; Zhang, T.; Dong, J.; Qiao, H.; Wang, H.; Xu, Z.; Wei, Q.; Zhao, Y.; Fong, H. Preparation, morphology and properties of electrospun lauric acid/pet form-stable phase change ultrafine composite fibres. *Polym. Polym. Compos.* **2011**, *19*, 773–780. [\[CrossRef\]](#)
11. Colmenares, J.C.; Varma, R.S.; Lisowski, P. Sustainable hybrid photocatalysts: Titania immobilized on carbon materials derived from renewable and biodegradable resources. *Green Chem.* **2016**, *18*, 5736–5750. [\[CrossRef\]](#)
12. Cuppett, J.D.; Duncan, S.E.; Dietrich, A.M. Evaluation of copper speciation and water quality factors that affect aqueous copper tasting response. *Chem. Senses* **2006**, *31*, 689–697. [\[CrossRef\]](#) [\[PubMed\]](#)
13. Dąbrowski, A. Adsorption—From theory to practice. *Adv. Colloid Interface Sci.* **2001**, *93*, 135–224. [\[CrossRef\]](#)
14. Das, P.; Tiwari, P. Thermal degradation study of waste polyethylene terephthalate (PET) under inert and oxidative environments. *Thermochim. Acta* **2019**, *679*, 178340. [\[CrossRef\]](#)
15. Elmorsi, T.M. Equilibrium isotherms and kinetic studies of removal of methylene blue dye by adsorption onto Miswak leaves as a natural adsorbent. *J. Environ. Prot.* **2011**, *2*, 817–827. [\[CrossRef\]](#)
16. Van Emmerik, T.; Schwarz, A. Plastic debris in rivers. *Wiley Interdiscip. Rev. Water* **2020**, *7*, e1398. [\[CrossRef\]](#)
17. Van Gerven, T.; Stankiewicz, A. Structure, energy, synergy, time—The fundamentals of process intensification. *Ind. Eng. Chem. Res.* **2009**, *48*, 2465–2474. [\[CrossRef\]](#)
18. Günay, A.; Arslankaya, E.; Tosun, I. Lead removal from aqueous solution by natural and pretreated clinoptilolite: Adsorption equilibrium and kinetics. *J. Hazard. Mater.* **2007**, *146*, 362–371. [\[CrossRef\]](#)
19. Gupta, V.K.; Ali, I.; Saleh, T.A.; Siddiqui, M.N.; Agarwal, S. Chromium removal from water by activated carbon developed from waste rubber tires. *Environ. Sci. Pollut. Res.* **2013**, *20*, 1261–1268. [\[CrossRef\]](#)
20. Haider, S.; Park, S.-Y. Preparation of the electrospun chitosan nanofibers and their applications to the adsorption of Cu (II) and Pb (II) ions from an aqueous solution. *J. Membr. Sci.* **2009**, *328*, 90–96. [\[CrossRef\]](#)
21. Haryani, S.; Kurniawan, C. Kasmui Kinetic and mechanism formation reaction of complex compound Cu with di-n-butylthiocarbamate (dbdtc) ligand. *IOP Conf. Ser. Mater. Sci. Eng.* **2018**, *349*, 012060. [\[CrossRef\]](#)
22. Hurt, A.P.; Kotha, A.K.; Trivedi, V.; Coleman, N.J. Bioactivity, biocompatibility and antimicrobial properties of a chitosan-mineral composite for periodontal tissue regeneration. *Polímeros* **2015**, *25*, 311–316. [\[CrossRef\]](#)
23. Kaneko, K. Determination of pore size and pore size distribution: 1. Adsorbents and catalysts. *J. Membr. Sci.* **1994**, *96*, 59–89. [\[CrossRef\]](#)
24. Kecili, R.; Hussain, C.M. Mechanism of adsorption on nanomaterials. *Nanomater. Chromatogr. Curr. Trends Chromatogr. Res. Technol. Tech.* **2018**, 89–115. [\[CrossRef\]](#)
25. Khakpay, A.; Ghorbanian, S.A.; Bagheri, N. Investigation of adsorption isotherms of benzoic acid on activated carbon. In Proceedings of the 1st National Conference on Industrial Water and Wastewater Treatment, Mahshahr, Iran, 29 November 2012.
26. Kumar, K.V.; Porkodi, K.; Rocha, F. Isotherms and thermodynamics by linear and non-linear regression analysis for the sorption of methylene blue onto activated carbon: Comparison of various error functions. *J. Hazard. Mater.* **2008**, *151*, 794–804. [\[CrossRef\]](#)
27. Laatikainen, M.; Sirola, K.; Paatero, E. Binding of transition metals by soluble and silica-bound branched poly(ethyleneimine): Part I: Competitive binding equilibria. *Colloids Surfaces A Physicochem. Eng. Asp.* **2007**, *296*, 191–205. [\[CrossRef\]](#)
28. Lee, A.Y.W.; Lim, S.F.; Chua, S.N.D.; Sanaullah, K.; Baini, R.; Abdullah, M.O. Adsorption equilibrium for heavy metal divalent ions (Cu²⁺, Zn²⁺, and Cd²⁺) into zirconium-based ferromagnetic sorbent. *Adv. Mater. Sci. Eng.* **2017**, *2017*, 1–13. [\[CrossRef\]](#)
29. Letcher, T.M. Introduction to plastic waste and recycling. *Plast. Waste Recycl.* **2020**, *3–12*, 3–12. [\[CrossRef\]](#)
30. Li, X.; Li, B.; Wu, S.; Li, J.; Xu, Q.; Yang, Z.; Liu, Y.; Wang, S.; Chen, D. Silica-based 2-aminomethylpyridine functionalized adsorbent for hydrometallurgical extraction of low-grade copper ore. *Ind. Eng. Chem. Res.* **2012**, *51*, 15224–15232. [\[CrossRef\]](#)
31. Lim, J.H.; Kang, H.M.; Kim, L.H.; Ko, S.O. Removal of heavy metals by sawdust adsorption: Equilibrium and kinetic studies. *Environ. Eng. Res.* **2008**, *13*, 79–84. [\[CrossRef\]](#)
32. Lowell, S.; Shields, J.E.; Thomas, M.A.; Thommes, M. Adsorption isotherms. In *Characterization of Porous Solids and Powders: Surface Area, Pore Size and Density*; Particle Technology Series; Springer: Dordrecht, The Netherlands, 2004; pp. 11–14. [\[CrossRef\]](#)
33. Mahmoud, A.M.; Ibrahim, F.A.; Shaban, S.; Youssef, N.A. Adsorption of heavy metal ion from aqueous solution by nickel oxide nano catalyst prepared by different methods. *Egypt. J. Pet.* **2015**, *24*, 27–35. [\[CrossRef\]](#)
34. Mohammad, N.; Atassi, Y. Adsorption of methylene blue onto electrospun nanofibrous membranes of polylactic acid and polyacrylonitrile coated with chloride doped polyaniline. *Sci. Rep.* **2020**, *10*, 1–19. [\[CrossRef\]](#)
35. Morillo Martín, D.; Magdi Ahmed, M.; Rodríguez, M.; García, M.A.; Faccini, M. Aminated polyethylene terephthalate (PET) nanofibers for the selective removal of Pb (II) from polluted water. *Materials* **2017**, *10*, 1352. [\[CrossRef\]](#)
36. Mousavi, S.; Shahraki, F.; Aliabadi, M.; Haji, A.; Deuber, F.; Adhart, C. Surface enriched nanofiber mats for efficient adsorption of Cr (VI) inspired by nature. *J. Environ. Chem.* **2019**, *7*, 102817. [\[CrossRef\]](#)

37. Strain, I.N.; Wu, Q.; Pourrahimi, A.M.; Hedenqvist, M.S.; Olsson, R.T.; Andersson, R.L. Electrospinning of recycled PET to generate tough mesomorphic fibre membranes for smoke filtration. *J. Mater. Chem. A* **2015**, *3*, 1632–1640. [CrossRef]
38. Ndayambaje, G.; Laatikainen, K.; Laatikainen, M.; Beukes, E.; Fatoba, O.O.; van der Walt, N.; Petrik, L.; Sainio, T. Adsorption of nickel (II) on polyacrylonitrile nanofiber modified with 2-(2'-pyridyl) imidazole. *Chem. Eng. J.* **2016**, *284*, 1106–1116. [CrossRef]
39. Nordin, N.A.; Rahman, N.A.; Abdullah, A.H. Effective removal of Pb(II) ions by electrospun PAN/Sago lignin-based activated carbon nanofibers. *Molecules* **2020**, *25*, 3081. [CrossRef]
40. Ouyang, D.; Zhuo, Y.; Hu, L.; Zeng, Q.; Hu, Y.; He, Z. Research on the adsorption behavior of heavy metal ions by porous material prepared with silicate tailings. *Minerals* **2019**, *9*, 291. [CrossRef]
41. Parker, G.R. Optimum isotherm equation and thermodynamic interpretation for aqueous 1,1,2-trichloroethene adsorption isotherms on three adsorbents. *Adsorption* **1995**, *1*, 113–132. [CrossRef]
42. Pereao, O.; Laatikainen, K.; Bode-Aluko, C.; Fatoba, O.; Omoniyi, E.; Kochnev, Y.; Nechaev, A.; Apel, P.; Petrik, L. Synthesis and characterisation of diglycolic acid functionalised polyethylene terephthalate nanofibers for rare earth elements recovery. *J. Environ. Chem. Eng.* **2021**, *9*, 105902. [CrossRef]
43. Pereao, O.; Opeolu, B.; Fatoki, O. Microplastics in aquatic environment: Characterization, ecotoxicological effect, implications for ecosystems and developments in South Africa. *Environ. Sci. Pollut. Res.* **2020**, *27*, 22271–22291. [CrossRef] [PubMed]
44. Pereao, O.K. Functionalisation of Electrospun Nanofibre for Lanthanide Ion Adsorption from Aqueous Solution. Ph.D. Thesis, University of the Western Cape, Cape Town, South Africa, 2018. Available online: <https://etd.uwc.ac.za/handle/11394/6393> (accessed on 11 November 2021).
45. Quiñones, I.; Guiochon, G. Derivation and application of a jovanovic–freundlich isotherm model for single-component adsorption on heterogeneous surfaces. *J. Colloid Interface Sci.* **1996**, *183*, 57–67. [CrossRef]
46. Sen, T.; Kawajiri, Y.; Realff, M.J. Adsorption process intensification through structured packing: A modeling study using zeolite 13X and a mixture of propylene and propane in hollow-fiber and packed beds. *Ind. Eng. Chem. Res.* **2018**, *58*, 5750–5767. [CrossRef]
47. Shafqat, S.S.; Khan, A.A.; Zafar, M.N.; Alhaji, M.H.; Sanaullah, K.; Shafqat, S.R.; Murtaza, S.; Pang, S.C. Development of amino-functionalized silica nanoparticles for efficient and rapid removal of COD from pre-treated palm oil effluent. *J. Mater. Res. Technol.* **2019**, *8*, 385–395. [CrossRef]
48. El Sikaily, A.; Khaled, A.; Nemr, A.E.; Abdelwahab, O. Removal of methylene blue from aqueous solution by marine green alga *Ulva lactuca*. *Chem. Ecol.* **2006**, *22*, 149–157. [CrossRef]
49. Sing, K.S. Reporting physisorption data for gas/solid systems with special reference to the determination of surface area and porosity. *Pure Appl. Chem.* **1985**, *57*, 603–619. [CrossRef]
50. Sirola, K.; Laatikainen, K.; Lahtinen, M.; Paatero, E. Removal of copper and nickel from concentrated ZnSO₄ solutions with silica-supported chelating adsorbents. *Sep. Purif. Technol.* **2008**, *64*, 88–100. [CrossRef]
51. Sirola, K.; Laatikainen, M.; Paatero, E. Effect of temperature on sorption of metals by silica-supported 2-(aminomethyl)pyridine. Part I: Binding equilibria. *React. Funct. Polym.* **2010**, *70*, 48–55. [CrossRef]
52. De Smedt, C.; Ferrer, F.; Leus, K.; Spanoghe, P. Removal of pesticides from aqueous solutions by adsorption on zeolites as solid adsorbents. *Adsorpt. Sci. Technol.* **2015**, *33*, 457–485. [CrossRef]
53. Thommes, M.; Kaneko, K.; Neimark, A.V.; Olivier, J.P.; Rodriguez-Reinoso, F.; Rouquerol, J.; Sing, K.S.W. Physisorption of gases, with special reference to the evaluation of surface area and pore size distribution (IUPAC Technical Report). *Pure Appl. Chem.* **2015**, *87*, 1051–1069. [CrossRef]
54. Tolentino, R.; Knaebel, K.S. *Adsorbent Selection*; International Journal of Trend in Research and Development: Dublin, OH, USA, 2004; p. 43016.
55. Ungureanu, O.I.; Bulgariu, D.; Mocanu, A.M.; Bulgariu, L. Functionalized PET waste based low-cost adsorbents for adsorptive removal of Cu (II) ions from aqueous media. *Water* **2020**, *12*, 2624. [CrossRef]
56. Veleirinho, B.; Rei, M.F.; Lopes-Da-Silva, J.A. Solvent and concentration effects on the properties of electrospun poly (ethylene terephthalate) nanofiber mats. *J. Polym. Sci. Part B Polym. Phys.* **2008**, *46*, 460–471. [CrossRef]
57. Wang, Y.H.; Hu, H.P.; Qiu, X.J. Fixed-bed column study for deep removal of copper (II) from simulated cobalt electrolyte using polystyrene-supported 2-aminomethylpyridine chelating resin. *J. Central South Univ.* **2019**, *26*, 1374–1384. [CrossRef]
58. Ben Yahia, M.; Ben Torkia, Y.; Knani, S.; Hachicha, M.A.; Khalfaoui, M.; Ben Lamine, A. Models for type VI adsorption isotherms from a statistical mechanical formulation. *Adsorpt. Sci. Technol.* **2013**, *31*, 341–357. [CrossRef]
59. Yilmaz, V.T.; Caglar, S.; Harrison, W.T.A. A one-dimensional lead (II) coordination polymer with bridging saccharinate and 2-aminomethylpyridine ligands: Synthesis, IR spectra, and crystal structure of [Pb(ampy)(μ-sac)₂]_n. *Z. Für Anorg. Und Allg. Chem.* **2004**, *630*, 948–951. [CrossRef]
60. Zhang, Y.; Wang, F.; Wang, Y. Recent developments of electrospun nanofibrous materials as novel adsorbents for water treatment. *Mater. Today Commun.* **2021**, *27*, 102272. [CrossRef]
61. Zhu, Y.; Millan, E.; Sengupta, A.K. Toward separation of toxic metal (II) cations by chelating polymers: Some noteworthy observations. *React. Polym.* **1990**, *13*, 241–253. [CrossRef]

Article

A Molecularly Imprinted Polymer Based SPR Sensor for 2-Furaldehyde Determination in Oil Matrices

Maria Pesavento ^{1,*}, Nunzio Cennamo ², Luigi Zeni ² and Letizia De Maria ³¹ Department of Chemistry, University of Pavia, Via Taramelli 12, 27100 Pavia, Italy² Department of Engineering, University of Campania L. Vanvitelli, Via Roma 29, 81031 Aversa, Italy; nunzio.cennamo@unicampania.it (N.C.); luigi.zeni@unicampania.it (L.Z.)³ RSE SpA, Via Rubattino 54, 20134 Milan, Italy; Letizia.DeMaria@rse.web.it

* Correspondence: maria.pesavento@unipv.it

Featured Application: The work shows the development of an optical chemosensor based on a synthetic receptor, a molecularly imprinted polymer, for a furanic compound, 2-furaldehyde, with a good possibility of application in liquid samples, even very complex, and with high refractive index as a vegetable oil. This opens the way for the wide application of this sensing technique on site and in matrices of high industrial interest.

Abstract: Optical chemosensors with surface plasmon resonance (SPR) transduction are widely employed, even in complex environments, such as those outside the laboratory. In this context, not only the chemical nature but also the physical form of the receptor layer is particularly relevant. Synthetic receptors as molecularly imprinted polymers (MIPs) are well suited. This is demonstrated here in the case of an SPR sensor platform based on a multimode plastic optical fiber, which is very promising for on site application due to the low dimensions and low cost. A specific MIP was used as the receptor, with high affinity for the substance to be determined, 2-furaldehyde, in water. Here, a medium of high refractive index, i.e., vegetable oil, was considered because of the high interest for its determination in industrial diagnostics. The effects of the MIP layer thickness and the washing extent on the quality of the analytical signal were investigated. Better spectra were generated at the thinner MIP layer, while a lower detection limit is reached with extended washing.

Keywords: molecularly imprinted polymer; optical sensor; plastic optical fiber; surface plasmon resonance; 2-furaldehyde; vegetable oil

Citation: Pesavento, M.; Cennamo, N.; Zeni, L.; De Maria, L. A Molecularly Imprinted Polymer Based SPR Sensor for 2-Furaldehyde Determination in Oil Matrices. *Appl. Sci.* **2021**, *11*, 10390. <https://doi.org/10.3390/app112110390>

Academic Editor: Andrei Sarbu

Received: 16 October 2021

Accepted: 1 November 2021

Published: 5 November 2021

Publisher's Note: MDPI stays neutral with regard to jurisdictional claims in published maps and institutional affiliations.



Copyright: © 2021 by the authors. Licensee MDPI, Basel, Switzerland. This article is an open access article distributed under the terms and conditions of the Creative Commons Attribution (CC BY) license (<https://creativecommons.org/licenses/by/4.0/>).

1. Introduction

The need for low-cost and easy-to-use sensing systems is constantly increasing in different application areas, in particular for health, food and environmental controls and rapid screening of contaminants. A wide interest for sensing systems is also present in several industrial contexts, for example for early warnings of failures, with the aim of reducing maintenance costs, or as effective data sources for big data applications and predictive analysis [1,2].

This work focuses on the application of a sensor for the selective detection of furfural, 2-furaldehyde (2-FAL), in vegetable oil. The 2-FAL detection in this kind of matrix is becoming interesting for diagnostic purposes, since it is recognized that the presence of 2-FAL in the oil of oil-insulated electrical equipment is an important marker of the degradation of the insulating system. 2-FAL can be present as a byproduct of the thermal degradation of cellulose, so 2-FAL detection in insulating oil is a crucial task for preventing accelerated aging phenomena of oil-paper insulation (paper windings, pressboards) in transformers [3–5]. These phenomena heavily influence the effective lifetime of power transformers.

Traditional monitoring techniques are typically based on laboratory analyses, mainly chromatographic methods, of representative field-collected samples; this necessitates

considerable time, effort and expense, and can produce some changes in the sample composition before analysis. An alternative approach consists of portable monitoring systems relying on sensing methods. They appear to be well suited to complement standard analytical methods and, also, can be permanently installed at monitoring sites and can transmit data remotely.

Considering the wide range of application areas, a huge number of bio- and chemoreceptor-based sensors have been described in the last twenty years, among which those based on optical transduction, and in particular on optical fibers, have been shown as well suited for numerous applications [6–11]. The sensing platform used here for the determination of 2-FAL in vegetable oil is based on an optical transduction method, surface plasmon resonance (SPR), on optical fiber, and based on a synthetic chemical receptor, a molecularly imprinted polymer (MIP). It has been previously used for a number of applications in aqueous matrices [12–14], but a different matrix was also considered, i.e., a mineral oil of the isolated transformers [15]. The optical fiber sensing platforms based on SPR allow marker-free detection, and plastic optical fibers (POFs) are especially advantageous for low-cost sensing systems due to their excellent flexibility, easy manipulation, great numerical aperture, large diameter and the fact that plastic can withstand smaller bend radii than glass [16].

The platform proposed here consists of a planar surface of an exposed POF core, embedded in a resin block (D-shaped POF platform), covered with a dielectric layer of photoresist with high RI and a thin gold layer [17]. The receptor layer is deposited on the gold surface. The flat shape of the sensing part is particularly suitable for measurements in a drop, for which no expensive and bulky flow-through cell is required.

MIPs are a class of artificial solid receptors [18–20] containing sites functionally and dimensionally complementary to the target molecular structure, similar to the receptor sites in bioreceptors. The process of MIP preparation is based on a template-assisted synthesis [19]. MIPs often possess recognition properties analogous to natural receptors but have the stability, ease of preparation, micromachining, integrability and low cost of production typical of synthetic materials. Moreover, MIPs can be easily produced as layers in tight contact with the transducing surfaces [12,14]. In this form, MIPs are different from the usual bioreceptors, for example, antibodies or aptamers, since the thickness of the layer, while being not larger than a few hundred nanometers, is certainly much higher than that of the bioreceptors layers, usually constituted by only one or a few molecular layers. This is a favorable aspect for sensing applications when considering real matrices with high refractive index (RI).

In the D-shaped POF-SPR platform proposed here, an MIP layer can be easily deposited by a drop coating and spinning procedure, as previously described in several cases [12–14]. In this study, the effect of different factors on the sensor response to 2-FAL when used in a matrix with high RI is investigated, considering as a proof of principle a vegetable insulating oil as the liquid medium, with an RI as high as 1.47. In particular, the effect of the thickness of the MIP layer was examined. The idea is that measurements in a medium with high RI, i.e., higher than those detectable by the sensing platform and the experimental setup proposed here, can still be carried out, taking advantage of the fact that the MIP layer may have an RI lower than that of the considered vegetable oil and that its thickness can be modulated in a simple way. Depending on the thickness of the MIP, the plasmonic wave can penetrate only the MIP layer, or it can reach the fluid above. This has been shown in a previous work in the case of aqueous media [14].

2. Materials and Methods

2.1. Chemicals and Instrumentation

Divinylbenzene [1321–74–0] (DVB), ethylene glycol dimethacrylate [97–90–5] (EGDMA), methacrylic acid [79–41–4] (MAA), 2,2'-azobisisobutyronitrile [78–67–1] (AIBN) and 2-furaldehyde [98–01–1] (2-FAL) were obtained from Sigma-Aldrich, Merk (Darmstadt, Germany). MAA and DVB were purified before use to remove stabilizers by fluxing the

liquid through a 4 cm column of alumina (Sigma-Aldrich). All other chemicals were of analytical reagent grade. Pure water was obtained by a Milli-Q system (Merck Millipore, Billerica, MA, USA). A stock solution with 11,600 mg L⁻¹ of 2-FAL was prepared by weighing the liquid and dissolving it in 96% ethanol. The standard solutions were obtained by successive dilution in the considered solvent, i.e., vegetable oil, obtained from the market and containing less than 0.01 mg L⁻¹ of furanic compounds. The measurement apparatus consisted of a halogen lamp (HL-2000-LL, Ocean Optics, Dunedin, FL, USA) and a spectrometer connected to a PC (USB2000+UV-VIS spectrometer, Ocean Optics, Dunedin, FL, USA). The emission wavelength range of the white light source was from 360 nm to 1700 nm, whereas the detection range of the spectrometer was from 350 nm to 1023 nm. The transmission spectra were saved and processed by SpectraSuite software (Ocean Optics, Dunedin, FL, USA). An outline of the experimental setup making possible the spectral interrogation is reported in Figure 1a.

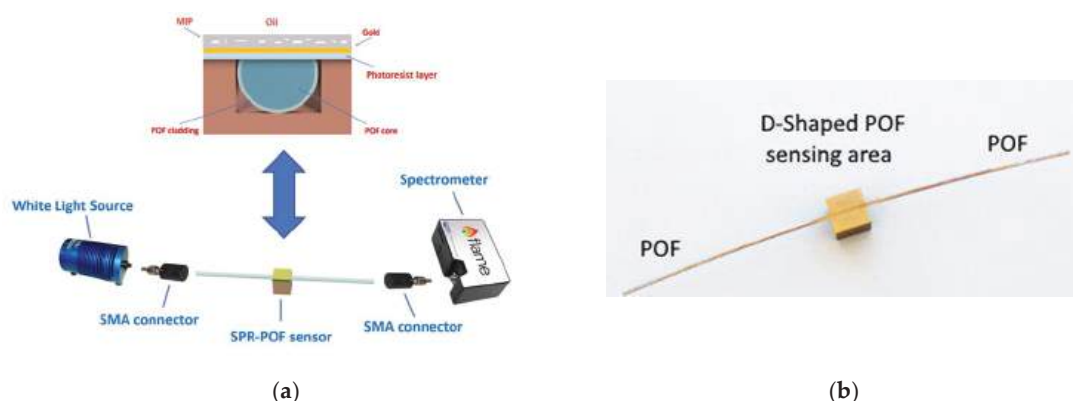


Figure 1. Optical chemical sensor system. (a) Outline of the experimental setup with a schematic representation of the D-shaped multilayer SPR-POF platform. The brown block represents the resin support (1 cm × 1 cm × 1 cm) in which the POF (in red) is embedded. The grey layer is the photoresist buffer, and the blue layer is the receptor. SMA is the subminiature version of the connector. The different parts are not in scale. (b) Picture of the SPR-POF platform.

2.2. Preparation of the D-Shaped Fiber Optic Platform

The optical platform was based on a multimode POF with a characteristic D-shaped sensing region, obtained as previously reported [12–14]. Briefly, the cladding and partially the core of the POF, held in a specially designed resin support 1 cm long, were manually erased, producing a flat surface (see Figure 1). One half of the fiber was erased, and a multilayer structure was built up over the exposed core by first depositing a buffer layer (Microposit photoresist, MicroChemCorp., Westborough, MA, USA) of high refractive index with respect to the core, 1.5 µm thick, deposited by dropping and spinning at 6000 rpm, a thin metal film (gold, 60 nm thick, deposited by sputtering with an SCD 500, Leica Microsystems, Wetzlar, Germany) and, finally, an MIP layer as a specific chemical receptor for 2-FAL detection.

2.3. Deposition of the Specific MIP Layer

The prepolymeric mixture was composed of the reagents at molar ratio 1 (2-FAL):4 (MAA):40 (DVB), according to the method previously described [14]. No porogen solvent was used. The cross-linker divinylbenzene (DVB) also acted as the solvent in which the functional monomer (methacrylic acid (MAA)) and the template, 2-FAL, were dissolved. The mixture was uniformly dispersed by sonication and de-aerated with nitrogen for 10 min. Then, the radical initiator AIBN (23 mg/mL of prepolymeric mixture) was added

to the mixture. An MIP with the same molar composition, but containing ethylene glycol dimethacrylate (EGDMA) instead of DVB, was prepared for comparison purposes.

The MIP layer was prepared by dropping directly over the flat part of the platform a small volume (about 50 μL) of the prepolymeric mixture on the platform maintained in a flat position with the help of the resin support. The prepolymeric mixture expanded spontaneously to cover the erased surface of the POF and of the resin support. The whole structure was spun at a given spin rate, typically at 1000 or 500 rpm for 2 min, and then placed in an oven for 16 h at 75 $^{\circ}\text{C}$ for thermal polymerization in air. Finally, the template and oligomeric polymer fragments were removed by repeated washings with 96% ethanol.

Layers with different thicknesses could be obtained by spinning the prepolymeric mixture at different rates or by depositing multiple layers of MIP. The thickness of the MIP layer is particularly relevant when liquids with high RI are examined.

2.4. Measurement

The D-shaped optical platforms embedded in the resin block allowed performing the measurement in a drop simply deposited over the flat surface, 1 cm \times 1 cm wide. The platform was fixed in a miniholder, which was designed to keep the sensing surface in a flat position. A sample drop (50 μL) was deposited over the flat part of the sensor, allowed to expand over the sensing surface and the support and equilibrated for 5 min. During this time, the oil drop tended to cover the whole flat surface of the support due to the lipophilic nature of the MIP, which was mainly constituted by DVB or EGDMA.

All the measurements were performed in an air-conditioned room at 25 $^{\circ}\text{C}$.

The spectra were recorded directly in the drop of the liquid sample positioned over the sensing surface. Depending on the penetration depth of the plasmonic wave, the RI of the dielectric can be influenced by the RI of the liquid, and if this is sufficiently high, the resonance wavelength could even exceed the detectable range. If so, the solvent exchange method [14] must be applied, which is, however, quite complex and time consuming.

The transmission spectra of the SPR-POF-MIP sensors in air, water and oil were normalized to the spectrum of the corresponding bare sensor (SPR-POF-bare) in air (reference spectrum).

2.5. Characterization of the Optical Sensitivity of the Bare Platform

Characterization was carried out by measuring the shift of the resonance wavelength in liquid with different refractive indices. These were solutions of glycerin in water at different concentrations, the refractive index of which was measured by an Abbe refractometer [17].

2.6. Characterization of the Sensor Response in Oil

Dose–response curves were obtained by plotting the variation of the resonance wavelength in the normalized transmission spectra ($\Delta\lambda$) in the function of the concentration of 2-FAL. $\Delta\lambda$ refers to the resonance wavelength of a blank solution, i.e., a solution with the same composition of the sample but not containing the analyte of interest.

Considering the limited number of receptor sites in sensors based on MIPs, the response to the concentration of the template can be modeled by an equation derived from the Langmuir adsorption model, which has been successfully applied in previous investigations carried out in aqueous matrices [14]. The relation between the response (DL) and the concentration of the molecule of interest [A] (in mg L^{-1} or M L^{-1}), assuming that the signal is directly proportional to the amount of the template in the sensing layer ($\Delta\lambda = k \cdot g \cdot c_{\text{Aint}}$), is given by the following equation:

$$\Delta\lambda = \frac{k g c_{\text{int}} K_{\text{aff}} [A]}{1 + K_{\text{aff}} [A]} = \frac{\Delta\lambda_{\text{max}} K_{\text{aff}} [A]}{1 + K_{\text{aff}} [A]} \quad (1)$$

K_{aff} (in $\text{mg}^{-1} \text{L}$ or $\text{M}^{-1} \text{L}$) is the affinity constant of the adsorption equilibrium, c_{int} is the concentration of the specific sites of the MIP (in mg g^{-1}), g is the polymer mass (in grams) and $\Delta\lambda_{\text{max}} = k \cdot g \cdot c_{\text{int}}$ is the maximum $\Delta\lambda$ at high concentrations of the analyte (i.e., when the analyte saturates all the specific sites).

If the analyte concentration at the equilibrium in the sample, $[A]$, is equal to the total concentration (c_A), i.e., when the concentration of the analyte adsorbed is negligible, Equation (1) can be used for evaluating the parameters, in particular K_{aff} , which is useful for characterizing the adsorption equilibria. The second parameter, $\Delta\lambda_{\text{max}}$, depends on the number of sites but also on the sensitivity of the transduction method, which is in principle unknown. Thus, it can only be used for comparative purposes. The parameters of Equation (1) were obtained by Solver, a Microsoft Excel add-on program.

3. Results

3.1. Characterization of SPR-POF-Bare Platforms

A few D-shaped optical platforms on POF were manually prepared as described (from SPR-POF-A1bare to SPR-POF-A5bare). The spectra in water normalized on the spectra of the same platform in air, registered immediately before the measurement in water, are reported in Figure 2.

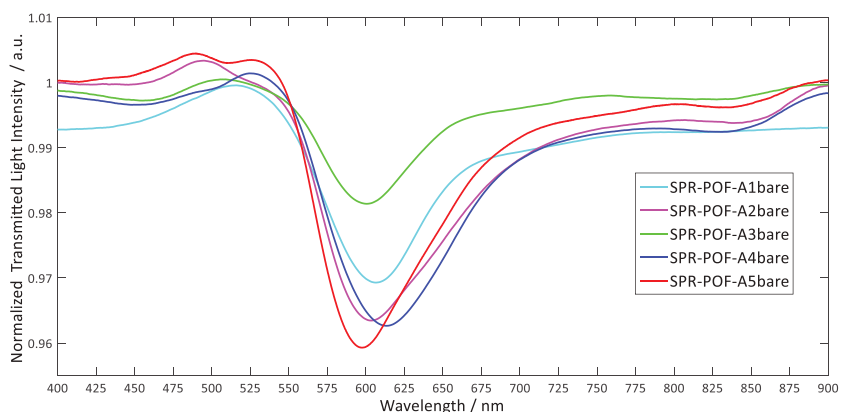


Figure 2. SPR spectra in water of the bare optical platforms, normalized to the spectra in air.

The spectra present some dips between 500 and 510 nm and at about 600 nm (average value of $603.5 (\pm 2.8)$ nm).

The depths of the dips are different, which could reflect the irreproducibility of the manual preparation. The optical sensitivity was determined for two platforms, SPR-POF-A4bare and SPR-POF-A5bare, which show somewhat different spectra in water (see Figure 2). Nevertheless, the sensitivity curves of the two sensors (Figure 3) are similar, showing that the sensitivity is very low below $n = 1.33$ and is higher at high RI (about 3500 RIU/nm).

3.2. SPR Spectra of POF-MIP Sensors

In order to investigate the effect of the thickness of the MIP layer, two kinds of sensors were considered: the first one was prepared on the platform SPR-POF-A5bare by depositing the prepolymeric mixture at 1000 rpm and the second one was prepared by depositing two layers of MIP (SPR-POF-A1MIP2 and SPR-POF-A2MIP2), each one at a spinning rate of 500 rpm. They should be covered by a larger amount of MIP than SPR-POF-A5MIP1.

As an example, the spectra in the water of the bare platforms of SPR-POF-A5bare and SPR-POF-A2bare are shown in Figure 4. In both cases, the spectra of the corresponding MIP sensor in air and water, normalized to the spectrum of the bare sensor in air, present several dips, which are sharper and better defined for SPR-POF-A5MIP1. Additionally, the difference between the spectrum in air and that in water is higher in the case of SPR-POF-A5MIP1, which confirms that a lower amount of MIP is deposited.

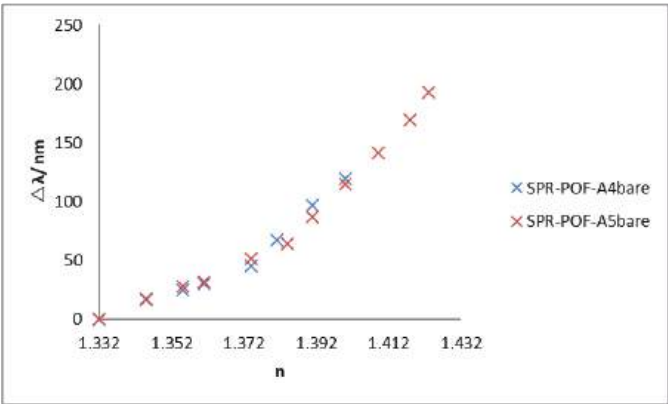
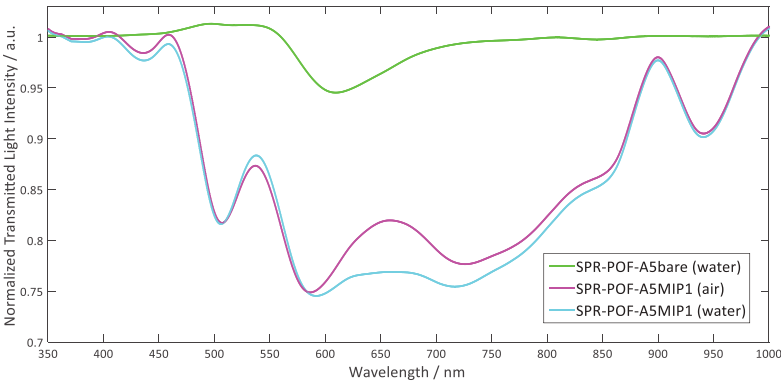
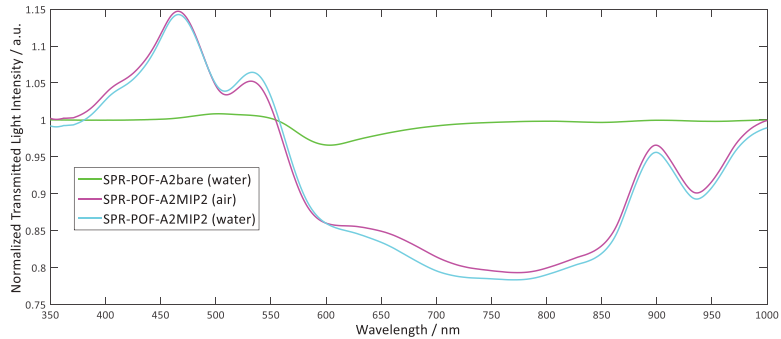


Figure 3. Sensitivity curves of SPR-POF-A4bare and SPR-POF-A5bare in water–glycerin solutions at different RIs.



(a)



(b)

Figure 4. Spectra in air and water normalized on the spectrum of the corresponding bare sensor in air of the sensors: (a) SPR-POF-A5MIP1; (b) SPR-POF-A2MIP2.

The effect of the different thicknesses can be more easily appreciated by comparing the same spectra but normalized to the SPR-POF-MIP in air, as reported in Figure 5. In both cases, the main resonance dip is shifted to higher wavelengths with respect to that obtained at the bare sensor, demonstrating that the MIP layer is present and that it modifies the RI of the dielectric layer. Its RI must be higher than that of water. As proposed in a previous work [14], the resonance wavelength shift with respect to that of the same platform not derivatized with MIP in pure water depends on the amount of MIP deposited, being different for SPR-POF-A5MIP1 and SPR-POF-A1MIP2.

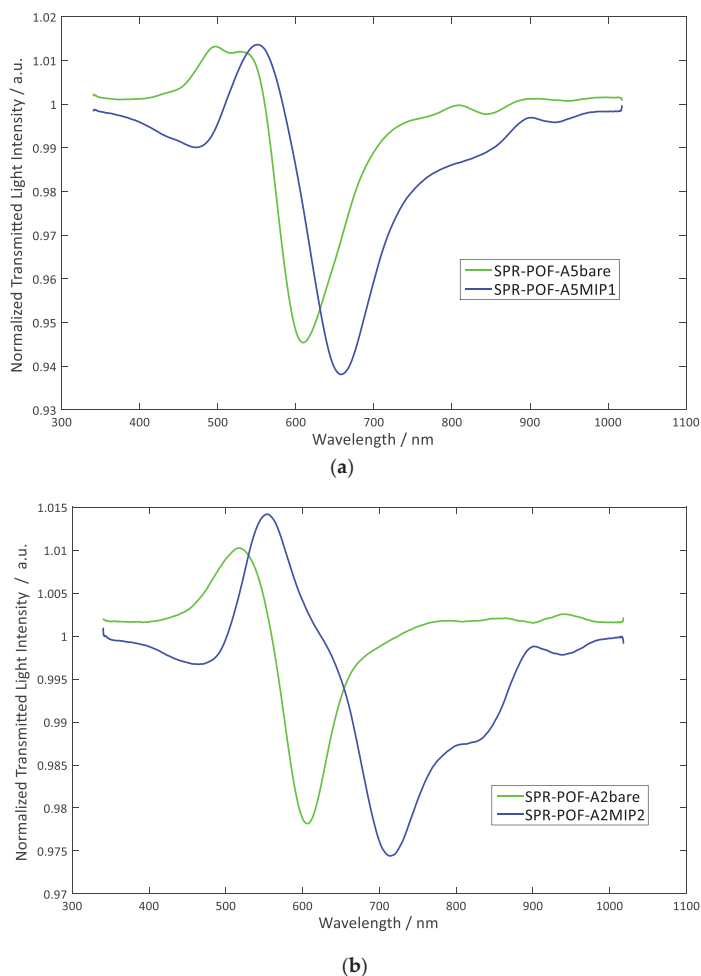


Figure 5. Spectra in water of the bare and MIP derivatized platforms normalized to the corresponding platform in air: (a) spectra of SPR-POF-A5bare and SPR-POF-A5MIP1 in water; (b) spectra of SPR-POF-A2bare and SPR-POF-A2MIP2.

By increasing the number of MIP layers, the resonance wavelength increases, and a shift to higher wavelengths (red shift) is observed (from 660 nm to 720 nm). This could be due either to a direct sensing of the RI of the fluid overlaying the MIP or to some solvation effects. As a matter of fact, the polymer considered here contains carboxylic groups from the functional monomer MAA, which can easily interact with water.

3.3. SPR-POF-MIP EGDMA Sensor

The MIP based on DVB as the cross-linker is highly lipophilic, which can be of help when dealing with oil samples, since a good contact between the receptor and the dissolved molecule is assured, but at the same time, the measurement in a drop is more difficult due to the fact that the drop tends to expand and fall. In order to reduce the lipophilic character of the MIP, a more polar cross-linker was used for the polymer preparation, EGDMA. Despite this, the surface of the sensor obtained was still lipophilic, since the oil drop expanded in the same way as that on the MIP DVB surface. The spectra of this sensor in different media normalized on the corresponding bare platform in air are reported in Figure 6.

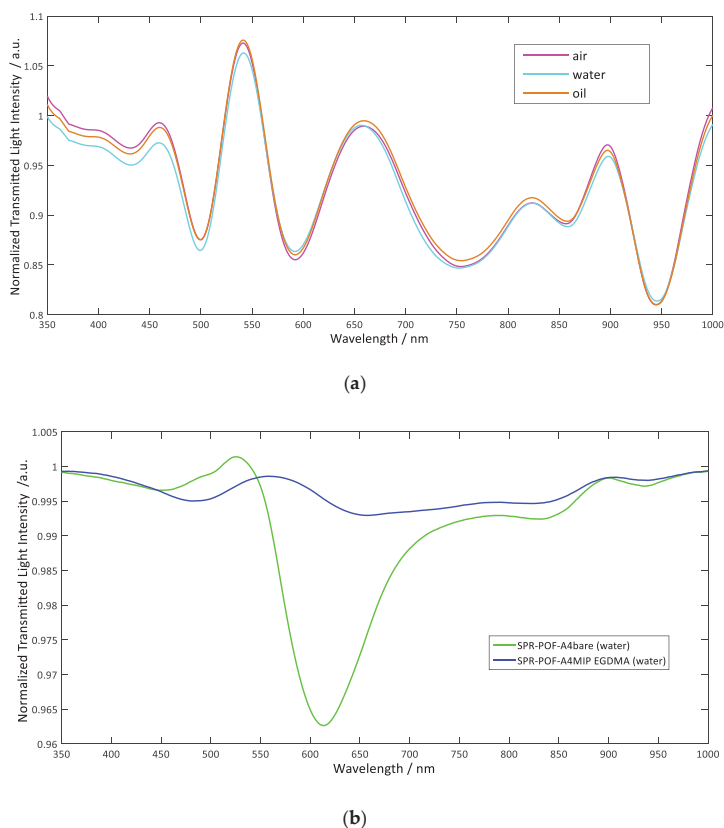


Figure 6. Spectra of SPR-POF-A4MIP EGDMA in different media: (a) normalized on the bare platform in air; (b) normalized on the MIP derivatized platform in air.

Spectra in air and water are very similar and so are those in oil, except that at about 740 nm, which has a different shape. Moreover, the spectra are similar to those of the sensors with DVB-based MIP obtained by spinning the prepolymeric mixture at 1000 rpm, with well-defined multiple dips instead of a large band with multiple minima. The spectra in water normalized on the corresponding MIP EGDMA derivatized sensor in air are noticeably different from those obtained on SPR-POF-MIP sensors, since only shallow dips at 480 nm and 655 nm are formed. This indicates that the different cross-linker (EGDMA) produces a polymer that is practically insensitive to water, despite the polar nature of the cross-linker, probably because of the high rigidity.

3.4. Characterization of the Response of the SPR-POF-MIP Sensors

The response of the sensor to the concentration of the substance of interest, 2-FAL, was investigated by determining the dose–response curve, and by applying the Langmuir adsorption model, assuming that the adsorption takes place through combination at specific sites, which in this case, are the imprinted sites. The model makes it possible to evaluate the affinity constant of the template for the MIP exactly in the form in which it is used in the sensing system, i.e., as a layer. This approach has been previously applied for the adsorption from water [14].

As an example, in Figure 7, the SPR spectra in oil, at different concentrations of 2-FAL, of the two sensors with MIP layers of different thickness, SPR-POF-A1MIP2 and SPR-POF-A5MIP1, normalized on the corresponding bare sensor in air, are reported. The washing between successive standards consisted of five repeated flushing with ethanol.

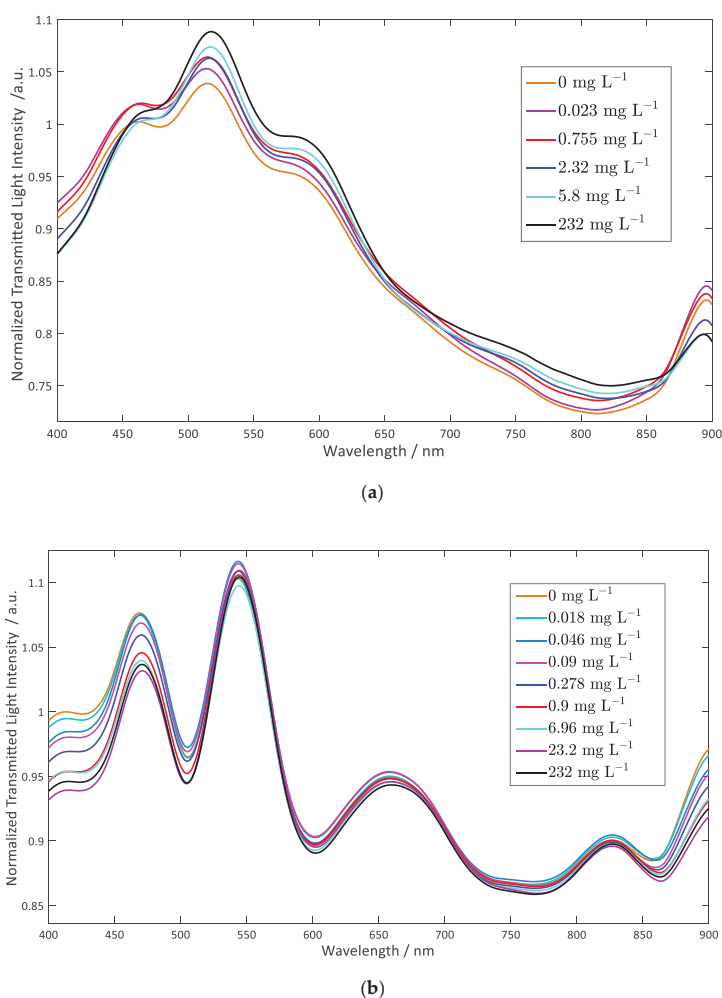


Figure 7. SPR spectra in oil, at different concentrations of 2-FAL, of two sensors with MIP layers of different thickness normalized on the corresponding bare sensor in air: (a) SPR-POF-A1MIP2; (b) SPR-POF-A5MIP1.

In both cases, multiple resonance dips are present, much better defined in the case of the sensor with a lower amount of MIP deposited. The resonance depending on the 2-FAL concentration is, respectively, 880 nm and 812 nm for the two considered sensors. This indicates that in the case of SPR-POF-A1MIP2, the MIP layer is sufficiently thick to avoid the effect of the fluid over the MIP (no effect of the sample bulk), while in the case of SPR-POF-A5MIP1, which contains a lower amount of MIP, there is a strong effect of the RI of the overlying liquid, which is high for the considered oil, 1.47. Nevertheless the resonance wavelength is still useful, being 880 nm.

The corresponding two standardization curves are shown in Figure 8.

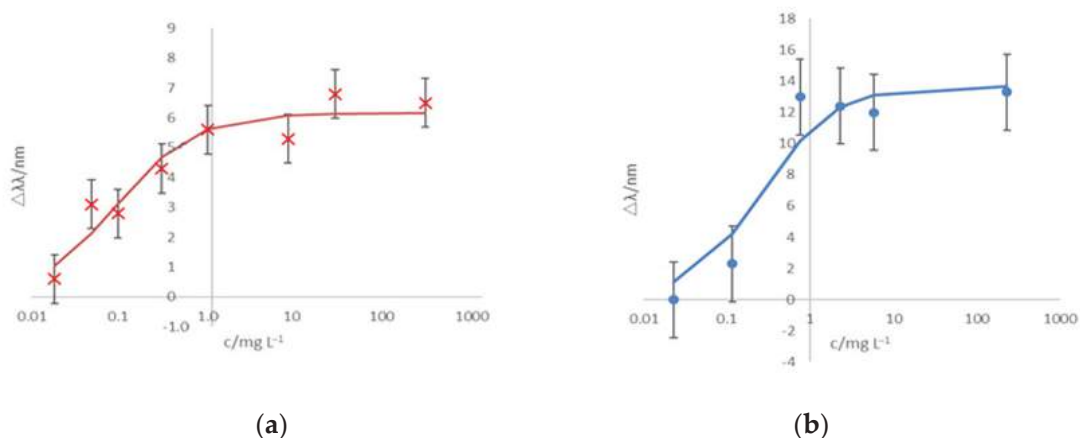


Figure 8. Dose–response curves for 2-FAL in vegetable oil of: (a) SPR-POF-A5MIP1; (b) SPR-POF-A1MIP2.

The dose–response curves are similar, but the maximum signal is higher when a higher amount of polymer is deposited, possibly corresponding to the presence of a larger number of accessible combination sites when more polymer is deposited. The parameters of the dose–response curve (Equation (1)) are reported in Table 1.

Table 1. Parameters of the dose–response curve for 2-FAL in vegetable oil for different SPR-POF-MIP sensors.

	K_{aff} (L M ^{−1})	Sens (nm mg ^{−1} L)	SEy (nm)	LOD (μg L ^{−1})
SPR-POF-A5MIP1 (N = 6)	1.09×10^6	70	0.66	18
SPR-POF-A1MIP2 (N = 5)	3.69×10^5	53	1.69	64
SPR-POF-A4MIP EGDMA (N = 7)	2.60×10^5	70	0.14	52

SEy is the error of the response, $\Delta\lambda$; N indicates the number of standards considered.

The error on the resonance wavelength shift, and the detection limit, is lower for SPR-POF-A5MIP1, for which the resonance dips are better defined, than for SPR-POF-A1MIP2. The affinity is high enough to make the determination at a low concentration level possible, useful for application in different fields, for example for the determination of 2-FAL in vegetable oils. Nevertheless, it could be too high for other applications. A possible improvement could take place by applying a more extensive washing procedure.

For the sensor SPR-POF-A4MIP EGDMA, the spectra in oil, normalized to those of the bare platform in air, are similar to the spectra in water and in air. The peak at 850 nm is shifted to higher wavelengths when the concentration of 2-FAL increases. By applying the Langmuir model to the dose–response curve (Equation (1)), the parameters could be evaluated, and they are reported for comparison in Table 2. The affinity constant is lower for SPR-POF-A4MIP EGDMA than for the sensors prepared with DVD as the cross-linking agent, despite the fact that the functional polymer is always MAA at the same concentration. It could be guessed that some interaction between the MAA and EGDMA

can somewhat lower the affinity of the sites for the template. Notice the lower value of SEy, which corresponds to the better sharpness of the peak obtained in this case.

Table 2. Parameters of the dose–response curve for 2-FAL in vegetable oil, at an SPR platform extensively cleaned, for different washing procedures between measurements.

	K_{aff} (L M ^{−1})	Sens (nm mg ^{−1} L)	SEy (nm)	$\Delta\lambda_{\text{max}}$ (nm)	LOD (μg L ^{−1})
SPR-POF-A2MIP2 (N = 6) stand with washing in water	8.32×10^7	8.18×10^7	0.13	0.98	0.3
SPR-POF-A2MIP2 (N = 5) stand with washing in ethanol	1.77×10^8	2.70×10^8	0.19	1.52	0.14

SEy is the error of the response, $\Delta\lambda$; N indicates the number of standards considered.

The repeatability of the sensor was demonstrated by repeating three times every ten days (the sensor was stored in the air between the successive measurements) the dose–response curve for 2-FAL in vegetable oil and evaluating the parameters of the curve. The average values with the relative standard deviation are: $K_{\text{aff}} = 1.02 (0.01) \times 10^6 \text{ M}^{-1}$ and $\Delta\lambda_{\text{max}} = 8.2 (2.9) \text{ nm}$. The repeatability, measured by the relative standard deviation, of the affinity constant is good, while that of $\Delta\lambda_{\text{max}}$ is somewhat lower, which could be due to the poor reproducibility of the cleaning procedure.

3.5. Effect of Extended Washing and Conditioning

A sensor (SPR-POF-A2MIP2) was washed by flushing five times with ethanol, which is the usual procedure, and then further washed alternately with ethanol and the same oil used for the successive measurements. The idea is that while ethanol is able to extract 2-FAL and other hydrophilic components of the polymer, oil can extract hydrophobic impurities, which could cause a large irreproducibility during the successive measurements in oil if not completely extracted. This could also contribute to making stronger combination sites free. The spectra in oil with different concentrations of 2-FAL were then registered. The washing procedure of the sensor between successive standards consisted of five repeated flushing with ethanol. All the spectra were normalized on the same spectrum of the bare sensor in air. An example of the spectrum of a sensor with thicker MIP film in oil after extended extraction and by washing with ethanol between successive standards is reported in Figure 9.

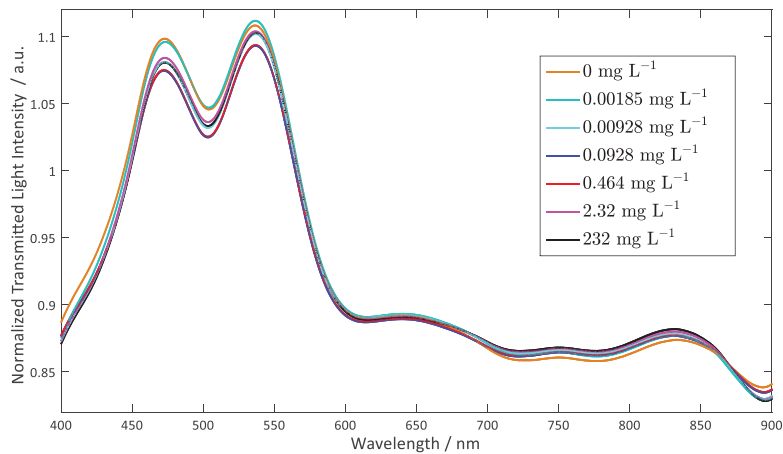


Figure 9. Spectra of SPR-POF-A2MIP2 (with extended cleaning) in oil.

Notice the presence of the peak at 500 nm, with two counter dips at 460 nm and 530 nm, which could be due to the particular spectrum used for normalization, the same for all the reported curves.

Table 2 shows the parameters obtained from two dose–response curves, one obtained by washing in ethanol between successive standards and the other with water. The results are substantially similar.

The more relevant point is that the affinity constant of the sites revealed after extended washing is about two magnitude orders higher than that with rapid flushing with ethanol. As a consequence, the LOD was also much lower.

Evidently, only by this washing procedure, the 2-FAL molecules linked to the stronger interaction sites can be extracted.

4. Discussion and Conclusions

The spectra of the SPR-POF-MIP platforms in fluids with different refractive indices, such as air, water and oil, are characterized by the presence of multiple dips and even large bands, the general shape of which depends in part on the amount of polymer overlaying the gold resonant surface. Better-defined dips are obtained by the deposition of lower amounts of MIP; however, in this case, there is a larger effect of the RI of the overlaying medium, which is higher when the polymer layer is thinner. As a matter of fact, when dealing with samples with high RI, there is the possibility that the resonance wavelength exceeds the range of the detectable wavelength. However, it has been shown that this is not the case in the systems considered here, even when relatively thin MIP layers are deposited. The fact that in this kind of sensor better dips are obtained highly facilitates the evaluation of the peak position, i.e., the resonance wavelength. The thickness of the layer seems to have only a minor influence on the affinity of the MIP for 2-FAL and thus on the detection limit of the sensing device. An affinity constant of about 10^6 M^{-1} L is evaluated in the vegetable oil, near to that from water previously evaluated [14]. A large effect on the affinity is due to the washing procedure. An affinity constant about two orders of magnitude higher is found after extended cleaning, indicating that sites with higher affinity are made free.

Author Contributions: Conceptualization, M.P., N.C. and L.D.M.; Data curation, M.P. and L.D.M.; Formal analysis, M.P., N.C., L.Z. and L.D.M.; Investigation, M.P. and L.D.M.; Methodology, M.P., N.C., L.Z. and L.D.M.; Resources, M.P. and L.D.M.; Supervision, M.P., N.C. and L.D.M.; Validation, M.P. and L.D.M.; Writing—original draft, M.P., N.C., L.Z. and L.D.M.; Writing—review and editing, M.P., N.C. and L.D.M. All authors have read and agreed to the published version of the manuscript.

Funding: This research was funded by the Research Fund for the Italian Electrical System in compliance with the Decree of Minister of Economic Development 16 April 2018.

Institutional Review Board Statement: Not applicable.

Informed Consent Statement: Not applicable.

Data Availability Statement: The data are available on reasonable request from the corresponding author.

Acknowledgments: Authors acknowledge F. Scatiggio and G. Campi from A&A Fratelli Parodi S.p.A for providing the vegetable oil samples.

Conflicts of Interest: The authors declare no conflict of interest.

References

- Hoffmann, M.W.; Wildermuth, S.S.; Gitzel, R.; Boyaci, A.; Gebhardt, J.; Kaul, H.; Amihai, I.; Forg, B.; Suriyah, M.M. Integration of novel sensors and machine learning for predictive maintenance in medium voltage switchgear to enable the energy and mobility revolutions. *Sensors* **2020**, *20*, 2099. [[CrossRef](#)] [[PubMed](#)]
- Lopez, P.; Mabe, J.; Miró, G.; Etxeberría, L. Low cost photonic sensor for in-line oil quality monitoring: Methodological development process towards uncertainty mitigation. *Sensors* **2018**, *18*, 2015. [[CrossRef](#)] [[PubMed](#)]
- Lundgaard, L.E.; Hansen, W.; Linhjell, D.; Painter, T.J. Aging of oil-impregnated paper in power transformers. *IEEE Trans. Power Deliv.* **2004**, *19*, 230–239. [[CrossRef](#)]

4. N'cho, J.S.; Fofana, I.; Hadjadj, Y.; Beroual, A. Review of physicochemical-based diagnostic techniques for assessing insulation condition in aged transformers. *Energies* **2016**, *9*, 367. [\[CrossRef\]](#)
5. N'cho, J.S.; Fofana, I. Review of fiber optic based diagnostic techniques used in power transformers. *Energies* **2020**, *13*, 1789. [\[CrossRef\]](#)
6. Leung, A.; Shankar, P.M.; Mutharasan, R. A review of fiber-optic biosensors. *Sens. Actuators B Chem.* **2007**, *125*, 688–703. [\[CrossRef\]](#)
7. Gupta, B.D.; Verma, R.K. Surface plasmon resonance-based fiber optic sensors: Principle, probe designs, and some applications. *J. Sens.* **2009**, *2009*, 1–12. [\[CrossRef\]](#)
8. Caucheteur, C.; Guo, T.; Albert, J. Review of plasmonic fiber optic biochemical sensors: Improving the limit of detection. *Anal. Bioanal. Chem.* **2015**, *407*, 3883–3897. [\[CrossRef\]](#)
9. Wang, X.D.; Wolfbeis, O.S. Fiber-optic chemical sensors and biosensors (2008–2012). *Anal. Chem.* **2013**, *85*, 487–508. [\[CrossRef\]](#)
10. Wang, X.D.; Wolfbeis, O.S. Fiber-optic chemical sensors and biosensors (2013–2015). *Anal. Chem.* **2016**, *88*, 203–227. [\[CrossRef\]](#) [\[PubMed\]](#)
11. Cennamo, N.; Pesavento, M.; Zeni, L. A review on simple and highly sensitive plastic optical fiber probes for bio-chemical sensing. *Sens. Actuators B Chem.* **2021**, *331*, 129393. [\[CrossRef\]](#)
12. Cennamo, N.; D'Agostino, G.; Galatus, R.; Bibbò, L.; Pesavento, M.; Zeni, L. Sensors based on surface plasmon resonance in a plastic optical fiber for the detection of trinitrotoluene. *Sens. Actuators B Chem.* **2013**, *188*, 221–226. [\[CrossRef\]](#)
13. Cennamo, N.; D'Agostino, G.; Pesavento, M.; Zeni, L. High selectivity and sensitivity sensor based on MIP and SPR in tapered plastic optical fibers for the detection of L-nicotine. *Sens. Actuators B Chem.* **2014**, *191*, 529–536. [\[CrossRef\]](#)
14. Pesavento, M.; Zeni, L.; De Maria, L.; Alberti, G.; Cennamo, N. SPR-optical fiber-molecularly imprinted polymer sensor for the detection of furfural in wine. *Biosensors* **2021**, *11*, 72. [\[CrossRef\]](#) [\[PubMed\]](#)
15. Cennamo, N.; De Maria, L.; Chemelli, C.; Profumo, A.; Zeni, L.; Pesavento, M. Markers detection in transformer oil by plasmonic chemical sensor system based on POF and MIPs. *IEEE Sens. J.* **2016**, *16*, 7663–7670. [\[CrossRef\]](#)
16. Trouillet, A.; Ronot-Trioli, C.; Veillas, C.; Gagnaire, H. Chemical sensing by surface plasmon resonance in a multimode optical fibre. *Pure Applied Opt.* **1996**, *5*, 227–237. [\[CrossRef\]](#)
17. Cennamo, N.; Massarotti, D.; Conte, L.; Zeni, L. Low cost sensors based on SPR in a plastic optical fiber for biosensor implementation. *Sensors* **2011**, *11*, 11752–11760. [\[CrossRef\]](#) [\[PubMed\]](#)
18. Arshady, R.; Mosbach, K. Synthesis of substrate-selective polymers by host-guest polymerization. *Makromol. Chem.* **1981**, *182*, 687–692. [\[CrossRef\]](#)
19. Uzun, L.; Turner, A.P.F. Molecularly-imprinted polymer sensors: Realising their potential. *Biosens. Bioelectron.* **2016**, *76*, 131–144. [\[CrossRef\]](#) [\[PubMed\]](#)
20. Chen, L.; Wang, X.; Lu, W.; Wu, X.; Li, J. Molecular imprinting: Perspectives and applications. *Chem. Soc. Rev.* **2016**, *45*, 2137–2211. [\[CrossRef\]](#) [\[PubMed\]](#)

Article

Role of Functional Monomers upon the Properties of Bisphenol A Molecularly Imprinted Silica Films

Ana-Mihaela Gavrilă ¹, Ionuț-Cristian Radu ², Hermine Stroescu ³, Anamaria Zaharia ¹, Elena-Bianca Stoica ¹, Ana-Lorena Ciurlică ¹, Tanța-Verona Iordache ^{1,*} and Andrei Sârbu ^{1,*}

- ¹ Advanced Polymer Materials and Polymer Recycling Group, The National Institute for Research & Development in Chemistry and Petrochemistry ICECHIM, Splaiul Independenței no. 202, 060021 Bucharest, Romania; anamihaela.florea@gmail.com (A.-M.G.); anamaria.lungu1984@gmail.com (A.Z.); elena.bianca.georgescu@gmail.com (E.-B.S.); analorena11.ac@gmail.com (A.-L.C.)
- ² Advanced Polymer Materials Group, University Politehnica of Bucharest, 060042 Bucharest, Romania; radu.ionucristian@gmail.com
- ³ Institute of Physical-Chemistry “Ilie Murgulescu” of Romanian Academy, Surface Chemistry and Catalysis Laboratory, 060021 Bucharest, Romania; hermine25@yahoo.com
- * Correspondence: tanta-verona.iordache@icechim.ro (T.-V.I.); andr.sarbu@gmail.com (A.S.); Tel.: +4-0755-159-896 (T.-V.I.); +4-0724-237-351 (A.S.)

Abstract: In this study, two types of bisphenol A molecularly imprinted films (BPA-MIP) were successfully prepared via sol-gel derived methods using two different organosilane functional monomers N-(2-aminoethyl)-3-aminopropyltrimethoxysilane (DAMO-T) or (3-mercaptopropyl)trimethoxysilane (MPTES). The physical-chemical characterization of films, in terms of morphology, structure, thermal analysis, and optical features, suggested that thinner films with a homogenous porous structure were more likely to retain BPA molecules. The MIP films revealed the rapid and quantitative adsorption of BPA, registering the most specific binding in the first five minutes of contact with the BPA-MIP film. Silica films were effectively regenerated for further usage for at least five times, demonstrating their high stability and reusability. Even if the performance of films for BPA uptake dropped dramatically after the third adsorption/reconditioning cycle, this synthesis method for BPA-MIP films has proven to be a reliable and cheap way to prepare sensitive films with potential application for re-usable optical sensors.

Keywords: sol-gel; molecularly imprinted films; bisphenol A; organosilane monomer

Citation: Gavrilă, A.-M.; Radu, I.-C.; Stroescu, H.; Zaharia, A.; Stoica, E.-B.; Ciurlică, A.-L.; Iordache, T.-V.; Sârbu, A. Role of Functional Monomers upon the Properties of Bisphenol A Molecularly Imprinted Silica Films. *Appl. Sci.* **2021**, *11*, 2956. <https://doi.org/10.3390/app11072956>

Academic Editor: Raed Abu-Reziq

Received: 26 February 2021

Accepted: 24 March 2021

Published: 25 March 2021

Publisher’s Note: MDPI stays neutral with regard to jurisdictional claims in published maps and institutional affiliations.



Copyright: © 2021 by the authors. Licensee MDPI, Basel, Switzerland. This article is an open access article distributed under the terms and conditions of the Creative Commons Attribution (CC BY) license (<https://creativecommons.org/licenses/by/4.0/>).

1. Introduction

Bisphenol A (BPA) [2,2-bis (4-hydroxyphenyl)propane], an endocrine disruptor chemical (EDC), is known as the most widely used and toxic additive in the production of plastic together with polycarbonates, epoxy and polyester resins, and others (flame retardants, polyacrylate, polysulfone resins, polyetherimide). Many studies revealed that BPA leaches out from plastic products used for food packaging such as: plastic (baby) bottles, industrial supplies, dental sealant, medical devices, or sport equipment [1–4]. Despite the ongoing COVID-19 pandemic that has affected the sales of paints and coatings in 2020, the global volume consumption of BPA is growing dynamically and is estimated to reach more than ten million metric tons by 2022 [5]. In 2019, the European Commission decided to form a research cluster namely EURION to find novel testing and screening methods to identify EDC [6]. BPA is easily released into the atmosphere and the natural environment through direct discharge, landfill leachate, is and frequently found in food and water sources [7,8]. Long-term exposure to BPA alters endocrine function, causing many diseases as diabetes, obesity, cardiovascular diseases, chronic respiratory, thyroid and immune systems diseases, and even cancer [9–11]. Exposure to BPA occurs mostly via the oral route (approximately 90%) meaning dietary contamination and non-dietary sources such as sea water and cosmetics [12]. So far, several analytical methods have been established and

extensively used to measure BPA, from which gas chromatography–mass spectrometry (GC-MS), immunoassay detection, liquid chromatography–mass spectrometry (LC-MS), and spectrophotometric and optical sensors are frequently used [13]. Yet, most of these methods are expensive, with time-consuming manipulation steps, complicated instrumentation, highly skilled operators, and a large amount of chemicals. Notwithstanding the many available techniques, there is an urgent need to establish a simple, rapid, and low-cost method for monitoring BPA.

Ever since molecular recognition systems with artificial receptors have emerged, the attention of the research community for designing effective separation systems and chemical/sensors has increased significantly. Such molecular recognition systems, named molecularly imprinted polymers (MIPs) are prepared using the molecular imprinting (MI) technique. This is a versatile and inexpensive method to synthesize artificial polymers that mimic the behavior of natural receptors binding sites. The procedure usually involves the polymerization and crosslinking of functional monomers in the presence of a template molecule (that interacts with the polymer network via hydrogen, covalent, or ionic bonding interactions). After the removal of the template molecule, specific binding cavities toward the target molecules are left in the resulting polymers. Thus, the complementary molecular information of the template is transposed into the polymer, endowing the final material with specificity for this analyte but also with selectivity vs. other structural-resemblant analytes. Furthermore, the resulted MIPs are robust, exhibiting reusability, long-term stability and low production cost [14,15]. Using this MI technique and the various polymerization procedures, MIPs in different shapes and sizes were developed, e.g., pearls [16], particles [17,18], membranes [19–21], thin films [22,23], nanospheres/nanofibers [24,25], or electrochemical sensing receptors [13,17,26]. Nevertheless, depending on the polymerization procedure (for instance bulk polymerization [27]), MIPs can still present some inherent drawbacks, such as heterogeneous distribution of binding sites, low binding capacity, and poor site accessibility, which is why a great deal of attention should be focused on finding the proper procedure for delivering performant MIPs adequate for the targeted application. In this context, the preparation of MIPs for sensing applications was performed, in recent years, by combining MI with sol–gel techniques as an alternative approach to overcome these shortcomings [28,29]. The method is simple and implies deposition/casting of thin films on various surfaces (for example nanowires, nanotubes, glass, ceramic and plastic substrates).

Literature studies are minimal when it comes to BPA imprinting for obtaining MIP films via sol–gel methods. One of these studies include that of Huang et al. [30], who described the electrochemical deposition of imprinted sol–gel films with specific binding sites for BPA on a gold electrode. This work implied the use of expensive nanomaterials and the minimal characterization of the sol–gel film hampers the assessment of efficiency. A recent study of Yang and Park [31] used the surface-initiated atom transfer radical polymerization (SI-ATRP) for the synthesis of BPA-imprinted poly(4-vinyl pyridine-co-ethylene glycol dimethacrylate) films on a specific surface of silica inverse opal-formed quartz crystals (QCs). It is also worth mentioning the paper of Ardekani et al., who prepared molecularly imprinted nanofibers based on 3-aminopropyltriethoxysilane (APTES) as functional monomer and nylon 6 as the matrix, using the sol–gel and the electrospinning techniques, which can absorb BPA in water samples [32]. Another valuable study of Kalogiouri and co-workers [33] reported the use of APTES and phenyl triethoxysilane to prepare imprinted sol–gel sorbents for the BPA removal from moat waters and tap water. Although the MIP sorbent can be used up to ten times, the extraction protocol involves numerous steps and materials.

With regard to the recent literature, the present study provides a simpler and more reproducible procedure to prepare BPA-MIPs, with the use of MI and sol–gel derived techniques. The methodology is original and consisted of casting the BPA-MIP layer on top of previously degreased glass support. According to the present literature, this combined procedure of BPA imprinting has never been used to prepare MIP films.

Thereby, the aim of this work was to prepare and characterize two types of BPA-MIP films, based on two different organosilane monomers, meaning N-(2-aminoethyl)-3-aminopropyltrimethoxysilane (DAMO-T) and (3-mercaptopropyl)trimethoxysilane (MPTES). The films BPA-MIP_{DAMOT} and BPA-MIP_{MPTES} were obtained by spraying the sol-gel precursor solutions directly on previously degreased glass slides. The proposed sol-gel approach for BPA-MIP preparation seemed to be suitable due to the low temperature processing conditions (for polycondensation at 25 °C and for the maturation of films at 60 °C). The prepared BPA-MIP films were well characterized by Fourier-Transform Infrared spectroscopy (FTIR), Scanning Electron Microscopy (SEM), and Atomic Force Microscopy (AFM), as well as thermogravimetric analysis (TGA). The optical behavior of films was investigated by ellipsometry, to establish the imprinting effect over the final properties of the obtained BPA-MIPs. The BPA-MIP films were further tested in terms of rebinding measurements in liquid state via spectrophotometric techniques, to assess their potential as sensing elements for optic sensors. The reusability and stability of the sol-gel films were also discussed.

2. Experimental Section

2.1. Materials

The functional organosilane monomers N-(2-aminoethyl)-3-aminopropyltrimethoxysilane (DAMO-T, 98%), (3-Mercaptopropyl) trimethoxysilane (MPTES, 98 %), tetraethoxysilane (TEOS, 98 %), and the template Bisphenol A (BPA, 99%) were all purchased from Sigma-Aldrich Co. (St. Louis, MO, USA). Ammonium hydroxide (NH₄OH, 25 %) as catalyst and other solvents like acetic acid (AcA), obtained from Chimopar (Bucharest, Romania) were used as received. Ethanol (EtOH, 99.6%) was supplied by Fisher Scientific (Schwerte, Germany). The organic solvents used were analytical grade. Distilled water obtained from our laboratory purification system was used to prepare all aqueous solutions. The glass supports were obtained from Sigma-Aldrich Co. (St. Louis, MO, USA).

2.2. Instruments and Characterization

All measurements were performed at room temperature (RT considered 25 °C). The prepared BPA-MIP and NIP films were analyzed morpho-structurally and thermally using various equipment and techniques. Fourier Transform Infrared Spectroscopy (FTIR) of films was performed on Bruker Tensor 37 (ATR) in 400–4000 cm^{−1} domain, a resolution of 4 cm^{−1} and 16 scans. Thermogravimetric analysis (TGA) was carried out under nitrogen atmosphere at a 10 °C/min heating rate with TA Q2000 IR Instrument with auto-sampler. The thermal stability of sol-gel films was investigated in order to underline the effect of imprinting upon the organosilica materials, as complementary results to FTIR measurements. Estimation of films thickness was made by ellipsometry with UV-VIS-NIR Ellipsometer VASE[®] model (J.A. Woollam Co, Inc., Lincoln, NE, USA), in the 300–1000 nm wavelength range at 70 °AOI with a 2 nm wavelength step and 20 scans/measurement (microspot). It is relevant to note that a translucent scotch tape was fixed on the glass slides back in order to prevent the effect of ‘backside reflection’. The surface morphology of the films deposited on glass slides was investigated with an Environmental Scanning Electron Microscope (ESEM) FEI Quanta 200 from Philips, equipped with gaseous secondary electron detector (GSED). Topography was performed by Atomic Force Microscopy using XE 100 instrument from Park Systems, in non-contact tapping mode at resonance frequency of Z-scanner: 5 kHz. All AFM measurements were recorded using silicon tips with a scan range of XY-scanner of (max) 50 µm, and a working distance of Z-scanner: 12 µm. The AFM images were elaborated with the XEI program (v 1.8.0—Park Systems) for exhibiting roughness evaluation. The UV-2501-PC spectrometer (Shimadzu Co., Tokyo, Japan) was used to perform the BPA batch re-binding experiments and the washing procedures for BPA removal in the 200–1000 nm wavelength range, with a 10 mm quartz cuvette.

2.3. Synthesis of Bisphenol A-Molecularly Imprinted Polymer (BPA-MIP) Films

Two types of BPA-imprinted organosilica films (i.e., BPA-MIP_{MP TES} and BPA-MIP_{DAMOT}) were successfully prepared by directly spraying the precursor solutions on glass supports, according to a similar one-step procedure described by our group, with slight modifications [34]. In a typical batch for BPA-MIP preparation, two solutions were prepared separately at room temperature (RT considered 25 °C), the catalyst and the precursor solution. The catalyst consisted of an aqueous solution of 25% ammonia hydroxide (0.565 mL NH₄OH/0.225 mL H₂O). The precursor solution was prepared by dissolving the functional monomer DAMO-T or MP TES and the template BPA in 1 mL of ethanol under stirring (molar ratio monomer: BPA = 10:1). After stirring for 30 min at 200 rpm, in the precursor solution containing DAMO-T a structural monomer (0.13 mL TEOS) was also added to ensure the adhesion to the glass support. The precursor monomer solution was magnetically stirred for 1 h after which it was gradually added in the catalytic medium and mechanically stirred at 200 rpm, for 2 h (sol-gel time, *t*_{sg}), when the partial hydrolysis reaction occurs, generating sols. The resulted solution was applied by directly spraying it onto cleaned glass supports to form crosslinked networks by alcohol/aldol polycondensation of sols. The obtained films were matured for 48 h at 25 °C (until complete polycondensation), followed by curing for 48 h at 60 °C in an oven.

The cured films were then washed two times according to the following procedure: step 1—washing with ethanol, for 8 h at room temperature, for removing unreacted monomers and step 2—extraction of BPA molecules with ethanol-acetic acid (9:1, *v/v*) for 4 h assisted by ultrasound (at 35 kHz frequency). As shown in Figure S1, a rigorous control of the supernatant solutions was performed by UV-Visible spectroscopy in order to assess the efficiency of the washing/extraction procedures. It can be observed in the second washing/extraction cycle that BPA was successfully extracted from the imprinted films (as confirmed by the absence of specific absorption peaks of BPA). Afterward, all films were dried at 60 °C overnight until constant weight and stored in dried conditions until use. By contrast, non-imprinted control films (noted by analogy NIP) were synthesized, conditioned, and washed respecting the same procedures as for the MIPs; the only difference was the absence of BPA from the synthesis.

2.4. Batch Binding Measurements and Regeneration of BPA Films

Binding experiments were performed to investigate the specificity of MIP films by measuring the adsorbed amount of BPA onto MIPs and NIPs. The binding tests referred to contacting the MIP and NIP films with 35 mL BPA solution of a known concentration (experiments conducted in batch conditions in duplicate) and measuring the initial and the final concentration of BPA. Due to BPA poor solubility in water, organic solvent-based assays were employed. The UV-visible absorption spectrum of bisphenol A in ethanol is given in Figure S2. The specific wavelengths of bisphenol A were registered at 229 nm and 278 nm. Since the value at 229 nm is susceptible to the influence of the solvent, the quantification of BPA was performed against the value at 278 nm as characteristic wavelength for BPA adsorption [35]. Thus, the calibration of BPA at $\lambda = 278$ nm was obtained in ethanol using a series of standard solutions containing BPA in the 0.2–0.008 g/L concentration range. The concentration of BPA was found to have a good linear relationship with $r^2 = 0.997$ (according to Figure S3). Herein, the concentration limits chosen for the study, meaning 0.008 and 0.2 g/L, represented the lowest and the highest quantity of BPA that can be detected by UV.

The kinetic of BPA rebinding was studied in the first 120 min of contact with 0.2 g/L BPA solution in ethanol. Afterward, using various concentrations of BPA (i.e., 0.2, 0.15, 0.1, and 0.08 g BPA/L in ethanol), the adsorbed amount of BPA was measured after a period of only 5 min, considered proper for specificity.

The reusability of the BPA-MIPs and NIPs deposited on glass slides was also investigated by using the same batch of films through the adsorption-desorption studies in five consecutive cycles.

The re-binding capacities, Q (mg BPA g^{-1} polymer film), of BPA-MIP and NIP films were calculated using Equation (1); where $C_{N,i}$ (g/L) and $C_{N,f}$ (g/L) are the initial and final concentration of BPA in the feed solution, m_p (mg) the films weight ($m_p = 40 \pm 1$ mg) and V_s (L) is the volume of the feed solution (i.e., 35 mL).

$$Q = \frac{(C_{N,i} - C_{N,f}) \cdot V_s}{m_p} \quad (1)$$

Imprinting factors, F , expressed by Equation (2), quantified the specificity with which BPA-MIP films re-bind BPA, compared to their corresponding NIPs, where Q_{MIP} and Q_{NIP} are the re-binding capacities of BPA-MIP and NIP, respectively.

$$F = \frac{Q_{MIP}}{Q_{NIP}} \quad (2)$$

3. Results and Discussion

3.1. Preparation of the BPA-MIP Films

This work was aimed at obtaining BPA-MIP films having two different organosilane functional monomers i.e., DAMO-T and MPTES. It is worth to mention that sol-gel hybrid films have attracted attention due to their efficient immobilization on various substrates, their enhanced stability and, in this case, easy access to the recognition cavities thus created. In this respect, the MPTES organosilane monomer was chosen for its adhesive properties and the ability to interact with the template, whereas DAMO-T monomer was expected to create stronger interactions with the template due to its diamino functionalities. For the later formulation, the adhesive properties to the substrate were compensated by addition of TEOS. Furthermore, the preparation method of films via sol-gel was very simple, quick, and did not require expensive chemicals or instrumentation.

The synthesis recipes for the precursor solutions used to obtain BPA-MIP and NIP films are given in Table 1. Previously reported results showed that aromatic templates are difficult to extract from MIP films with over 4–5 μm thickness and thinner films under 100 nm detach from the glass slide after multiple washing procedures [21]. Therefore, the monomer(s)/solvent/catalyst ratios were similar to the ones reported previously.

Table 1. The synthesis recipes for control NIP and BPA-MIP films.

Notation	DAMO-T (mmoles)	MPTES (mmoles)	TEOS (mmoles)	BPA (mmoles)
BPA-MIP _{MPTES}	0	0.364	0	0.0364
NIP _{MPTES}	0	0.364	0	0
BPA-MIP _{DAMOT}	0.364	0	0.0058	0.0364
NIP _{DAMOT}	0.364	0	0.0058	0

The schematic representation for BPA imprinting in sol-gel films and deposition on glass substrates is given in Figure 1. An alkaline solution (1 N NaOH) was used to clean the surface of the glass substrates before film casting. The cleaning per glass slide was carried out in triplicate by immersing it in 10 mL of alkaline solution for 30 min. Finally, it was dried in a vacuum oven at 60 °C for 2 h. Herein, monolayers of polymeric films were prepared by spraying the obtained precursor solutions directly on cleaned glass substrates. In the first step, following the MI principle, a polymerizable complex between the organosilane precursors DAMO-T or MPTES and BPA molecules is formed in ethanol and, further on, a partial hydrolysis of this assembly takes place in basic medium (NH_4OH , H_2O) [22]. The second step consists of sols formation [34]. Non-hydrolyzed and partially hydrolyzed DAMO-T/MPTES-BPA molecules undergo a polycondensation reaction to form cross-linked and homogeneous tridimensional networks in the third step [14,36]. After

a suitable maturation/curing protocol [28], the hybrid MIP films were washed several times and BPA was properly extracted with the formation of specific imprints.

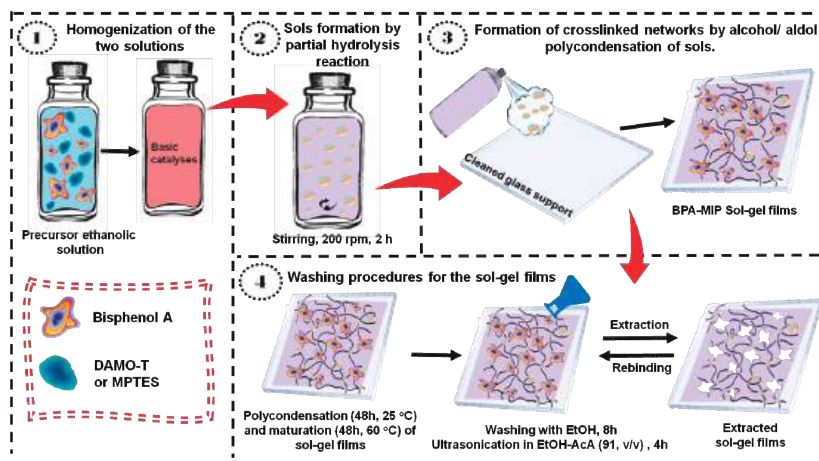


Figure 1. Steps undertaken for the preparation of the BPA-MIPs films.

3.2. Structure of BPA-MIP and NIP Films

FTIR spectroscopy was used to characterize the films and specifically to prove the presence of BPA molecules upon the organosilica matrix. In Figure 2a,b, FTIR spectra of imprinted sol-gel films BPA-MIP_{MPTES} and BPA-MIP_{DAMOT} and non-imprinted homologues NIP_{MPTES} and NIP_{DAMOT}, respectively, were compared with the spectrum of BPA template molecule. FTIR analysis of BPA-MIP and NIP films presented some similarities and showed the main characteristic polymeric bands.

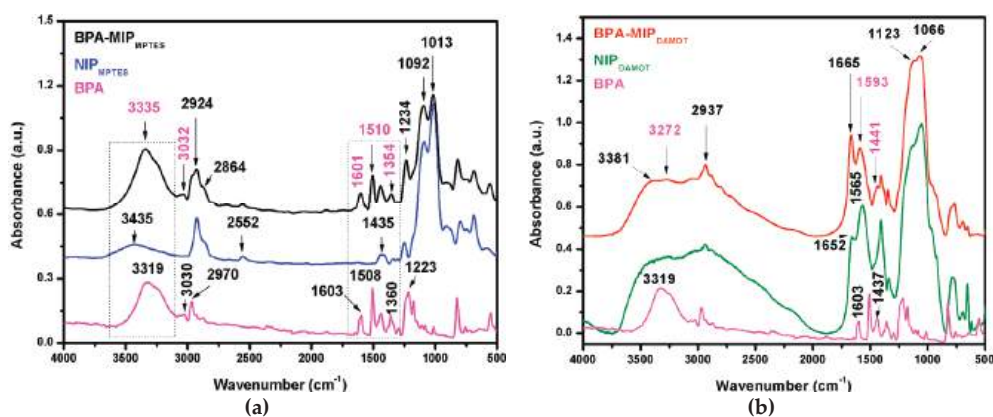


Figure 2. FTIR spectra (KBr pellets) of (a) BPA-MIP_{MPTES} and corresponding NIP_{MPTES} and (b) BPA-MIP_{DAMOT} and its control NIP_{DAMOT} sol-gel films, compared to the spectrum of BPA.

The stretching vibrations characteristic to the organic functionalities of the two monomers, ν_{CH_2} and ν_{CH} , recorded in the 2950–2920 cm^{-1} and 650–680 cm^{-1} region were observed in the spectra of all films. Distinctive bands of the organosilica backbone network (i.e., Si–O–Si, Si–OH and Si–O stretching vibrations) were identified in all the spectra of films in the 1250–850 cm^{-1} spectral range (bands overlapping in the spectra of

BPA-MIPs and NIPs). For MPTES-based films (Figure 2a), the band at 2552 cm^{-1} revealed the presence of mercapto group (-SH) in the organosilica matrix. In addition to mercapto band, other characteristic bands in the BPA-MIP_{MPTES} spectrum were distinguished as follows: the bands of the methoxy groups, asymmetric ν_{asym} (Si-OCH₃) and symmetric ν_{sym} (Si-OCH₃) stretching vibrations at 2924 and 2864 cm^{-1} . In Figure 2b, spectra of films with DAMO-T, some of the characteristic bands of N-H bonds from DAMO-T were spotted at 3381 cm^{-1} ($\nu_{\text{N-H}}$) and the bending vibrations at 1652 cm^{-1} ($\delta_{\text{N-H}}$). The results indicate that the organosilica functional monomers were quantitatively incorporated into the hybrid crosslinked networks by alcohol/aldol polycondensation of DAMO-T or MPTES.

In the spectrum of BPA (Figure 2a,b), we can distinguish the characteristic band of the aromatic ring $\nu_{\text{C}=\text{C}}$ (Ar-C=C) recorded at 1603 cm^{-1} and bands recorded at 1508 , 1437 , and 1360 cm^{-1} assigned to the C-H bending. The stretching vibrations from 3319 cm^{-1} (very intense band) and $2970/3030\text{ cm}^{-1}$ were assigned to the ν_{OH} (Ar-OH) and $\nu_{\text{-CH}_3}$ (C-CH₃) bonds, respectively. The band recorded at 1223 cm^{-1} is due to C-O stretching. Figure 2a also revealed the characteristic bands of BPA in the spectrum of BPA-MIP_{MPTES} film, meaning the aromatic rings vibration at 1601 cm^{-1} , the bands for C-H bending at 1510 cm^{-1} , 1437 , and 1354 cm^{-1} and the stretching of C-O bonds given by the spiked intensity of the band at 1234 cm^{-1} , indicating that BPA molecules were successfully imprinted in the matrix [37,38]. For BPA-MIP_{DAMOT}, Figure 2b, these bands overlap with those of DAMO-T. Yet, a hint to BPA imprinting was given by the significant shifting of bands from 1652 and 1565 cm^{-1} (in the spectrum of NIP) to 1665 and 1593 cm^{-1} (in the spectrum of BPA-MIP_{DAMOT}) and the presence of a band assigned to C-H bending at 1441 cm^{-1} .

The bands at 3335 cm^{-1} (sharp band) and 3032 cm^{-1} in BPA-MIP_{MPTES} and 3272 cm^{-1} (wide band) in BPA-MIP_{DAMOT} spectra were attributed to the stretching and bending mode of O-H groups from BPA implied in the monomer-template interactions through hydrogen bonding. When comparing the spectra of the two imprinted films, it is important to point out that a more visible imprinting effect was highlighted for BPA-MIP_{MPTES} (as compared to BPA-MIP_{DAMOT}).

3.3. Morphology of BPA-MIP and NIP Films

The surface morphology evaluation of prepared sol-gel films was firstly explored by scanning electron microscopy (SEM, Figure 3) and, afterwards, with atomic force microscopy (AFM, Figure 4). The SEM images of BPA-MIP_{MPTES} and BPA-MIP_{DAMOT} and their corresponding NIP_{MPTES} and NIP_{DAMOT}, respectively, are presented in Figure 3, where significant changes of surface morphology can be noticed. The micrographs of BPA-MIPs and NIPs films clearly indicated morphological differences even though the main network is chemically resemblant (Si-O-Si).

Comparing the morphology of the NIPs with that of BPA-MIPs, the difference was striking. NIP films presented smoother surfaces with little visible asperities or pores, ascribed to the absence of imprinted sites. An overview at lower scales revealed an aggregated structure of the NIP_{MPTES} film (Figure 3b) with rather large gaps instead of pores. Interestingly, BPA-MIP_{MPTES} exhibited a dense structure of pores consisting of aggregated sols, in which case it can be due to the presence of monomer-template assemblies that clearly influenced the growth mode of the entire sol-gel network (Figure 3a). This porous structure of BPA-MIP_{MPTES} films is very beneficial for the mass transfer, BPA re-binding, and may lead to shorter periods for equilibrium adsorption [39]. For BPA-MIP_{DAMOT} films, an interesting, elongated structure (like pine branches) was observed in Figure 3c, unveiling again the result of a preferential arrangement and growth of the network in the presence of monomer-template assemblies. Unlike BPA-MIP_{MPTES}, the surface of BPA-MIP_{DAMOT} seemed to be more compact, which may be caused by the addition of TEOS that conferred rigidity to the whole structure.

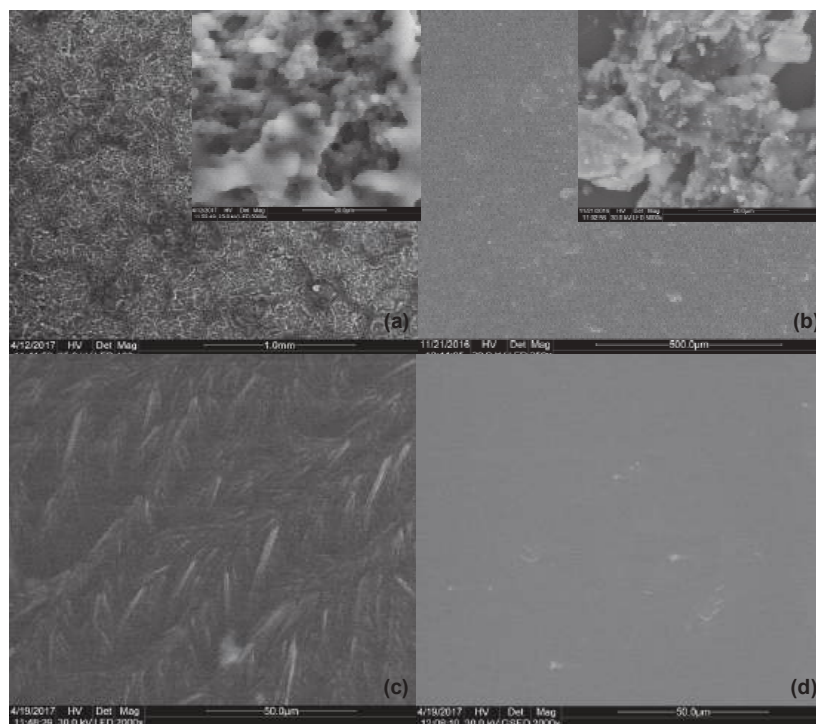


Figure 3. Surface SEM micrographs of both sets of sol-gel films, at different magnitude levels: (a) BPA-MIP_{MPTES} and (b) NIP_{MPTES} at 1mm/500 μm scale with 20 μm insets (c) BPA-MIP_{DAMOT} and (d) NIP_{DAMOT} at 50 μm .

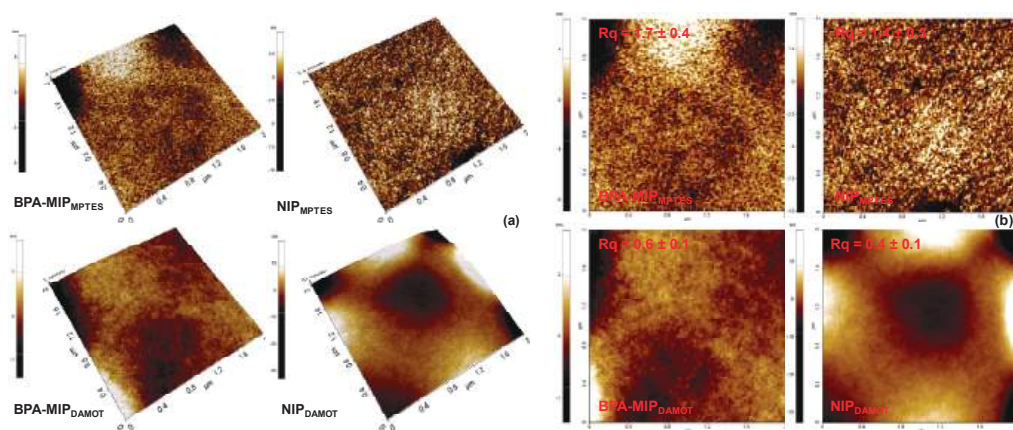


Figure 4. 3D (a) and 2D (b) topography images by atomic force microscopy (AFM) of the surface of BPA-MIP_{MPTES}/BPA-MIP_{DAMOT} films, compared to control NIPs, scan area of $2 \times 2 \mu\text{m}$; RMSR values included on each AFM image (in red).

The topography and roughness of both BPA-MIP films and their corresponding NIPs were investigated by AFM (Figure 4), as well. The surface roughness of the sol-gel films was evaluated using the root-mean-square roughness (RMSR) function of XEI AFM software.

As shown in Figure 4b, five different topographic images were chosen to calculate the arithmetic average leading to the RMSR results. The AFM images of NIPs and BPA-MIP films emphasized again the changes that occur in surface topography due to the presence of monomer-template assemblies. In agreement with the SEM analysis, the 3D images of the BPA-MIP_{MPTES}/NIP_{MPTES} films (Figure 4a) pair displayed a fully different porous architecture compared to the flatter and smoother surface of the other pair, BPA-MIP_{DAMOT}/NIP_{DAMOT} (Figure 4a). Compared to SEM, the AFM footage revealed a very dense porous structure for the BPA-MIP_{DAMOT} film, as well. Yet, in this case the pore sizes are much smaller than the ones observed on the surface of BPA-MIP_{MPTES}, which may lead to a slow diffusion of BPA during rebinding trials and low binding efficiency [40]. The presence of BPA led to higher surface roughness values for BPA-MIP_{MPTES} and BPA-MIP_{DAMOT} (with a RMSR of 1.7 nm and 0.6 nm, respectively) compared to those of the corresponding NIPs (1.4 nm and 0.4 nm, respectively). The differences of RMSR values can be explained by the presence of template molecules that exert a steric effect during the growth of the sol-gel network. Meaning, the physical volume occupied by the template molecules, which translates later into imprinted cavities, is responsible for the formation of small gaps between the neighboring SiO₂ chains.

Thereby, from the morphological analysis, one conclusion may be drawn with regard to the type of organosilane monomer (or better yet the organic functionalities of the monomer), i.e., the nature of the functionalities influenced the films morphology and the growth pattern of the sol-gel network.

3.4. Thermal Stability of BPA-MIP and NIP Films

Thermogravimetric analysis, performed under nitrogen gas at a 10 °C/min heating rate, indicated similar decomposition trends for the two types of sol-gel films (Figure 5). The thermal degradations of BPA-MIP_{DAMOT} and BPA-MIP_{MPTES} and their non-imprinted NIP_{DAMOT} and NIP_{MPTES} revealed that all films were thermally stable. Three main degradation steps were observed for all the samples. For DAMO-T-based films, a higher mass loss was observed between 50 and 150 °C and it was attributed to the evaporation of intrinsic water, hence confirming the FTIR spectroscopy results where significant amount of water was retained in the structure of DAMO-T-based film.

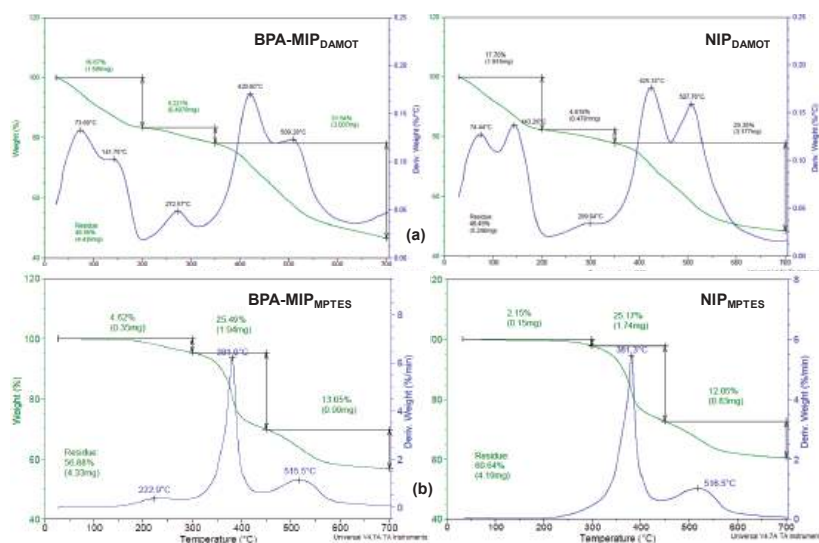


Figure 5. Thermogravimetric curves (TG) and their derivatives (DTG) for (a) BPA-MIP_{DAMOT} and NIP_{DAMOT} (b) BPA-MIP_{MPTES} and NIP_{MPTES} films.

The first degradation step was recorded in the 200–300 °C temperature range, with maximums registered at 273 °C and 223 °C for BPA-MIP_{DAMOT} and BPA-MIP_{MPTES}, respectively, and attributed to BPA degradation according to the thermogram of BPA provided in Figure S4 ($T_{max} = 268$ °C). The shift to lower or higher maximum decomposition temperatures is not unusual and this observation can help explain two interesting phenomena that may occur during imprinting in soft and rigid sol-gel networks [21,36,41]. For instance, in the case of BPA-MIP_{MPTES} films (Figure 5b), the low stability of BPA indicated that interactions between the template and the functional SH groups of the monomer, potentially weaken the (C-CH₃) bonds from BPA which led to the fragmentation of the molecule. On the other hand, the BPA imprinted in the BPA-MIP_{DAMOT} film (Figure 5a) degraded at higher temperatures due to the inherent rigidity of the sol-gel network, given by the addition of TEOS. It should also be mentioned that a small mass loss was also registered for the NIP based on DAMO-T in this same region and may be linked with the loss of amino fragments from DAMO-T.

The second degradation stage occurred between 300 and 500 °C and was generally attributed with the total degradation/fragmentation of the pendant groups (i.e., methyl/ethyl fragment types, amino-ethyl/methyl, mercaptopropyl). The degradation of the polymer backbone occurred in the last degradation step, between 500–800 °C, [34]. It should be underlined that for both BPA-MIPs the residues were up to 57 wt.% and slightly lower compared to their corresponding NIPs, up to 61 wt.%, confirming a similar behavior between them but also their good thermal stability considering their structural differences.

3.5. Optical Properties of BPA-MIP and NIP Films

The spectroscopic ellipsometry (SE) measurements were performed to highlight the effect of imprinting on the optical properties of films, in terms of refractive index and transmittance. The refractive index of the films was measured in the 200–1000 nm wavelength domain and the transmittance profiles were evaluated up to 900 nm spectral range, respectively, in different points of the films surface. In this respect, the Cauchy dispersion model was used for modelling the ellipsometric experimental data (Figures S5.1–S5.4, SM) which delivered reliable values for the films thickness and surface roughness.

The thickness and surface roughness for both prepared sets of films, summarized in Table 2, revealed major differences as function of the various employed monomers. For MP_{TES}-based films the thickness varied between 230 and 290 nm, while for the DAMO-T-based films was 10-fold higher. A similar trend was registered for the roughness, as well. The thickness and roughness discrepancy between the two types of films was attributed to the different growth mechanism of the organosilica matrix upon BPA addition and to the presence of TEOS, supporting the results attained in the morphological assessment.

Table 2. Data on films thickness (d_{layer}), roughness and mean square error (MSE) for thickness determined by ellipsometry.

Film	d_{layer} [nm]	Roughness [nm]	MSE
BPA-MIP _{DAMOT}	2897.58	0.62	0.49
NIP _{DAMOT}	3156.57	0.32	0.52
BPA-MIP _{MPTES}	237.36	1.31	0.46
NIP _{MPTES}	290.33	0.97	1.63

Figure 6 shows the refractive index, n , and the transmittance spectra of BPA-MIP_{DAMOT} and BPA-MIP_{MPTES} films against their corresponding NIPs. Pronounced modifications of the optical features (transmittance and refractive index) for both type of films were recorded particularly in the 300–550 nm wavelength region. The variance of refractive index and transmittance presented similar profiles for both MIP films, indicating the presence of BPA in both film structures. The refractive index (Figure 6a) showed great fluctuations for both types of films. For example, the n values registered for the MIP/NIP films with DAMO-T were affected by thickness and, thus, their whole profile is shifted towards higher n values

compared to the MIP/NIP pair with MP TES. However, the same trend is maintained between the imprinted and non-imprinted films suggesting that light travels faster through the non-imprinted material (as lower n values were registered in both cases compared to the ones of MIPs).

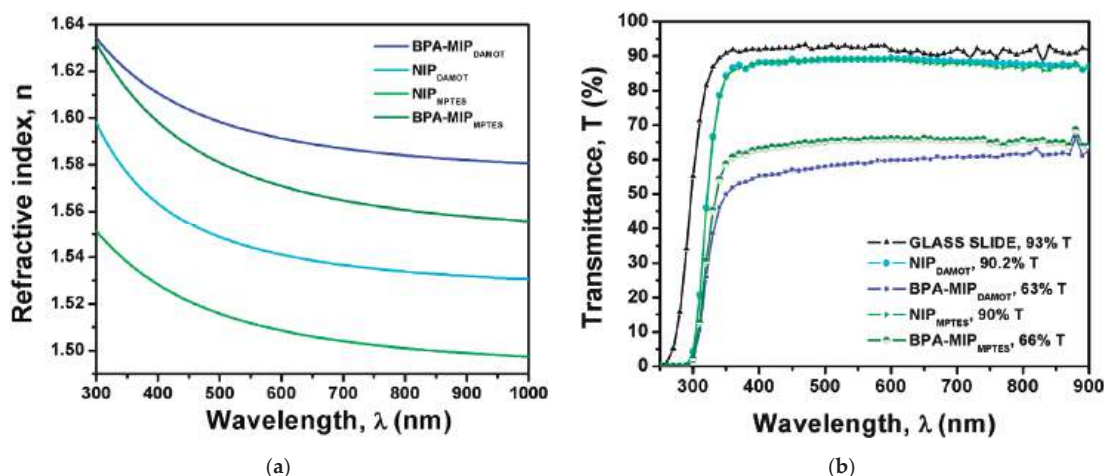


Figure 6. Optical properties of BPA-MIP films compared to their corresponding NIP in terms of (a) Refractive index, n , variation measured in the 200–1000 nm spectral range and (b) Measured transmittance spectra as a function of wavelength, in the 250–900 nm range.

In accordance with the refractive index, the transmittance profiles of the BPA-MIP films registered a drop of about 25% T compared to the NIPs (Figure 6b). This sudden decrease from 90% T to around 66% T was again attributed to the presence of BPA. Yet, the BPA-MIP_{DAMOT} film led to a more obvious decrease of transmittance as the film thickness is 10-fold higher than the one of BPA-MIP_{MP TES}.

Both the refractive index and transmittance profiles are consistent with the findings from previous studies [22,34]. These results strengthen the belief that ellipsometric data may better underline the effect of imprinting and the presence of the template when preparing thin and transparent MIP films. Hence, it can be used as a complementary method to characterize the optical features of MIP films and decide upon the potential of such films to be used as sensitive elements for building optical sensors. In addition, the small values of the roughness for the MP TES-based films obtained in this work are considered suitable for optical sensing applications [42].

3.6. Batch Rebinding of BPA on BPA-MIP and NIP Films

The rebinding studies of BPA consisted of adsorption kinetics analysis and isotherm batch adsorption assays, carried out for the two types of BPA-MIP films (i.e., BPA-MIP_{MP TES} and BPA-MIP_{DAMOT}) and their corresponding blank NIP_{MP TES} and NIP_{DAMOT} as references. The specificity for BPA uptake was assessed by calculating the adsorption capacities, Q (mg/g) and imprinting factors, F of films (Figure 7a,b). From this point of view, the quantification of bonded BPA was conducted indirectly by determining the un-bonded BPA from the supernatants at 278 nm (characteristic wavelength for BPA absorbance).

Figure 7a shows the adsorption kinetics of the two BPA-MIP films and their corresponding blank NIPs from a 0.20 g/L BPA solution. The adsorption capacity of all films increased rapidly in the first 20 min, especially for the BPA-MIP films. This trend was followed by a plateau after which the binding equilibrium (Q_e) was attained, at 60 min. The NIP films presented similar adsorption profiles over time compared to BPA-MIP films

and attained lower values for the adsorption capacity due to the lack of specific binding sites. More importantly, the imprinting factor (F) of BPA-MIP_{MPTES} (Figure 7b) was 3.03 in the first 5 min, indicating not only excellent imprinting of BPA but also the recommended time of contact for attaining the most specific adsorption of BPA.

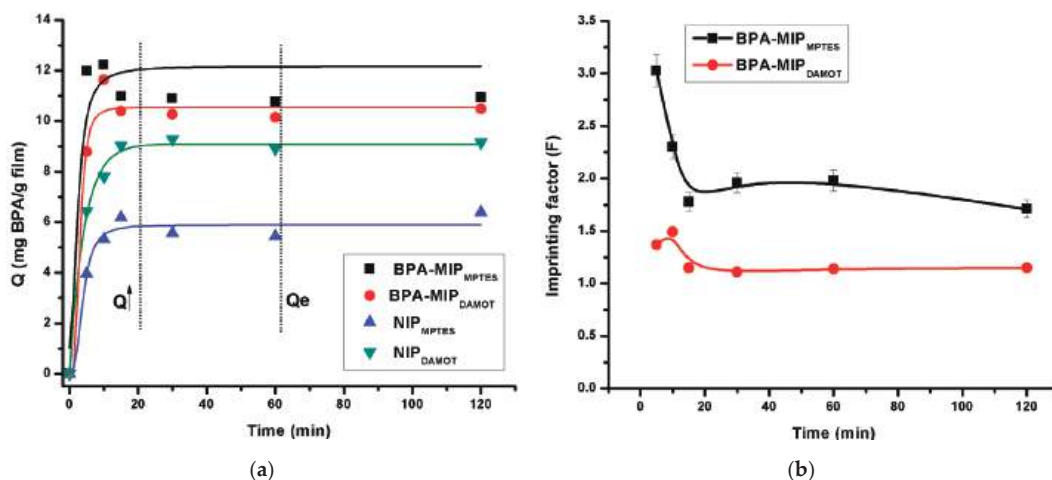


Figure 7. (a) Adsorption kinetic curves of BPA after contact with BPA-MIP films and their control NIP (variation of Q in mg of BPA per g of BPA-MIP/NIP films) and (b) Variation of imprinting factor (F) for both BPA-MIP films over time (5–120 min) from a BPA solution of 0.20 g/L).

As a result, the following isothermal adsorption of BPA in ethanol was determined after only 5 min of contact with the two types of films, in a concentration range varying from 0.08 to 0.2 g/L. As shown in Figure 8, the rebinding amounts of BPA increased gradually with the increasing BPA concentration. The rebinding of BPA, for both BPA-MIP films, exhibited an incremental increase of the adsorption capacity values [28]. As expected, the bonded amount of BPA to the MIP was higher than the one bonded to the NIP. Considering that the concentration of BPA feed solution (C_i) was varied between 0.08–0.20 g/L, the maximum adsorption capacity values were registered at 0.20 g/L, for both the BPA-MIP_{MPTES} and NIP_{MPTES} (Q_{max} 11.98 and 3.96 mg g^{−1}, respectively). This high difference in BPA binding affinity to the BPA-MIP and NIP clearly indicated the role of the imprinting in the formation of specific binding sites. Moreover, comparing the adsorption capacity values of the two imprinted films, it was observed that BPA-MIP_{DAMOT} registered a maximum adsorption capacity of 8.78 mg/g for the same BPA feed solution (C_i = 0.20 g/L). These results highlighted the impact of the film thickness and the discrete porous structure of BPA-MIP_{DAMOT} film upon the rebinding performance. Chang et al. [2] reported a maximum BPA adsorption of silica MIPs nanospheres of 444.6 μmol g^{−1} and Yang and Park [31] reported a Q_{max} of 170 mg g^{−1}. Hence, in this case, it seems like thinner films are more efficient for rebinding BPA and the maximum capacities are in good agreement with other reported values.

Considering that the best results were obtained for thinner BPA-MIP_{MPTES} films, it was expected to have better performances for NIP_{MPTES} vs. NIP_{DAMOT} films. Thereby, it seemed like the different growth mechanism of the organosilica matrix upon BPA addition somehow affected the following binding properties of BPA-MIP_{DAMOT} films as compared to the MIP/NIP system with MPTEs.

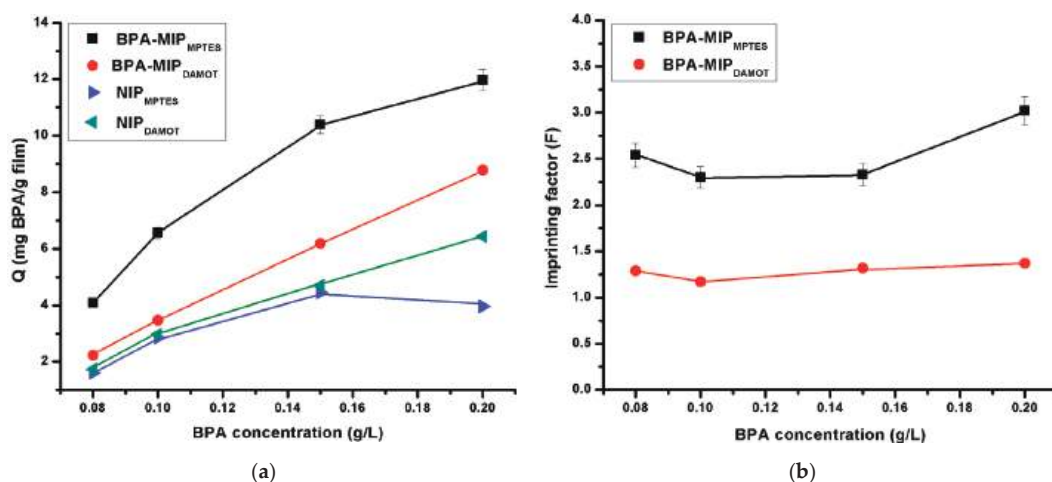


Figure 8. Variation of (a) binding capacity, Q , in mg of BPA per g of BPA-MIP/NIP films on BPA-MIP films and their control NIP, and (b) Imprinting factor (F) obtained by batch experiments after 5 min with various BPA feed solutions, C_i (0.08–0.2 g/L^{−1}).

Nevertheless, both imprinted films, BPA-MIP_{MPTES} and BPA-MIP_{DAMOT}, exhibited higher affinity for BPA than the corresponding non-imprinted films leading to the maximum imprinting factors of 3.03 and 1.37, respectively (Figure 8b). Therefore, it can be seen that BPA-MIP_{MPTES} films were more efficient for BPA recognition concluding that the imprinting effect was clearly distinguished by these preliminary batch rebinding tests. The higher values of the imprinting factor and of the binding capacity registered for BPA-MIP_{MPTES}, compared to BPA-MIP_{DAMOT} were in agreement with the conclusions drawn from the morpho-structural evaluation of films. According to other reported values for the imprinting factor, such as the one reported for nylon nanofibers (3.4 [32]) and the one reported by Yang and Park (2.15 [31]), the maximum F value of 3.03 found in this study is quite adequate.

3.7. Reusability and Stability of Films

The reusability and stability of the prepared BPA-MIP and NIP films were also evaluated. Reusability and, implicitly, stability are some of the most important features of MIPs due to the fact that are decisive factors for establishing the whole cost-effectiveness of the process. Thereby, in order to evaluate the performance at repeated use, the films were subjected to 5 reutilization cycles. As shown in Figure 9, all the films can be effectively regenerated for further usage with only around 35% loss of the initial rebinding capacity after three cycles, demonstrating high stability and reusability in BPA recognition. After the 4th cycle the binding capacity drops dramatically, up to 65% in the final cycle. Therefore, the BPA-MIP films proved to maintain their structure after several reuse. Yet, it is recommended to use the films only for 3 cycles as the specificity is also altered after the 4th and 5th cycles; the binding capacities of the NIP presented a much lower binding capacity loss. The relative standard deviation (RSD) value of 2.1% ascribed to the good repeatability of the films. It is relevant to mention that all the films were able to withstand the conditions for reconditioning and rebinding for at least five cycles without detaching from the glass support. In terms of long-term stability, the films were kept in dry conditions for several months at room temperature when not in use.

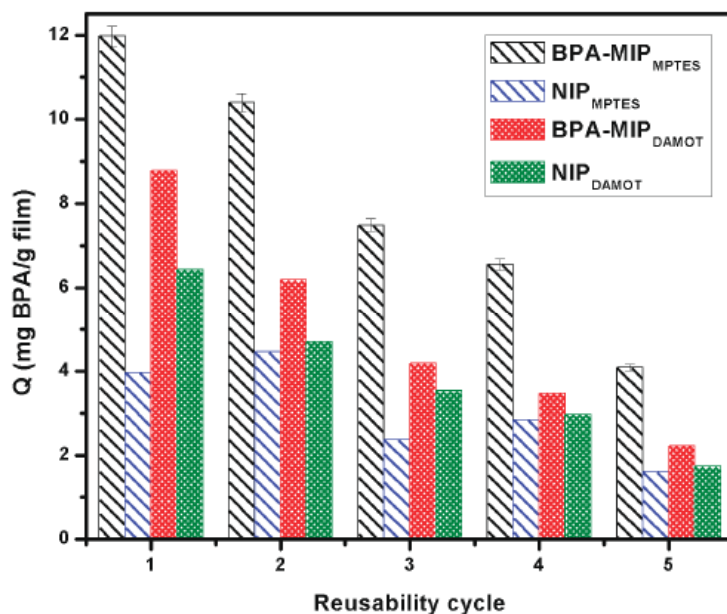


Figure 9. Reusability experiments of BPA-MIP and NIP films.

4. Conclusions

The study provides significant information regarding the role of functional monomers in the molecular imprinting process of BPA in silica networks. The two sets of BPA molecularly imprinted films (i.e., BPA-MIP_{DAMOT} and BPA-MIP_{MPTES}) were successfully prepared via sol-gel derived methods using N-(2-aminoethyl)-3-aminopropyltrimethoxysilane (DAMO-T) and (3-mercaptopropyl)trimethoxysilane (MPTES) as functional organosilane monomers.

Morpho-structural, thermal, and optical studies were undertaken to assess the influence of the monomers' functionalities upon the overall features of films but also to highlight the meaningful changes brought by the addition of BPA. Ellipsometry results suggested that there is much potential for application of such BPA-MIP films in optical sensing applications. An evaluation of specificity for BPA was conducted and the relevant results on adsorption capacities and imprinting factors for both types of films- were in agreement with their morpho-structural properties.

The overall results have shown that thinner films with better-defined porous morphology, meaning BPA-MIP_{MPTES} were more likely to retain BPA molecules. In this case, the most specific binding of BPA was registered in the first five minutes after contact ($F = 3.03$). BPA-MIP films were effectively regenerated for further usage 5 times and the adsorption capacity of films decreased only by 35% after three cycles, demonstrating high stability and reusability.

In order to ascertain the real application potential of the prepared sol-gel imprinted films for BPA detection, the next challenges will assume an investigation of the selective adsorption of BPA-MIP films using compounds with similar structure and application of the methodology for real samples contaminated with BPA. Considering that the BPA-MIPs films enable stability and reusability, the real-time response can be estimated in terms of quantification limit (LOQ) in the range of ng–µg in aqueous samples. Although further investigations are required, this work is a step forward to develop simple and cost-effective molecularly imprinted silica films for optical sensors.

Supplementary Materials: The following are available online at <https://www.mdpi.com/2076-3417/11/7/2956/s1>, Figure S1: The UV-visible absorption spectra after two steps of washing (1) 1st washing protocol with ethanol and (2) 2nd washing with ethanol-acetic acid (9:1, v/v) for imprinted BPA-MIP_{MPTES} and BPA-MIP_{DAMOT} and their non-imprinted NIP_{MPTES} and NIP_{DAMOT}; Figure S2. UV-visible absorption spectra of 1.5 µg/mL bisphenol A in ethanol; Figure S3. The calibration curve of BPA in ethanol solution; Figure S4. Thermogravimetric curve (TG) and its derivative (DTG) for BPA template; Figure S5. Fitting of the experimental ellipsometric data.

Author Contributions: Conceptualization of the paper by A.-M.G. and T.-V.I.; Methodology by A.-M.G., E.-B.S. and A.-L.C.; Formal analysis by A.-M.G., I.-C.R. and H.S.; Investigation by A.Z.; Writing of Original Draft was done by A.-M.G. and T.-V.I.; Writing—review and editing by T.-V.I.; Supervision by A.S.; Project administration by A.S., T.-V.I.; All authors have read and agreed to the published version of the manuscript.

Funding: This research was funded by Romanian Funding Agency UEFISCDI, through the support projects NUCLEU PN.19.23.02.01. and by the 255PED/2020.

Institutional Review Board Statement: Not applicable.

Informed Consent Statement: Not applicable.

Data Availability Statement: The data presented in this study are available in the article.

Conflicts of Interest: The authors declare no conflict of interest.

References

1. Ensafi, A.A.; Amini, M.; Rezaei, B. Molecularly imprinted electrochemical aptasensor for the attomolar detection of bisphenol A. *Microchim. Acta* **2018**, *185*, 265. [CrossRef] [PubMed]
2. Chang, T.; Yan, X.; Liu, S.; Liu, Y. Magnetic Dummy Template Silica Sol–Gel Molecularly Imprinted Polymer Nanospheres as Magnetic Solid-Phase Extraction Material for the Selective and Sensitive Determination of Bisphenol A in Plastic Bottled Beverages. *Food Anal. Methods* **2017**. [CrossRef]
3. Dermer, O.C. *Encyclopedia of Chemical Processing and Design*; McKelta, J.J., Weismantel, G.E., Dekker, M., Eds.; Publisher: New York, NY, USA, 1999; p. 406.
4. Rubin, B.S. Bisphenol A: An endocrine disruptor with widespread exposure and multiple effects. *J. Steroid Biochem. Mol. Biol.* **2011**, *127*, 27–34. [CrossRef] [PubMed]
5. Quinete, N.; Hauser-Davis, R.A. Drinking water pollutants may affect the immune system: Concerns regarding COVID-19 health effects. *Environ. Sci. Pollut. Res.* **2021**, *28*, 1235–1246. [CrossRef]
6. Available online: <http://eurion-cluster.eu> (accessed on 8 February 2021).
7. Corrales, J.; Kristofco, L.A.; Steele, W.B.; Yates, B.S.; Breed, C.S.; Williams, E.S.; Brooks, B.W. Global assessment of bisphenol A in the environment: Review and analysis of its occurrence and bioaccumulation. *Dose Response* **2015**, *13*, 1559325815598308. [CrossRef] [PubMed]
8. Zhang, C.; Li, Y.; Wang, C.; Niu, L.; Cai, W. Occurrence of endocrine disrupting compounds in aqueous environment and their bacterial degradation: A review. *Crit. Rev. Environ. Sci. Technol.* **2016**, *46*, 1–59. [CrossRef]
9. Leemans, M.; Couderq, S.; Demeneix, B.; Fini, J.-B. Pesticides with Potential Thyroid Hormone-Disrupting Effects: A Review of Recent Data. *Front. Endocrinol.* **2019**, *10*, 1. [CrossRef]
10. Rezg, R.; El-Fazaa, S.; Gharbi, N.; Mornagui, B. Bisphenol A and human chronic diseases: Current evidences, possible mechanisms, and future perspectives. *Environ. Int.* **2014**, *64*, 83–90. [CrossRef]
11. Ma, Y.; Liu, H.; Wu, J.; Yuan, L.; Wang, Y.; Du, X.; Wang, R.; Marwa, P.W.; Petlulu, P.; Chen, X. The adverse health effects of bisphenol A and related toxicity mechanisms. *Environ. Res.* **2019**, *176*, 108–575. [CrossRef]
12. Shehreen, A.; Md Saidur, R.; Myung-Geol, P. Role of Antioxidants in Alleviating Bisphenol A. *Biomolecules* **2020**, *10*, 1105. [CrossRef]
13. Ragavan, K.V.; Rastogi, N.K.; Thakur, M.S. Review-Sensors and biosensors for analysis of bisphenol-A. *Trends Anal. Chem.* **2013**, *52*, 248–260. [CrossRef]
14. Sarbu, A.; Iordache, T.V.; Florea, A.-M. Trends in the Molecular Imprinting of Small Molecules: Organic and Hybrid Polymers. In *Molecularly Imprinted Polymers (MIPs): Challenges*; Quinn, T., Ed.; NOVA Publishers, Publisher: New York, NY, USA, 2017; pp. 119–174.
15. Kupai, J.; Razali, M.; Buyuktyraki, S.; Kecili, R.; Szekely, G. Long-term stability and reusability of molecularly imprinted polymers. *Polym. Chem.* **2017**, *8*, 666–673. [CrossRef]
16. Florea, A.M.; Iordache, T.V.; Branger, C.; Ghiurea, M.; Avramescu, S.; Hubca, G.; Sarbu, A. An innovative approach to prepare hypericin molecularly imprinted pearls using a phyto-template. *Talanta* **2016**, *148*, 37–45. [CrossRef] [PubMed]
17. Mba, E.V.; Branger, C.; Bikanga, R.; Florea, A.M.; Istamboulie, G.; Calas-Blanchard, C.; Noguer, T.; Sarbu, A.; Brisset, H. Detection of Bisphenol A in aqueous medium by screen printed carbon electrodes incorporating electrochemical molecularly imprinted polymers. *Biosens. Bioelectron.* **2018**, *112*, 156–161.

18. Florea, A.M.; Iordache, T.V.; Branger, C.; Brisset, H.; Zaharia, A.; Radu, A.L.; Hubca, G.; Sarbu, A. One-step preparation of molecularly imprinted hollow beads for pseudohypericin separation from *Hypericum perforatum* L. Extracts. *Eur. Polym. J.* **2018**, *100*, 48–56. [\[CrossRef\]](#)
19. Lazau, C.; Iordache, T.V.; Florea, A.M.; Orha, C.; Bandas, C.; Radu, A.L.; Sarbu, A.; Rotariu, T. Towards developing an efficient sensitive element for trinitrotoluene detection: TiO₂ thin films functionalized with molecularly imprinted copolymer films. *Appl. Surf. Sci.* **2016**, *384*, 449–458. [\[CrossRef\]](#)
20. Yang, Q.; Wu, X.; Peng, H.; Fu, L.; Song, X.; Li, J.; Xiong, H.; Chen, L. Simultaneous phase-inversion and imprinting based sensor for highly sensitive and selective detection of bisphenol A. *Talanta* **2018**, *176*, 595–603. [\[CrossRef\]](#)
21. Stoica, E.-B.G.; Gavrilă, A.-M.F.; Iordache, T.-V.; Sarbu, A.; Iovu, H.; Sandu, T.; Brisset, H. Molecularly imprinted membranes obtained via wet phase inversion for ephedrine retention. *U. P. B. Sci. Bull.* **2020**, *82*, 2.
22. Gavrilă, A.-M.; Iordache, T.V.; Lazau, C.; Rotariu, T.; Cernica, I.; Stroescu, H.; Stoica, M.; Orha, C.; Bandas, C.E.; Sarbu, A. Biomimetic Sensitive Elements for 2,4,6-Trinitrotoluene Tested on Multi-Layered Sensors. *Coatings* **2020**, *10*, 273. [\[CrossRef\]](#)
23. Boysen, R.I.; Schwarz, L.J.; Nicolau, D.V.; Hearn, M.T. Molecularly imprinted polymer membranes and thin films for the separation and sensing of biomacromolecules. *J. Sep. Sci.* **2017**, *40*, 314–335. [\[CrossRef\]](#) [\[PubMed\]](#)
24. Rechichi, A.; Cristallini, C.; Vitale, U.; Ciardelli, G.; Barbani, N.; Vozzi, G.; Giusti, P. New biomedical devices with selective peptide recognition properties. Part 1: Characterization and cytotoxicity of molecularly imprinted polymers. *J. Cell. Mol. Med.* **2007**, *11*, 1367–1376. [\[CrossRef\]](#)
25. Criscenti, G.; De Maria, C.; Longoni, A.; van Blitterswijk, C.A.; Fernandes, H.A.M.; Vozzi, G.; Moroni, L. Soft-molecular imprinted electrospun scaffolds to mimic specific biological tissues. *Biofabrication* **2018**, *10*, 045005. [\[CrossRef\]](#)
26. Ait-Touchente, Z.; Sakhraoui, H.E.E.Y.; Fourati, N.; Zerrouki, C.; Maouche, N.; Yaakoubi, N.; Touzani, R.; Chehimi, M.M. High Performance Zinc Oxide Nanorod-Doped Ion Imprinted Polypyrrole for the Selective Electrosensing of Mercury II Ions. *Appl. Sci.* **2020**, *10*, 7010. [\[CrossRef\]](#)
27. Zhang, Z.; Li, L.; Wang, H.; Guo, L.; Zhai, Y.; Zhang, J.; Yang, Y.; Wang, H.; Yin, Z.; Yixia, L. Preparation of molecularly imprinted ordered mesoporous silica for rapid and selective separation of trace bisphenol A from water samples. *Appl. Surface Sci.* **2018**, *448*, 380–388. [\[CrossRef\]](#)
28. Gavrilă, A.M.; Zaharia, A.; Paruch, L.; Perrin, F.X.; Sarbu, A.; Olaru, A.G.; Paruch, A.M.; Iordache, T.V. Highly efficient materials working in tandem against pathogenic bacteria in wastewaters. *J. Hazard. Mater.* **2020**, *399*, 123026. [\[CrossRef\]](#)
29. Bakas, I.; Hayat, A.; Piletsky, S.; Piletska, E.; Chehimi, M.; Noguer, T.; Rouillon, R. Electrochemical impedimetric sensor based on molecularly imprinted polymers/sol-gel chemistry for methidathion organophosphorous insecticide recognition. *Talanta* **2014**, *130*, 294–298. [\[CrossRef\]](#)
30. Huang, J.; Zhang, X.; Lin, Q.; He, X.; Xing, X.; Huai, H.; Lian, W.; Zhu, H. Electrochemical sensor based on imprinted sol-gel and nanomaterials for sensitive determination of bisphenol A. *Food Control* **2011**, *22*, 786–791. [\[CrossRef\]](#)
31. Yang, J.C.; Park, J. Molecular Imprinting of Bisphenol A on Silica Skeleton and Gold Pinhole Surfaces in 2D Colloidal Inverse Opal through Thermal Graft Copolymerization. *Polymers* **2020**, *12*, 1892. [\[CrossRef\]](#)
32. Ardekani, R.; Borhani, S.; Rezaei, B. Selective molecularly imprinted polymer nanofiber sorbent for the extraction of bisphenol A in a water sample. *Polym. Int.* **2020**, *69*, 780–793. [\[CrossRef\]](#)
33. Kalogiouri, N.P.; Tsalbouris, A.; Kabir, A.; Furton, K.G.; Samanidou, V.F. Synthesis and application of molecularly imprinted polymers using sol-gel matrix imprinting technology for the efficient solid-phase extraction of BPA from water. *Microchem. J.* **2020**, *157*, 104965. [\[CrossRef\]](#)
34. Stoica, E.B.; Gavrilă, A.M.; Branger, C.; Brisset, H.; Dyshlyuk, A.V.; Vitrik, O.B.; Iovu, H.; Sarbu, A.; Iordache, T.V. Evaluation of molecularly imprinted thin films for ephedrine recognition. *Mater. Plast.* **2019**, *4*, 865–874. [\[CrossRef\]](#)
35. Zhuang, Y.; Zhou, M.; Gu, J.; Li, X. Spectrophotometric and high performance liquid chromatographic methods for sensitive determination of bisphenol A. *Spectrochim. Acta A Mol. Biomol. Spectrosc.* **2014**, *122*, 153–157. [\[CrossRef\]](#)
36. Florea, A.M.; Sarbu, A.; Donescu, D.; Radu, A.L.; Zaharia, A.; Iordache, T.V. The structure effect upon gallic acid re-binding in molecularly imprinted organosilica. *J. Sol-Gel Sci. Technol.* **2015**, *76*, 529–541. [\[CrossRef\]](#)
37. Gao, P.; Wang, H.; Li, P.; Gao, W.; Zhang, Y.; Chen, J.; Jia, N. In-site synthesis molecular imprinting Nb₂O₅-based photoelectrochemical sensor for bisphenol A detection. *Biosens. Bioelectron.* **2018**, *121*, 104–110. [\[CrossRef\]](#) [\[PubMed\]](#)
38. Pei, D.-N.; Zhang, A.-Y.; Pan, X.-Q.; Si, Y.; Yu, H.-Q. Electrochemical Sensing of Bisphenol A on Facet-Tailored TiO₂ Single Crystals Engineered by Inorganic-Framework Molecular Imprinting Sites. *Anal. Chem.* **2018**, *90*, 3165–3173. [\[CrossRef\]](#) [\[PubMed\]](#)
39. Liu, R.; Feng, F.; Chen, G.; Liu, Z.; Xu, Z. Barbell-shaped stir barsorptive extraction using dummy template molecularly imprinted polymer coatings for analysis of bisphenol A in water. *Anal. Bioanal. Chem.* **2016**, *408*, 5329–5335. [\[CrossRef\]](#)
40. Anirudhan, T.S.; Athira, V.S.; Chithra Sekhar, V. Electrochemical sensing and nano molar level detection of Bisphenol-A with molecularly imprinted polymer tailored on multiwalled carbon nanotubes. *Polymer* **2018**, *146*, 312–320. [\[CrossRef\]](#)
41. Iordache, T.-V.; Sarbu, A.; Donescu, D.; Nicolae, C.A.; Jerca, F.A.; Dima, S.O. Selecting the nature of imprinted molecular organosilica sieves with gallic acid via thermal analyses. *J. Therm. Anal. Calorim.* **2014**, *118*, 1039–1048. [\[CrossRef\]](#)
42. Shaikh, H.; Sener, G.; Memon, N.; Bhanger, M.I.; Nizamani, S.M.; Üzek, R.; Denizli, A. Molecularly imprinted surface plasmon resonance (SPR) based sensing of bisphenol A for its selective detection in aqueous systems. *Anal. Methods* **2015**, *7*, 4661–4670. [\[CrossRef\]](#)

Review

Modern and Dedicated Methods for Producing Molecularly Imprinted Polymer Layers in Sensing Applications

Ana-Mihaela Gavrilă [†], Elena-Bianca Stoica [†], Tanța-Verona Iordache ^{*} and Andrei Sârbu ^{*}

Advanced Polymer Materials and Polymer Recycling Group, The National Institute for Research & Development in Chemistry and Petrochemistry ICECHIM, Splaiul Independentei no. 202, 060021 Bucharest, Romania; ana.gavrila@icechim.ro (A.-M.G.); bianca-elena.stoica@icechim.ro (E.-B.S.)

^{*} Correspondence: tanta-verona.iordache@icechim.ro (T.-V.I.); andrei.sarbu@icechim.ro (A.S.);

Tel.: +4-0755-159-896 (T.-V.I.); +4-0724-237-351 (A.S.)

[†] These authors contributed equally to this work.

Abstract: Molecular imprinting (MI) is the most available and known method to produce artificial recognition sites, similar to antibodies, inside or at the surface of a polymeric material. For this reason, scholars all over the world have found MI appealing, thus developing, in this past period, various types of molecularly imprinted polymers (MIPs) that can be applied to a wide range of applications, including catalysis, separation sciences and monitoring/diagnostic devices for chemicals, biochemicals and pharmaceuticals. For instance, the advantages brought by the use of MIPs in the sensing and analytics field refer to higher selectivity, sensitivity and low detection limits, but also to higher chemical and thermal stability as well as reusability. In light of recent literature findings, this review presents both modern and dedicated methods applied to produce MIP layers that can be integrated with existent detection systems. In this respect, the following MI methods to produce sensing layers are presented and discussed: surface polymerization, electropolymerization, sol-gel derived techniques, phase inversion and deposition of electroactive pastes/inks that include MIP particles.

Keywords: molecularly imprinted layers; surface polymerization; electropolymerization; sol-gel derived techniques; phase inversion; electroactive pastes and inks

Citation: Gavrilă, A.-M.; Stoica, E.-B.; Iordache, T.-V.; Sârbu, A. Modern and Dedicated Methods for Producing Molecularly Imprinted Polymer Layers in Sensing Applications. *Appl. Sci.* **2022**, *12*, 3080. <https://doi.org/10.3390/app12063080>

Academic Editor: Jean-Michel Guenet

Received: 22 February 2022

Accepted: 14 March 2022

Published: 17 March 2022

Publisher's Note: MDPI stays neutral with regard to jurisdictional claims in published maps and institutional affiliations.



Copyright: © 2022 by the authors. Licensee MDPI, Basel, Switzerland. This article is an open access article distributed under the terms and conditions of the Creative Commons Attribution (CC BY) license (<https://creativecommons.org/licenses/by/4.0/>).

1. Introduction

Chemical and biochemical sensors are modern devices in analytical chemistry that simplify and miniaturize analytical determinations. Analytical methods based on modern sensor technology have solved many difficult analytical issues in research and society. Many scientific groups are working at the global level in the field and are reporting interesting results [1]. In general, conventional analytical methods have been extensively used due to their accuracy; nevertheless, most of these methods are expensive and require complex equipment, laboratory facilities, a high reagent consumption and well-trained personnel [2]. These drawbacks have prompted the research community to build more performant sensors for specific analysis of samples with complex matrices and very low concentrations, all at a lower reagent cost with inexpensive and easily-handled equipment, in order to perform in situ and on-site determinations [3].

Generally, a sensor is composed of three integrated parts (Figure 1), as follows: (i) a receptor for detecting the target analyte in a selective and sensitive manner, (ii) a physical transducer that converts the information obtained from the sensitive receptor into a measurable signal (usually an electric signal), and (iii) a suitable analytical device to process and show the significant signals formed by transducers and to calculate the results [4].

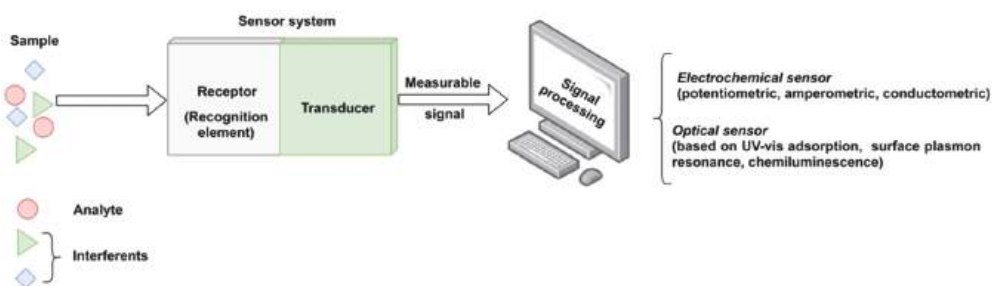


Figure 1. The functional scheme of a typical sensor system.

Biosensors are defined as analytical devices incorporating as a receptor biological material, such as enzymes, antibodies, nucleic acids, whole cells and tissues, a biologically derived material (i.e., engineered proteins, aptamers or recombinant antibodies) or a biomimetic material (i.e., molecularly imprinted polymers or combinatorial ligands). Depending on the incorporated sensitive material, the biosensors are classified as enzymatic, immune affinity recognition, DNA or whole-cell sensors; while considering the type of transducer, sensors can be classified as electrochemical, optical, acoustical, piezoelectrical, gravimetric or thermal [1]. Each type of sensor class has other subclasses. For instance, the electrochemical sensors maybe amperometric (the majority), potentiometric, voltametric, etc. [5]. However, due to high production costs and the restricted operating conditions of these natural receptors, the development of artificial receptors with molecular recognition capacity, so-called synthetic receptors, have attracted a great interest as appropriate alternatives for the biological elements. Hence, among the existing techniques for the development of artificial receptors, high expectations are set out in the design of molecularly imprinted polymers (MIPs).

MIPs are polymeric materials that are designed and produced with built-in molecular recognition properties. As a result of this fundamental attribute, a growing interest has been observed in their development as inexpensive and robust materials with sensitive and selective molecular recognition. Some of the top current applications that include the use of MIPs are associated with catalysis, separation sciences and monitoring/diagnostic devices for chemicals, biochemicals and pharmaceuticals [6,7]. MIPs have proven to possess important advantages as an alternative sensing material for biosensors, including the ease of preparation, storage stability, low cost, repeated uses without loss of activity, high mechanical strength and resistance to heat and pressure as well as to harsh chemical environments [8,9]. In a typical approach, the MI process (Figure 2) allows the creation of specific molecular recognition sites by the polymerization of a functional monomer in the presence of target molecules (called template) and of a high concentration of crosslinker. Following the template removal, by specific extraction procedures, the specific recognition cavities are revealed [10–12]. This approach endows MIPs with tremendous specific binding properties, as they possess cavities with complementary size, shape and electronic environment with the target molecule [13].

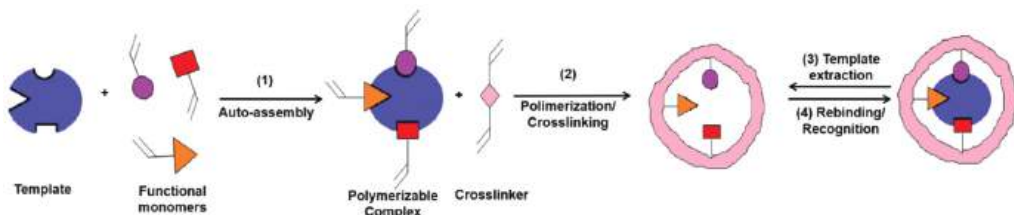


Figure 2. Molecular imprinting process (adapted from [14]).

In the classical imprinting process, a complex is formed between the template and functional monomer(s), by covalent, semi-covalent or non-covalent bonds, the non-covalent approach being preferred because of the simplicity in complex forming and the ease of the template extraction. In this case, polymerization takes place in the presence of an initiator and a porogen solvent, the latter having the role to create pores in the polymer matrix that facilitate the access of target molecules near the imprinted sites, during the rebinding assays [15]. A large amount of crosslinker is needed, as well, in order to stabilize the structure. Finally, the template is extracted from the crosslinked polymer and, thus, the imprinted cavities are created. This approach is also called the bulk method [16] because a solid block is first obtained, which is later on crushed for obtaining irregular-shaped particles. This method has little productivity because many of the recognition sites are destroyed during the crushing. This is the main reason why other methods were developed for enhancing the specificity and selectivity of MIPs, such as suspension [17], emulsion [18] or precipitation polymerization [19].

Molecular imprinting (MI) was applied initially for organic small molecule templates and ions [20], due to the molecular size, complexity, conformational flexibility and diffusion difficulties of large molecules [8]. Nevertheless, in the last 15 years, large molecules, such as proteins, were also successfully imprinted. For instance, by using the so-called epitope approach [21], only a characteristic part of the biomacromolecule is imprinted, and the following rebinding process is based on recognizing this part alone. Another clever approach developed from necessity allows the preparing of MIPs for labile, dangerous or very expensive targets, by performing the imprinting using a “dummy” template, meaning a safer or more available compound with a similar structure to that of the target analyte [22].

MIPs can also be used to design enzymatic and immunoaffinity sensors. In agreement with the classification of biosensors, MIP-based devices can work according to two different detection schemes: (1) affinity sensors (“plastic antibodies”) and (2) catalytic sensors (“plastic enzymes”) [2,23]. In this respect, MIP layers are usually deposited directly on the transducer surface of a sensor chip to produce the recognition unit [24,25]. As a result of this rather simple procedure, many researchers have found various methodologies for producing MIP layers as receptors for producing sensing devices, such as spin coating of a precursor solution to form a thin film, followed by *in situ* chemical polymerization [26]; electropolymerization of a pre-assembled complex of an electroactive functional monomer with a template [27,28]; dropcasting of a precursor polymer from solution [25,29,30]; dripping a composite solution containing a conducting material (e.g., graphene), MIP particles, and a binder (e.g., PVC) [31]; and, self-assembly of monolayers [32]. Thereby, the target of this review is to present both modern and dedicated methods for the preparation of MIP-sensitive layers, which are presented in detail in the next sections. In all cases, the authors describe the synthesis procedure and properties of prepared MIPs, giving quantifiable results relative to the control samples, non-imprinted polymers (NIP).

2. Molecular Imprinting by Surface Polymerization

In the surface imprinting process, the recognition sites are formed at the surface of a substrate [33]. Due to this fact, the recognition sites are more accessible and promote faster binding kinetics, compared to monolith MIPs for example. This means that template–polymer interactions are not governed by diffusion processes to the same extent as usually encountered in bulk imprinting [34]. Therefore, the technique is applicable especially for the imprinting of large biomolecules such as proteins [35,36], microorganisms and cells. Moreover, surface imprinting requires lower amounts of template molecules compared to the amounts used for other imprinting techniques because imprinting occurs right at the surface of the films [37].

In principle, the method consists of the preparation of a polymerization mixture, containing the functional monomer, the template, the initiator, the porogen solvent and the crosslinker, similar to the bulk method (see Figure 3). An amount of this mixture is cast on a solid surface, as for instance the sensor surface, and the formed thin film is

polymerized thermally or by UV light curing; the latter being largely preferred. At the end, the template is extracted, thus generating the surface imprinted polymer [16].

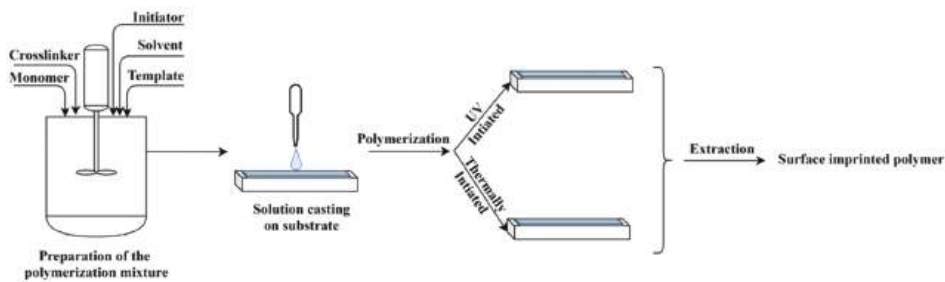


Figure 3. The principle of MIP layer preparation by surface polymerization.

Nonetheless, there are many variants of surface imprinting such as soft lithography, template immobilization, surface imprinting via grafting (pre-grafting polymerization and post-crosslinking/imprinting and grafting polymerization synchronized with crosslinking/imprinting [38]), emulsion and precipitation polymerization or epitope imprinting [16].

For example, Cennamo et al. [39], developed a biomimetic optical sensor based on MIP and surface plasmon resonance (SPR) transduction, in connection with tapered plastic optical fiber (POF) to detect selectively low molecular weight substances. The prepared SPR sensor was tested for l-nicotine ((–)-1-methyl-2-(3-pyridyl) pyrrolidine, MW = 162.24). In order to realize this SPR sensor, the plastic optical fiber, without protective jacket, was heated and stretched to yield a thinner part with a length of 10 mm, after which it was embedded in a resin block and a thin gold film was sputtered on its surface. According to the MIP classical procedure, the pre-polymerization mixture was prepared using l-nicotine as template, methacrylic acid (MAA) as functional monomer, divinylbenzene (DVB) as crosslinker, in a molar ratio of l-nicotine:MAA:DVB = 1:4:24. The developed device was able to be detected and discriminate between l- and d-nicotine using a small volume of sample, but with sensitivity strongly depending on the characteristics of the optical fiber [39]. Some examples of newsworthy MIP layers via the grafting approach are listed in Table 1.

Table 1. MIP-based sensors obtained by surface polymerization.

Synthesis Method	Receptor	Support	Analyte	Characterization Method(s)	LOD	Refs.
Spincoating	MIP film MIP nanoparticles	Glass	Atrazine	RIfS ¹ measurements.	>1.7 ppm	[40]
Precipitation polymerization/ polymer casting	MIP layer	SERS substrate ²	Enrofloxacin hydrochloride	Raman	10 ^{−7} mol·L ^{−1}	[41]
Casting	MIP membrane	Screen-printed gold electrode	Myoglobin	EIS ³ SWV ⁴	2.25 µg·mL ^{−1}	[42]
Grafting polymerization synchronized with crosslinking/ imprinting	MIP film	GCE ⁵	Olaquinox	CV ⁶ , DPV ⁷ , EIS	7.5 nmol L ^{−1}	[43]
Covalent imprinting/ drop casting	MIP film	Au-TFME ⁸	SARS-CoV-2 spike protein subunit S1	CV, SWV	4.8 pg·mL ^{−1}	[44]
Dropcasting	MIP membrane	QCM ⁹ crystal chip	Human serum albumin	Langmuir, Freundlich, Langmuir–Freundlich isotherm	0.026 µg mL ^{−1}	[45]

¹ RIfS: reflectometric interference spectroscopy; ² SERS: surface-enhanced raman scattering; silver nanoparticles modified by 3-methacryloxypropyltrimethoxysilane; ³ EIS: electrochemical Impedance spectroscopy; ⁴ SWV: square wave voltammetry; ⁵ glassy carbon electrode; ⁶ cyclic voltammetry; ⁷ differential pulse voltammetry; ⁸ MicruX™ gold-based thin-film metal electrodes; ⁹ QCM: quartz crystal microbalance.

Another optical sensor is described by Belmont et al. [40], in which case reflectometric interference spectroscopy (RIfS) was employed as a detection method, while the MIP films were prepared with the pesticide atrazine as the template molecule. In their study, the MIP films were deposited on glass transducers by two different methods: (i) spin-coating of pre-polymerization mixture containing polyvinyl acetate as a sacrificial polymeric porogen, followed by in situ surface polymerization of thin films, and (ii) auto-assembly of MIP nanoparticles with the aid of polyethylene imine (PEI) as an associative linear polymer. The results obtained upon assessment of atrazine solutions in toluene were reproducible for both types of films. However, the film prepared with auto-assembled MIP nanoparticles was more sensitive, tracking atrazine down to 1.7 ppm.

An example of the template immobilization approach is given in reference [42], where Moreira et al. developed a reusable sensor for Myo based on an MIP, prepared by assembling a polymer layer of carboxylated poly(vinyl chloride) (PVC COOH). This polymer was cast on the gold working area of a screen-printed electrode (Au-SPE), creating in this manner a novel disposable device relying on plastic antibodies. The MIP/Au-SPE sensor displayed a linear behavior by electrochemical impedance spectroscopy (EIS) and a limit of detection set-out at 2.25 µg/mL. The MIP/Au-SPE sensor also displayed good results in terms of selectivity. The error found for each interfering species were 11% for BSA, 7% for troponin T and 2% for creatine kinase MB, respectively. Overall, the MIP modification over the Au-SPE was found suitable for producing an electrochemical sensor for screening Myo in biological fluids [43].

One epitope approach by surface polymerization for MIP selective layers is also illustrated by Ma and co-workers [44]. In the first step, the MIP was synthesized, using the epitope of human serum albumin as a template and afterwards, a coating method was applied to produce the quartz crystal microbalance sensor (EMIP-QCM). The MIP solution was prepared using zinc acrylate as a functional monomer, EGDMA as crosslinker and dimethylformamide (DMF) as porogen solvent. The gel precipitate was separated, washed and lyophilized. In order to obtain the sensor, a quartz crystal microbalance (QCM) crystal chip was used to drop-cast the MIP solution. The final MIP-QCM sensor displayed good selectivity and sensibility for human serum albumin, with a detection limit of 0.026 µg/mL. Furthermore, the sensor has also proven good accuracy and reproducibility when real samples were tested [45]. Further on, the study presented by Boysen and co-workers [46] is a typical example of a soft lithography approach and describes the design and synthesis of layer-by-layer MIPs via surface polymerization. The double-layered patterned MIP1/MIP2 was prepared on a silicon wafer. To enable chemical binding of MIP1 layer on the silicon, the surface of the wafer was first activated by sonication and exposed to UV-light, after which the surface was silanized with 3-(trimethoxysilyl)propyl methacrylate. The MIP pre-polymerization mixture was prepared by dissolving the template (*N*-dansyl-L-phenylalanine) and MAA with a crosslinker and a photo-initiator in a porogen solvent. This solution was spincoated onto the silanized silicon wafers and photo-polymerized. After template extraction, a 4-vinylpyridine-MIP thin film layer was deposited by photolithographic etching onto the first MIP film of PMAA, resulting in a grid-patterned surface in which two different MIPs, with pre-determined selectivity for *N*-dansyl-L-phenylalanine, alternated at a micron scale. Selectivity differences towards fluorescent template analogues were inspected using fluorescence microscopy [46].

MIP films can be prepared by surface polymerization also on organic support, such as multiwall carbon nanotubes (MWCNT) [47]. In this report, the used template was lysozyme (Lys) from egg white. The functional monomer was acrylamide (AAm), the crosslinker, methylene bis acrylamide (MBA) and the solvent, phosphate buffer (PBS). Besides using PBS for the protein protection, a redox initiation was employed consisting of ammonium persulfate (APS) and *N,N,N',N'*-tetramethylethylenediamine (TEMED), allowing to perform the surface polymerization at room temperature. The selectivity assays showed that the Lys-MIP film registered higher capacity and affinity for Lys than for the other competitive proteins, such as cytochrome C (Cyt C), myoglobin (Myo), hemoglobin

(Hb) and bovine serum albumin (BSA). The relative selectivity coefficients for Lys/Cyt C, Lys/Myo, Lys/Hb, and Lys/BSA were 1.30, 1.30, 3.12 and 2.82, respectively, while the adsorption capacity of the Lys-MIP film was 1.86 times higher than that of the non-imprinted polymer (NIP). Although the material was intended for selective separation of lysozyme, it may also be of interest for sensor application as a result of excellent electric conductivity of MWNT [47].

In recent decades, an extensive interest in the application of controlled radical polymerization methods (CRPs) for the imprinting of biomacromolecules has been observed [48]. Generally, MIPs are prepared by a conventional free radical polymerization mechanism, mainly due the fact that it is not disturbed by a large range of functional groups of the monomers and of the template, but also due to mild reaction conditions that can be employed. However, free radical polymerization has a major drawback due to the fact that chain propagation and termination reactions are hard to control, which makes the synthesis of surface imprinted polymer films with constant and targeted thickness difficult. Furthermore, free radical polymerization normally yields crosslinked polymer networks with heterogeneous structures, which might be responsible for the increased heterogeneity of binding sites, and thus, for the decreased affinity and selectivity [49]. On the other hand, the negligible chain termination in CRPs and their thermodynamically-controlled processes allow for more constant rates of the polymer chain growth, leading to more homogeneous polymer networks with narrower distributions of the chain length. This is the reason why several CRPs were developed so far for surface polymerization, in which case the most preferred methods refer to iniferter-induced radical polymerization [50,51], atom transfer radical polymerization (ATRP) [38,52] and reversible addition-fragmentation chain transfer (RAFT) polymerization [38,53]. Some of the successful procedures are provided next.

A selective surface plasmon resonance (SPR) sensor, based on surface polymerization, for the detection of Ochratoxin A (OTA) contamination in dried fig was developed by Akgönüllü et al. [54]. OTA is one of the most common mycotoxins that contaminate a wide range of agricultural products, which is why its assessment is very important for the monitoring of the food quality. The MIP layer was produced onto the SPR sensor chip by light-initiated polymerization of *N*-methacryloyl-L-phenylalanine (MAPA) and 2-hydroxyethyl methacrylate (HEMA) using OTA as a template. In a first step, the gold surface of the chip sensor was modified with allyl groups, by allyl mercaptan. This pre-treatment was performed because thiol-end will bind to the gold SPR chip, and the other end, allyl group, will interact with the polymer, insuring the good adherence of the MIP film on the chip. For the preparation of the MIP film, MAPA and OTA were mixed to obtain a pre-complex with the molar ratio of 1:3 for OTA:MAPA. The pre-polymerization complex was then mixed with HEMA, a crosslinker and a radical initiator in methanol. This reaction mix was dripped onto the SPR gold chip surface, distributed uniformly using a spin coater and, finally, polymerized by UV-light to produce the MIP film. The MIP-SPR chip was able to detect the OTA with high specificity (around 4.24 higher than that of the NIP), while the detection limit was close to 1 ng/mL and the response time was about 8 min [54].

Another interesting study on surface imprinting via the grafting (grafting from) method is provided by Heetal [55], which described the obtaining of a sensor for testosterone starting from porous silica by covalently binding azo-initiators and then photo-grafting. First, glycidoxo groups were immobilized on the surface of silica particles by the reaction of silanol groups with 3-glycidoxo-propyltrimethoxysilane (GPS), after which the glycidoxo groups were modified with an azo-initiator (4,4'-Azobis(4-cyanopentanoic acid)) to yield azo group-introduced silica particles. The following polymer grafting was carried out by photopolymerization of MAA as the functional monomer, ethylene glycol dimethacrylate (EGDMA) as the crosslinker, and testosterone as the template, on the surface of the azo-modified particle, which served as the initiator. The prepared particles with specific recognition ability for testosterone (imprinting factor of 1.52) were used for liquid chromatography [55]. Nevertheless, it is obvious that they can also be used for sensor development by nanoparticle auto-assembly [40].

In reference [56], a “grafting from” method is provided by Tarannum and Singh, who reported water-compatible surface imprinting of “baclofen” on silica surface. As a supporting matrix, a silica gel was used and the synthesis of the MIP for a skeletal muscle relaxant, namely baclofen (4-amino-3-p-chlorophenylbutyric acid) was carried out on the surfaces of silica gel. An imprinting network of sulfobetaine polyelectrolyte was prepared in aqueous medium only. This was grafted onto the silica gel matrix using 3-aminopropyltriethoxysilane (APTES) as a silane coupling agent and Michael addition reaction for further propagating the polymer grafting procedure. The rebinding studies showed that the MIP displayed good recognition for baclofen as compared to NIPs. Meanwhile, selectivity tests proved that MIP had a high affinity to baclofen in the presence of interferants (close structural analogues). Hence, a facile, specific, selective and water-compatible technique to detect baclofen in the presence of various interferants is provided. The prepared materials can be applied in HPLC as well as in capillary electrochromatography (CEC).

An interesting “dummy” imprinting approach by surface polymerization is described by Shahhoseini et al. [57]. In order to prepare sensitive layers for tricyclic antidepressants (TCAs) measurement in blood, the surface polymerization was performed on steel blades. In this respect, the pre-polymerization solution was obtained using a dummy template: benzyl(3-(10,11-dihydro-5H-dibenzo[b,f]azepin-5-yl)propyl)(methyl) carbamate, MAA and EGDMA and cast on the steel blades. Subsequently, the photo initiator was added and the layers were covered with a glass cover. The idea of using a dummy template, in this case, was derived from the necessity to prevent template bleeding. For trace analysis, such as the one targeted in this work, the risk of false positive results can also be due to incomplete template removal. Thus, to avoid such issues a pseudo-template was employed. The prepared MIPs were used as sensitive layers for liquid chromatography in which case the adsorption efficiencies for the MIPs were 3 to 5 times better than for the non-imprinted analogous, confirming that the use of the pseudo-template led to improved performance in this case.

The work of Hudson et al. [58] provides some insights regarding the surface molecular imprinting polymerization for obtaining a fluorescence sensor for the thermal and optical detection of nafcillin. The production of MIP films and particles was realized by integrating a fluorescent moiety that serves both as an element for template interaction and signaling. Fluorescein methacrylate (FluMa) was synthesized and introduced during the molecular imprinting process, first as the sole monomer and afterwards in an equimolecular mixture with MAA. The thin MIP films were deposited onto functionalized glass slides (to serve as electrodes) and the following UV-light initiated polymerization was performed in the presence of template species, nafcillin sodium salt. Although the specificity of films was not as high as that registered for the particles, the MIPs with FluMa and MAA were by far more performant than the ones with FluMa alone. Hence, the results are promising for developing a portable sensor for antibiotics [58].

3. Molecular Imprinting by Electropolymerization

Electrochemical polymerization is a method used to synthesize conductive polymers that are widely used for the development of biosensors and chemical sensors. This technique involves the deposition of a polymer layer on an electrode surface [59]. The electropolymerization can be performed by two methods, i.e., oxidation or reduction. Of the two methods, oxidation is the most commonly used for the obtaining conducting polymers. Anodic electropolymerization involves the monomer oxidation, thus obtaining cationic radicals, that lead to the formation of the polymer on the electrode surface [60,61]. Pyrrole, aniline and thiophene are the most important classes of conductive monomers, due to their low oxidation potential. Thus, by electropolymerization, polypyrrole, polyaniline and polythiophene are obtained. These polymers find their use in a wide range of domains because of certain advantages, referring to price, stability and synthesis complexity [62,63].

The electrochemical polymerization can be carried out using a three-electrode system (working electrode, counter electrode and reference electrode) or screen-printed electrodes ("3 in 1 electrode"). In a typical procedure, the following components are required: electrode system, solvent, supporting electrolyte, monomer(s) and template molecule (in case of MIP synthesis) [64]. The polymer layer deposition takes place on the working electrode (WE) surface (given schematically in Figure 4). The most common electrodes are made of gold, carbon and platinum, but other options are also available such as silver or indium tin oxide. Since, the properties of the polymer film are influenced by the electrode material, electrode surface, supporting electrolyte, electropolymerization technique, solvent and monomer, the overall procedure usually requires an optimization [65].

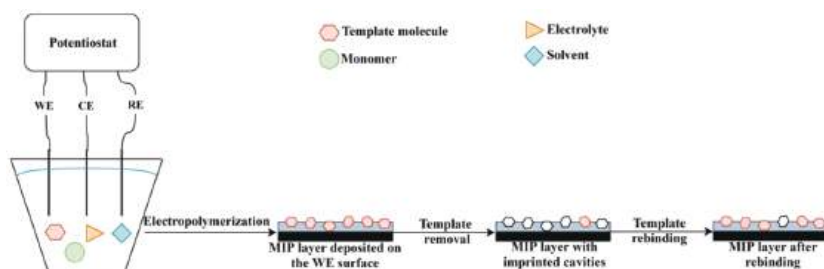


Figure 4. The principle of MIP deposition by electropolymerization.

The electropolymerization can be performed using different techniques, including potentiodynamic (cyclic voltammetry), potentiostatic (constant potential) and galvanostatic (constant current) [66]. The potentiodynamic technique involves the formation of the polymer via cyclic voltammetry (CV). The polymer is formed upon applying a potential, which is changing between the oxidative and reductive state, resulting in a doped and undoped polymer [67]. On the other hand, potentiostatic polymerization is performed at a constant potential. In case of oxidative polymerization, the applied potential is positive, resulting in a doped polymer. In addition, the potential should be high enough to oxidize the monomer in order to initiate the polymerization process, but at the same time, it should be low enough to avoid secondary reactions [61]. Last but not least, the galvanostatic polymerization is carried out at a constant current, thus resulting in a doped polymer. This method has important advantages, such as simplicity, and most importantly, the thickness of the polymer depends on the electropolymerization time [68].

In recent decades, MIPs synthesized by electropolymerization have been widely used in the development of electrochemical sensors. An electrochemical sensor is a device consisting of a recognition element (in this case, MIP selective layer) and the electrochemical transducer. The principle of an electrochemical sensor relies on the interaction of the receptor with the analyte, which is transformed into an analytical signal (Figure 4). The main types of electrochemical sensors include conductometric, potentiometric, impedimetric and amperometric sensors [69,70]. Due to the improved selectivity, sensitivity and stability, limit of detection and low cost that MIPs provide, such MIP-based sensors are widely reported nowadays [71]. According to the recent literature, MIP-based electrochemical sensors are used in various applications in areas of human health, environmental pollution and pharmaceutical domain. The most significant results with MIP-based electrodes prepared by electropolymerization are provided in Table 2.

For instance, Menon and her co-workers [72] prepared an MIP-based electrochemical sensor for acetaminophen detection. Acetaminophen is an analgesic that can be harmful if used in excess. The synthesis of the film was conducted using a three-electrode system consisting of a gold (Au) electrode (working electrode), Ag/AgCl (reference electrode) and platinum electrode (counter electrode). In the first step, the gold electrode surface was modified with AuNPs. After that, the MIP film was deposited onto the modified electrode surface by electropolymerization. The MIP synthesis was performed by cyclic

voltammetry, at a potential ranging from 0 to 1.3 V, at a scan rate of 100 mV/s for 30 scan cycles. The prepared electrodes were analyzed by CV and EIS. The performance of the MIP sensor was also studied by square wave voltammetry (SWV), in a concentration range between 4.5×10^{-5} and 5×10^{-7} M, resulting in a limit of detection of 2.3×10^{-9} M [72].

Table 2. MIP-based sensors obtained by electropolymerization.

Synthesis Method	Receptor	Support	Analyte	Electrochemical Characterization Method(s)	LOD	Refs.
CV ¹	MIP film	Au electrode ²	Acetaminophen	CV, EIS ³ and SWV ⁴	2.3×10^{-9} M	[72]
CV	MIP film	GCE ⁵	Dimetridazole	DPV ⁶	10^{-10} M	[73]
Potentiostatic conditions	MIP film	Au electrode	Erythromycin	DPV	1×10^{-10} M	[74]
CV	MIP film	Au electrode	Tetracycline	LSV ⁷	2.2×10^{-16} M	[75]
CV	MIP film	GCE	Sunset yellow	CV	5×10^{-9} M	[76]
CV	MIP film	GCE	Tetra-bromo-bisphenol A	DPV	2.7×10^{-10} M	[77]
CV	MIP film	Modified ITO ⁸ electrode	Resveratrol	CV and EIS	7.1×10^{-12} M	[78]
CV	MIP film	Au electrode	Atrazine	CV and DPV	1×10^{-9} M	[79]
CV	MIP film	Au electrode	Sodium lauryl sulfate	CV, DPV and EIS	1.8×10^{-10} g/L	[80]
CV	MIP film	SPCE ⁹	Diclofenac	DPV	2×10^{-7} M	[81]
CV	MIP film	GCE	Epinephrine	CV and DPV	7.6×10^{-8} M	[82]
CV	MIP film	Modified SPCE	Naloxone	DPV	2×10^{-7} M	[83]
CV	MIP film	Modified SPCE	Naloxone	DPV	1.6×10^{-7} M	[84]
CV	MIP film	Screen-printed gold electrode	Methylone	SWV	1.1×10^{-6} M	[85]
CV	MIP film	Cr/Au film	Melamine	Resonance Wavelength Modulation	5.1×10^{-12} M	[86]
CV	MIP film	GCE	Melamine	CV and SWV	4.47×10^{-10} M	[87]
CV	MIP film	Modified GCE	Asulam	CV, DPV and EIS	1.7×10^{-13} M	[88]
CV	MIP film	ITO electrode	Luteolin	DPV	2.4×10^{-8} M	[89]
CV	MIP film	Modified electrode based on graphene and HAuCl ₄	4-nonylphenol	CV and DPV	0.01 ng·mL ⁻¹	[90]
CV	MIP film	GCE	Anthracene	SWV	1.2×10^{-8} M	[91]
CV	MIP film	SPCE	Cocaine	SWV and EIS	2.9×10^{-9} M	[92]
CV	MIP film	GCE	Entacapone	EIS and DPV	5×10^{-8} M	[93]

¹ CV: cyclic voltammetry; ² Au electrode: gold electrode; ³ EIS: electrochemical impedance spectroscopy; ⁴ SWV: square wave voltammetry; ⁵ GCE: glassy carbon electrode; ⁶ DPV: differential pulse voltammetry; ⁷ LSV: linear sweep voltammetry; ⁸ ITO: electrode indium tin oxide; ⁹ SPCE: screen-printed carbon electrode.

Another concerning problem is the side effect related to the use of dimetridazole beyond the permitted limits. Recently, Ali et al. [73] depicted the preparation of a poly-arginine MIP based sensor that can be used for electrochemical detection of dimetridazole. In this study, the MIP film synthesis was carried out by CV, using a three-electrode system (glassy carbon electrode GCE–working electrode, Ag/AgCl electrode–reference electrode and platinum wire electrode–counter electrode) and a solution consisting of L-arginine, dimetridazole dissolved in PBS. The electropolymerization conditions consisted of a potential range between −2 and 2.2 V, a scan rate of 100 mV/s and 12 scan cycles. The recognition experiments were performed by differential pulse voltammetry (DPV), using solutions with different concentration (10^{-10} to 10^{-5} M). The limit of detection for such sensors was 0.1 nM, which represents a promising future for dimetridazole detection [73].

In the past few years, both the production and consumption of antibiotics increased, which has led to a rise in environmental pollution. In recent years, sensors for antibiotics have been studied in order to improve the quality of life. For example, Ayankojó and co-workers [74] developed a sensor based on MIP for erythromycin detection, using a screen-printed electrode with Au working electrode. The electropolymerization was performed under potentiostatic condition, meaning a constant potential of 0.63 V, using *m*-phenylenediamine as monomer. The recognition and the rebinding capacity of the sensors were studied by DPV, pointing to a limit of detection of 0.1 nM and also a good selectivity. The results presented in this study may represent a solution for erythromycin

detection in aqueous solutions [74]. Another research group prepared an electrochemical sensor for tetracycline detection [75]. They were able to synthesize an MIP film by electropolymerization on the surface of the gold electrode surface. A three-electrode system consisting of Au electrode (working electrode), saturated calomel electrode (reference electrode) and a platinum (Pt) electrode (counter electrode), was used in the electropolymerization process. A first step involved in synthesizing gold nanoparticles, further used in the development of the sensor. The films were prepared by CV upon applying a potential between 0.35 and 0.8 V, at a scan rate of 100 mV/s, for 10 scan cycles, after which the conditions were changed to a fixed potential (0.8 V). The performance of the sensor was studied by linear sweep voltammetry (LSV) and indicated quite high sensitivity, down to 0.22 fM tetracycline in aqueous solutions [75].

Given the toxic effect of dyes on human health, controlling their presence in the food becomes mandatory. Thus, Arvand et al. [76] proposed the development of an electrochemical sensor based on an MIP layer that can be used for food analysis. In this case, the authors used a three-electrode system consisting of a working electrode (functionalized GCE), reference electrode (saturated Ag/AgCl electrode) and counter electrode (Pt electrode). MWCNTs were used for the functionalization of the GCE. The electropolymerization was carried out by CV, in a potential range between -1.4 V and -0.4 V, for 15 scan cycles, using a solution containing AAm as the functional monomer, *N*, *N*-methylene-bis-acrylamide (MBA) as the crosslinker, sodium persulfate as the initiator, sunset yellow as the template molecule and sodium nitrate as the electrolyte dissolved in PBS. Ultimately, the sensor was electrochemically tested using CV and was demonstrated to possess good recognition properties for sunset yellow in the 0.05 – 100 μ M concentration range and a low limit of detection (LOD) of 5 nM [76].

Shen et al. [77] described the preparation of an electrochemical sensor based on MIP for tetra-bromo-bisphenol A (TBBPA) detection. TBBPA is widely used for plastics and electronics manufacturing, and it may have negative effects on human health, including neurological and thyroid dysfunctions. Thus, the MIP films were prepared by electropolymerization onto GCE surface, using CV, in a potential range between -0.5 and 0.5 V, at 70 mV/s for 10 scan cycles. The solution used for electropolymerization consisted of ethanol, dopamine, TBBPA (template molecule) and PBS. MIPs showed a good sensitivity for TBBPA, in the 1 – 50 nM concentration range. Moreover, the MIP films presented selectivity and an LOD of 0.27 nM. The results are promising and comparable with further HPLC applications [77].

Wang and co-workers [78] prepared an MIP based sensor on indium tin oxide (ITO) bare for the determination of resveratrol. In this respect, prior to electropolymerization, the ITO electrode was modified with Ag nanoparticles using cyclic voltammetry and after that with a HAuCl_4 (chloroauric acid) solution. Following this procedure, the MIP film was deposited onto the modified electrode surface via electropolymerization, by CV, applying a potential between 0 and 0.8 V at a scan rate of 50 mV/s, for 30 scan cycles. The electrochemical behavior of the sensors was studied by CV and EIS, in which case a linear response between 2.0×10^{-11} to 9.0×10^{-9} M was reported. The detection limit was determined to be 7.1×10^{-12} M. Moreover, the sensor was tested using structural analogues and proved good selectivity [78].

Li [79] described the development of an MIP sensor for atrazine detection. The MIP film synthesis was carried out by electropolymerization using a classical electrochemical cell. For producing the MIP film, the electrochemical cell consisted of an Au electrode (working electrode), a saturated calomel electrode (reference electrode), a Pt electrode (counter electrode), *o*-Phenylenediamine (monomer), electrolyte and atrazine (template molecule). In this case, the employed electropolymerization conditions referred to applying a potential between 0 and 0.8 V at a scan rate of 50 mV/s for 15 scan cycles. CV and DPV assays have proven that the prepared sensor can detect atrazine at different concentration, having a very low LOD of 1×10^{-9} M [79].

Motia et al. proposed an electrochemical sensor based on an MIP layer for sodium lauryl sulfate (SLS) detection. In this study, a “3 in 1” electrode with Au electrode as working electrode, Ag electrode as reference electrode and gold strip plate as counter electrode, was used. The MIP film was deposited by electropolymerization of 2-Aminothiophenol (2-ATP), in the presence of SLS (template molecule), by applying a potential between -0.35 and 0.80 V for 10 scan cycles at 100 mV/s. Prior to electropolymerization, the surface of the electrode was modified with a layer of 2-ATP by dripping the solution on the electrode surface. The electrochemical response, by CV, DPV and EIS, indicated that the sensor presented good affinity for the SLS, with a limit of detection of 0.18 pg/mL [80].

Seguro et al. [81] have recently present an electrochemical MIP-based sensor for diclofenac detection. The development of the voltametric sensor involved the synthesis of an MIP film by CV directly on screen printed carbon electrode (SPCE) surface, using a solution containing dopamine as monomer, diclofenac sodium as template molecule and KCl as electrolyte. The electrodeposition was performed in a potential range between -0.5 V and 1 V at a scan rate of 100 mV/s. Ultimately, the sensor was tested by DPV, and, according to the authors, the imprinting factor was 2.5 . Furthermore, a LOD of 70 nM and a limit of quantification (LOQ) of 200 nM were obtained [81].

Another sensor based on Au nanoparticles and MIPs was introduced by Liu and her group [82] for epinephrine detection. The authors used a three-electrode system consisting of GCE (working electrode), saturated calomel electrode (reference electrode) and a Pt electrode (counter electrode). The working electrode was modified previously with HAuCl_4 , after which the electrodeposition was performed by applying a potential between -0.2 and 1.2 V for 20 scan cycles in the presence of epinephrine and 3-thiophene boronic acid (3-TBA). CV and DPV techniques were used to evaluate the performance of the final sensor, in which case a detection limit of 7.6×10^{-8} M was recorded [82].

Lopes and his group [83] proposed a sensor for naloxone detection. In this respect, the MIP film was synthesized by electropolymerization on the screen-printed carbon electrode that was firstly modified with MWCNT. The MIP film was prepared by CV when applying a potential in a range between -0.2 and 1 V, for 20 scan cycles at a scan rate of 100 mV/s, using a solution of 4-aminobenzoic acid and naloxone in PBS. The performance of the sensor was further studied using DPV and a detection limit of 0.2 μM was acquired [83]. Three years later, Shaabani and co-workers [84] also studied a sensor for naloxone detection, whereas the MIP film was deposited under similar conditions as described by Lopes et al. [83]. Yet, in this case, the SPCE surface was modified with Au nanoparticles and the CVs were obtained after applying a potential between -0.2 and 1 V at a scan rate of 50 mV/s for 15 scan cycles. By doing so, a lower detection limit (0.16 μM) was achieved.

Methylone is a synthetic drug, which produces psychotropic effects similar to ecstasy. Considering the side effects of this drug that include hypertension, paranoia and tachycardia, Couto et al. [85] presented a method for preparing an MIP-based sensor for methylone detection. The film was deposited on screen-printed gold electrode by electropolymerization of 2-mercaptobenzimidazole (monomer) in presence of the template molecule (methylone). The process was performed by CV when applying a potential in a range between -0.2 and 1.3 V for 15 scan cycles. A good performance of the sensor was obtained by SWV, in which case a detection limit of 1.1 μM was obtained. Moreover, the sensor also showed good stability and selectivity [85].

Melamine is a synthetic compound that can be used in the plastic industry as well as the milk industry. Considering the side effects of the melamine on human health (e.g., kidney problems, kidney stones), the monitoring of food is required. In this respect, Li and colleagues [86] developed an SPR sensor based on MIP films for melamine detection. The three-electrode system consisted of an optical fiber probe coated with Cr/Au film (working electrode), an Ag/AgCl electrode (reference electrode) and Pt electrode (counter electrode), while the MIP film was synthesized by electropolymerization of *o*-aminophenol (functional monomer) in the presence of melamine, by applying a potential between -0.3 and 1.2 V for 30 scan cycles at 50 mV/s. In order to estimate the performance of the

sensor, several melamine solutions with different concentrations were used, leading to an LOD of 5.1×10^{-12} M, which indicated a good sensitivity of the sensor [89]. Two years later, Regasa et al. [87] proposed a sensor for melamine detection that involved the electropolymerization of aniline in order to obtain the MIP film. In this case, a three-electrode system with GCE (working electrode), Pt electrode (counter electrode) and Ag/AgCl electrode (reference electrode) was employed and the electrodeposition of the MIP film was carried out in potentiodynamic conditions, by applying a potential between -0.2 and 1 V for 10 scan cycles. This group [87] evaluated the properties of prepared sensors by CV and SWV, in which case they obtained a higher detection limit (4.47×10^{-10} M) compared to the previous work [86].

Roushani and his team [88] developed an MIP sensor for electrochemical detection of asulam herbicide or methyl *N*-(4-aminophenylsulfonfyl)carbamate. In the first step, the GCE was modified with g-C₃N₄ (synthesized powder) and, subsequently, used for the electrodeposition of the MIP. The MIP solution consisted of monomer (dopamine), the template molecule (asulam) and electrolyte (KCl) dissolved in tris-buffered saline (TBS) (pH = 7), which was electropolymerized in the -0.5 to 0.5 V potential range, for 10 cycles. The electrochemical behavior was analyzed using different methods, including CV, DPV and EIS, which led to the conclusion that the sensors possess high selectivity and affinity towards asulam, with an LOD close to 0.17 pM [88].

Wei and colleagues [89] studied and developed a sensor based on MIP for electrochemical detection of luteolin, using a three-electrode system (ITO as the working electrode, SCE as a reference electrode and Pt electrode as counter electrode). The MIP film synthesis was achieved by electropolymerization of β -cyclodextrin (monomer) in the presence of luteolin, applying a potential between -0.8 and 1.1 V for 20 cycles. Rebinding and selectivity experiments were performed by contacting the sensor with luteolin, respectively with quercetin and apigenin solutions and studied by DPV. In this case, the sensor detection limit for luteolin was near 2.4×10^{-8} M [89].

Zheng and co-workers [90] proposed a two-step fabrication process of an electrochemical MIP-based sensor for detection of 4-nonylphenol (4-NP) in milk samples. In the first step, a multilayer electrode was obtained using reduced graphene and HAuCl₄. In the second step, the MIP film was prepared by electropolymerization of p-aminothiophenol (monomer), in presence of 4-NP as template molecule, upon applying a potential between -1 and 1 V. CV and DPV were employed for determining the sensor characteristics, in which case indicated a good selectivity and a LOD of 0.01 ng/mL [90].

The study by Mathieu-Scheers and her group [91] presented an MIP sensor for electrochemical detection of anthracene using GCE. The procedure was performed in a potential range between 0 and 1.4 V or 0 and 1.2 V, at a scanning rate of 10 mV/s, for 5 scan cycles, using pyrrole as a monomer and anthracene as a template molecule. The rebinding of anthracene was detected by SWV when a detection limit of 12 nM was calculated [91].

Recently, Grothe et al. [92] proposed a sensor based on MIP that allowed for detecting and identifying components from cocaine samples. Identification of the components provides important information regarding the origin of the cocaine. Herein, the MIP film was synthesized by electropolymerization of 3-amino-4-hydroxybenzoic in the presence of anesthetic benzocaine as the template molecule, on the carbon electrode of a SPCE. The electropolymerization process was performed in a potential range between 0 and 1.5 V for 10 scan cycles at a scan rate of 100 mV/s. SWV and EIS were used to study the electrochemical behavior of the films after contact with artificial urine (containing benzocaine) or caffeine, aminopyrine and procaine, in which case a limit of detection of 2.9 nM was achieved [92].

Radi and co-workers [93] have also described a sensor developed using MIP films that can be used for entacapone detection. A three-electrode system involving a WE (GCE), CE (platinum wire electrode) and RE (Ag/AgCl/KCl) was employed herein, while the MIP layers were prepared using polyphenylenediamine (monomer) and entacapone (template). Electropolymerization was performed using CV by applying a potential between

0 and 0.8 V at a scan rate of 100 mV/s and electrochemical behavior of the films was studied using EIS and DPV. As a result of the study, the sensor presented a good selectivity for entacapone vs. levodopa and carbidopa, with a limit of detection near 5×10^{-8} M [93].

4. Molecular Imprinting Using MIP Particles Embedded in Pastes or Inks

This section brings to the scientific community newsworthy studies through reviews and original articles concerning strategies for preparing pastes or inks, used for the fabrication of molecularly imprinted polymers (MIPs)-decorated layers or films. Currently, preparation of sensitive layers on electrode surfaces is certainly the most frequently used technique for MIP-modified electrodes. Among the reviewed methods for forming MIP layers, dropcasting of a pre-prepared polymer paste and coating processes such as drop/dip or spin coating and screen printing, or through self-assembled monolayers (SAMs) [94] are shortly discussed hereafter. Hence, this part of the review focuses more on the performances of the resulting MIP-modified layers via their preparation and deposition techniques.

Research on pastes or inks for applicability within areas of electrochemistry and electroanalysis began in the mid-1950s [95]. Since then, preparing and deposition of paste (ink)-based electrodes modified with MIP soon became very attractive for sensing applications and photoelectrochemical devices; carbon pastes (CPs) belonged among the most popular electrode materials for preparation of various sensors, justified by their low price, ease of fabrication, fast response time, renewable surfaces, high sensitivity and low background current [96]. Generally, CP, defined as a heterogeneous mixture of a carbonaceous moiety with a suitable (usually liquid) binder, is a graphite/carbon-black paste aimed at the deposition of metal-free, electrically conductive layers by screen-printing or coating techniques [97].

Likewise, the composition of the pastes used for deposition of the successive layers may be altered by the addition of nanostructured materials [98] such as cofactors, stabilizers and mediators. More recently, silver nanoparticles (AgNPs), Ag nanowires (AgNWs), CuNWs, CuNPs, carbon nanotubes (CNTs), and reduced graphene oxide (rGO) have also been explored as nano-inks [99,100] and further incorporated either in these pastes or in a later stage on the working electrode. The most applied and comfortable routes to prepare MIP layers using inks and pastes are illustrated in Figure 5.

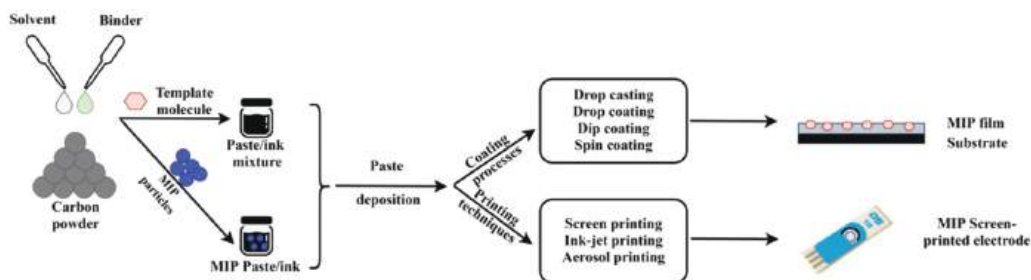


Figure 5. Routes for preparing MIP layers using inks or pastes.

Screen-printing technology [101] has emerged as a low-cost thick film technique commonly used in the mass production of highly reproducible and sensitive disposable sensing platforms with application in pharmaceutical, environmental and industrial analysis as well in (bio) chemical sensing, energy storage and microelectronics [102]. Being considered an easily controlled and automatic process due to electrode thickness and electrode composition, screen-printing permits the miniaturization of sensors, a wide choice of materials and incorporation of functionalized materials inside the screen-printing ink [103]. As expected, SPCE have attracted large interest due to their known unique properties, for instance, inexpensiveness, inertness, excellent stability and conductivity. By 2015, numerous newsworthy papers referring to screen-printing techniques, ink formulations and substrate

materials were published [102,104,105]. Nowadays, taking into account the type of ink and substrate, printing technologies that should be mentioned are screen printing (more than 60%, according to Wahyuni, et al. [98]), gravure printing, stereolithography, inkjet printing and aerosol jet printing [100].

The process of screen printing consists of layer-by-layer depositions of proper ink through a patterned mesh or screen onto a solid substrate, followed by a thermal curing treatment. Hence, successive layers can be deposited by this procedure and repeat patterns can be designed onto the same screen to enhance production speed. SPE usually combine a three-electrode configuration (working, reference and counter electrode) printed on different chemically inert substrates, i.e., flexible plastic (polycarbonate, polyimide, polyvinyl chloride and PEEK), ceramic, paper or glass substrates [106]; the substrates are easily modifiable with a great variety of commercial or self-made inks.

The pastes most commonly reported in SPE production are conductive (containing the polymer base dispersed in a solvent and the conductive material) or dielectric inks (often based on polymers or ceramics and form the encapsulating layer of the sensor) [98,107]. Among the solvents that participate in the ink components [108], there are two categories: organic and water-based. Organic solvents, such as ketone, esters and hydrocarbons, in general, have a low flash point, which promotes faster drying of the ink and low viscosity, which are generally qualities that facilitate the processing of inks. Recently, considering the performance and the environmental strategies, water-based inks have also been employed [109–111]. Gold paste is also employed in SPEs but less than carbon due to its higher cost [112]. The composition of the various inks used for printing on the electrodes determines the selectivity and sensitivity required for each analysis. It is important to point out that proper ink formulation is owned by the manufacturer as proprietary information and it has been shown that differences in ink composition e.g., type, size or loading of graphite particles and in the printing and curing conditions can strongly affect the electron transfer reactivity and the overall analytical performance of the resulting carbon sensors.

An extensively studied path used in the preparation of modified layers is based on the incorporation of pre-synthesized MIP microparticles/nanoparticles [113,114] (acting as a selective recognition element and a pre-concentrator agent for the determination of different templates) into layers or polymer matrices or containing a conducting material and binder (e.g., PVC) (e.g., carbon nanotubes (CNTs), graphene, graphite, or carbon black) [110,115] (Table 3). Cervini and Cavalheiro [116] revealed the most significant approaches for electrodes modified with MIP (including spin and drop coating and self-assembling of films on metal nanoparticles). Thus, the mentioned authors used a graphite-polyurethane composite matrix to prepare electrodes used in paracetamol (APAP) determination. Interference of phenacetin in the APAP response decreased remarkably when the proposed electrode was used.

Khosrokhavar et al. [117] described the successful preparation of an MIP nanoparticle/graphene suspension drop-coated as a thin layer onto the surface of the SPCE. For this purpose, two inks including silver ink (containing silver and PVC powders with mass percentages of 97 and 3% respectively in 1:1 (v/v) acetone/cyclohexanone solution) and carbon ink (containing 80% graphite, 12% dibutyl phthalate (DBP) and 8% PVC in 1:1 (v/v) acetone-cyclohexanone solution) were prepared. The electrochemical sensor used for the selective detection of an antidepressant drug, sertraline (STR) exhibited good sensitivity ($177.25 \mu\text{A L } \mu\text{mol}^{-1}$) and recoveries above 98%.

Another significant study was described by Nontawong et al. [118], where the team reported the preparation of dual-imprinted electrodes modified with graphene to simultaneously determine 8-hydroxy-2'-deoxyguanosine (8-OHdG) and 3-nitrotyrosine (3-NT) and assesses oxidative and nitrative biomarkers in urine and plasma samples. The synthesized composites, mixed separately with graphene ink, were further screened as hydrophobic barrier layers on filter paper. The smart devices revealed selectivity and sensitivity leading to low detection limits of $0.0027 \mu\text{M}$ for 3-NT and $0.0138 \mu\text{M}$ for 8-OHdG.

In another screen-printing preparation strategy, a graphite ink made of a mixture of graphite powder and hydroxyethyl cellulose was chosen [119]. The electrochemical MIPs were incorporated in a composite paste SPE for the detection of an organic pollutant, Bisphenol A (BPA). The results proved the reliability of the device with an LOD as low as 0.06 nM and also the selectivity vs. carbamazepine and ketoprofen. BPA was also detected using a simple and ultra-low-cost, disposable paper-based potentiometric sensor, reported by Kamel et al. [120]. The prepared BPA-MIP nanobeads were mixed with the PVC membrane cocktail and incorporated by dropcasting into recyclable and biodegradable paper. The sensor was proven to be selective towards other phenols, exhibiting a detection limit of 0.15 μ M.

An entrapment agent such as poly(methyl methacrylate) (PMMA) was suitable to carry out the incorporation of the synthesized MIP particles. For example, a QCM-based sensor for volatile organic compounds was prepared by spin coating a dispersion containing the MIP particles and PMMA on an AT quartz crystal resonator. The resulting devices tested towards toluene or p-xylene vapor showed potential for developing QCM sensors with MIP [121].

An interesting design of a biosensor for detecting lipopolysaccharides (LPS) derived from *Pseudomonas aeruginosa* was proposed by Iordache et al. [122] using MIP-modified SPCE. As described in their research, the strategy was based on doping the mixture with electroactive particles of zinc oxide, while the sol-gel precursor solution was dripped directly onto the SPCE using the dropcasting method. The MIP films prove stability at re-use, recognizing the LPS from *Pseudomonas aeruginosa* to a greater extent than the LPS from *Escherichia coli*, when using 16.7 μ g/mL aqueous LPS solutions.

Another successful attempt, accomplished by Blanco-López et al. [30], for preparing electrodes modified with MIP layers, refers to imprinting rifamycin SV (RSV), a macrocyclic antibiotic. Their study involved the drop coating of the electrode surface with a solution of a preformed polymer (polyphosphazenes) as recognition element. The final electrode exhibited selectivity towards dopamine and NADH as well as excellent reusability up to 25 times without signs of film loss or memory effects. The same group investigated the behavior of diclofenac by modifying carbon composite electrodes of different nature (polytetrafluoroethylene-graphite, epoxy graphite and epoxy-carbon black) with MIP particles. The drop coating method was also used for the modification of hanging a mercury drop electrode (HMDE) with MIP-DMF casting solution, which was applied in the determination of ascorbic acid [123].

One interesting approach used in the preparation of electrodes modified with MIP, is based on spin coating. The study carried out by Liuduan and co-workers [124] targeted the preparation of a sensor for phenylephrine detection. In this respect, a precursor solution for MIP, prepared in the presence of phenylephrine (as template), was dropped onto the surface of a GCE and the excess solution was eliminated by spin coating. The modified electrode was used in the determination of phenylephrine. Some years later, Ebarvia et al. [125] developed a biomimetic piezoelectric quartz crystal sensor for the determination of antibiotic chloramphenicol in food products. In their work, an MIP sensing layer was obtained by spin coating using a home-made device. The performance of this sensor refers to a sensitivity of about 73 Hz/log (conc., μ g·mL⁻¹), a detection limit of 7×10^{-8} μ g·mL⁻¹ and good repeatability (rsd below 10%). The development of an electrochemical sensor for 1-hydroxypyrene (1-OHP) based on a molecular imprinted TiO₂ gel matrix was also described by the group of Yang [126]. The 1-OHP-imprinted films were prepared by spincoating using film-forming stock solutions on quartz plates. The resultant 1-OHP-imprinted sensor had a detection limit of 3.353×10^{-10} M with the linear range 1×10^{-9} M– 2×10^{-7} M.

Another approach for MIP preparation relies on the self-assembly-copolymerization of mixtures containing the template and the monomers [127]. Shin et al. [128] reported the preparation of a thin polymer film on a self-assembled monolayer with 4-mercaptophenol and benzenethiol on a gold plate for the recognition of cholesterol. The poly(methyl

methacrylate) (PMMA) was then spincoated on the monolayer, leading to excellent recognition ability. The authors assumed that the difference of regularity and flatness, around 0.233 nm roughness value, after spincoating has an effect on the cholesterol recognition ability.

Roushani and colleagues [129] investigated an MIP electrochemical sensor for fast and direct determination of trazosine (TR). The large effective surface area and good electrical conductivity were obtained through a layer of AuNPs. MIP/AuNPs/SPCE was developed by directly dropping the synthesized MIP onto the surface of the AuNPs/SPCE, exhibiting great electrochemical signals in the potential range 0.6 mV for detecting trace TR with a good selectivity and a low detection limit (S/N = 3) of 0.3 μM.

Liu et al. [130] reported a composite of reduced graphene oxide/Fe₃O₄-ionic liquid-based MIP, which was dropcasted onto a GCE. RGO/Fe₃O₄-IL-MIP layer was used to construct an electrochemical sensor for diphenylamine (DPA). The performances of the sensor revealed a detection limit of 0.05 μM (S/N = 3) with a linear range of 0.1–30 μM proving the recognition in real samples.

Meanwhile, Angelis et al. [131] functionalized carbon black (fCB) by the insertion of oxygenated functional groups upon acid treatment with HNO₃ and H₂SO₄, developing an MIP-fCBPE (functionalized carbon black paste electrode) for imazethapyr (IMT) determination in rice samples. This method was applied after microwave-assisted extraction of IMT, leading to 96.3–105.7% accuracy by recovery assays. The electrochemical properties rely on the incorporation of molecularly imprinted polyvinylimidazole (MIP-VN) in the fCBPE, obtaining a limit of detection of 0.03 μmol L^{−1} and good reproducibility of the measurements (RSD% = 3.6).

Table 3. MIP-based sensors obtained using MIP particles embedded in pastes or inks.

Synthesis Method	Receptor	Support	Analyte	Characterization Method(s)	LOD	Refs.
Drop coating	MIP film	SPCE ¹	Sertraline	CV ² and DPV ³	1.99 × 10 ^{−9} M	[117]
Coating	MIP film	Paper-based device	8-hydroxy-20-deoxyguanosine and 3-nitrotyrosine	CV and SWV ⁴	1.38 × 10 ^{−8} M and 2.7 × 10 ^{−9} M	[118]
Dropcasting	MIP film	SPCE	Bisphenol A	CV and HPLC ⁵	6.0 × 10 ^{−11} M	[119]
Dropcasting	Membrane	Chromatography paper used as electrode	Bisphenol A	Potentiometric detection	1.5 × 10 ^{−7} M	[120]
Spincoating	MIP Membrane	GCE ⁶	Phenylephrine	DPV and HPLC	-	[124]
Spincoating	MIP film	Au electrode quartz crystal	Chloramphenicol	Oscillation frequency	7 × 10 ^{−8} μg·mL ^{−1}	[125]
Spincoating	MIP film	Quartz plates	1-hydroxypyrene	CV	3.353 × 10 ^{−10} M	[126]
Dropping	Film	SPCE	Trazosin	CV, DPV and EIS ⁷	3.0 × 10 ^{−7} M	[129]
Dropcasting	Film	GCE	Diphenylamine	DPV	5.0 × 10 ^{−8} M	[130]
Functionalization of carbon black paste electrode	Layer	Functionalized Carbon black	Imazethapyr	DPV	3.0 × 10 ^{−8} M	[131]

¹ SPCE: screen-printed carbon electrode; ² CV: cyclic voltammetry; ³ DPV: differential pulse voltammetry; ⁴ SWV: square wave voltammetry; ⁵ HPLC: high performance liquid chromatography; ⁶ GCE: glassy carbon electrode; ⁷ EIS: electrochemical impedance spectroscopy.

5. Molecular Imprinting by Sol–Gel Derived Techniques

The interest in materials obtained by sol–gel method has grown considerably in recent years, as evidenced by the multitude of published papers. The materials obtained by this method can be used in different applications, including chemical sensors and biosensors, coatings and catalysts [132].

Overall, the sol–gel process implies several actions such as activation of precursor (usually involves hydrolysis), polycondensation, gelation, aging, washing, drying and stabilization [133,134]. The sol–gel process involves the transition from liquid state to a “sol” and then into a “gel” network structure [135]. In this respect, metal alkoxides undergo hydrolysis in aqueous media to obtain hydroxyl groups. The next step involves

the obtaining of a 3D network by the formation of Si–O–Si bonds resulting from the polycondensation reaction of hydroxyl groups and remaining alkoxy groups. The reaction can be performed under basic or acidic conditions depending on the morphology of the material that is required.

The porosity and the morphology of the sol–gel materials depend on several parameters, i.e., the solvents, the pH, drying process, reaction conditions and catalysts. These aspects are very important because, given the porosity and morphology, the obtained materials can be used for different applications [133,136–138]. This synthesis method presents multiple advantages, namely mild synthesis conditions (for example, the synthesis can be performed at room temperature), the obtained materials possess good optical properties, high thermal stability and high porosity, which can be correlated with a high surface area [139–141]. The sol–gel materials can be prepared in different forms, including thin films (for sensors and coatings) [14,141–143], composites (such as alumina reinforced materials), particles (for solid-phase extraction or for incorporation in thin films for sensor development) [138].

By combining the sol–gel method with molecular imprinting, performant sensitive layers can be obtained for sensor development (Figure 6). The sol–gel MIP films can be prepared by the drop coating or spin coating method and also by electrodeposition [144,145]. Due to the good optical and semi-conductive properties, sol–gel thin films can be used for the development of optical sensors as well as for electrochemical sensors. Thereby, in this section of the review, sensors based on sol–gel MIP films are presented (according to the two procedures presented in Figure 6). Thus, in the first part of the section, MIP sensor recognition elements based on sol–gel are presented, while the second part presents some examples of hybrid methods based on the combined sol–gel/electropolymerization method. Table 4 presents the use of sol–gel technique for MIP-based sensors and their performances.

Guney and his team [146] proposed the preparation of an MIP film using sol–gel method, in order to develop an electrochemical sensor for theophylline (TP) detection. The film was deposited on a GCE surface, which was modified prior to MIP deposition. The functionalization was made using a functional monomer: CoG–TEICPS (Crocein orange G-triethoxy(3-isocyanatopropyl)silane) and TEOS (tetraethyl orthosilicate) in acidic conditions, after which the MIP film was deposited by spin coating using the same recipe but with the addition of the template, TP. The electrochemical behavior of the films was studied using two methods: CV and DPASV (differential pulse anodic stripping voltammetry), which revealed that the sensor was selective and attained a low limit of detection of 1.4×10^{-9} M [146].

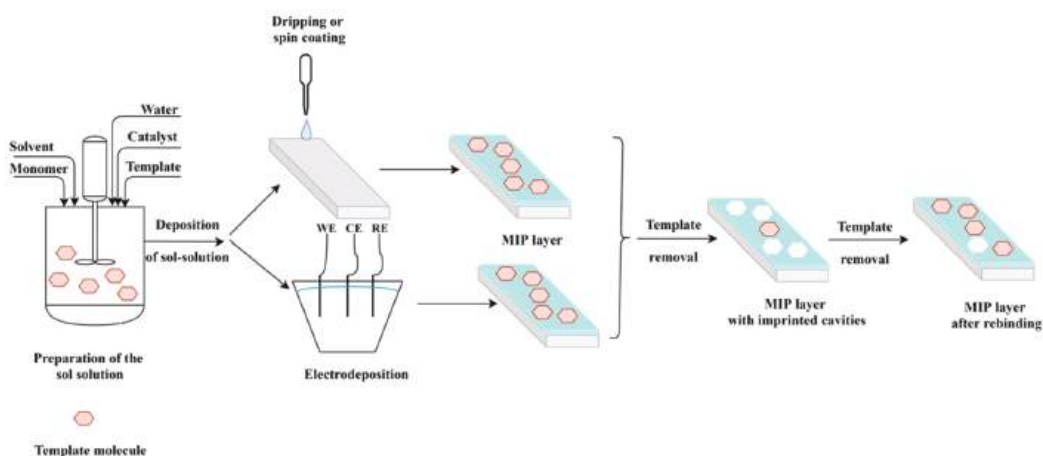


Figure 6. Sol–gel and combined sol–gel/electropolymerization methods for the preparation of MIP layers.

Table 4. MIP-based sensors obtained by sol–gel method.

	Deposition Method	Receptor	Support	Analyte	Characterization Method(s)	LOD	Refs.
Sol–gel method	Spin coating	MIP film	Modified GCE ¹	Theophylline	CV ² and DPASV ³	1.4×10^{-9} M	[146]
	Immersion	MIP film	Modified Au ⁴ electrode	Melamine	CV and SWV ⁵	0.4×10^{-9} M	[147]
	Spin coating	MIP film	Au surface of SPR device	Amoxicillin	SPR ⁶ and CV	7.3×10^{-11} M	[148]
	Spin coating	MIP film	Au modified glass substrate	Cis-jasmone	FT-IR ⁷ , LSPR ⁸	3.5 ppm	[149]
	Spin coating	MIP film	SPR substrate	Trinitrotoluene	SPR	0.26 ppb	[150]
	Immersion	MIP film	Modified GCE	Chlorogenic acid	DPV ⁹	3.2×10^{-8} M	[151]
	Dripping	MIP film	SPE ¹⁰	Europium	CV, EIS ¹¹ , DPV	1×10^{-7} M	[152]
	Dripping	MIP film	GCE	Aspartic acid	SWSV ¹²	1.77×10^{-6} M	[153]
	Coating	MIP film	MCNTs ¹³	Aristolochic acid	Adsorption experiments	0.034 µg/mg	[154]
	Immersion	MIP film	GCE	Trichlorfon	EIS and CV	2.8×10^{-9} g/mL	[155]
Hybrid sol–gel method	Electrochemical	MIP film	Au electrode	Clenbuterol	DPV	3.1×10^{-8} M	[156]
	Electrochemical	MIP film	GCE	Melamine	DPV	6.8×10^{-8} M	[157]
	Electrochemical	MIP film	Modified ITO ¹⁴ electrode	Naloxone	CV and DPV	2×10^{-8} M	[158]
	Electrochemical	MIP film	GCE	Mephedrone	SWV	8×10^{-10} M	[159]
	Electrochemical	MIP film	Modified GCE	Diethylstilbestrol	DPV	24.3 fg/mL	[160]
	Electrochemical	MIP film	Pencil graphite electrode	Ketamine	EIS and SWV	7×10^{-10} M	[161]

¹ GCE: glassy carbon electrode; ² CV: cyclic voltammetry; ³ DPASV: differential pulse anodic stripping voltammetry; ⁴ Au electrode: gold electrode; ⁵ SWV: square wave voltammetry; ⁶ SPR: surface plasmon resonance; ⁷ FT-IR: Fourier transform-infrared spectroscopy; ⁸ LSPR: localized surface plasmon resonance; ⁹ DPV: differential pulse voltammetry; ¹⁰ SPE: screen-printed electrode; ¹¹ EIS: electrochemical impedance spectroscopy; ¹² SWSV: square wave stripping voltammetry; ¹³ MCNTs: magnetic carbon nanotubes; ¹⁴ ITO: indium tin oxide electrode.

Bengamra et al. [147] developed a sensor based on an MIP membrane for electrochemical detection of melamine. The gold electrode was first modified with a mercaptopropyltrimethoxysilane (MPTMOS) layer. Subsequently, the MIP layer was obtained in acidic conditions using TEOS, phenyltrimethoxysilane (PTMOS) and methyltrimethoxysilane (MTMOS), after immersing the modified electrode in a solution of melamine. The final sensors were characterized by CV and SWV, resulting in a LOD of 0.4×10^{-9} M [147].

A selective SPR sensor based on an MIP film was developed by Ayankojo and co-workers [155], for detecting amoxicillin. The sol–gel precursor solution for MIP films consisted of methacrylamide (MAAM, functional monomer), TEOS, vinyltrimethoxysilane (VTES, coupling agent) and the template (amoxicillin), which was further used to coat uniformly the gold surface of an SPR sensor. The obtained sensors, tested using SPR and CV, recorded an LOD of 73 pM and a good selectivity for amoxicillin [148].

Another example of sensor based on MIP film is presented by Shang et al. [149]. In this case, a LSPR (localized surface plasmon resonance) sensor for cis-jasmone detection was developed using a sol–gel technique. The synthesis of the films involved the preparation of a solution containing TBOT (Tetrabutoxy titanium), the monomer (PTMOS, PTEOS), initiated with TiCl₄. Prior to MIP film deposition by spin coating, the glass substrate was modified with gold. For such LSPR sensors, the registered LOD was 3.5 ppm for cis-jasmone detection in vapor state [149].

In 2016, Giustina and co-workers [150] proposed an MIP-based SPR sensor for trinitrotoluene (TNT) detection. The sol–gel films were prepared by dissolving the silanes (APTES, TEOS and MPTMOS) and template (TNT) in ethanol and gelation took place in basic conditions. The films were deposited by spin coating onto the SPR substrate and the final sensor was analyzed by SPR in the 4.9 ± 2.8 ppb concentration range. In this case, a limit of detection for TNT of 0.26 ppb was estimated [150].

Ribeiro and her team [151] studied a sensor for the detection of chlorogenic acid in food samples. In a first step, the GCE electrode surface was modified with a layer consisting of MWCNTs and VTES. Following this procedure, an MIP sol–gel layer was deposited on

the surface of the modified electrode by immersing the electrode in the MIP solution and rotating at 1500 rpm. In this case, the MIP solution was prepared by mixing TEOS, PTMOS and APTES in 2-ethoxyethanol, with the catalyst solution of HCl containing the template (chlorogenic acid). The detection limit of the prepared sensor was 0.032 μM , which was suitable for chlorogenic acid detection [151].

Considering the toxic effect of europium on human health, Chen and co-workers [152] focused their interest on the development of a sensor for its detection. In this respect, they modified the surface of a SPE by electropolymerization using catechol, resulting in a poly (catechol) layer, after which the MIP layer was deposited. The precursor gel solution for the MIP was obtained by mixing TEOS, PTMOS and MTMOS with a solution of europium, in acidic conditions. The imprinted film was obtained by dripping the precursor solution on the modified electrode surface and dried at room temperature. The electrochemical behavior of the sensors was tested by different methods (CV, EIS, DPV), out of which DPV technique revealed a detection limit of 10^{-7} M for europium [152].

Chen and his team [153] developed a sol–gel MIP-based sensor for aspartic acid recognition. The MIP precursor solution was prepared by dissolving PEG (Polyethyleneglycol) in ethanol and, after stirring the template molecule [(L-Asp) $\text{Cu}_2^+(\text{NC-L-Asp})$] was added. Finally, TEOS was added to this solution, at reflux, and the films were cast in double layer, by dripping the solution on the GCE surface. In this case, a limit of detection of 1.77 μM was achieved by SWSV (square-wave stripping voltammetry) [153].

Studies on the effects on human health for the use of aristolochic acid have led to a link between its presences and liver cancer. Therefore, Li and her co-workers [156] developed a sensor based on an MIP, using the sol–gel technique, for aristolochic acid detection. In this respect, they prepared a precursor solution containing the template and the monomer (PTMOS) and kept it in the refrigerator, after which magnetic carbon nanotubes (MCNTs), previously functionalized with carboxyl groups, crosslinker (TEOS) and the catalyst were added. The modified MIP–MCNTs were extracted from the solution with a magnet and tested in rebinding experiments. The imprinting factor of MIP particles was 3.17, with the detection limit 0.034 $\mu\text{g}/\text{mg}$ [154].

Other concerning compounds that may affect human health are insecticides. For example, trichlorfon can cause memory problems, depression, disorientation, etc. Thus, Gao and co-workers [155], proposed an electrochemical sensor for its detection. The MIP film was synthesized by a sol–gel method in acidic condition, which involved the use of TEOS, PTMOS, MTMOS and the template (trichlorfon). The authors used a GCE as support for the MIP film deposition, which was performed by immersing the electrode in the previously prepared precursor solution. The films were analyzed by different electrochemical technique, i.e., EIS, CV and presented good sensitivity and selectivity, with a LOD of 2.8×10^{-9} g/mL [155].

In the next part of this section hybrid methods for sol–gel MIP films synthesis are presented. In this respect, many studies were found for MIP film synthesis by combining the sol–gel method with electropolymerization (according to the procedure sketched in Figure 6). In this case, the MIP solutions are prepared by sol–gel methods, whereas the deposition on the electrode surface is carried out by electropolymerization.

Recently, Liu and co-workers [156] developed a sensor for clenbuterol detection. Clenbuterol is used as veterinary medication. At the same time, if identified in human samples (athletes), it may be corroborated with doping. Therefore, in this study, a three-electrode system was used for sensor development and the imprinted films were deposited on the gold electrode surface. To this end, a sol–gel solution was prepared by dissolving the monomer (APTES), the crosslinker (TEOS), the template (clenbuterol) and KCl in ethanol, followed by electrochemical deposition at -0.8 V for 30 min. The prepared films were characterized by various techniques, from which DPV revealed a good value for the LOD of 31 nM [156].

The group of Xu [157] proposed an electrochemical sensor based on MIP for melamine detection. The MIP solution was prepared by dissolving TEOS, PTMOS, MTMOS and

melamine in ethanol/water/HCl, in which the GCE of the sensor system was immersed. The film was obtained after electrodeposition, by CV, when applying a potential range between 0 and 1.9 V at 50 mV/s. Ultimately, the films were analyzed by DPV using melamine solutions, in which case an LOD of 6.8×10^{-8} M was calculated [157].

In 2021, Shaabani et al. [158] proposed the development of an MIP-based sensor for naloxone detection. For this reason, the authors used a MWCNTs modified ITO electrode for the following sol-gel MIP film deposition. The sol-gel solution was prepared by mixing PTEOS, TEOS, trifluoroacetic acid (TFA) and the template in ethanol/water. After homogenization, pyrrole and LiClO_4 were added to this solution as well. The ITO modified electrode was immersed in this precursor solution and the film was obtained by electrodeposition in the -0.8 and 0.4 V potential range, for 10 scan cycles at a scan rate of 50 mV/s. CV and DPV were used to evaluate the performance of the MIP film, resulting in a limit of detection of $0.02 \mu\text{M}$. Moreover, the sensor presented a good selectivity when contacting compounds with similar structures [158].

Another interesting approach for MIP-based sensors was presented by Razavipanah and his co-workers [159] for mephedrone detection. Mephedrone is a stimulant drug from the class of amphetamines. In their study, a precursor solution containing PTEOS, TEOS, H_2O , ethanol, TFA and mephedrone was prepared, after which another solution containing tyramine, MWCNT@AuNPs nanocomposite and sodium dodecyl sulfate (SDS) was added. The electrode was placed into this final solution, and the MIP films were obtained by electrodeposition (potential between -0.8 and 1.2 V at 50 mV/s). The synthesized films were studied by different techniques. The ability of the films to detect the mephedrone was quantified by SWV, which indicated a detection limit of 0.8 nM [159].

In 2018, Bai and colleagues [160] developed an MIP-based sensor for diethylstilbestrol detection. This compound is used as a growth promoter for animals and produces negative effects on humans. During the experiments, a classical three-electrode system containing a GCE (working electrode), an Ag/AgCl (reference electrode) and a Pt electrode (counter electrode) was used. In this study, the MIP film was deposited on the GCE after its modification with MWCNTs, chitosan and AuNPs. For the synthesis of films, a precursor MIP solution was prepared from APTES, OTOMS (octyltriethoxysilane), TEOS, template, 2-ethoxyethanol/ water and hydrochloric acid as catalyst. Subsequently, the electrode was immersed in this solution to obtain the MIP film by electrodeposition (potential range -0.5 and 0.5 V). The electrochemical behavior of the films was studied by DPV, resulting a low LOD of 24.3 fg/mL [162].

Deiminiat and colleagues [161] proposed an electrochemical MIP-based sensor for determining the content of ketamine. In this respect, sol-gel films were deposited on the surface of a pencil graphite electrode. The precursor solution contained TEOS, PTEOS, water and ethanol mixed with a solution containing TFA and ketamine. After 2 h, this solution was mixed with another solution containing tyramine, SDS and MWCNT@AuNPs in DMF, and afterwards used for film electrodeposition, by cyclic voltammetry (potential range -0.8 and 1.2 V for 10 scan cycles). The characteristics of the films were studied using EIS and SWV, in which case a limit of detection of 0.7 nM was registered. Moreover, the sensors presented reproducibility, sensitivity and selectivity [161].

6. Molecular Imprinting by Phase-Inversion

Bio-sensing systems based on molecularly imprinted membranes (or MIMs), have received considerable attention from researchers in various fields. In these types of systems, the recognition component is represented by the imprinted membranes, which are integrated with a transducer component. The possibility of direct and rapid determination of the target analyte by the interaction with the recognition element was a stimulating factor for the application of such systems, which are excellent alternatives to the classical bio-analytical methods. The biomimetic sensor-based membranes are used for food, environmental and clinical determinations, due to their high sensitivity, specificity and stability [162].

The first reports about the MIMs were published about 30 years ago [163–165], in which case free-standing membranes or thin polymer membranes were prepared on the surface of a solid support, following classical imprinting recipes [163,164]. Only one of these studies [164] employed a phase-inversion method starting from linear polymer precursors.

Generally, the phase inversion method consists of the use of an already prepared polymer, which is solubilized in a solvent in the presence of the template, so that a complex is formed between the target analyte and the functional polymer (Figure 7). During phase inversion, the template is included in the membrane. The template is extracted afterwards from the solid membrane leading to the formation of a MIM. Phase inversion can be performed using two methods, as follows: (i) wet phase inversion (WPI), in which case the membrane is obtained by coagulation in a coagulation bath, as long as the template is not soluble in the coagulation bath (the solvent diffuses from the polymer solution in the coagulation bath, while the polymer changes to a solid membrane, Figure 7), and (ii) dry phase inversion (DPI), in which case the membrane is obtained by solvent evaporation, as long as the polymer can withstand the heating process (the solvent is evaporated, while the polymer changes to a solid membrane, as shown in Figure 7).

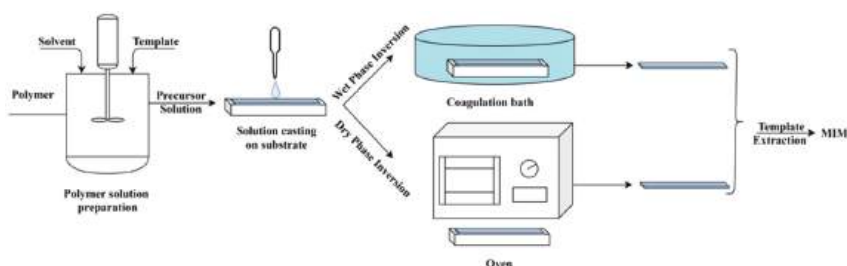


Figure 7. Synthesis of molecular imprinted membranes by phase inversion.

Rarely, after the phase inversion, a chemical crosslinking reaction of membranes follows; this is because in most of the cases, the physical crosslinking is sufficient for endowing the MIM with chemical and mechanical stability. The physical crosslinking means that the polymer chains are “fixed” by hydrogen bonds or other physical interactions in the presence of a template by solvent evaporation [166] or phase-inversion precipitation [167]. This process is very similar to “bioimprinting” in proteins, whereas the structure is “frozen” either by lyophilization or by chemical crosslinking in the presence of a template. A range of structures are initially formed when the template interacts with the linear polymer, the heterogeneity of folded structures formed during phase inversion being very similar with the structure formed when the polymer chains crosslink covalently.

Usually, the interactions between the template and the polymer are non-covalent for the phase inversion method. Nevertheless, some studies have presented the possibility for the chemical functionalization of a monomer with the template molecules, and this latter monomer is further polymerized to serve as a functional polymer for the subsequent phase inversion. In this case, the template extraction from the MIMs is performed by destroying the covalent bonds between the template and the polymer.

The advantage of the phase inversion refers to the fact that it usually implies mild conditions for coagulation without affecting the properties of sensible templates. Thus, phase inversion is very much adequate for preparing MIMs for templates with low chemical, thermal or light stability. Moreover, the functional polymer can be prepared in optimum conditions with no interference from the presence of template molecules, which in some cases can inhibit the polymerization process. Thereby, the phase inversion method is appealing; yet, it is somehow limited by the fact that it usually applies for functional (co)polymer and templates, for which a common solvent can be found, to prepare the precursor solution. Another issue encountered when approaching the WPI is the medium-high solubility of the template in the coagulation bath, which leads to low specificity of the

prepared MIM. In this case, to avoid the diffusion of the template during the imprinting process, the DPI can be applied. On the other hand, if the polymer is susceptible to degradation during DPI and an adequate non-solvent for the polymer and template can be found, the preferred method to prepare MIMs is the WPI.

The copolymers of acrylonitrile (AN) with acrylic acid (AA) or MAA are often used for membrane preparation by phase inversion for sensor application [168–170]. AN is used as a structural monomer, due to cyan polar groups that render stability to the imprinted cavities via strong hydrogen bonding, while AA or MAA are chosen as functional monomers due to their ability to interact with polar compounds. For instance, Kobayashi and his group [171] were the first to develop a quartz-crystal microbalance (QCM) sensor employing a PAN copolymer imprinted membrane for the detection of the stimulant drug caffeine. The authors used the phase inversion precipitation method to prepare two imprinted PAN copolymers membranes.

A typical preparation of an electrochemical sensor by WPI is described by Yang et al. [172]. In this respect, a molecularly imprinted film (MIF) was deposited on the surface of a Ti/TiO₂ electrode and used as recognition element of an electrochemical sensor with high selectivity and sensitivity for bisphenol A (BPA). In a first step, p(AN-co-AA) was synthesized according to solution radical copolymerization method using AN and AA in dimethyl sulfoxide (DMSO) with radical initiator AIBN. Step two referred to preparing the precursor solution of p(AN-co-AA) in DMSO, containing BPA as template molecule, followed by casting it directly onto the pretreated Ti/TiO₂ electrode. The MIF resulted after precipitation in the coagulation bath and the sensor assembly was kept in ultrapure water. Maintaining the membrane in the wet form after template removal is necessary, in order to preserve the imprinted network. If the membrane is dried by conventional methods, the shrinkage affects drastically the shape and size of the imprinted cavities which may collapse during this procedure. The Ti/TiO₂/MIF sensor showed a linearity within the range 4.4 nM–0.13 mM, and a very low detection limit of 1.3 nM. Additionally, the sensor presented excellent recognition selectivity for BPA in competition with analogue compounds. This sensor was applied to detect BPA in paper cup samples and seawater, with high recoveries of 86–110% and with low relative standard deviations of 1.3–3.2%. Table 5 summarizes different methods via phase inversion applied for the preparation of MIP-based layers for sensors.

Another paper describing the use of PAN copolymers in the WPI process is that of Stoica et al. [168], where the preparation of a MIM that may be applied for preparing sensors for ephedrine detection is depicted. In this approach, two copolymers of AN and MAA with different weight ratios (80:20 and 75:25) were prepared by emulsion polymerization and used to obtain two membrane variants, using ephedrine chlorohydrate as template. The membranes were tested by batch adsorption measurements in the attempt of finding the optimum recipe for preparing a film with affinity for ephedrine. In this regard, the MIMs with 20 wt% MAA were found to be more adequate to retain ephedrine with an adsorption capacity of 122 mg ephedrine/g polymer and an imprinting factor of 3.4. Furthermore, this same group [173] also used similar copolymer precursors to prepare sensitive membranes for the detection of explosives, more precisely, trinitrotoluene (TNT). The composition of the p(AN-co-AA) was varied this time using the following ratios AN:AA= 80:20 and 85:15.

Another method for TNT and dinitrotoluene (DNT) retention is described by Turner et al. [174]. Using a phase inversion method with the introduction of the template after the polymer synthesis, a range of molecularly imprinted polymer films were prepared consisting of AN as a matrix monomer and methacrylamide (MAAm) as a functional monomer (96:4). After template removal, the films exhibited no rebinding activity, probably due to a collapse of the films' porous structure. The addition of a crosslinker (EGDMA) stabilized the macroscopic structure of the films, which provided, though limited, adsorption properties.

Besides PAN copolymers, many other synthetic polymers such as polyamide [175], polystyrene and polysulfonemay be used for preparing MIMs by the phase inversion. For example, an amperometric immunosensor for the determination of antirabbit IgG

was developed using phase inversion to prepare a porous conductor polymer graphite-polysulfone electrode [176]. Poly(ethylene-co-vinyl alcohol) copolymers (EVAL), with an ethylene molar content of 32% and 44% were used to produce MIMs, by phase inversion for the selective recognition of saccharides of biomedical interest [177].

Another polymer with great film-forming properties used for MIMs preparation is polyvinyl alcohol (PVA). However, when using PVA, chemical crosslinking is needed. In the two reports from Sarbu and colleagues [178,179], polyvinyl alcohol with a hydrolysis degree of over 99% and molecular weight of 1500 g/mol was used for MIMs forming and the wet membranes were crosslinked by acetylation with glutaraldehyde (GA). The templates in these two studies were the pesticides triclofon (*O,O*-dimethyl-1-hydroxy-2,2,2-trichloroethyl phosphanate) [178] and atrazine (1-Chloro-3-ethylamino-5-isopropylamino-2,4,6-triazine) [179], respectively. The procedure of crosslinking was optimized using various concentrations of GA in sulfuric acid/sodium sulfate media. The crosslinked MIMs were insoluble in water or any other solvents, thus proving the success of the crosslinking reaction. Further in the study, the authors used the remaining free aldehyde groups on the membrane surface to immobilize enzymes covalently (i.e., Tyrosinase). Thereby, these interesting studies may be useful for preparing future immuno-enzymatic electrochemical sensors.

Another important advantage of the phase inversion technology is that natural (bio)polymers are not excluded, since the whole methodology is based on using previously prepared polymers [180]. An example of a biopolymer MIM prepared by DPI is provided by Ma and co-workers [181], in which case a MIM was prepared in aqueous media using chitosan (CS) as the functional polymer, naringin (NG) as the template and polyethylene glycol (PEG) as the porogen. The best performance of imprinted membranes was recorded for a weight ratio of CS: NG = 15:1, when sulfuric acid was used as crosslinker. The FT-IR spectra proved that non-covalent interactions appear between the functional polymer and the template molecules. The prepared membrane was used to separate NG from neohesperidin/NG mixtures in aqueous media.

For the preparation of a hybrid natural-synthetic MIM for α -amylase retention, Silvestri et al. [182] used a mixture of dextran (Mw 76,900 Da) and poly (ethylene-co-vinyl alcohol) EVAL (intrinsic viscosity 8.44 dl/g) having an ethylene molar content of 40%. Solutions in DMSO with 15 wt% polymers were prepared with two ratios of dextran: EVAL = 30:70 and 40:60, after which α -amylase was added. In this study, the WPI took place in two steps, as follows: first, the casted solutions were immersed in DMSO:H₂O = 50:50 solution (first phase-inversion bath) and afterwards in water (second phase-inversion bath). Interestingly, the selectivity results showed that α -amylase was selectively retained by 1.96-fold compared to albumin.

Lee and his co-workers [183] also described an interesting method for the preparation of hybrid MIM by WPI using a covalently bonded dummy template. A hybrid MIM has the advantage of combining the selectivity of molecular imprinting with the mechanical resistance of the support membrane. It is well known that a membrane presents a great specific surface area and possess a great number of binding sites, at the same time, due to the porous structure that offers a facile access of analyte solutions. In this work, core-shell polymer particles were first produced using 1-naphthol as mimic (dummy) template for CIT (Citrinin). The template was covalently bonded to the matrix, by using α naphthol methacrylate (NAM) monomer to create a polymeric shell around divinyl benzene (DVB) particles. In the second step, hybrid MIMs were prepared by mixing the resultant core-shell MIP particles with polyether sulphone (PES) in a *N*-methyl pyrrolidone (NMP) solution. The latter solution was cast on glass plates and transformed into MIMs by WPI in a water coagulation bath. The assessment of CIT was performed by liquid chromatography with fluorescence detection (HPLC-FD), in which case the LOD and LOQ were found to be 0.5 and 1.7 ng g⁻¹, respectively. The overall results pointed towards sufficient sensitivity of the MIMs for CIT, being recommended for the analysis of CIT in rice [183].

Table 5. MIP-based sensors obtained by phase inversion method.

Synthesis Method	Receptor	Support	Analyte	Characterization Method(s)	LOD	Refs.
Casting	MIP film	Ti/TiO ₂ electrode	Bisphenol A	Amperometric measurements	1.3 × 10 ^{−9} M	[173]
Casting	Hybrid MIP membrane	Glass support	Citrinin	Batch binding, HPLC ¹	0.5 ng·g ^{−1}	[182]
Casting	MIP Membrane	Conductive graphite	Trimethoprim	Potentiometric measurements	4.01 × 10 ^{−7} M	[184]
Casting	MIP Membrane	Conductive graphite	Enrofloxacin	Potentiometric measurements	0.9 µg·mL ^{−1}	[185]
Dropwise	MIP Film	Screen-printed gold electrode	Regenerating Protein 1B	CV ²	0.1 pg·mL ^{−1}	[186]
3D-Imprinting	MIP Membrane	Polyvinylidene fluoride/carbon black membrane	Non-woven (Polyester-17153) and 5000 mesh fabric	Morpho-structural, CV	/	[187]

¹ High performance liquid chromatography; ² CV: cyclic voltammetry.

It is important to mention that hybrid membranes can also be prepared using alternative methods. Such hybrid membranes for sensor development are described by Rebelo and his group [184], where the MIP particles are synthesized by non-covalent complexation of the template with the functional monomers. Herein, the polymeric sensor was prepared using MIP particles, synthesized from MAA and 2-vinyl pyridine as functional monomers, and trimethoprim (TMP) as a template, while the polymer matrix was polyvinylchloride (PVC). Hence, theMIM membrane was obtained without the use of phase inversion. The sensors prepared in this manner displayed a linear behavior against the TMP logarithmic concentration, in a wide concentration range. A very similar method is described in [185], using enrofloxacin as a template.

The epitope approach can be applied for MIP preparation not only by surface polymerization but also by phase inversion. An example of the epitope dry phase inversion is described by Jurcevic and his group [186]. EVAL copolymers were dissolved in DMSO containing the following template peptides: SCSGFKKKWKDESCCK (Peptide 2), KSWDT-GSPSSANAGYCAS (Peptide 4) and KESSTDDSNVWIG (Peptide 6) of REG1B. The preparation of peptide–MIMs was performed by the dropwise addition of thisprecursor solutionon the gold substrate of a screen-printed electrode. The urine samples from patients with pancreatic cancer revealed higher electrochemical response in comparison with samples from healthy persons, which was consistent with their elevated levels of the marker protein.

7. Conclusions

This review provided an overview on the progress of MIP layers synthesized by various modern and dedicated techniques such as surface polymerization, electropolymerization, sol–gel technique, phase-inversion and hybrid methods including MIP-dropped inks/pastes or combined methods of sol–gel and electropolymerization. In this respect, using different systems of monomers, template molecules and solvents, some very sensitive and promising sensing tools were developed. In most of the cases, the sensors showed high sensitivity, selectivity, reproducibility and most importantly, low limit of detection. However, electropolymerization seems to be by far the most promising method to prepare highly sensitive sensors, especially MIP-based electrochemical sensors. From the examples described in Section 3, for detecting different pollutants (dyes, polycyclic aromatic hydrocarbon), drugs (antibiotics), illicit drugs (cocaine), the reported limit of detection for such sensors ranges from 1 µM to 1 fM. On the other hand, the combined sol-gel/electropolymerization and ink-based sensors are somewhat less complex and cheaper to produce, but with higher values of LOD, in the µM range.

It is also important to note that surface modification or the sol–gel technique is usually preferred for preparing optical and spectroscopic sensors, while the phase inversion method is more applicable to electrochemical sensors and chromatographic applications. Although the electrochemical sensors are generally the most sensible, the use of MIP for

other detection techniques led in some cases to significant improvements of sensibility and selectivity relative to the state-of-the-art of detection methods applied for optical, spectroscopic or chromatographic applications.

Future challenges in the field of MIP layer preparation targets further improvements of the sensitivity, selectivity and reproducibility for real sample applications, especially for peptides and protein detection [42,44,45]. Due to the intrinsic properties of the MIP sensors such as robustness, reliability, accuracy, reproducibility, long-term stability and portability, future requirements should be considered in scenarios where MIP layers can potentially be tools for routine applications. For instance, MIP layers for optical biosensors could have a significant impact in targeted applications considering that users are interested in solutions with low maintenance and servicing, such as for environmental monitoring (e.g., screening of estrogen [188] or the sensing of small organic contaminants [189,190]).

Author Contributions: Conceptualization, A.S.; funding acquisition, T.-V.I. and A.-M.G.; writing—original draft, A.-M.G., E.-B.S., T.-V.I. and A.S.; writing—review and editing, T.-V.I., A.S. and A.-M.G.; supervision, A.S.; project administration, A.-M.G. and T.-V.I. All authors have read and agreed to the published version of the manuscript.

Funding: This research was funded by the Romanian Funding Agency UEFISCDI, through the supporting project 255PED/2020 TOXINSENS and by the Ministry of Research, Innovation and Digitalization through project NUCLEU PN.19.23.02.01 (Sub-theme MAT-INNOVA).

Institutional Review Board Statement: Not applicable.

Informed Consent Statement: Not applicable.

Data Availability Statement: The data presented in this study are available in the article.

Acknowledgments: The authors thank the Romanian Funding Agency UEFISCDI the Ministry of Research, Innovation and Digitalization for funding the projects (255PED/2020 TOXINSENS and NUCLEU PN.19.23.02.01.MAT-INNOVA) that made possible the research for this review.

Conflicts of Interest: The authors declare no conflict of interest.

References

- Plata, M.R.; Contento, A.M.; Ríos, A. State-of-the-Art of (Bio)Chemical Sensor Developments in Analytical Spanish Groups. *Sensors* **2010**, *10*, 2511–2576. [\[CrossRef\]](#)
- Martínez-Cisneros, C.S.; Ibáñez-García, N.; Valdés, F.; Alonso, J. LTCC microflow analyzers with monolithic integration of thermal control. *Sens. Actuators A* **2007**, *138*, 63–70. [\[CrossRef\]](#)
- Gallardo, J.; Alegret, S.; Valle, M. Flow-injection electronic tongue based on potentiometric sensors for the determination of nitrate in the presence of chloride. *Sens. Actuators B* **2004**, *101*, 72–80. [\[CrossRef\]](#)
- Uygun, Z.O.; Uygun, H.D.E.; Ermiş, N.; Canbay, E. Chapter 3—Molecularly Imprinted Sensors—New Sensing Technologies. In *Biosensors—Micro and Nanoscale Applications*; Intech: London, UK, 2015; pp. 85–108.
- Upadhyay, S.; Sharma, M.K.; Shaik, M.; Das, R.; Rao, V.K. Sensors—A Nanotechnological Approach for the Detection of Organophosphorous Compounds/Pesticides. In *The Impact of Pesticides*, 1st ed.; AcademyPublish.org: Wyoming, MI, USA, 2012; pp. 391–415.
- Boysen, R.I.; Schwarz, L.J.; Nicolau, D.V.; Hearn, M.T.W. Molecularly imprinted polymer membranes and thin films for the separation and sensing of biomacromolecules. *J. Sep. Sci.* **2017**, *40*, 314–335. [\[CrossRef\]](#) [\[PubMed\]](#)
- Cheong, W.J.; Yang, S.H.; Ali, F. Molecular imprinted polymers for separation science: A review of reviews. *J. Sep. Sci.* **2013**, *36*, 609–628. [\[CrossRef\]](#) [\[PubMed\]](#)
- Li, S.; Ge, Y.; Piletsky, S.A.; Lunec, J. *Molecularly Imprinted Sensors: Overview and Applications*, 1st ed.; Elsevier: Amsterdam, The Netherlands, 2012; p. 388.
- Ye, L.; Haupt, K. Molecularly imprinted polymers as antibody and receptor mimics for assays, sensors and drug discovery. *Anal. Bioanal. Chem.* **2004**, *378*, 1887–1897. [\[CrossRef\]](#) [\[PubMed\]](#)
- Chen, L.; Xua, S.; Li, J. Recent advances in molecular imprinting technology: Current status, challenges and highlighted applications. *Chem. Soc. Rev.* **2011**, *40*, 2922–2942. [\[CrossRef\]](#) [\[PubMed\]](#)
- Verheyen, E.; Schillemans, J.P.; Van Wijk, M.; Demeinix, M.-A.; Hennink, W.E.; Van Nostrum, C.F. Challenges for the effective molecular imprinting of proteins. *Biomaterials* **2011**, *32*, 3008–3020. [\[CrossRef\]](#)
- Guo, T.; Deng, Q.; Fang, G.; Liu, C.; Huang, X.; Wang, S. Molecularly imprinted upconversion nanoparticles for highly selective and sensitive sensing of Cytochrome C. *Biosens. Bioelectron.* **2015**, *74*, 498–503. [\[CrossRef\]](#)

13. Tretjakov, A.; Syritski, V.; Reut, J.; Boroznjak, R.; Öpik, A. Molecularly imprinted polymer film interfaced with Surface Acoustic Wave technology as a sensing platform for label-free protein detection. *Anal. Chim. Acta* **2016**, *902*, 182–188. [\[CrossRef\]](#)
14. Gavrilu, A.M.; Zaharia, A.; Paruch, L.; Perrin, F.X.; Sarbu, A.; Olaru, A.G.; Paruch, A.M.; Iordache, T.V. Highly efficient materials working in tandem against pathogenic bacteria in wastewaters. *J. Hazard. Mater.* **2020**, *399*, 123026. [\[CrossRef\]](#)
15. Pešić, M.P.; Todorov, M.D.; Becskerek, G.; Horvai, G.; Verbić, T.Ž.; Tóth, B. A novel method of molecular imprinting applied to the template cholesterol. *Talanta* **2020**, *217*, 121075. [\[CrossRef\]](#)
16. Ertürk, G.; Mattiasson, B. Molecular Imprinting Techniques Used for the Preparation of Biosensors. *Sensors* **2017**, *17*, 288. [\[CrossRef\]](#)
17. Liu, X.; Wu, F.; Au, C.; Tao, Q.; Pi, M.; Zhang, W. Synthesis of molecularly imprinted polymer by suspension polymerization for selective extraction of p-hydroxybenzoic acid from water. *J. Appl. Polym. Sci.* **2019**, *136*, 46984. [\[CrossRef\]](#)
18. Zhao, G.; Liu, J.; Liu, M.; Han, X.; Peng, Y.; Tian, X.; Liu, J.; Zhang, S. Synthesis of Molecularly Imprinted Polymer via Emulsion Polymerization for Application in Solanesol Separation. *Appl. Sci.* **2020**, *10*, 2868. [\[CrossRef\]](#)
19. Pardeshi, S.; Singh, S.K. Precipitation polymerization: A versatile tool for preparing molecularly imprinted polymer beads for chromatography applications. *RSC Adv.* **2016**, *6*, 23525–23536. [\[CrossRef\]](#)
20. Branger, C.; Meouche, W.; Margaillan, A. Recent advances on ion-imprinted polymers. *React. Funct. Polym.* **2013**, *73*, 859–875. [\[CrossRef\]](#)
21. Janiak, D.S.; Kofinas, P. Molecular imprinting of peptides and proteins in aqueous media. *Anal. Bioanal. Chem.* **2007**, *389*, 399–404. [\[CrossRef\]](#)
22. Zhang, Z.; Cao, X.; Zhang, Z.; Yin, J.; Wang, D.; Xu, Y.; Zheng, W.; Li, X.; Zhang, Q.; Liu, L. Synthesis of dummy-template molecularly imprinted polymer adsorbents for solid phase extraction of aminoglycosides antibiotics from environmental water samples. *Talanta* **2020**, *208*, 120385. [\[CrossRef\]](#)
23. Moreno-Bondí, M.C.; Urraca, J.L.; Benito-Pena, E.; Navarro-Villoslada, F.; Martins, S.A.; Orellana, G.; Sellergren, B. Molecularly imprinted polymers as biomimetic receptors for fluorescence-based optical sensors. In Proceedings of the Third European Workshop on Optical Fibre Sensors (SPIE), Naples, Italy, 2 July 2007; Volume 6619.
24. Sharma, P.S.; Dabrowski, M.; D'Souza, F.; Kutner, W. Surface development of molecularly imprinted polymer films to enhance sensing signals. *TrAC Trends Anal. Chem.* **2013**, *51*, 146–157. [\[CrossRef\]](#)
25. Holthoff, E.L.; Bright, F.V. Molecularly templated materials in chemical sensing. *Anal. Chim. Acta* **2007**, *594*, 147–161. [\[CrossRef\]](#) [\[PubMed\]](#)
26. Guan, G.; Wang, S.; Zhou, H.; Zhang, K.; Liu, R.; Mei, Q.; Wang, S.; Zhang, Z. Molecularly imprinted polypyrrole nanonecklaces for detection of herbicide through molecular recognition-amplifying current response. *Anal. Chim. Acta* **2011**, *702*, 239–246. [\[CrossRef\]](#) [\[PubMed\]](#)
27. Sharma, P.S.; Pietrzyk-Le, A.; D'Souza, F.; Kutner, W. Electrochemically synthesized polymers in molecular imprinting for chemical sensing. *Anal. Bioanal. Chem.* **2012**, *402*, 3177–3204. [\[CrossRef\]](#) [\[PubMed\]](#)
28. Malitesta, C.; Mazzotta, E.; Picca, R.A.; Poma, A.; Chianella, I.; Piletsky, S.A. MIP sensors—The electrochemical approach. *Anal. Bioanal. Chem.* **2012**, *402*, 1827–1846. [\[CrossRef\]](#)
29. Blanco-López, M.C.; Lobo-Castañón, M.J.; Miranda-Ordieres, A.J.; Tuñón-Blanco, P. Electrochemical sensors based on molecularly imprinted polymers. *TrAC Trends Anal. Chem.* **2004**, *23*, 36–48. [\[CrossRef\]](#)
30. Blanco-López, M.C.; Gutiérrez-Fernández, S.; Lobo-Castañón, M.J.; Miranda-Ordieres, A.J.; Tuñón-Blanco, P. Electrochemical sensing with electrodes modified with molecularly imprinted polymer films. *Anal. Bioanal. Chem.* **2004**, *378*, 1922–1928. [\[CrossRef\]](#)
31. Diaz-Diaz, G.; Antuna-Jimenez, D.; Blanco-López, M.C.; Lobo-Castañón, M.J.; Miranda-Ordieres, A.J.; Tuñón-Blanco, P. New materials for analytical biomimetic assays based on affinity and catalytic receptors prepared by molecular imprinting. *TrAC Trends Anal. Chem.* **2012**, *33*, 68–80. [\[CrossRef\]](#)
32. Balamurugan, S.; Spivak, D.A. Molecular Imprinting in Monolayer Surfaces. *J. Mol. Recognit.* **2011**, *24*, 915–929. [\[CrossRef\]](#)
33. Zahedi, P.; Ziaee, M.; Abdouss, M.; Farazin, A.; Mizaiakoff, B. Biomacromolecule template-based molecularly imprinted polymers with an emphasis on their synthesis strategies: A review. *Polym. Adv. Technol.* **2016**, *27*, 1124–1142. [\[CrossRef\]](#)
34. Qin, L.; He, X.-W.; Yuan, X.; Li, W.-Y.; Zhang, Y.-K. Molecularly imprinted beads with double thermosensitive gates for selective recognition of proteins. *Anal. Bioanal. Chem.* **2011**, *399*, 3375–3385. [\[CrossRef\]](#)
35. Ge, Y.; Turner, A.P. Too large to fit? Recent developments in macromolecular imprinting. *Trends Biotechnol.* **2008**, *26*, 218–224. [\[CrossRef\]](#)
36. Lv, Y.; Tan, T.; Svec, F. Molecular imprinting of proteins in polymers attached to the surface of nanomaterials for selective recognition of biomacromolecules. *Biotechnol. Adv.* **2013**, *31*, 1172–1186. [\[CrossRef\]](#)
37. Hillberg, A.; Tabrizian, M. Biomolecule imprinting: Developments in mimicking dynamic natural recognition systems. *IRBM* **2008**, *29*, 89–104. [\[CrossRef\]](#)
38. Dong, C.; Shi, H.; Han, Y.; Yang, Y.; Wang, R.; Men, J. Molecularly imprinted polymers by the surface imprinting technique. *Eur. Polym. J.* **2021**, *145*, 110231. [\[CrossRef\]](#)
39. Cennamo, N.; D'Agostino, G.; Pesavento, M.; Zenia, L. High selectivity and sensitivity sensor based on MIP and SPR tapered plastic optical fibers for the detection of l-nicotine. *Sens. Actuators B Chem.* **2014**, *191*, 529–53638. [\[CrossRef\]](#)
40. Belmont, A.-S.; Jaeger, S.; Knopp, D.; Niessner, R.; Gauglitz, G.; Haupt, K. Molecularly imprinted polymer films for reflectometric interference spectroscopic sensors. *Biosens. Bioelectron.* **2007**, *22*, 3267–327239. [\[CrossRef\]](#)

41. Wang, M.; Wang, Y.; Qiao, Y.; Wei, M.; Gao, L.; Wang, L.; Yan, Y.; Li, H. High-sensitive imprinted membranes based on surface-enhanced Raman scattering for selective detection of antibiotics in water. *Spectrochim. Acta Part A Mol. Biomol. Spectrosc.* **2019**, *222*, 117116. [\[CrossRef\]](#)
42. Moreira, F.T.C.; Dutra, R.A.F.; Noronha, J.P.C.; Sales, M.G.F. Electrochemical biosensor based on biomimetic material for myoglobin detection. *Electrochim. Acta* **2013**, *107*, 481–487. [\[CrossRef\]](#)
43. Bai, X.; Zhang, B.; Liu, M.; Hu, X.; Fang, G.; Wang, S. Molecularly imprinted electrochemical sensor based on polypyrrole/dopamine@graphene incorporated with surface molecularly imprinted polymers thin film for recognition of olaquinox. *Bioelectrochemistry* **2020**, *132*, 107398. [\[CrossRef\]](#)
44. Ayankojo, A.G.; Boroznjak, R.; Reut, J.; Öpik, A.; Syritski, V. Molecularly imprinted polymer based electrochemical sensor for quantitative detection of SARS-CoV-2 spike protein. *Sens. Actuators B Chem.* **2022**, *353*, 131160. [\[CrossRef\]](#)
45. Ma, X.-T.; He, X.-W.; Li, W.-Y.; Zhang, Y.-K. Epitope molecularly imprinted polymer coated quartz crystal microbalance sensor for the determination of human serum albumin. *Sens. Actuators B Chem.* **2017**, *246*, 879–88656. [\[CrossRef\]](#)
46. Boysen, R.I.; Li, S.; Chowdhury, J.; Schwarz, L.J.; Hearn, M.T.W. Selectivity optimisation of biomimetic molecularly imprinted polymer thin films. *Microelectron. Eng.* **2012**, *97*, 81–84. [\[CrossRef\]](#)
47. Fang, G.; Zhai, X.; Deng, Q.; Yuan, S.; Cao, M.; Wang, S. Preparation and Evaluation of Lysozyme Molecularly Imprinted Polymer Film on the Surface of Multi-wall Carbon Nanotubes. *Curr. Org. Chem.* **2012**, *16*, 1461–1467. [\[CrossRef\]](#)
48. Zhang, H. *Molecular Imprinting: Principles and Applications of Micro- and Nano-Structured Polymers*, 1st ed.; Pan Stanford Publishing Pte Ltd.: Singapore, 2012; pp. 87–130.
49. Zhang, H. Recent Advances in Macromolecularly Imprinted Polymers by Controlled Radical Polymerization Techniques. *Mol. Imprinting* **2015**, *3*, 35–46. [\[CrossRef\]](#)
50. Patra, S.; Roy, E.; Madhuri, R.; Sharma, P.K. Nano-iniferter based imprinted sensor for ultra-trace level detection of prostate-specific antigen in both men and women. *Biosens. Bioelectron.* **2015**, *66*, 1–10. [\[CrossRef\]](#) [\[PubMed\]](#)
51. Chen, R.R.; Qin, L.; Jia, M.; He, X.W.; Li, W.Y. Novel surface modified molecularly imprinted membrane prepared with iniferter for permselective separation of lysozyme. *J. Membr. Sci.* **2010**, *363*, 212–220. [\[CrossRef\]](#)
52. Gai, Q.Q.; Qu, F.; Liu, Z.J.; Dai, R.J.; Zhang, Y.K. Superparamagnetic lysozyme surface-imprinted polymer prepared by atom transfer radical polymerization and its application for protein separation. *J. Chromatogr. A* **2010**, *1217*, 5035–5042. [\[CrossRef\]](#)
53. Titirici, M.M.; Sellergren, B. Thin molecularly imprinted polymer films via reversible addition-fragmentation chain transfer polymerization. *Chem. Mater.* **2006**, *18*, 1773–1779. [\[CrossRef\]](#)
54. Akgönlü, S.; Armutcu, C.; Denizli, A. Molecularly imprinted polymer film based plasmonic sensors for detection of ochratoxin A in dried fig. *Polym. Bull.* **2021**. [\[CrossRef\]](#)
55. He, C.; Liu, F.; Li, K.; Liu, H. Molecularly Imprinted Polymer Film Grafted from Porous Silica for Selective Recognition of Testosterone. *Anal. Lett.* **2006**, *39*, 275–286. [\[CrossRef\]](#)
56. Tarannum, N.; Singh, M. Water-compatible surface imprinting of ‘baclofen’ on silica surface for selective recognition and detection in aqueous solution. *Anal. Methods* **2012**, *4*, 3019–3026. [\[CrossRef\]](#)
57. Shahhoseini, F.; Langille, E.A.; Azizi, A.; Bottaro, C.S. Thin film molecularly imprinted polymer (TF-MIP), a selective and single-use extraction device for high-throughput analysis of biological samples. *Analyst* **2021**, *146*, 3157–3168. [\[CrossRef\]](#)
58. Hudson, A.D.; Jamieson, O.; Crapnell, R.D.; Rurack, K.; Soares, T.C.C.; Mecozzi, F.; Laude, A.; Gruber, J.; Novakovic, K.; Peeters, M. Dual detection of nafcillin using a molecularly imprinted polymer-based platform coupled to thermal and fluorescence read-out. *Mater. Adv.* **2021**, *2*, 5105–5115. [\[CrossRef\]](#)
59. Fourati, N.; Blel, N.; Lattach, Y.; Ktari, N.; Zerrouki, C. Chemical and Biological Sensors from Conducting and Semiconducting Polymers. In *Reference Module in Materials Science and Materials Engineering*; Elsevier: Amsterdam, The Netherlands, 2016.
60. Inzelt, G. *Conducting Polymers—A New Area in Electrochemistry*; Springer: Berlin/Heidelberg, Germany, 2008; pp. 123–135.
61. Heinze, J.; Frontana-Urbe, B.A.; Ludwigs, S. Electrochemistry of conducting polymers-persistent models and new concepts. *Chem. Rev.* **2010**, *110*, 4724–4771. [\[CrossRef\]](#)
62. Palma-cando, A.; Rendon-Enriquez, I.; Tausch, M.; Scherf, S. Thin functional polymer films by electropolymerization. *Nanomaterials* **2019**, *9*, 1125. [\[CrossRef\]](#)
63. Riaz, U.; Ashraf, S.M. Conductive Polymer Composite and Blends: Recent Trends. In *Nanostructured Polymer Blends*; Thomas, S., Shanks, R., Sarathchandran, C., Eds.; William Andrew Publishing: Norwich, NY, USA, 2014; pp. 509–538.
64. De Leon, A.; Advincula, R.C. Chapter 11—Intelligent Coatings for Corrosion Control Conducting Polymers with Superhydrophobic Effects as Anticorrosion Coating. In *Intelligent Coatings for Corrosion Control*; Tiwari, A., Rawlins Hihara, L.H., Eds.; Butterworth-Heinemann: Oxford, UK, 2015; pp. 409–430.
65. Gvozdenović, M.M.; Jugović, B.Z.; Stevanović, J.S.; Grgur, B.N. Electrochemical synthesis of electroconducting polymers. *Chem. Ind.* **2014**, *68*, 673–684. [\[CrossRef\]](#)
66. Wallace, G.G.; Tsekouras, G.; Wang, C. Chapter 11—Inherently conducting polymers via electropolymerization for energy conversion and storage. In *Electropolymerization: Concepts, Materials and Applications*; Cosnier, S., Karyakin, A., Eds.; Wiley-VCH: Weinheim, Germany, 2010; p. 216.
67. Mu, S.; Yang, Y. Spectral characteristics of polyaniline nanostructures synthesized by using cyclic voltammetry at different scan rates. *J. Phys. Chem. B* **2008**, *112*, 11558–11563. [\[CrossRef\]](#)

68. Gupta, V.; Miura, N. Large-area network of polyaniline nanowires prepared by potentiostatic deposition process. *Electrochem. Commun.* **2005**, *7*, 995–999. [\[CrossRef\]](#)
69. Antuna-Jimenez, S.; Diaz-Diaz, G.; Blanco-Lopez, M.C.; Lobo-Castanon, M.J.; Miranda-Ordieres, A.J.; Tunon-Blanco, P. Chapter 1—Molecularly imprinted electrochemical sensors: Past, present, and future. In *Molecularly Imprinted Sensors: Overview and Applications*; Li, S., Ge, Y., Piletsky, S.A., Lunec, J., Eds.; Elsevier: Amsterdam, The Netherlands, 2012; pp. 1–34.
70. Ahmad, O.S.; Bedwell, T.S.; Esen, C.; Garcia-Cruz, A.; Piletsky, S.A. Molecularly imprinted polymers in electrochemical and optical sensors. *Trends Biotechnol.* **2019**, *37*, 294–309. [\[CrossRef\]](#)
71. Gui, R.; Jin, H.; Guo, H.; Wang, Z. Recent advances and future prospects in molecularly imprinted polymers-based electrochemical biosensors. *Biosens. Bioelectron.* **2018**, *100*, 56–70. [\[CrossRef\]](#)
72. Menon, S.; Jesny, S.; Kumar, K.G. A voltammetric sensor for acetaminophen based on electropolymerized molecularly imprinted poly(*o*-aminophenol) modified gold electrode. *Talanta* **2018**, *179*, 668–675. [\[CrossRef\]](#) [\[PubMed\]](#)
73. Ali, M.R.; Bacchu, M.S.; Daizy, M.; Tarafder, C.; Hossain, M.S.; Rahman, M.M.; Khan, M.Z.H. A highly poly-arginine based MIP as an electrochemical sensor for selective detection of dimetridazole. *Anal. Chim. Acta* **2020**, *1121*, 11–16. [\[CrossRef\]](#) [\[PubMed\]](#)
74. Ayankojo, A.G.; Reut, J.; Ciocan, V.; Opik, A.; Syritski, V. Molecularly imprinted polymer-based sensor for electrochemical detection of erythromycin. *Talanta* **2020**, *209*, 120502. [\[CrossRef\]](#) [\[PubMed\]](#)
75. Bougrini, M.; Florea, A.; Cristea, C.; Sandulescu, R.; Vocanson, F.; Errachid, A.; Bouchikhi, B.; El Bari, N.; Jaffrezic-Renault, N. Development of a novel sensitive molecularly imprinted polymer sensor based on electropolymerization of a microporous-metal-organic framework for tetracycline detection in honey. *Food Control* **2016**, *59*, 424–429. [\[CrossRef\]](#)
76. Arvand, M.; Zamani, M.; Ardaki, M.S. Rapid electrochemical synthesis of molecularly imprinted polymers on functionalized multi-walled carbon nanotubes for selective recognition of sunset yellow in food samples. *Sens. Actuators B* **2017**, *243*, 927–939. [\[CrossRef\]](#)
77. Shen, J.; Gan, T.; Jin, Y.; Wang, J.; Wu, K. Electrochemical sensor based on electropolymerized dopamine molecularly imprinted film for tetrabromobisphenol A. *J. Electroanal. Chem.* **2018**, *826*, 10–15. [\[CrossRef\]](#)
78. Wang, D.; Wang, J.; Zhang, J.; Li, Y.; Zhang, Y.; Li, Y.; Ye, B.C. Novel electrochemical sensing platform based on integration of molecularly imprinted polymer with Au@Ag hollow nanoshell for determination of resveratrol. *Talanta* **2019**, *196*, 479–485. [\[CrossRef\]](#)
79. Li, X.; He, Y.; Zhao, F.; Zhang, W.; Ye, Z. Molecularly imprinted polymer-based sensors for atrazine detection by electropolymerization of *o*-phenylenediamine. *RSC Adv.* **2015**, *5*, 56534–56540. [\[CrossRef\]](#)
80. Motia, S.; Tudor, I.A.; Popescu, R.M.; Bouchikhi, B.; Bari, N. Development of a novel electrochemical sensor based on electropolymerized molecularly imprinted polymer for selective detection of sodium lauryl sulfate in environmental waters and cosmetic products. *J. Electroanal. Chem.* **2018**, *823*, 553–562. [\[CrossRef\]](#)
81. Seguro, I.; Pacheco, J.G.; Delerue-Matos, C. Low cost, easy to prepare and disposable electrochemical molecularly imprinted sensor for diclofenac detection. *Sensors* **2021**, *21*, 1975. [\[CrossRef\]](#)
82. Liu, F.; Kan, X. Conductive imprinted electrochemical sensor for epinephrine sensitive detection and double recognition. *J. Electroanal. Chem.* **2019**, *836*, 182–189. [\[CrossRef\]](#)
83. Lopes, F.; Pacheco, J.G.; Rebelo, P.; Delerue-Matos, C. Molecularly imprinted electrochemical sensor prepared on a screen-printed carbon electrode for naloxone detection. *Sens. Actuators B* **2017**, *243*, 745–752. [\[CrossRef\]](#)
84. Shaabani, N.; Chan, N.W.C.; Lee, W.E.; Jemere, A.B. Electrochemical determination of naloxone using molecularly imprinted poly(para-phenylenediamine) sensor. *J. Electrochem. Soc.* **2020**, *167*, 137508. [\[CrossRef\]](#)
85. Couto, R.A.S.; Mounsef, B., Jr.; Carvalho, F.; Rodrigues, C.M.P.; Braga, A.A.C.; Aldous, L.; Goncalves, L.M.; Quinaz, M.B. Methylone screening with electropolymerized molecularly imprinted polymer on screen-printed electrodes. *Sens. Actuators B Chem.* **2020**, *316*, 128133. [\[CrossRef\]](#)
86. Li, W.; Zheng, Y.; Zhang, T.; Wu, S.; Zhang, J.; Fang, J. A surface plasmon resonance-based optical fiber probe fabricated with electropolymerized molecular imprinting film for melamine detection. *Sensors* **2018**, *18*, 828. [\[CrossRef\]](#)
87. Regasa, M.B.; Soreta, T.R.; Femi, O.E.; Ramamurthy, P.C.; Kumar, S. Molecularly imprinted polyaniline molecular receptor-based chemical sensor for electrochemical determination of melamine. *J. Mol. Recognit.* **2020**, *33*, 1–11. [\[CrossRef\]](#)
88. Roushani, M.; Zalpour, N. Selective detection of Asulam with in-situ dopamine electropolymerization based electrochemical MIP sensor. *React. Funct. Polym.* **2021**, *169*, 105069. [\[CrossRef\]](#)
89. Wei, M.; Geng, X.; Liu, Y.; Long, H.; Du, J. A novel electrochemical sensor based on electropolymerized molecularly imprinted polymer for determination of luteolin. *J. Electroanal. Chem.* **2019**, *842*, 184–192. [\[CrossRef\]](#)
90. Zhen, L.; Zhang, C.; Ma, J.; Hong, S.; She, Y.; El-Aty, A.M.A.; He, Y.; Yhu, H.; Liu, H.; Wang, J. Fabrication of a highly sensitive electrochemical sensor based in electropolymerized molecularly imprinted polymer hybrid nanocomposites for the detection of 4-nonylphenol in packaged milk samples. *Anal. Biochem.* **2018**, *559*, 44–50. [\[CrossRef\]](#)
91. Mathieu-Scheers, E.; Bouden, S.; Grillot, C.; Bicolle, J.; Warmont, F.; Bertagna, V.; Cagnon, B.; Vautrin-UI, C. Trace anthracene electrochemical detection based on electropolymerized-molecularly imprinted polypyrrole modified glassy carbon electrode. *J. Electroanal. Chem.* **2019**, *848*, 113253. [\[CrossRef\]](#)
92. Grothe, R.A.; Lobato, A.; Mounsef, B., Jr.; Tasic, N.; Braga, A.A.; Maldaner, A.O.; Aldous, L.; Paixao, T.R.L.C.; Goncalves, L.M. Electroanalytical profiling of cocaine samples by means of an electropolymerized molecularly imprinted polymer using benzocaine as the template molecule. *Analyst* **2021**, *146*, 1747–1759. [\[CrossRef\]](#)

93. Radi, A.E.; Abd-Ellatief, M.R. Molecularly imprinted poly-o-phenylenediamine electrochemical sensor for entacapone. *Electroanalysis* **2021**, *33*, 1578–1584. [\[CrossRef\]](#)
94. Leibl, N.; Haupt, K.; Gonzato, C.; Duma, L. Molecularly Imprinted Polymers for Chemical Sensing: A Tutorial Review. *Chemosensors* **2021**, *9*, 123. [\[CrossRef\]](#)
95. Adams, R.N. Carbon paste electrodes. *Anal. Chem.* **1958**, *30*, 1576. [\[CrossRef\]](#)
96. Švancara, I.; Kalcher, K. *Carbon Paste Electrodes, Electrochemistry of Carbon Electrodes*, 1st ed.; Wiley-VCH: Weinheim, Germany, 2015; pp. 379–423.
97. Materon, E.M.; Wong, A.; Gomes, L.M.; Ibañez-Redi, G.; Joshi, N., Jr.; Oliveira, N.O.; Faria, R.C. Combining 3D printing and screen-printing in miniaturized, disposable sensors with carbon paste electrodes. *J. Mater. Chem. C* **2021**, *9*, 5633–5642. [\[CrossRef\]](#)
98. Wahyuni, W.T.; Putra, B.R.; Fauzi, A.; Ramadhanti, D.; Rohaeti, E.; Heryanto, R. A Brief Review on Fabrication of Screen-Printed Carbon Electrode: Materials and Techniques. *Indo. J. Chem. Res.* **2021**, *8*, 210–218. [\[CrossRef\]](#)
99. Kant, T.; Shrivastava, K.; Dewangan, K.; Kumar, A.; Jaiswal, N.K.; Deb, M.K.; Pervez, S. Design and development of conductive nanomaterials for electrochemical sensors: A modern approach. *Mater. Today Chem.* **2022**, *24*, 100769. [\[CrossRef\]](#)
100. Zhang, J.; Ahmadi, M.; Fargas, G.; Perinka, N.; Reguera, J.; Lanceros-Méndez, S.; Llanes, L.; Jiménez-Piqué, E. Silver Nanoparticles for Conductive Inks: From Synthesis and Ink Formulation to Their Use in Printing Technologies. *Metals* **2022**, *12*, 234. [\[CrossRef\]](#)
101. Stefano, J.S.; Orzari, L.O.; Silva-Neto, H.A.; Neiva de Ataíde, V.; Mendes, L.F.; Coltro, W.K.T.; Paixão, T.R.L.C.; Janegitz, B.C. Different approaches for fabrication of low-cost electrochemical sensors. *Curr. Opin. Electrochem.* **2022**, *32*, 100893. [\[CrossRef\]](#)
102. Fletcher, S. *Electrochemistry of Carbon Electrodes, Screen-Printed Carbon Electrodes*, 1st ed.; Wiley-VCH: Weinheim, Germany, 2015; pp. 425–443.
103. Jewell, E.; Philip, B.; Greenwood, P. Improved Manufacturing Performance of Screen Printed Carbon Electrodes through Material Formulation. *Biosensors* **2016**, *6*, 30. [\[CrossRef\]](#)
104. Hart, J.P.; Wring, S.A. Recent developments in the design and application of screen-printed electrochemical sensors for biomedical, environmental, and industrial analyses. *TrAC Trends Anal. Chem.* **1997**, *16*, 89–103. [\[CrossRef\]](#)
105. Morrin, A.; Killard, A.J.; Smyth, M.R. Electrochemical Characterization of Commercial and Home-Made Screen-Printed Carbon Electrodes. *Anal. Lett.* **2003**, *36*, 2021–2039. [\[CrossRef\]](#)
106. Andreotti, I.A.D.A.; Orzari, L.O.; Camargo, J.R.; Faria, R.C.; Marcolino-Junior, L.H.; Bergamini, M.F.; Gatti, A.; Janegitz, B.C. Disposable and flexible electrochemical sensor made by recyclable material and low cost conductive ink. *J. Electroanal. Chem.* **2019**, *840*, 109–116. [\[CrossRef\]](#)
107. Dimitriou, E.; Michailidis, N. Printable conductive inks used for the fabrication of electronics: An overview. *Nanotechnology* **2021**, *32*, 502009. [\[CrossRef\]](#) [\[PubMed\]](#)
108. Philip, B.; Jewell, E.; Worsley, D. The impact of solvent characteristics on performance and process stability of printed carbon resistive materials. *J. Coat. Technol. Res.* **2016**, *13*, 911–920. [\[CrossRef\]](#)
109. Ding, H.; He, P.; Yang, J.; Liu, C.; Zhao, H.; Derby, B. Water-based highly conductive graphene inks for fully printed humidity sensors. *J. Phys. D Appl. Phys.* **2020**, *53*, 455304. [\[CrossRef\]](#)
110. Unger, C.; Lieberzeit, P.A. Molecularly imprinted thin film surfaces in sensing: Chances and challenges. *React. Funct. Polym.* **2021**, *161*, 104855. [\[CrossRef\]](#)
111. Camargo, J.R.; Silva, T.A.; Rivas, G.A.; Janegitz, B.C. Novel eco-friendly water-based conductive ink for the preparation of disposable screen-printed electrodes for sensing and biosensing applications. *Electrochim. Acta* **2022**, *409*, 139968. [\[CrossRef\]](#)
112. Li, M.; Li, Y.-T.; Li, D.-W.; Long, Y.-T. Recent developments and applications of screen-printed electrodes in environmental assays—A review. *Anal. Chim. Acta* **2012**, *734*, 31–44. [\[CrossRef\]](#)
113. Gavrilă, A.M.; Iordache, T.V.; Sârbu, A.; Ciurlică, A.L.; Zaharia, A.; Chiriac, A.L.; Sandu, T.; Stoica, E.B.; Apostol, S. Sensitive Hybrid Films Molecularly Imprinted with Thiodiglycol Coating Screen Printed Carbon Electrodes, and Process for Manufacturing them. Ro. Patent RO135012A2, 28 May 2021.
114. Ghorbani, A.; Ojani, R.; Ganjali, M.R.; Raoof, J. Direct voltammetric determination of carbendazim by utilizing a nanosized imprinted polymer/MWCNTs-modified electrode. *J. Iran. Chem. Soc.* **2021**, *18*, 3109–3118. [\[CrossRef\]](#)
115. Suresh, R.R.; Lakshmanakumar, M.; Jayalatha, J.B.B.A.; Rajan, K.S.; Sethuraman, S.; Krishnan, U.M.; Rayappan, J.B.B. Fabrication of screen-printed electrodes: Opportunities and challenges. *J. Mater. Sci.* **2021**, *56*, 8951–9006. [\[CrossRef\]](#)
116. Cervini, P.; Cavalheiro, É.T.G. Strategies for preparation of molecularly imprinted polymers modified electrodes and their application in electroanalysis: A review. *Anal. Lett.* **2012**, *45*, 297–313. [\[CrossRef\]](#)
117. Khosrokhavar, R.; Motaharian, A.; Hosseini, M.R.M.; Mohammadsadegh, S. Screen-printed carbon electrode (SPCE) modified by molecularly imprinted polymer (MIP) nanoparticles and graphene nanosheets for determination of sertraline antidepressant drug. *Microchem. J.* **2020**, *159*, 105348. [\[CrossRef\]](#)
118. Nontawong, N.; Ngaosri, P.; Chunta, S.; Jarujamrus, P.; Nacapricha, D.; Lieberzeit, P.A.; Amatongchai, M. Smart sensor for assessment of oxidative/nitrate stress biomarkers using a dual-imprinted electrochemical paper-based analytical device. *Anal. Chim. Acta* **2022**, *1191*, 339363. [\[CrossRef\]](#)
119. Mba, E.V.; Branger, C.; Bikanga, R.; Florea, A.M.; Istamboulie, G.; Calas-Blanchard, C.; Noguier, T.; Sarbu, A.; Brisset, H. Detection of Bisphenol A in aqueous medium by screen printed carbon electrodes incorporating electrochemical molecularly imprinted polymers. *Biosens. Bioelectron.* **2018**, *112*, 156–161.

120. Kamel, A.H.; Jiang, X.; Li, P.; Liang, R. A paper-based potentiometric sensing platform based on molecularly imprinted nanobeads for determination of bisphenol A. *Anal. Methods* **2018**, *10*, 3890–3895. [\[CrossRef\]](#)
121. Chacón, A.H.; Cetó, X.; Del Valle, M. Molecularly imprinted polymers—Towards electrochemical sensors and electronic tongues. *Anal. Bioanal. Chem.* **2021**, *413*, 6117–6140. [\[CrossRef\]](#)
122. Stoica, B.E.; Gavrilă, A.-M.; Sarbu, A.; Iovu, H.; Brisset, H.; Miron, A.; Iordache, T.-V. Uncovering the behavior of screen-printed carbon electrodes modified with polymers molecularly imprinted with lipopolysaccharide. *Electrochem. Commun.* **2021**, *124*, 106965. [\[CrossRef\]](#)
123. Prasad, B.B.; Srivastava, S.; Tiwari, K.; Sharma, P.S. Ascorbic acid sensor based on molecularly imprinted polymer-modified hanging mercury drop electrode. *Mater. Sci. Eng.* **2009**, *29*, 1082–1087. [\[CrossRef\]](#)
124. Liuduan, Y.; Youwen, T.; Weipeng, Z.; Zhaof, H. An electrochemical sensor for phenylephrine based on molecular imprinting. *Anal. Sci.* **2009**, *25*, 1089–1093.
125. Ebarvia, B.S.; Ubando, I.E.; Sevilla, F.B., III. Biomimetic piezoelectric quartz crystal sensor with chloramphenicol-imprinted polymer sensing layer. *Talanta* **2015**, *144*, 1260–1265. [\[CrossRef\]](#) [\[PubMed\]](#)
126. Yang, D.-H.; Lee, C.-S.; Jeon, B.-H.; Choi, S.M.; Kim, Y.-D.; Shin, J.S.; Kim, H. An electrochemical nanofilm sensor for determination of 1-hydroxypyrene using molecularly imprinted receptors. *J. Ind. Eng. Chem.* **2017**, *51*, 106–112. [\[CrossRef\]](#)
127. García-Mutio, D.; Gomez-Caballero, A.; Gotiandia, A.; Larrauri, I.; Goicolea, M.A.; Barrio, R.J. Controlled grafting of molecularly imprinted films on gold microelectrodes using a self-assembled thiol iniferter. *Electrochim. Acta* **2018**, *279*, 57–65. [\[CrossRef\]](#)
128. Shin, M.J.; Shin, Y.J.; Shin, J.S. Cholesterol recognition system by molecular imprinting on self-assembled monolayer. *Colloids Surf. A* **2018**, *559*, 365–371. [\[CrossRef\]](#)
129. Roushani, M.; Jalilian, Z.; Nezhadali, A. A novel electrochemical sensor based on electrode modified with gold nanoparticles and molecularly imprinted polymer for rapid determination of trazosin. *Colloids Surf. B Biointerfaces* **2018**, *172*, 594–600. [\[CrossRef\]](#)
130. Liu, L.; Zhu, X.; Zeng, Y.; Wang, H.; Lu, Y.; Zhang, J.; Yin, Z.; Chen, Z.; Yang, Y.; Li, L. An Electrochemical Sensor for Diphenylamine Detection Based on Reduced Graphene Oxide/Fe₃O₄-Molecularly Imprinted Polymer with 1,4-Butanediyl-3,3'-bis-1-vinylimidazolium Dihexafluorophosphate Ionic Liquid as Cross-Linker. *Polymers* **2018**, *10*, 1329. [\[CrossRef\]](#)
131. Angelis, P.N.; Casarin, J.; Júnior, A.C.G.; Rocha, L.R.; Prete, M.C.; Tarley, C.R.T. Development of a Novel Molecularly Imprinted Polyvinylimidazole/Functionalized Carbon Black Nanocomposite-based Paste Electrode for Electrochemical Sensing of Imazethapyr in Rice Samples. *Electroanalysis* **2021**. [\[CrossRef\]](#)
132. De los Santos, D.M.; Montes, A.; Sanchez-Coronilla, A.; Navas, J. Sol-gel applications for consolidating stones: An example for project-based learning in a physical chemistry lab. *J. Chem. Educ.* **2014**, *91*, 1481–1485. [\[CrossRef\]](#)
133. Figueira, R.B. Hybrid sol-gel coatings for corrosion mitigation: A critical review. *Polymers* **2020**, *12*, 689. [\[CrossRef\]](#)
134. Landau, M.V. Chapter 2.3.4—Sol-gel process. In *Handbook of Heterogeneous Catalysis*; Ertl, G., Knözinger, H., Schüth, F., Weitkamp, J., Eds.; Wiley-VCH: Weinheim, Germany, 2008; pp. 119–159.
135. Danks, A.E.; Hall, S.R.; Zchnep, Z. The evolution of ‘sol-gel’ as a technique for materials synthesis. *Mater. Horiz.* **2016**, *3*, 91. [\[CrossRef\]](#)
136. Montilla, F.; Cotarelo, M.A.; Morallon, E. Hybrid sol-gel-conducting polymer synthesised by electrochemical insertion: Tailoring the capacitance of polyaniline. *J. Mater. Chem.* **2008**, *19*, 305–310. [\[CrossRef\]](#)
137. Wang, D.H.; Bierwagen, G.P. Sol-gel coatings on metals for corrosion protection. *Prog. Org. Coat.* **2009**, *64*, 327. [\[CrossRef\]](#)
138. Dehghanghadikolaei, A.; Ansary, J.; Ghoreishi, R. Sol-gel process applications: A mini-review. *Proc. Nat. Res. Soc.* **2018**, *2*, 02008. [\[CrossRef\]](#)
139. Wang, Y.-L.; Gao, Y.-L.; Wang, P.-P.; Shang, H.; Pan, S.-Y.; Li, X.-J. Sol-gel molecularly imprinted polymer for selective solid phase microextraction of organophosphorus pesticides. *Talanta* **2013**, *115*, 920–927. [\[CrossRef\]](#)
140. Pandey, S.; Mishra, S.B. Sol-gel derived organic-inorganic hybrid materials: Synthesis, characterization and applications. *J. Sol-Gel. Sci. Technol.* **2011**, *59*, 73–94. [\[CrossRef\]](#)
141. Gavrilă, A.-M.; Radu, I.C.; Stroescu, H.; Zaharia, A.; Stoica, E.-B.; Ciurlica, A.-L.; Iordache, T.-V.; Sărbu, A. Role of Functional Monomers upon the Properties of Bisphenol A Molecularly Imprinted Silica Films. *Appl. Sci.* **2021**, *11*, 2956. [\[CrossRef\]](#)
142. Sarbu, A.; Iordache, T.V.; Florea, A.-M.; Georgescu, E.-B.; Apostol, S. Molecularly Imprinted Polymer Films with Drugs and Process for Their Obtaining. Ro. Patent RO133363B1, 29 April 2021.
143. Gavrilă, A.-M.; Iordache, T.V.; Lazau, C.; Rotariu, T.; Cernica, I.; Stroescu, H.; Stoica, M.; Orha, C.; Băndă, C.E.; Sarbu, A. Biomimetic Sensitive Elements for 2,4,6-Trinitrotoluene Tested on Multi-Layered Sensors. *Coatings* **2020**, *10*, 273. [\[CrossRef\]](#)
144. Mujahid, A.; Lieberzeit, P.A.; Dickert, F.L. Chemical sensors based on molecularly imprinted sol-gel materials. *Materials* **2010**, *3*, 2196–2217. [\[CrossRef\]](#)
145. Meng, Z.-H. Chapter 13—Molecularly imprinted sol-gel sensors. In *Molecularly Imprinted Sensors*; Songjun, L., Ge, L., Piletsky, S.A., Lunec, J., Eds.; Elsevier: Amsterdam, The Netherlands, 2012; pp. 303–337.
146. Guney, S.; Cebeci, F.C. Selective electrochemical sensor for theophylline based on an electrode modified with imprinted sol-gel film immobilized on carbon nanoparticle layer. *Sens. Actuators B Chem.* **2015**, *208*, 307–314. [\[CrossRef\]](#)
147. Bengamra, M.; Grayaa-Jaoued, N.; Khelifi-Riani, A.; Chehimi, M.M.; Kalfat, R. Highly selective molecularly imprinted sol-gel membrane grafted to gold for the detection of melamine. *Silicon* **2019**, *11*, 2267–2274. [\[CrossRef\]](#)
148. Ayankojo, A.G.; Reut, J.; Opik, A.; Furchner, A.; Syritski, V. Hybrid molecularly imprinted polymer for amoxicillin detection. *Biosens. Bioelectron.* **2018**, *118*, 102–107. [\[CrossRef\]](#)

149. Shang, L.; Liu, C.; Chen, B.; Hayashi, K. Development of molecular imprinted sol-gel LSPR sensor for detection of volatile cis-jasmone in plant. *Sens. Actuators B Chem.* **2018**, *260*, 617–626. [\[CrossRef\]](#)
150. Giustina, G.D.; Sonato, A.; Gazzola, E.; Ruffato, G.; Brusa, S.; Romanato, F. SPR Enhanced molecular imprinted sol-gel film: A promising tool for gas-phase TNT detection. *Mater. Lett.* **2016**, *162*, 44–47. [\[CrossRef\]](#)
151. Ribeiro, C.M.; Miguel, E.M.; Dos Silva, J.S.; Da Silva, C.B.; Goulart, M.O.F.; Kubota, L.T.; Gonzaga, F.B.; Santos, W.J.R.; Lima, P.L. Application of a nanostructured platform and imprinted sol-gel film for determination of chlorogenic acid in food samples. *Talanta* **2018**, *156–157*, 119–125. [\[CrossRef\]](#) [\[PubMed\]](#)
152. Chen, J.; Bai, H.; Xia, J.; Li, Z.; Liu, P.; Cao, Q. Electrochemical sensor for detection of europium based on poly-catechol and ion-imprinted sol-gel film modified screen-printed electrode. *J. Electroanal. Chem.* **2018**, *824*, 32–38. [\[CrossRef\]](#)
153. Chen, X.; Zhang, S.; Shan, X.; Chen, Z. Derivative chiral copper(II) complexes as template of an electrochemical molecular imprinting sol-gel sensor for enantioselective recognition of aspartic acid. *Anal. Chim. Acta.* **2019**, *1072*, 54–60. [\[CrossRef\]](#) [\[PubMed\]](#)
154. Li, F.; Gao, J.; Li, X.; Li, Y.; He, X.; Chen, L.; Zhang, Y. Preparation of magnetic molecularly imprinted polymers functionalized carbon nanotubes for highly selective removal of aristolochic acid. *J. Chromatogr. A* **2019**, *1602*, 168–177. [\[CrossRef\]](#) [\[PubMed\]](#)
155. Gao, W.; Wan, F.; Ni, W.; Wang, S.; Zhang, M.; Yu, J. Electrochemical sensor for detection of trichlorfon based on molecularly imprinted sol-gel films modified glassy carbon electrode. *J. Inorg. Organomet. Polym.* **2012**, *22*, 37–41. [\[CrossRef\]](#)
156. Liu, L.; Long, C.; Wei, S.; Sun, Y. Electrochemical sensor based on molecularly imprinted film for high sensitivity detection of clenbuterol prepared using sol-gel method. *Int. J. Electrochem. Sci.* **2021**, *16*, 210411. [\[CrossRef\]](#)
157. Xu, G.; Zhang, H.; Zhong, M.; Zhang, T.; Lu, X.; Kan, X. Imprinted sol-gel electrochemical sensor for melamine direct recognition and detection. *J. Electroanal. Chem.* **2014**, *713*, 112–118. [\[CrossRef\]](#)
158. Shaabani, N.; Chan, N.W.C.; Jemere, A.B. A molecularly imprinted sol-gel electrochemical sensor for naloxone determination. *Nanomaterials* **2021**, *11*, 631. [\[CrossRef\]](#)
159. Razavipanah, I.; Alipour, E.; Deiminat, B.; Rounaghi, G.H. A novel electrochemical imprinted sensor for ultrasensitive detection of the psychoactive substance “Mephedrone”. *Biosens. Bioelectron.* **2018**, *119*, 163–169. [\[CrossRef\]](#)
160. Bai, J.; Zhang, X.; Peng, Y.; Hong, X.; Liu, Y.; Jiang, S.; Ning, B.; Gao, Z. Ultrasensitive sensing of diethylstilbestrol based on AuNPs/MWCNTs-CS composites coupling with sol-gel molecularly imprinted polymer as a recognition element of an electrochemical sensor. *Sens. Actuators B Chem.* **2017**, *238*, 420–426. [\[CrossRef\]](#)
161. Deiminat, B.; Rounaghi, G.H. Fabrication of a new electrochemical imprinted sensor for determination of ketamine based on modified polytyramine/sol-gel/f-MWCNTs@AuNPs nanocomposite/pencil graphite electrode. *Sens. Actuators B Chem.* **2018**, *259*, 133–141. [\[CrossRef\]](#)
162. Algeri, C.; Drioli, E.; Guzzo, L.; Donato, L. Bio-Mimetic Sensors Based on Molecularly Imprinted Membranes. *Sensors* **2014**, *14*, 13863–13912. [\[CrossRef\]](#)
163. Hedborg, E.; Winqvist, F.; Lundstrom, I.; Andersson, L.I.; Mosbach, K. Some studies of molecularly imprinted polymer membranes in combination with field-effect devices. *Sens. Actuators A* **1993**, *37–38*, 796–799. [\[CrossRef\]](#)
164. Kobayashi, T.; Wang, H.Y.; Fujii, N. Molecular imprinting of theophylline in acrylonitrile–acrylic acid copolymer membrane. *Chem. Lett.* **1995**, *10*, 927–928. [\[CrossRef\]](#)
165. Mathew-Krotz, J.; Shea, K.J. Imprinted polymer membranes for the selective transport of targeted neutral molecules. *J. Am. Chem. Soc.* **1996**, *118*, 8154–8155. [\[CrossRef\]](#)
166. Yoshikawa, M. Molecularly imprinted polymeric membranes. *Bioseparation* **2001**, *10*, 277–286. [\[CrossRef\]](#)
167. Kobayashi, T.; Fukaya, T.; Abe, M.; Fujii, N. Phase inversion molecular imprinting by using template copolymers for high substrate recognition. *Langmuir* **2002**, *18*, 2866–2872. [\[CrossRef\]](#)
168. Stoica, E.-B.G.; Gavrilă, A.-M.F.; Iordache, T.-V.; Sarbu, A.; Iovu, H.; Sandu, T.; Brisset, H. Molecularly imprinted membranes obtained via wet phase inversion for ephedrine retention. *UPB Sci. Bull.* **2020**, *82*, 15–26.
169. Brisbane, C.; McCluskey, A.; Bowyer, M.; Holdsworth, C.I. Molecularly imprinted films of acrylonitrile/methyl methacrylate/acrylic acid terpolymers: Influence of methyl methacrylate in the binding performance of l-ephedrine imprinted films. *Org. Biomol. Chem.* **2013**, *11*, 2872–2884. [\[CrossRef\]](#) [\[PubMed\]](#)
170. Guillen, G.R.; Pan, Y.; Li, M.; Hoek, E.M.V. Preparation and Characterization of Membranes Formed by Nonsolvent Induced Phase Separation: A Review. *Ind. Eng. Chem. Res.* **2011**, *50*, 3798–3817. [\[CrossRef\]](#)
171. Kobayashi, T.; Murawaki, Y.; Reddy, P.S.; Abe, M.; Fujii, N. Molecular imprinting of caffeine and its recognition assay by quartz-crystal microbalance. *Anal. Chim. Acta* **2001**, *435*, 141–149. [\[CrossRef\]](#)
172. Yang, Q.; Wu, X.; Peng, H.; Fu, L.; Song, X.; Li, J.; Xiong, H.; Chen, L. Simultaneous phase-inversion and imprinting based sensor for highly sensitive and selective detection of bisphenol A. *Talanta* **2018**, *176*, 595–603. [\[CrossRef\]](#)
173. Florea, A.-M.; Sârbu, A.; Iordache, T.-V.; Zaharia, A.; Radu, A.-L.; Apostol, S.; Iancu, S.; Duldner, M.; Lazau, C.; Hubca, G. TNT-molecularly imprinted membranes via phase inversion method. In Proceedings of the Greener and Safer Energetic and Ballistic Systems Conference, Bucharest, Romania, 10–23 May 2015; pp. 24–31.
174. Turner, N.W.; Holmes, N.; Brisbane, C.; McGeachie, A.B.; Bowyer, M.C.; McCluskey, A.; Holdsworth, C.I. Effect of template on the formation of phase-inversed molecularly imprinted polymer thin films: An assessment. *Soft Matter* **2009**, *5*, 3663–3671. [\[CrossRef\]](#)
175. Kausar, A. Phase Inversion Technique-Based Polyamide Films and Their Applications: A Comprehensive Review. *Polym. Plast. Technol. Eng.* **2017**, *56*, 1421–1437. [\[CrossRef\]](#)

176. Ciobanu, M.; Marin, L.; Cozan, V.; Bruma, M. Aromatic polysulfones used in sensor applications. *Rev. Adv. Mater. Sci.* **2009**, *22*, 89–96.
177. Barbani, N.; Rosellini, E.; Donati, M.; Costantino, P.; Cristallini, C.; Ciardelli, G. Molecularly imprinted polymers by phase inversion technique for the selective recognition of saccharides of biomedical interest in aqueous solutions. *Polym. Int.* **2017**, *66*, 900–907. [[CrossRef](#)]
178. Udrea, I.; Sarbu, A.; Stefan, V.I.; Beda, M.; Nechifor, G.; Sarbu, L.; Radu, L.; Neata, M. Covalent immobilization of enzymes on molecularly imprinted polymers for biosensors. In Proceedings of the Conference CEEX, Brasov, Romania, 22–24 October 2006; pp. 1–8.
179. Udrea, I.; Sarbu, A.; Radu, G.L.; Nechifor, G.; Bradu, C.; Nicoleta, M.; Beda, M.; Sarbu, L.; Diaconu, M. Molecularly imprinted membranes with covalently immobilized enzymes for biosensors. In Proceedings of the Conference CEEX, Brasov, Romania, 24–26 October 2007; pp. 1–6.
180. Salehi, E.; Khajavian, M.; Sahebamee, N.; Mahmoudi, M.; Drioli, E.; Matsuura, T. Advances in nanocomposite and nanostructured chitosan membrane adsorbents for environmental remediation: A review. *Desalination* **2022**, *527*, 115565. [[CrossRef](#)]
181. Ma, X.; Chen, R.; Zheng, X.; Youn, H.; Chen, Z. Preparation of molecularly imprinted CS membrane for recognizing naringin in aqueous media. *Polym. Bull.* **2011**, *66*, 853–863. [[CrossRef](#)]
182. Silvestri, D.; Barbani, N.; Cristallini, C.; Giusti, P.; Ciardelli, G. Molecularly imprinted membranes for an improved recognition of biomolecules in aqueous medium. *J. Membr. Sci.* **2006**, *282*, 284–295. [[CrossRef](#)]
183. Lee, T.P.; Saad, B.; Nakajima, L.; Kobayashi, T. Preparation and Characterization of Hybrid Molecularly Imprinted Polymer Membranes for the Determination of Citrinin in Rice. *Sains Malays.* **2019**, *48*, 1661–1670. [[CrossRef](#)]
184. Rebelo, T.S.C.R.; Almeida, S.A.A.; Guerreiro, J.R.L.; Montenegro, M.C.B.S.M.; Sales, M.G.F. Trimethoprim-selective electrodes with molecularly imprinted polymers acting as ionophores and potentiometric transduction on graphite solid-contact. *Microchem. J.* **2011**, *98*, 21–28. [[CrossRef](#)]
185. Kamel, A.H.; Moreira, F.T.C.; Rebelo, T.S.C.R.; Sales, M.G.F. Molecularly-imprinted materials for potentiometric transduction: Application to the antibiotic enrofloxacin. *Anal. Lett.* **2011**, *44*, 2107–2123. [[CrossRef](#)]
186. Jurcevic, S.; Lee, M.-H.; Thomas, J.L.; Liao, C.-L.; Crnogorac-Jurcevic, T.; Lin, H.-Y. Polymers imprinted with three REG1B peptides for electrochemical determination of Regenerating Protein 1B, a urinary biomarker for pancreatic ductal adenocarcinoma. *Microchim. Acta* **2017**, *184*, 1773–1780.
187. Zakaria, N.A.; Zaliman, S.Q.; Leo, C.P.; Ahmad, A.L.; Ooi, B.S.; Poh, P.E. 3D imprinted superhydrophobic polyvinylidene fluoride/carbon black membrane for membrane distillation with electrochemical cleaning evaluation. *J. Environ. Chem. Eng.* **2022**, *10*, 107346. [[CrossRef](#)]
188. Meng, Y.; Chen, Y.; Lu, L.; Ding, Y.; Cusano, A.; Fan, J.A.; Hu, Q.; Wang, K.; Xie, Z.; Liu, Z.; et al. Waveguide-Based Fluorescent Immunosensor for the Simultaneous Detection of Carbofuran and 3-Hydroxy-Carbofuran. *Light Sci. Appl.* **2021**, *10*, 235. [[CrossRef](#)]
189. Sun, W.; Liu, L.; Memon, A.G.; Zhou, X.; Zhao, H. Waveguide-Based Fluorescent Immunosensor for the Simultaneous Detection of Carbofuran and 3-Hydroxy-Carbofuran. *Biosensors* **2020**, *10*, 191. [[CrossRef](#)]
190. Liu, L.; Shan, D.; Zhou, X.; Shi, H.; Song, B.; Falke, F.; Leinse, A.; Heideman, R. TriPleX™ waveguide-based fluorescence biosensor for multichannel environmental contaminants detection. *Biosens. Bioelectron.* **2018**, *106*, 117–121. [[CrossRef](#)]

MDPI
St. Alban-Anlage 66
4052 Basel
Switzerland
Tel. +41 61 683 77 34
Fax +41 61 302 89 18
www.mdpi.com

Applied Sciences Editorial Office
E-mail: appls@mdpi.com
www.mdpi.com/journal/appls



MDPI
St. Alban-Anlage 66
4052 Basel
Switzerland
Tel: +41 61 683 77 34
www.mdpi.com



ISBN 978-3-0365-5404-4